LOW-COST 5G WIRELESS ACCELEROMETER FOR CONDITION MONITORING

BY

BRAEDEN COOKE, B.TECH.

A Thesis Submitted to the School of Graduate Studies in Partial Fulfillment of the Requirements for the Degree Master of Applied Science

McMaster University © Copyright by Braeden Cooke, September 2025

Master of Applied Science (2025) McMaster University

Mechanical Engineering Hamilton, Ontario, Canada

TITLE: Low-Cost 5G Wireless Accelerometer for Condition

Monitoring

AUTHOR: Braeden Cooke, B.Tech.

(McMaster University, Hamilton, Ontario, Canada)

SUPERVISOR: Dr. Stephen C. Veldhuis

NUMBER OF PAGES: xxix, 209

Lay Abstract

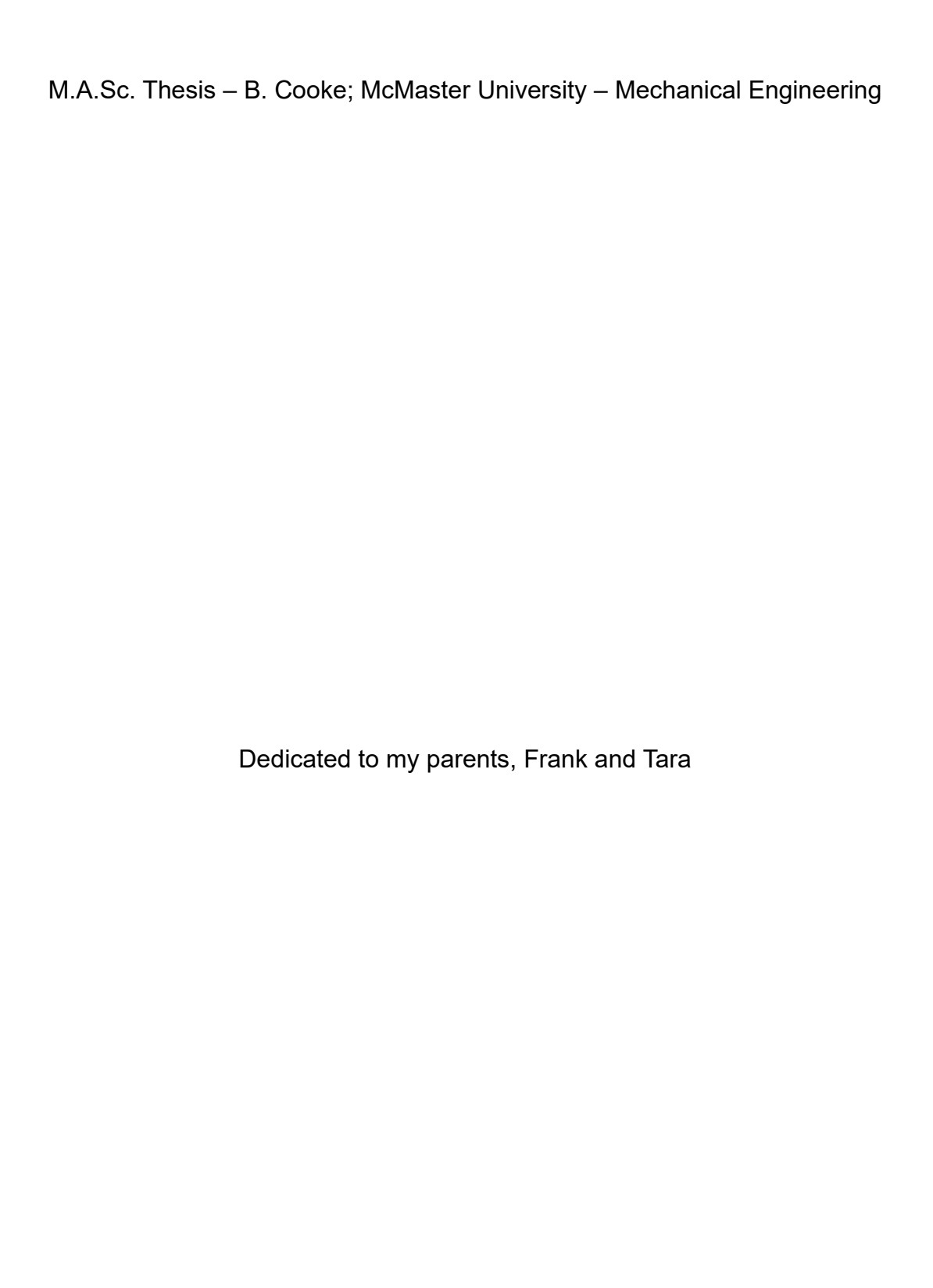
Manufacturing companies depend on machines to keep production running smoothly, but over time, wear and tear can lead to unexpected breakdowns, costly repairs, and lost productivity. One way to reduce these costs is condition-based monitoring, using sensors to monitor machine health and perform maintenance only when needed. However, the high cost and complex installation of traditional wired sensor systems limit their adoption. This research explores the use of low-cost, easy-to-deploy wireless sensors as an affordable alternative. While traditional wireless systems often require compromises in performance, this work investigates the use of emerging wireless technologies that maintain high data quality without the constraints of wired infrastructure. By addressing both hardware affordability and connectivity challenges, this study aims to make machine monitoring more accessible for manufacturers of all sizes, helping reduce downtime, lower costs, and improve productivity.

Abstract

Machine and equipment downtime have significant impacts on manufacturing costs, which has resulted in a long history of research into condition-based monitoring (CBM). While high-performance CBM systems exist in academic research settings, industrial implementation is usually limited to highly critical assets, due to high initial investment costs and network limitations. Even when used, industrial systems often employ manual periodic measurements performed by hand, resulting in data being missed that could improve decision making. Wireless sensors, utilizing lower cost modern micro-electrical mechanical system (MEMS) accelerometers, present an opportunity for wider CBM deployment in industry by lowering the required investment.

This thesis addresses these barriers by developing and evaluating a low-cost, wireless CBM system compatible with both 5G mmWave and Wi-Fi networks. A sensor prototype was developed using cost-effective MEMS accelerometers, specifically the ADXL-357 and ICM-42688-P, which have not been previously evaluated for CBM applications. The system's performance was compared to a high-end Integrated-electric piezoelectric (IEPE) system using a vibration shaker and a linear motion testbed. Results show that the low-cost MEMS sensors can provide data comparable to the IEPE reference, particularly for low frequency monitoring tasks. The 5G mmWave network performance testing showed that it can support high-throughput, low-latency data streams, with speeds and latencies

better than current wireless standards. Overall, this research shows that by combining low-cost MEMS sensors with next-generation wireless networks, it is feasible to create low-cost and scalable real-time wireless CBM systems, bridging the gap between academic research and industrial implementation.



Acknowledgements

First, I would like to thank my supervisor, Dr. Veldhuis, for his expertise and guidance throughout this research. His focus on great people, projects and equipment makes the MMRI an amazing place to study and work.

I am also grateful to the TERAGO team for their partnership on the 5G network at the MMRI and their support of this research. Special thanks to Clarence and Amir for their technical support, and to Daniel, Fadi, David, and Andrea for their support for MMRI 5G technical sessions and events.

I would also like to thank Kevin for his help with this project and for getting me involved at the MMRI in the first place. Andres, for his guidance throughout this project and for convincing me to pursue this degree. Also, the rest of the MMRI students and staff for their advice and feedback, and the entertaining lunch conversations.

Finally, I would like to thank my friends and family for their love and support. Including, but not limited to, my parents and sisters for cheering me on and Frances for keeping me fed and alive.

Table of Contents

Lay Abstract	iii
Abstract	iv
Acknowledgements	vii
Table of Contents	viii
List of Figures	xiv
List of Tables	xxiv
List of Abbreviations and Symbols	xxvii
Chapter 1: Introduction	1
1.1 Research Background and Motivation	1
1.2 Research Objectives & Contributions	3
1.3 Thesis Outline	5
Chapter 2: Literature Review	7
2.1 Condition-Based Monitoring (CBM)	7
2.2 Sensor Types for CBM	8
2.2.1 Vibration	9
2.2.2 Temperature	10
2.2.3 Current & Voltage	10

	2.2.4 Force	11
	2.2.5 Acoustic Emission (AE)	11
	2.2.6 Rotational speed	11
	2.2.7 Oil and Lubricant Condition Sensors	. 12
	2.2.8 Sensor Fusion (Multi-Sensor Systems)	. 12
2	.3 Accelerometer Types for CBM	. 13
	2.3.1 Piezoelectric Accelerometers	. 14
	2.3.2 MEMS Accelerometers	. 16
2	.4 Signal Acquisition Considerations	. 18
	2.4.1 Analog to Digital Conversion	. 19
	2.4.2 Sampling Rate and Nyquist Theory	. 20
	2.4.3 Filtering	. 20
2	.5 Industrial Networking & Wireless Sensor Networks	. 21
	2.5.1 Wired Networks	. 22
	2.5.2 Wireless Networking	. 22
	2.5.3 Current Wireless Standards	. 24
	2.5.4 Related Sensor Works	. 27
	2.5.5 Commercial Wireless Sensors	. 29
	2.5.6 Related Sensor Work from Literature	. 30

2	2.6 Current State of the Art	32
2	2.7 Summary & Research Gaps	34
Cha	apter 3: System Design & Implementation	36
3	3.1 System Considerations	36
	3.1.1 System Design Requirements/Criteria	36
	3.1.2 Sensor Strategy Considerations	38
3	3.2 Component Selection	41
	3.2.1 Accelerometer	42
	3.2.2 Microcontroller	54
	3.2.3 Battery	56
3	3.3 Electronics Design	58
3	3.4 Hardware Design	61
	3.4.1 Sensor Prototype Costs	61
3	5.5 Software Design	63
	3.5.1 Sensor Software	63
	3.5.2 Receiver Software	66
	3.5.3 Data formatting	67
Cha	apter 4: Chapter 4: Testing	70
4	.1 Testing Methodology	70

4.2 Accelerometer Test 1: Vibration Test Shaker	72
4.2.1 Test 1 Objectives and Setup	72
4.2.2 Test 1 Data Processing and Analysis	77
4.2.3 Test 1 Static Shaker Test Results	80
4.2.4 Test 1 Dynamic Shaker Test Results	95
4.2.5 Test 1 Conclusions	100
4.3 Accelerometer Test 2: Linear Motion Testbed	101
4.3.1 Test 2 Objectives and Setup	101
4.3.2 Test 2 Data Processing and Analysis	104
4.3.3 Test 2 Static Test Results	106
4.3.4 Test 2 Dynamic Test Results	112
4.4 Test 3: 5G mmWave Network Performance	131
Chapter 5: Discussion	136
5.1 Accelerometer Performance	136
5.2 Network Performance	137
Chapter 6: Conclusion and Future Work	139
6.1 Conclusions	139
6.2 Research Contributions	140
6.3 Future Work	141

6.3.1 Further ICM-42688-P Work	141
6.3.2 Multi 5G Wireless Sensor Setup	142
6.3.3 5G Native Microcontroller	143
6.3.4 Accelerometer Array	144
6.3.5 Accelerometer Alternatives	145
6.3.6 Database Integration	146
Chapter 7: References	148
Chapter 8: Appendix	154
8.1 Test 1 Graphs	154
8.1.1 ADXL-345 – Bolt Mounted, USB Powered, 1 g RMS	154
8.1.2 ADXL-357 – Bolt Mounted, USB Powered, 1 g RMS	162
8.1.3 ADXL-357 – Magnet Mounted, Battery Powered	168
8.1.4 ICM-42688-P – Magnet Mounted, Battery Powered, 5G, 4	kHz ODR
	181
8.1.5 IEPE Reference – PB352C03	198
8.2 Test 2 Graphs Static Data (Powered On vs Off)	199
8.2.1 ADXL-357 & IEPE (4 kHz Sampling Rate)	199
8.2.2 ICM-42688-P & IEPE (16 kHz Sampling Rate)	202
8.3 Test 2 High-Speed B3	205

M.A.Sc. Thesis – B. Cooke; McMaster University – Mechanical Engineer	ing
--	-----

8.3.1 ADXL-357 High-Speed B3 Graphs	. 206
8.3.2 ICM-42688-P High-Speed B3 Graphs	. 208

List of Figures

Figure 1: Shear type IEPE accelerometer	15
Figure 2: MEMS accelerometer	17
Figure 3: Typical high-end IEPE measurement chain	33
Figure 4: 5G mmWave high-end IEPE measurement chain	33
Figure 5: TERAGO 5G system map at the MMRI	39
Figure 6: 5G sensor communication	41
Figure 7: Sensor components	42
Figure 8: Accelerometer candidate comparison chart (based on [5])	51
Figure 9: GY-291 / EVAL-ADXL-345 (20.4 mm x 15.2 mm)	52
Figure 10: EVAL-ADXL-357Z PCB (0.8" x 0.8")	53
Figure 11: ICM-42688-P Evaluation PCB (0.8" x 0.8")	54
Figure 12: Wi-Fi sensor prototype electronics	60
Figure 13: 5G sensor prototype electronics	60
Figure 14: Sensor software basic functions	65
Figure 15: Sensor software file architecture	66
Figure 16: Receiver software basic functions	67
Figure 17: Testing plan	72
Figure 18: Cross-section of Handheld Vibration Shaker Head [84]	73
Figure 19: ADXL-345 mounted on shaker	74
Figure 20: ADXL-357 mounted on shaker	74

Figure 21: 5G Shaker testing setup diagram	75
Figure 22: Test 1 setup, ICM-42688-P 5G	76
Figure 23: Data processing steps	80
Figure 24: ADXL-345 x-axis PSD all ranges	81
Figure 25: ADXL-345 y-axis PSD all ranges	81
Figure 26: ADXL-345 z-axis PSD all ranges	82
Figure 27: ADXL-345 XYZ PSD all ranges	82
Figure 28: ADXL-357 x-axis PSD all ranges	84
Figure 29: ADXL-357 y-axis PSD all ranges	85
Figure 30: ADXL-357 z-axis PSD all ranges	85
Figure 31: ADXL-357 XYZ PSD 40 g range	86
Figure 32: ADXL-357 magnet mount x-axis PSD all ranges	88
Figure 33: ADXL-357 magnet mount y-axis PSD all ranges	88
Figure 34: ADXL-357 magnet mount z-axis PSD all ranges	89
Figure 35: ADXL-357 magnet mount XYZ PSD 40 g range	89
Figure 36: ICM-42688-P x-axis PSD all ranges	91
Figure 37: ICM-42688-P y-axis PSD all ranges	91
Figure 38: ICM-42688-P z-axis PSD all ranges	92
Figure 39: ICM-42688-P XYZ PSD all ranges	92
Figure 40: IEPE Reference PSD	94
Figure 41: Linear testbed component naming conventions	102
Figure 42: Test 2 sensor placements	102

Figure 43: Test 2 sensor installation	103
Figure 44: ADXL-357 10 g, B3 sensor, static noise testbed powered off	107
Figure 45: ADXL-357 10 g, B3 sensor, static noise testbed powered on	107
Figure 46: ADXL-357 10 g, LRR sensor, static noise testbed powered off	108
Figure 47: ADXL-357 10 g, LRR sensor, static noise testbed powered on	108
Figure 48: ICM-42688-P static noise testbed powered off	109
Figure 49: IEPE B3 static noise testbed powered off	110
Figure 50: ICM-42688-P static noise, testbed powered off (4 kHz cutoff)	110
Figure 51: ICM-42688-P static noise, testbed powered on	111
Figure 52: ICM-42688-P static noise, testbed powered on (4 kHz cutoff)	111
Figure 53: Time domain B3 ADXL-357 (Blue) vs IEPE (Yellow), low speed	115
Figure 54: FFT B3 ADXL-357 (Blue) vs IEPE (Yellow), low speed	116
Figure 55: Time domain B3 ADXL-357 (Blue) vs IEPE (Yellow), medium speed	i
	118
Figure 56: FFT B3 ADXL-357 (Blue) vs IEPE (Yellow), medium speed	119
Figure 57: Time domain LRR ADXL-357 (Blue) vs IEPE (Yellow), low speed	121
Figure 58: FFT LRR ADXL-357 (Blue) vs IEPE (Yellow), low speed	122
Figure 59: Time domain LRR ADXL-357 (Blue) vs IEPE (Yellow), static	123
Figure 60: Time domain LRR ADXL-357 (Blue) vs IEPE (Yellow), medium spee	ed
	124
Figure 61: FFT LRR ADXL-357 (Blue) vs IEPE (Yellow), medium speed	125
Figure 62: Time domain B3 ICM-42688-P (Blue) vs IEPE (Yellow), low speed.	127

Figure 63: FFT B3 ICM-42688-P (Blue) vs IEPE (Yellow), low speed	128
Figure 64: Time domain B3 ICM-42688-P (Blue) vs IEPE (Yellow), medium s	peed
	130
Figure 65: FFT B3 ICM-42688-P (Blue) vs IEPE (Yellow), medium speed	131
Figure 66: Iperf 5G network testing setup	132
Figure 67: 5G mmWave test points	133
Figure 68: Multi 5G sensor testbed setup	143
Figure 69: Network diagram, 5G sensors with server and database	147
Figure 70: ADXL-345 2 g Time-domain plot	154
Figure 71: ADXL-345 2 g Frequency-domain plot	155
Figure 72: ADXL-345 2 g Frequency-domain plot peak	155
Figure 73: ADXL-345 2 g Frequency-domain plot peak windowed	156
Figure 74: ADXL-345 4 g Time-domain plot	156
Figure 75: ADXL-345 4 g Frequency-domain plot	157
Figure 76: ADXL-345 4 g Frequency-domain plot peak	157
Figure 77: ADXL-345 4 g Frequency-domain plot peak windowed	158
Figure 78: ADXL-345 8 g Time-domain plot	158
Figure 79: ADXL-345 8 g Frequency-domain plot	159
Figure 80: ADXL-345 8 g Frequency-domain plot peak	159
Figure 81: ADXL-345 8 g Frequency-domain plot peak windowed	160
Figure 82: ADXL-345 16 g Time-domain plot	160
Figure 83: ADXL-345 16 g Frequency-domain	161

Figure 84: ADXL-345 16 g Frequency-domain plot peak	161
Figure 85: ADXL-345 16 g Frequency-domain plot peak windowed	162
Figure 86: ADXL-357 10 g Time-domain plot	162
Figure 87: ADXL-357 10 g Frequency-domain plot	163
Figure 88: ADXL-357 10 g Frequency-domain plot peak	163
Figure 89: ADXL-357 10 g Frequency-domain plot peak windowed	164
Figure 90: ADXL-357 20 g Time-domain plot	164
Figure 91: ADXL-357 20 g Frequency-domain plot	165
Figure 92: ADXL-357 20 g Frequency-domain plot peak	165
Figure 93: ADXL-357 20 g Frequency-domain plot peak windowed	166
Figure 94: ADXL-357 40 g Time-domain plot	166
Figure 95: ADXL-357 40 g Frequency-domain plot	167
Figure 96: ADXL-357 40 g Frequency-domain plot peak	167
Figure 97: ADXL-357 40 g Frequency-domain plot peak windowed	168
Figure 98: ADXL-357 magnet mounted 10 g Time-domain plot 1 g RMS	168
Figure 99: ADXL-357 magnet mounted 10 g Frequency-domain plot 1 g RMS	169
Figure 100: ADXL-357 magnet mounted 10 g Frequency-domain plot peak 1 g	g
RMS	169
Figure 101: ADXL-357 magnet mounted 10 g Frequency-domain plot peak	
windowed 1 g RMS	170
Figure 102: ADXL-357 magnet mounted 20 g Time-domain plot 1 g RMS	170

Figure 103: ADXL-357 magnet mounted 20 g Frequency-domain plot 1 g RMS
Figure 104: ADXL-357 magnet mounted 20 g Frequency-domain plot peak 1 g
RMS171
Figure 105: ADXL-357 magnet mounted 20 g Frequency-domain plot peak
windowed 1 g RMS172
Figure 106: ADXL-357 magnet mounted 40 g Time-domain plot 1 g RMS 172
Figure 107: ADXL-357 magnet mounted 40 g Frequency-domain plot 1 g RMS
Figure 108: ADXL-357 magnet mounted 40 g Frequency-domain plot peak 1 g
RMS
Figure 109: ADXL-357 magnet mounted 40 g Frequency-domain plot peak
windowed 1 g RMS174
Figure 110: ADXL-357 magnet mounted 10 g Time-domain plot 1 g Pk 174
Figure 111: ADXL-357 magnet mounted 10 g Frequency-domain plot 1 g Pk 175
Figure 112: ADXL-357 magnet mounted 10 g Frequency-domain plot peak 1 g Pk
Figure 113: ADXL-357 magnet mounted 10 g Frequency-domain plot peak
windowed 1 g Pk 176
Figure 114: ADXL-357 magnet mounted 20 g Time-domain plot 1 g Pk 176
Figure 115: ADXL-357 magnet mounted 20 g Frequency-domain plot 1 g Pk 177

Figure 116: ADXL-357 magnet mounted 20 g Frequency-domain plot peak 1 g l	Pk
1	77
Figure 117: ADXL-357 magnet mounted 20 g Frequency-domain plot peak	
windowed 1 g Pk1	78
Figure 118: ADXL-357 magnet mounted 40 g Time-domain plot 1 g Pk 1	78
Figure 119: ADXL-357 magnet mounted 40 g Frequency-domain plot 1 g Pk 1	79
Figure 120: ADXL-357 magnet mounted 40 g Frequency-domain plot peak 1 g	Pk
1	79
Figure 121: ADXL-357 magnet mounted 40 g Frequency-domain plot peak	
windowed 1 g Pk1	80
Figure 122: ICM-42688-P magnet mounted 2 g Time-domain plot 1 g RMS 1	81
Figure 123: ICM-42688-P magnet mounted 2 g Frequency-domain plot 1 g RMS	S
1	82
Figure 124: ICM-42688-P magnet mounted 2 g Frequency-domain plot peak 1	g
RMS1	82
Figure 125: ICM-42688-P magnet mounted 2 g Frequency-domain plot peak	
windowed 1 g RMS1	83
Figure 126: ICM-42688-P magnet mounted 4 g Time-domain plot 1 g RMS 1	83
Figure 127: ICM-42688-P magnet mounted 4 g Frequency-domain plot 1 g RMS	S
1	84
Figure 128: ICM-42688-P magnet mounted 4 g Frequency-domain plot peak 1	g
RMS	84

Figure 129: ICM-42688-P magnet mounted 4 g Frequency-domain plot peak	
windowed 1 g RMS1	85
Figure 130: ICM-42688-P magnet mounted 8 g Time-domain plot 1 g RMS 1	85
Figure 131: ICM-42688-P magnet mounted 8 g Frequency-domain plot 1 g RMS	S
1	86
Figure 132: ICM-42688-P magnet mounted 8 g Frequency-domain plot peak 1	g
RMS1	86
Figure 133: ICM-42688-P magnet mounted 8 g Frequency-domain plot peak	
windowed 1 g RMS1	87
Figure 134: ICM-42688-P magnet mounted 16 g Time-domain plot 1 g RMS 1	87
Figure 135: ICM-42688-P magnet mounted 16 g Frequency-domain plot 1 g RN	/IS
1	88
Figure 136: ICM-42688-P magnet mounted 16 g Frequency-domain plot peak 1	g
RMS1	88
Figure 137: ICM-42688-P magnet mounted 16 g Frequency-domain plot peak	
windowed 1 g RMS1	89
Figure 138: ICM-42688-P magnet mounted 2 g Time-domain plot 1 g Pk 1	90
Figure 139: ICM-42688-P magnet mounted 2 g Frequency-domain plot 1 g Pk1	90
Figure 140: ICM-42688-P magnet mounted 2 g Frequency-domain plot peak 1	g
Pk	91
Figure 141: ICM-42688-P magnet mounted 2 g Frequency-domain plot peak	
windowed 1 q Pk1	91

Figure 142: ICM-42688-P magnet mounted 4 g Time-domain plot 1 g Pk	192
Figure 143: ICM-42688-P magnet mounted 4 g Frequency-domain plot 1 g Pk	192
Figure 144: ICM-42688-P magnet mounted 4 g Frequency-domain plot peak 1	g
Pk	193
Figure 145: ICM-42688-P magnet mounted 4 g Frequency-domain plot peak	
windowed 1 g Pk	193
Figure 146: ICM-42688-P magnet mounted 8 g Time-domain plot 1 g Pk	194
Figure 147: ICM-42688-P magnet mounted 8 g Frequency-domain plot 1 g Pk	194
Figure 148: ICM-42688-P magnet mounted 8 g Frequency-domain plot peak 1	g
Pk	195
Figure 149: ICM-42688-P magnet mounted 8 g Frequency-domain plot peak	
windowed 1 g Pk	195
Figure 150: ICM-42688-P magnet mounted 16 g Time-domain plot 1 g Pk	196
Figure 151: ICM-42688-P magnet mounted 16 g Frequency-domain plot 1 g Pk	K
	196
Figure 152: ICM-42688-P magnet mounted 16 g Frequency-domain plot peak	1 g
Pk	197
Figure 153: ICM-42688-P magnet mounted 16 g Frequency-domain plot peak	
windowed 1 g Pk	197
Figure 154: IEPE Reference PB352C03 Time-domain plot	198
Figure 155: IEPE Reference PB352C03 Frequency-domain plot	198
Figure 156: IEPE Reference PB352C03 Frequency-domain plot peak	199

Figure 157: Test 2 static powered off – IEPE B3	200
Figure 158: Test 2 static powered on – IEPE B3	200
Figure 159: Test 2 static powered off – IEPR LRR	201
Figure 160: Test 2 static powered on – IEPE LRR	201
Figure 161: Test 2 static powered off, IEPE B3	202
Figure 162: Test 2 static powered on, IEPE B3	203
Figure 163: Test 2 static powered off, IEPE LRR (Full 8 kHz)	204
Figure 164: Test 2 static powered on, IEPE LRR (Full 8 kHz)	204
Figure 165:Time domain B3 ADXL-357 (Blue) vs IEPE (Yellow), high speed.	206
Figure 166: FFT B3 ADXL-357 (Blue) vs IEPE (Yellow), high speed	207
Figure 167: Time domain B3 ICM-42688-P (Blue) vs IEPE (Yellow), high spe	ed
	208
Figure 168: FFT B3 ICM-42688-P (Blue) vs IEPE (Yellow), high speed	209

List of Tables

Table 1: CBM sensor types [12-17]	9
Table 2: Wireless networking comparison [13, 17, 30, 43, 56-59]	. 24
Table 3: Initial design requirements	. 37
Table 4: Accelerometer candidate specifications	. 50
Table 5: Controller board options	. 55
Table 6: Wi-Fi sensor costs	. 63
Table 7: 5G sensor costs	. 63
Table 8: Sensor sample data formatting (20-bit ADXL-357 XYZ data)	. 68
Table 9: Sensor output bit rates (Using maximum bytes per sample)	. 68
Table 10: Summary of test 1 data collected	. 76
Table 11: ADXL-345 Average Noise Density results	. 83
Table 12: ADXL-357 Average Noise Density results	. 87
Table 13: ADXL-357 noise comparison USB vs battery powered	. 90
Table 14: ICM-42688-P Average Noise Density results	. 93
Table 15: Test 1 dynamic result comparison, time domain	. 96
Table 16: Test 1 dynamic result comparison, frequency domain	. 96
Table 17: Test 1 dynamic results ADXL-357 mounting comparison, time domain	n 97
Table 18: Test 1 dynamic results ADXL-357 mounting comparison, frequency	
domain	. 98
Table 19: Test 1 dynamic results ADXL-357 RMS and Pk modes, time domain	. 98

Table 20: ICM-42688-P test 1 dynamic results (time domain)
Table 21: Test 1 dynamic results ADXL-357 RMS and Pk modes, frequency
domain
Table 22: ICM-42688-P test 1 dynamic results (frequency domain)
Table 23: ADXL-357 vs ICM-42688-P average result test 1 dynamic comparison
(time domain)
Table 24: ADXL-357 vs ICM-42688-P average result test 1 dynamic comparison
(frequency domain)100
Table 25: Testbed operational parameters for test 2
Table 26: Test 2 ADXL-357 dynamic test B3 statistical results, low speed113
Table 27: Test 2 ADXL-357 dynamic test B3, low speed (MEMS – IEPE)114
Table 28: Test 2 ADXL-357 dynamic test B3, low speed (MEMS – IEPE, as
percentage)114
Table 29: Test 2 ADXL-357 dynamic test B3 statistical results, medium speed .117
Table 30: Test 2 ADXL-357 dynamic test B3, medium speed (MEMS – IEPE)117
Table 31: Test 2 ADXL-357 dynamic test B3, medium speed (MEMS – IEPE, as
percentage)117
Table 32: Test 2 ADXL-357 dynamic test LRR statistical results, low speed 120
Table 33: Test 2 ADXL-357 dynamic test LRR statistical results, medium speed
Table 34: Test 2 ICM-42688-P dynamic test statistical results, low speed 126
Table 35: Test 2 ICM-42688-P dynamic test, low speed (MEMS – IEPE) 126

Table 36: Test 2 ICM-42688-P dynamic test, low speed (MEMS – IEPE, as
percentage)
Table 37: Test 2 ICM-42688-P dynamic test statistical results, medium speed. 12
Table 38: Test 2 ICM-42688-P dynamic test, medium speed (MEMS – IEPE) 12
Table 39: Test 2 ICM-42688-P dynamic test, medium speed (MEMS – IEPE, as
percentage)
Table 40: Average 5G TCP test results
Table 41: Average 5G UDP test results
Table 42: 5G test results vs Wi-Fi
Table 43: Sensor array Noise Density (ND) vs cost

List of Abbreviations and Symbols

Definition	Abbreviation/Symbol
Acceleration due to Earth's gravity (9.8	
m/s²)	g
Analog to Digital Converter	ADC
Artificial Intelligence	Al
Change In Time	ΔΤ
Comma Separated Values	CSV
Compact Data Acquisition	cDAQ
Computer Numerical Control	CNC
Condition-Based Monitoring	CBM
Customer Premise Equipment	CPE
Data Acquisition System	DAQ
Download	DL
Electromagnetic Interference	EMI
Enhanced Mobile Broadband	eMBB
Fast Fourier Transform	FFT
Gigabits per Second	Gbps
Gigahertz	GHz
Hertz	Hz
Inertial Measurement Unit	IMU
Integrated-Electric Piezoelectric	IEPE
Inter-Integrated Circuit	I ² C
Internet Protocol	IP
Kilohertz	kHz
Line of Sight	LOS
Lithium Polymer	Li-Po
Local Breakout	LBO
Low Pass Filter	LPF
Machine Learning	ML
Massive Machine-Type Communication	mMTC
McMaster Manufacturing Research	MMRI
Institute	INIIAIL/I
Megabits per Second	Mbps
Megahertz	MHz
Microcontroller	MCU

Micro-Electromechanical System	MEMS
Micro-g per square root Hertz (noise	
density)	μg/√Hz
Millisecond	ms
MMRI Linear Axis Testbed	MLAT
National Instruments	NI
Network Interface Card	NIC
Nickel-Metal Hydride	NiMH
Output Data Rate	ODR
Peak	Pk
Peak to Peak	Pk-Pk
Power Over Ethernet	PoE
Power Spectral Density	PSD
Root Mean Square	RMS
Serial Peripheral Interface	SPI
Single Board Computer	SBC
Standard Deviation	STD Dev
State of the Art	SOTA
Structural Health Monitoring	SHM
Structured Query Language	SQL
Transmission Control Protocol	TCP
Ultra-Reliable Low-Latency	URLLC
Communication	
Upload	UL
User Datagram Protocol	UDP
User Equipment	UE
Wireless Sensor Networks	WSNs

M.A.Sc. Thesis – B. Cooke; McMaster University – Mechanical Engineering
Declaration of Academic Achievement
The research presented in this work was conducted at McMaster University's
McMaster Manufacturing Research Institute (MMRI) by Braeden Cooke under the
supervision of Dr. Stephen Veldhuis.

Chapter 1: Introduction

1.1 Research Background and Motivation

In manufacturing, machine downtime and maintenance have always been a significant challenge. As technologies and strategies mature, and companies battle to remain competitive, downtime has become an important economic challenge, with downtime and maintenance accounting for anywhere from 15-60% of total manufacturing costs [1]. Unplanned interruptions due to equipment failure can disrupt production schedules and increase operational expenses, with industrial manufacturers reportedly incurring losses estimated at \$50 billion annually due to such downtimes [2]. To face this challenge, condition-based monitoring (CBM) has emerged as a critical strategy, allowing machine operators and maintenance staff to leverage sensor technologies to monitor machine health, allowing for better, data-based maintenance decisions. By detecting operational anomalies early, CBM can allow for repairs to be pre-planned during scheduled downtime, reduces the risk of catastrophic failures, and can enhance operations cost-efficiency, a key driver of competitiveness for manufacturing companies [3].

CBM implementation can come in many forms, depending on the criticality of the equipment, overall strategies, and company investment priorities. Most strategies can be categorized into one of three strategic methods: periodic, semi-continuous, and continuous monitoring. Periodic, non-continuous, monitoring is the most

common CBM strategy in industry [4], this involves temporarily installing sensors during scheduled maintenance windows to collect machine health data sets. This is most common because it minimizes the required initial investment by allowing a sensor to be shared among machines requiring the same data type collected. This strategy also leaves the most gaps in data sets where a sudden machine health change can be missed until the next interval, leading to missed diagnostic information [3, 4]. Semi-continuous monitoring is like periodic, with timed intervals between collections, but usually uses permanently installed sensors. This allows for data collection to be triggered by specific events or measurement thresholds, and for periodic data to be collected outside of maintenance windows because an operator does not have to manually reinstall or move the sensor each time. Finally, continuous monitoring, with constant data collection, offers superior fault detection capabilities but is rare in industry due to the high sensor costs and networking costs driven by the data throughput of constant collection [4, 5]. As an example, current high-end integrated-electric piezoelectric (IEPE) accelerometers, widely used for vibration analysis in CBM, due to their low-noise and high frequency performance, can exceed \$5000 for a single tri-axial monitoring system before accounting for networking expenses [6]. Additionally, industrial environments pose significant networking challenges, due to high electromagnetic interference (EMI) from metallic surfaces and low ceilings, often forcing these CBM systems to use costly wired installations, or compromise on data collections settings, such as lowering the sampling rate, to reduce network traffic [7, 8].

Due to the difference in implementation strategies, much of the newest CBM research and latest improvements are under utilized in industry. This work seeks to help bridge the gap between the advanced research-grade CBM systems and systems practical for large scale implementation in industry by addressing two of the primary barriers: sensor system cost, and industrial wireless networking limitations.

First, to lower system costs, it explores the replacement of expensive IEPE accelerometers with lower cost digital Micro-electromechanical Systems (MEMS) alternatives. Second, it investigates high-speed wireless data streaming using the McMaster Manufacturing Research Institute's (MMRI's) 5G mmWave network as a low-latency, high throughput alternative to Wi-Fi and wired networks. Improved wireless network performance would allow for real-time wireless sensor data collection for CBM. This will be tested with the MMRI's 5G mmWave private network, deployed in partnership with TERAGO Inc., allowing for real world performance testing in an industrial research environment. TERAGO, which owns a major portion of mmWave spectrum in Canada, deployed the network to support Industry 4.0 and advanced manufacturing use cases for private 5G mmWave networks, including real time monitoring, as demonstrated in this project.

1.2 Research Objectives & Contributions

This work aims to lower barriers to CBM adoption in industry by reducing the cost of sensor systems. The high cost of current sensor systems and their

accompanying networking restricts the availability of high-quality real-time data acquisition systems, which could provide more important information to allow for better data-based maintenance decisions.

The proposed solution addresses these barriers by leveraging highly mass-produced, cost-effective electronic systems and sensors, and wireless networking technologies. This work also provides insight into the performance and possible use cases for an emerging networking technology, 5G mmWave, that could address some of the current challenges in wireless networking for wireless sensor networks (WSNs).

The two main objectives of this thesis are:

- Investigate low-cost sensor alternatives for CBM to reduce adoption costs and bridge the gap between academic research and industrial implementation.
- Evaluate 5G mmWave as a wireless networking solution to overcome existing challenges in industrial WSNs.

The main contributions of this work are:

- Evaluation of two MEMS accelerometers not seen in previous literature as an alternative to state-of-the-art (SOTA) IEPE systems
- 2. Performance evaluation of a 5G mmWave network in an industrial environment

3. Development of a low-cost wireless sensor prototype utilizing the low-cost accelerometers and compatible with the MMRI 5G mmWave network

1.3 Thesis Outline

This thesis is split into six chapters:

Chapter 1: Introduction – Provides background on CBM and the challenges of implementing industrial WSNs. It introduces the research objectives, scope, and academic contributions of this work.

Chapter 2: Literature Review – Presents background information and previous research work into CBM and WSN challenges, including low-cost MEMS accelerometers as an alternative for IEPE and a review of wireless networking options. Introduces basics of 5G and 5G mmWave as a potential wireless alternative. Includes an overview of related sensor work from literature, commercial sensor options and current SOTA vibration measurement systems. This chapter concludes with a summary of current challenges and limitations of wireless sensors and the research gaps this work aims to address.

Chapter 3: System Design & Implementation – Reviews the design decisions made in the process of wireless sensor prototype development. Outlines component selection and sensor unit costs. Lastly this section includes information about the sensor and receiver software and message formatting.

Chapter 4: Testing – This chapter contains the details of the sensor prototype and 5G network testing, including the test setup information, planned data analysis, and results.

Chapter 5: Discussion – This section has further discussion on the sensor prototype design and performance, and 5G network performance from the test results presented in the previous chapter.

Chapter 6: Conclusions and Future Work – Final comments and summary of results and contributions. Concludes with suggestions for possible future research and sensor development opportunities.

Chapter 2: Literature Review

2.1 Condition-Based Monitoring (CBM)

CBM is a predictive maintenance strategy that uses sensors to provide machine health assessments and predict failures. Unlike reactive or time-based maintenance strategies, sensors are used to monitor changes in a machine or a component's condition, enabling data-based maintenance decisions, rather than fixed scheduling or based on timing of previous breakdowns. By utilizing sensors, data analytics and sometimes Artificial Intelligence (AI) or Machine Learning (ML), CBM efforts can help minimize downtime, improve operational efficiency, and avoid serious failures [2].

Most maintenance strategies in industry can be split into three categories: corrective, preventive, or predictive/condition-based maintenance [2]. Corrective maintenance is reactive, repairing machines when they start to fail. Depending on the criticality of the asset, this strategy can result in significant losses and high additional expenses because of unplanned downtime and maintenance [1, 9].

Therefore, depending on the importance and potential impacts of unplanned downtime, other strategies are used. Preventive maintenance attempts to avoid unplanned downtime by having scheduled maintenance at regular intervals, shorter than the expected time between machine failures. This can help avoid catastrophic failures but due to variability some failures will still occur. Additionally,

over-maintenance can become an issue, resulting in higher than required downtime and maintenance costs [10].

Lastly, predictive monitoring or CBM, which monitors the changes in assets over time with sensors to predict breakdowns before they occur, allowing for data-based maintenance decisions with actual machine information [10].

2.2 Sensor Types for CBM

There are many different types of sensors that can be used for machine monitoring, each providing different types and levels of information [11]. The type of sensor best for each situation will depend on a variety of factors, such as the type of equipment and the expected failure mode [11]. Even for the same situation the 'best' solution can change based on the required accuracy to detect the level of damage required to initiate maintenance procedures.

Different types of sensors are used to monitor different aspects of the process [12], some are highlighted below in Table 1. Each parameter to monitor and sensor type has distinct advantages, limitations, and technical requirements compared to other methods. Different situations require different sensor types to gather the best information so understanding the characteristics and technical requirements for each sensor type is essential when designing a system for CBM, especially for wireless and resource constrained applications. Table 1 contains some measurement types and sensor types used for their them.

Table 1: CBM sensor types [12-17]

Туре	Sensor Type
Force	Dynamometer
Force	Load cell, force sensor, strain gauge
Vibration	Accelerometer (IEPE, MEMS)
Temperature	Thermocouple
Temperature	Thermal imaging camera
Current	Current sensor
Acoustic Emission (AE)	AE sensor, microphone
Rotational speed	Encoder, tachometer, gyroscope
Oil and Lubrication	Dielectric / moisture / particle sensors

2.2.1 Vibration

Vibration sensors, such as accelerometers, velocity sensors, and displacement sensors are used to detect mechanical faults in rotating equipment, such as motors, turbines, fans and rolling components [11]. Accelerometers are usually used to identify high frequency faults, such as bearing wear [11, 18], while velocity and displacement sensors can be used for low and mid frequency faults, like misalignment or imbalance. Vibration is also commonly used for tool wear monitoring applications [12, 14-16]. Vibration monitoring can provide frequency data, allowing for predictive maintenance by diagnosing issues before they become severe and lead to catastrophic failures. Some challenges for vibration monitoring

include sensor placement and noise interference, which can require additional signal processing [12, 13, 17].

2.2.2 Temperature

Temperature sensors, including thermocouples, RTDs and infrared thermometers monitor heat generated by friction, electrical issues, or overloading in machinery. Higher temperatures can indicate bearing failures, lubrication issues or motor problems. These sensors are usually low cost and easy to install, but unlike vibration, it can be difficult to diagnose the specific problems being detected via temperature monitoring. Challenges for temperature monitoring include distinguishing fault conditions from normal operational heat, especially in variable processes, and ensuring sensor durability in harsh environments [13-15, 17].

2.2.3 Current & Voltage

Current and voltage sensors, such as current transformers, Hall-effect sensors, or voltage transducers, monitor the current or voltage input to motors and drives to detect faults such as rotor bar issues, winding failures or load imbalances. Current sensors and voltage sensors are usually cheap and easy to install, non-invasive sensing systems but the data can be difficult to interpret in variable speed applications [12-15, 17].

2.2.4 Force

Force sensors, including load cells, strain gauges and dynamometers, measure mechanical stress or load variations in components such as gears, shafts and bearings. Force can be used to detect issues like overload, misalignment and structural fatigue [13, 16]. These sensors are precise for specific applications but are often expensive and difficult to install. Some challenges for force sensors include calibrating for dynamic loads and long-term stability in harsh conditions [12, 15, 17].

2.2.5 Acoustic Emission (AE)

AE sensors detect high-frequency elastic waves generated by material stress, cracks or friction in machinery. Like vibration monitoring, frequency analysis can allow AE to provide early detection of faults and diagnosis based on specific fault signatures. AE sensors are often relatively expensive and require careful placement due to propagating or reflecting noise and external noise from the noisy industrial environments. An additional challenge for AE is the complex signal processing often required to interpret the resulting data [12-18].

2.2.6 Rotational speed

Some sensors used to monitor rotational speed include tachometers, proximity sensors, encoders or gyroscopes. Rotational speed can be used to detect anomalies such as speed fluctuations, belt slippage or coupling issues [9, 13, 19-22]. These are usually simple and cheap, but they are often sensitive to external

vibrations and like temperature, it can be difficult to diagnose specific faults based on these sensors alone.

2.2.7 Oil and Lubricant Condition Sensors

Oil and lubricant condition monitoring is commonly used for gearboxes and hydraulic systems. These sensors are often used to detect changes in viscosity, dielectric constant, water content or particle contamination. Depending on the application and monitoring goal, different sensors such as dielectric sensors, particle detectors, viscosity sensors or moisture sensors can be used. This type of monitoring can predict lubrication failure and wear debris generation before major mechanical symptoms arise. Some challenges for these methods are integration with fluid systems and interpreting complex degradation patterns [23, 24].

2.2.8 Sensor Fusion (Multi-Sensor Systems)

Sensor fusion is a strategy that combines multiple sensor types to provide a more complete view of machine health. This can lead to more accurate diagnosis outcomes but also comes at the cost of higher implementation costs, more complex data analysis and often requires expertise in system design and analysis to ensure all the sensors are providing useful information. Some systems combine multiple sensors with simple diagnostic methods and other researchers have implemented advanced algorithms, including machine learning and AI, to integrate and analyze the various data streams [13-15].

2.3 Accelerometer Types for CBM

Vibration based condition monitoring is commonly performed using accelerometers and is the most common sensor modality used in CBM, especially for rotary machinery such as bearings, fans, and motors. Vibration signals account for about 58% of the CBM market [25, 26] and are often acquired via accelerometer or AE sensors. This prevalence is due to vibration being an early fault indicator and enabling the possibility for both fault detection and component level diagnosis [27]. Some advantages of accelerometers are their high accuracy and sensitivity, wide flat frequency response ranges, lightweight, with good temperature properties allowing for high temperature applications. Additionally, accelerometers are robust, compared to AE sensors which can be susceptible to picking up external sounds [12], as mentioned in section 2.2.5 above.

This research focuses on accelerometers due to a few reasons, starting with their common use in CBM in both industrial and research applications [28]. Secondly, due to the associated IEPE equipment expenses, accelerometers are a sensor type with an opportunity for high cost reductions by using MEMS alternatives [29]. Lastly, due to the required resolution, sampling rate and number of channels, accelerometers have higher networking requirements compared to some other modalities, such as current or temperature [17]. This higher networking requirement is ideal for a wireless sensor prototype because other slower modalities will be easier to implement once a higher data rate sensor is working. A

sensor prototype created to support high frequency accelerometer acquisition should also be able to easily support current, temperature and other low-medium speed sensor types discussed in section 2.2 in terms of communication requirements, allowing for more future sensor types based on this work.

2.3.1 Piezoelectric Accelerometers

Piezoelectric accelerometers, including IEPE type, are the current academic standard, widely used throughout CBM research works. This is mainly because research uses high-performance systems, requiring superior measurement accuracy and preferring wide frequency bandwidths (up to 22 kHz) [30].

As seen below in Figure 1, these accelerometers utilize the piezoelectric effect, using quartz crystals or ceramic materials (mostly quartz) that generate an electric charge when the crystal is deformed under mechanical stress [26]. Since this charge is proportional to stress it can be measured and converted back into the force value with a single constant scaling factor. Piezoelectric accelerometers are designed so that acceleration force moves a mass which causes measurable deformation in a crystal which generates a charge that is converted using an amplifier into a voltage [30].

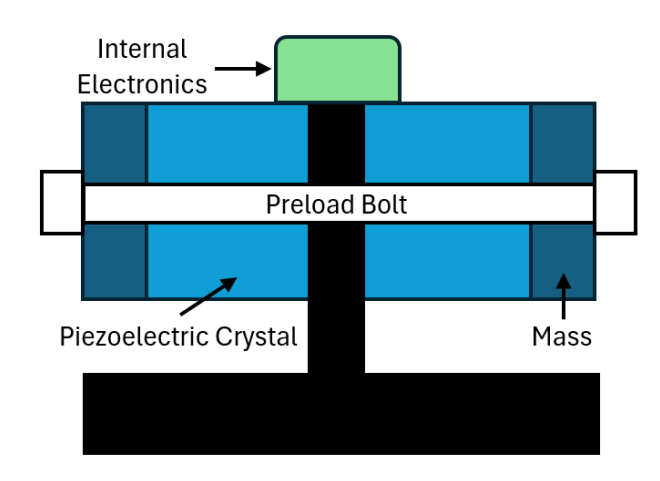


Figure 1: Shear type IEPE accelerometer

Two main designs are used, compression type and the more common shear type. Compression type works with a mass that compresses the crystal, and the shear type uses a mass to induce shear stress on the crystal [31]. The shear type accelerometers are most common because of the increased measurement stability offered [31]. IEPE accelerometers "integrated electronics" refers to the integrated charge amplifier included to convert this small crystal charge into a measurable, AC-coupled, DC-biased signal [31]. This signal requires a constant current power supply (2 - 20 mA), usually supplied at 4 mA [17], and specialized data acquisition equipment, driving the high costs for IEPE-based CBM systems.

With the high performance of the IEPE sensors comes the high associated costs. A single IEPE sensor generally costs \$100 - \$400 depending on the specifications, then for signal conditioning and data acquisition costs are added to this. At the MMRI, this takes the form of the National Instruments (NI) - 9234 IEPE acquisition card (\$5000) with 4 IEPE acquisition channels, with one channel required per axis,

and a NI c-DAQ chassis (\$1000+), providing connection between the IEPE acquisition card and the acquisition PC, similar to many setups from literature [32, 33]. With this a single tri-axial monitoring system would cost over \$6000 per asset, before accounting for the LabVIEW software licenses used to communicate with the NI Compact Data Acquisition (cDAQ) equipment and before any networking or power wiring.

These high investment costs are a leading limiting factor of CBM deployment in industry [25, 27]. Scaling the high-end NI measurement system to 10 machines with their own triaxial systems could easily exceed \$50000 in sensor equipment costs alone.

Some lower cost data acquisition systems are available, such as the USB-231 and Labjack U6, costing a few hundred dollars [27]. However, they often have a maximum total unit sampling rate around 50kHz, so either one is required per axis data channel or a lower sampling rate must be used [27]($21 \, kHz \times 2 = 42 \, kHz$ minimum sampling rate required according to Nyquist theorem, so one data acquisition system (DAQ) would be required per 42 kHz channel if acquiring at full capabilities of top IEPE sensors).

2.3.2 MEMS Accelerometers

MEMS are systems combining miniature mechanical and electrical components and are used for a wide range of applications. As seen in Figure 2, MEMS accelerometers use variable capacitance, the movement of the moving mass alters

the capacitance, measured at C1/C2 based on d1/d2, which is then amplified into a voltage signal [26, 30, 34, 35]. Unlike the IEPE systems, MEMS only require a simple DC power supply and have either analog or digital outputs. Digital sensors can remove the need for any external Analog to Digital Converter (ADC), allowing direct communication from the sensor to a microcontroller [32, 36].

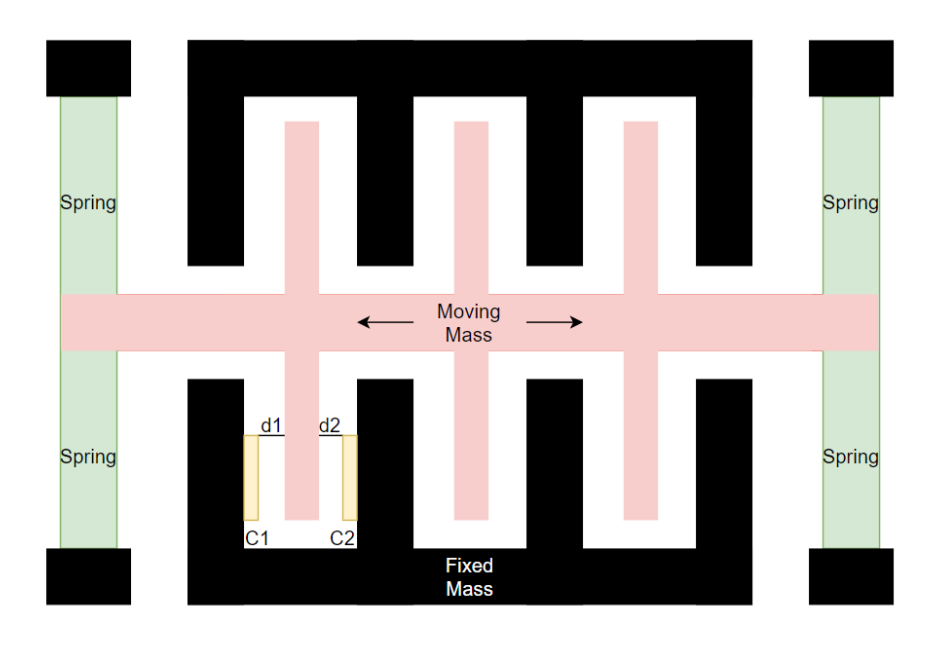


Figure 2: MEMS accelerometer

Due to the high economies of scale based on their use in consumer digital electronics such as cell phones and drones, MEMS accelerometers offer a low-cost alternative to the piezoelectric measurement. Research into this replacement began over two decades ago [34, 37], but early generations of MEMS accelerometers had very poor performance compared to IEPE so use was limited. The early MEMS accelerometers had low measurement ranges, low frequency bandwidths and high noise densities [5, 34, 38].

These limitations led to wider MEMS implementation in less demanding use cases, such as structural health monitoring [39, 40], which has seen wide use of wireless MEMS accelerometers, mostly driven by the lower acceptable sampling rate due to lower frequency range of interest, usually a few hundred Hz at most. Recent advancements in MEMS accelerometers have increased performance while keeping the low prices that originally made MEMS an attractive alternative [29, 34, 35, 38, 41, 42]. However, the implementation of high-performance MEMS accelerometers in industrial environments is still limited, and only high-end accelerometers have been used in long-term CBM installations [5].

MEMS accelerometers have many benefits besides lower costs, they come in small, compact sizes, they are power efficient [34, 35, 38]. However, even the newest generation of MEMS are still limited in some performance respects when compared to the piezoelectric accelerometers. The biggest limitation of MEMS for CBM applications is the high frequency performance, with most MEMS accelerometers having output bandwidths under 5kHz [34, 35, 38, 42]. Other limitations found in research include long-term signal drift, bias offset, and lower robustness vs more industrialized sensors [4].

2.4 Signal Acquisition Considerations

The signal measurement chain can have multiple parts with their own specifications, and each adding their own noise, which can result in different system performance levels for the same sensor depending on the other

components used. The signal measurement chain can consist of sensors, filters, signal processors, amplifiers, and ADC or DAQ [43].

2.4.1 Analog to Digital Conversion

Sensors generate continuous analog signals that need to be digitized for processing, storage and analysis. An ADC is used to convert the analog signal into discrete digital values by taking periodic samples of the signal at a specified sampling rate or sampling frequency. Each period, an approximation of the signal provides a digital representation of the signal [44].

The resolution of the ADC determines the smallest detectable change in the input analog signal that will result in a change in the digital representation. This is usually provided in terms of bits, determining the number of digital levels used to represent the signal. For example, a 24-bit ADC can represent 2^{24} discrete levels, while a 12-bit ADC would represent the same signal using only 2^{12} different output levels [44]. Higher resolution improves the ability to determine small changes (if allowed by the sensor) but also increase data storage and processing requirements. The increased data throughput of higher resolutions will result in requiring better sensor networking abilities and higher power consumption [43].

Quantization noise is the difference between the actual analog signal value and the nearest ADC digital level, the quantization error. This appears as white noise evenly in the frequency spectrum and the noise amplitude is inversely proportional to the ADC resolution. This makes resolution an important ADC specification to consider relative to the resolution of any analog sensor [45].

2.4.2 Sampling Rate and Nyquist Theory

As mentioned above, the sampling rate determines the frequency that the sensor is digitized at by the ADC. According to the Nyquist-Shannon theorem, the sampling rate must be at least twice the highest frequency component to avoid aliasing, which is when parts of high frequency signals fold into lower frequencies during sampling [44, 46]. Aliasing causes high frequency signals to be misinterpreted as low frequency content. Filtering is often used to help reduce the impact of aliasing on the final output value [13, 47].

2.4.3 Filtering

For aliasing prevention, filters must be applied to the signal before the ADC. Aliasing cannot be reversed once the signal is digitized [47]. The three main filter types are low-pass filters (LPF), high-pass filters and bandpass filters. Low-pass removes high frequency content outside the range of interest, high-pass removes the low frequency content, and bandpass can be used to isolate a specific range [43].

Sometimes filters are also implemented post-ADC for other reasons than antialiasing, such as for noise reduction or feature extraction [22]. Although filters are used to attenuate signals, practical real-life filters do not have an ideal immediate full cut off point. Instead, filters typically introduce gradual attenuation over a transition band near a cutoff frequency. The steepness of this filtering is impacted by filter type, filter order and design. As a result, high frequency components often leak into the sampled spectrum, especially when the cutoff frequency is close to the Nyquist limit [47].

Using over the Nyquist frequency (over 2x the highest frequency of interest), known as oversampling the signal, and using a conservative cutoff frequency compared to where the expected frequency content is can reduce the impacts of aliasing [48]. But this strategy comes with the costs associated with increased data throughput, storage and processing requirements.

2.5 Industrial Networking & Wireless Sensor Networks

As more industry 4.0 initiatives, such as CBM, are implemented in industry, there is a growing demand for flexible, cost-effective, reliable wireless networking options to support these new systems. The current standard for these systems are still wired networks, due to their reliable performance in terms of lifetime, data synchronization and data availability [26, 49]. However, the high installation costs, maintenance costs, inflexibility, and challenges in retrofitting pose significant limitations to wired networks [50, 51]. Routing cables through confined spaces or high traffic areas complicates deployment and cables can often be susceptible to noise, often requiring shielded cables. Additionally, cable stiffness and movement

can cause cables to break [26, 49], requiring downtime for cable repairs or replacement. As a result of these shortcomings, WSNs have been implemented and research for a long period as an alternative, using wireless communication technologies to address these drawbacks.

2.5.1 Wired Networks

Wired sensor networks are the current default option to deliver high-performance monitoring. Their reliability and high-performance give wired networking ideal characteristics for sensor networking. However, despite the high performance, literature consistently highlights their drawbacks. Initial installation is costly, and time consuming, often expensive shielded cable alternatives are required to mitigate EMI noise in the industrial environments [50-52]. Once installed, the cables also deteriorate over time, adding increased operational costs associated with downtime and materials for cable replacements. Moving or rotating components, popular assets for accelerometer based CBM, increase the pace of cable wear adding further costs [11]. Finally, once installed, the cables are in their place, providing little flexibility for floor layout changes [53, 54].

2.5.2 Wireless Networking

WSNs provide a flexible and cost-effective alternative to traditional wired systems by eliminating the need for extensive cabling infrastructure throughout a facility. As a result, WSNs enable large-scale monitoring with reduced installation complexity and downtime [52].

Wireless sensors also facilitate quicker deployment, allowing systems to be installed or reconfigured with minimal disruption to operations. Their adaptability also makes them particularly advantageous for monitoring moving or rotating components, where wired connections would be difficult to maintain [52]. Faster installation reduces setup time and therefore the downtime associated with sensor installation.

Although this work focuses on continuous monitoring, WSNs can also be an improvement for periodic monitoring. A magnetic, battery powered sensor node that can be quickly placed on machines and connected quickly within a wireless networked facility would be much more convenient than the current wired handheld systems, allowing wider data collection[55].

Despite these benefits, WSNs face notable challenges and trade-offs. A major constraint is energy consumption, especially for battery-powered nodes intended for long-term monitoring. Periodic communication for synchronization and data transmission imposes significant power demands [49]. Furthermore, time synchronization accuracy and data reliability are highly dependent on the wireless signal quality, which can be poor in industrial environments. Common issues for wireless networks in these industrial settings include signal attenuation due to metallic surfaces, electromagnetic interference, and multipath propagation [26, 49]. Additional complications include random packet loss and the need for retransmissions, which further increase power consumption. Compared to their

wired counterparts, wireless sensor nodes are generally limited in computational resources, storage capacity, and bandwidth, restricting their ability to handle high-rate or high-volume data streams efficiently [26]. To address these limitations, researchers have proposed strategies such as local digital signal processing and onboard data compression. While these approaches can reduce communication load and extend battery life, they may also introduce risks of information loss [26, 55]

2.5.3 Current Wireless Standards

A broad range of wireless networking technologies have been evaluated for WSN applications. Each technology presents specific trade-offs in terms of bandwidth, range, latency, energy consumption, and scalability, making them more or less suitable depending on the monitoring context needs. In the reviewed literature on wireless CBM networks, numerous wireless protocols have been tested, each revealing certain limitations that challenge deployment at scale, particularly for high-frequency, real-time data acquisition. Table 2 below contains a summary of current wireless networking standards and their relative performance.

Table 2: Wireless networking comparison [13, 17, 30, 43, 56-59]

Туре	Range	Range	Bandwidth	Bandwidth	Power Use
5G mmWave	Med.	100-300 m	Very high	1-10 Gbps	High
5G	Long	1-5 km	High	100 Mbps - 1	Med.
				Gbps	

4G LTE	Long	1-10 km	High	10-100 Mbps	Med.
Wi-Fi	Med.	30-100 m	High	10-100 Mbps	High
ВТ	Short	10-100 m	Low	1-3 Mbps	Low
BLE	Short	10-100 m	Low	<2 Mbps	Very low
LoRa	Very long	2-15 km	Low	< 50 kbps	Very low
Zigbee	Short	30-120 m	Low	20-250 kbps	Very low

2.5.3.1 Wi-Fi

Wi-Fi remains the most popular wireless standard for high-performance industrial installations, owing to its relatively high data rates (up to several hundred Mbps), moderate range, and widespread compatibility with commercial hardware. These characteristics make it suitable for CBM systems requiring high throughput and relatively low latency. However, Wi-Fi faces challenges in environments with high device densities, overlapping access points, and signal propagation issues, particularly in industrial settings with metallic structures and electromagnetic interference [13, 17, 30, 58-60]. These issues can result in inconsistent performance, increased packet loss, and reliability concerns under certain deployment conditions.

2.5.3.2 Bluetooth and Bluetooth Low Energy (BLE)

Bluetooth, especially its low-energy variant BLE, has become a widely used protocol for short-range, low-power wireless communication [30, 60]. BLE is optimized for minimal energy consumption, making it ideal for battery-powered sensors. However, this efficiency comes at the expense of throughput and range.

As a result, BLE is generally unsuitable for large-scale WSN deployments that require continuous, high-frequency data transmission, particularly in real-time monitoring scenarios [17, 30, 57-59].

2.5.3.3 Zigbee

Zigbee is a mesh-based protocol designed specifically for Internet of Things (IoT) applications. It supports longer-range communication via multi-hop transmission and operates efficiently in low-power environments. Nonetheless, Zigbee offers limited data throughput, making it insufficient for high-bandwidth sensor applications such as those found in vibration analysis or real-time diagnostics [17, 50, 57-59, 61, 62].

2.5.3.4 5G & 5G mmWave

The emerging 5G standard presents a potential solution to many of the limitations faced by existing WSN technologies. Built on three core performance pillars: enhanced mobile broadband (eMBB), ultra-reliable low-latency communication (URLLC), and massive machine-type communication (mMTC), 5G is designed to deliver significant improvements in speed, latency, and scalability. In particular, 5G mmWave, which operates at very high frequencies (24 GHz and above), promises data rates in the range of 1–10 Gbps, latencies below 1 ms, and the ability to support up to a million devices per square kilometer [56, 63].

These capabilities theoretically resolve key WSN constraints, including low bandwidth, inconsistent latency, and limited node density. Additionally, the use of

higher frequency bands may reduce susceptibility to certain types of EMI, although signal penetration remains a concern in obstructed or enclosed environments [56]. Furthermore, private 5G networks enable localized control, improved security, and dedicated bandwidth for industrial applications. This is particularly relevant for smart manufacturing and predictive maintenance systems requiring deterministic

However, despite these theoretical advantages, real-world deployments of private 5G and 5G mmWave in industrial environments remain sparse. As noted by Varga, empirical performance data in manufacturing contexts is limited, and many claims remain unvalidated under operational conditions [63]. Accordingly, this thesis explores the potential of 5G, particularly private 5G mmWave networks, to support high-frequency, real-time wireless sensor networks, comparing their performance against legacy standards.

2.5.4 Related Sensor Works

communication [56, 63-65].

MEMS accelerometers have been widely integrated WSNs, particularly in structural health monitoring (SHM) applications. SHM systems typically operate with lower bandwidth requirements, making them more amenable to existing wireless technologies. As a result, numerous studies have successfully demonstrated the use of MEMS-based WSNs in this domain [39, 53, 54, 66].

In contrast, CBM applications often require significantly higher sampling rates to capture the high-frequency vibrations and transient events characteristic of

machine faults. This shift introduces a new set of challenges, primarily related to data volume, wireless transmission bottlenecks, and power constraints. To address these issues, many sensor systems adopt event-based streaming, transmitting only snippets of data surrounding detected anomalies or threshold triggers. While this method conserves bandwidth and energy, it also introduces potential drawbacks. For instance, event-triggered streaming can miss important contextual information, and the absence of full signal histories limits post-event analysis and diagnostic flexibility [63].

Furthermore, real-time wireless streaming of high-frequency raw data remains largely impractical with current wireless technologies due to the combination of limited throughput and high-power consumption [56]. As a result, some systems accept long transmission delays, collecting and storing high-frequency data locally for later offloading [49]. Edge computing approaches have also been proposed to enable on-device analysis and decision making, reducing the need for continuous data transmission [6]. However, the implementation of such systems introduces additional complexity. Sophisticated diagnostic algorithms often demand high computational resources, accelerating battery depletion and potentially limiting deployment duration. Additionally, relying solely on pre-processed data risks discarding valuable raw information, which may be essential for developing or improving diagnostic models in the future.

2.5.5 Commercial Wireless Sensors

A review of commercially available wireless accelerometers reveals that most systems are designed for specific industrial applications, rather than as general-purpose test and measurement tools. These devices are typically optimized for long-term, low-frequency monitoring in well-defined, stable processes. Consequently, they often capture only limited amounts of data per day, which may be sufficient for routine monitoring but lacks the flexibility required for exploratory diagnostics, algorithm development, or research applications.

To conserve energy and reduce network load, many commercial wireless sensors employ onboard signal processing, transmitting only processed metrics or summary statistics [60]. While this approach extends battery life and improves network stability, it introduces a key limitation: users frequently do not have access to raw sensor data, which is essential for detailed analysis, verification, or reprocessing. In some cases, even systems marketed as supporting raw data only provide filtered or down sampled outputs, which may be inadequate for advanced diagnostics or high-resolution feature extraction [49, 60].

There is also a wide variety of wireless sensor system types on the market, ranging from academic prototype nodes to fully integrated commercial solutions. These systems differ in data acquisition and transmission strategies, including real-time continuous streaming, event-triggered transmission, and scheduled data uploads. Real-time systems are ideal for capturing high-frequency transients but are often

constrained by power and bandwidth limitations. Event-triggered and scheduled systems, on the other hand, reduce energy use and network traffic but risk omitting important context or failing to capture rare events with sufficient detail [27, 60].

Across both commercial and research-grade systems, the vast majority utilize MEMS-based accelerometers. This is primarily due to their low cost, small size, and low power requirements, which make them ideal for battery-powered wireless applications. Although alternative sensor technologies (IEPE accelerometers, AE sensors) may offer superior performance for certain high-frequency or high-dynamic-range applications, their integration into compact, low-power wireless platforms is less practical. As a result, most current wireless CBM systems compromise between performance, power consumption, and cost [49, 60].

These limitations collectively highlight the need for more flexible, high-performance wireless sensor platforms capable of capturing and transmitting raw, high-frequency data. The present study seeks to address this gap by evaluating the use of next-generation wireless technologies, specifically 5G, for enabling real-time, high-resolution data streaming in CBM applications.

2.5.6 Related Sensor Work from Literature

Koene combined wireless networking and MEMS accelerometers for monitoring rotor vibrations, replacing an IEPE sensor used currently. An ADXL-355 was compared to an IEPE alternative acquired via a cDAQ and NI-9234 card. The first sensor prototype used an ESP32 and communicated 1 kHz vibration data via Wi-

Fi, User Datagram Protocol (UDP) packets were used for transmission resulting in the sensor occasionally losing packets, losing possibly valuable sensor data [55]. To solve this problem, the second version read the sensor data and stored it locally on the senor, using an SD card. After acquisition, these sensor data files were available to download remotely via a web portal. This sensor version could acquire sensor data at 4 kHz sampling rate but could not send live data to the receiver [52]. Ompusunggu first compared the ADXL-001 series to an IEPE accelerometer [4], then updated to the newer ADXL-1001/2 sensors with a new low-cost wired sensor. This update saw a large improvement in noise performance for the MEMS sensor [3]. Although these sensors allowed for high frequency vibration monitoring with MEMS accelerometers, NI cDAQ hardware was still used to acquire the sensor signals with data transmission via ethernet. A case study using wireless access points to connect the DAQ and server were performed, with 220 days of data collected but many details missing. If this wireless test used the same as another case study performed, then it had 220 days of a 3 second sample every half hour during operating hours [5].

Vogl has performed extensive work related to low-cost inertial measurement units (IMUs) for CBM, combining low-cost accelerometers and gyroscopes to monitor linear axis with various iterations of a custom wired sensor [9, 19-22]. This work shows the use of a low-cost sensor alternative, even in demanding applications requiring very low noise. This work also demonstrates choosing a low-cost alternative that meets the needs for diagnosis while perhaps sacrificing some of

the high-end performance often sought after in academic work, with the version 2 "Industrial IMU" achieving significant cost reductions compared to version 1, but with a 4x accelerometer noise increase and bandwidth reduction.

2.6 Current State of the Art

Figure 3 shows the current measurement methods used at the MMRI and the same as the reference "high end" system used in many papers [3-5, 34, 62]. It consists of an IEPE accelerometer and NI DAQ hardware (ADC card, DAQ). Most situations in both lab and literature, these systems are directly wired to a pc located at the machine being monitored and controlled with LabVIEW. These systems can be altered to work wirelessly, as seen in Figure 4. This removes the cost of a PC and license at each PC, but the sensor hardware costs (~\$5000) were determined to still be too high for this project as they remain impractical for large-scale industrial deployments.

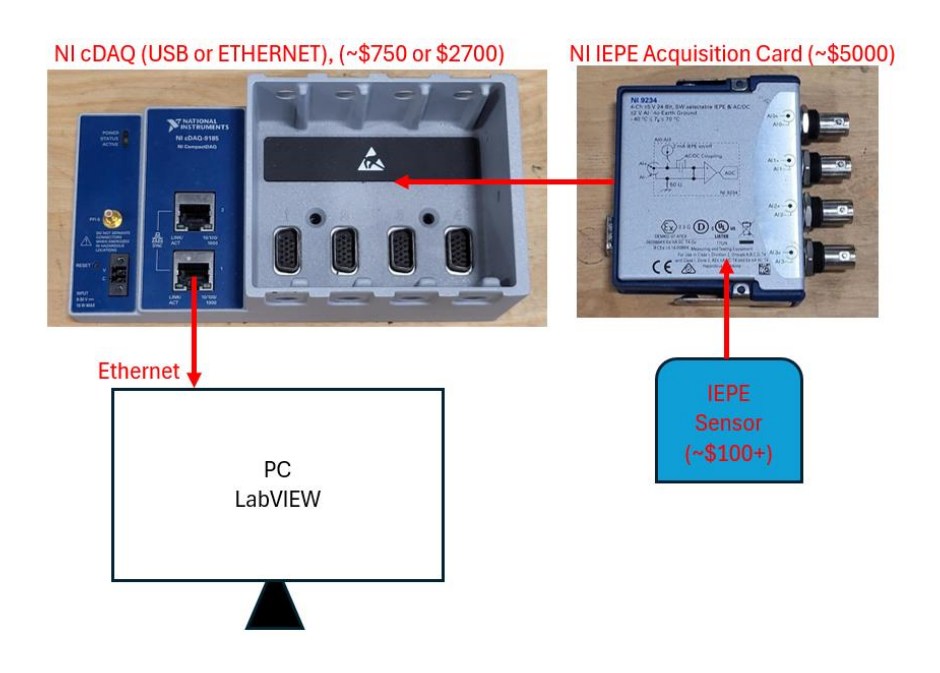


Figure 3: Typical high-end IEPE measurement chain

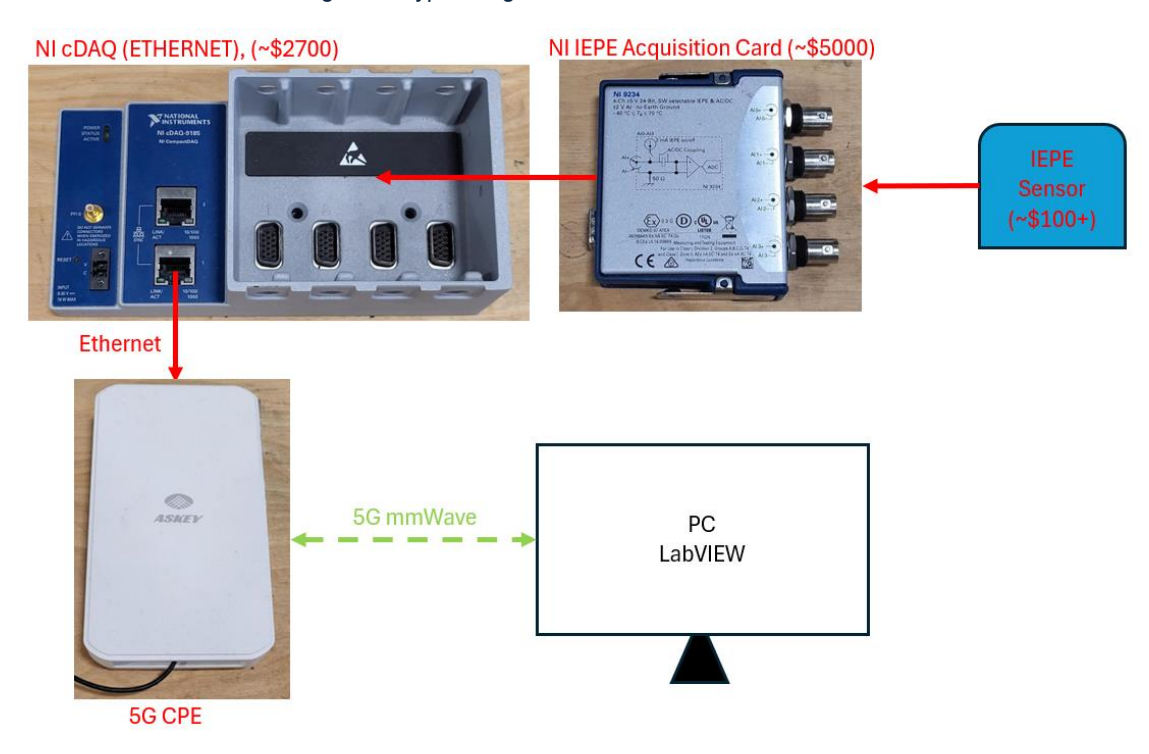


Figure 4: 5G mmWave high-end IEPE measurement chain

2.7 Summary & Research Gaps

The literature review underscores a significant gap in current WSN technologies for high-frequency, real-time CBM. While recent advances in MEMS and wireless communication technologies have enabled the deployment of small, cost-effective smart sensors [26], existing wireless systems remain fundamentally limited in their ability to support high-bandwidth, low-latency applications. Most reviewed works either reduce sensor sampling rates to accommodate wireless constraints [55] or relied on wired networks to meet their real-time performance demands [3, 4]. In some cases, sensors collect high-frequency data and store it locally, typically on SD cards, before transmitting it later in a time-delayed manner, which hinders real-time diagnostics and predictive capabilities [52].

As highlighted by Marcoochio [26], WSNs exhibit unique constraints including limited power, memory, and processing capabilities. These constraints are further exacerbated in industrial environments, where reliability, timing, and accuracy are critical requirements due to harsh operating conditions and electromagnetic interference. Despite progress in edge computing and low-power processing, current wireless systems remain performance-limited by their networking, not by their sensing capability [60].

A major research gap lies in the development of a wireless, high-frequency, real-time accelerometer system. To date, high-performance MEMS sensors (such as the ADXL-1001 from Analog Devices or TE's 805M1 series) are predominantly

used in wired test setups [3, 4, 25, 27, 32, 67, 68], as existing wireless platforms are not capable of supporting the required data rates and latency. The emergence of 5G and 5G mmWave technologies presents a promising opportunity to shift this paradigm. With their ability to support gigabit-per-second throughput, sub-millisecond latency, and high device density, 5G networks can remove the networking bottleneck and shift the performance limit back to the sensor itself. This opens the door for deploying higher-bandwidth MEMS accelerometers in wireless form, enabling real-time CBM at high sampling rates.

This thesis aims to address these gaps by evaluating the performance of a 5G-connected wireless acceleration sensing platform, focusing on its ability to support real-time, high-frequency data acquisition. An incremental testing strategy is adopted to assess lower-cost MEMS accelerometers before progressing to higher-cost, high-performance devices and ultimately providing a roadmap for next-generation wireless CBM solutions.

Chapter 3: System Design & Implementation

This section will outline the design decisions and implementation for the sensor prototype and the general design decision made when designing a sensor or selecting a sensor for deployment.

The sensor prototype developed was intentionally designed to be adaptable, supporting future expansion to other sensing modalities, such as temperature or current easy. This modular architecture with a focus on the data transmission at relatively high frequencies will allow any sensors with lower frequency data outputs to be easily connected.

3.1 System Considerations

3.1.1 System Design Requirements/Criteria

Based on the intended use of the system and the literature review, some key requirements or performance goals were created, as outlined in Table 3 below. Many of these design requirements were intended to be flexible, especially the accelerometer related parameters. Flexibility on these specifications was required as most MEMS sensors cannot reach the high requirements, and not all use cases require the high recommended specifications for high frequency bearing monitoring.

Table 3: Initial design requirements

Specification	Requirement	Comment
Form factor	Small, portable	
Easy installation	Magnetic mount	
Battery Life	>1 day/shift per charge	Can easily be removed
		and swapped out daily at
		the start or end of day
Accelerometer range	Up to 50 g max	To meet
		recommendations [3-5]
Accelerometer	2.5 kHz+	10 kHz+ recommended
bandwidth		for bearings [3-5]
Accelerometer noise	Low noise (>100	
density	μg/√Hz)	
Network connection	Ethernet	For 5G connection

Based on previous work using the intended linear axis testbed [69-71], 5 kHz sampling rate was used, indicating a minimum bandwidth of 2.5 kHz for this test. However, as the sensor is intended for flexible, diverse uses, a higher bandwidth would be ideal as it would enable more use cases for the end sensor prototype.

3.1.2 Sensor Strategy Considerations

After selecting equipment to monitor, the first step to implementing a CBM system is often sensor modality selection. As covered in the literature review, many sensor types are common in CBM use cases. The designer must pick an appropriate modality based on the type of equipment and the common failure modes.

Once a sensor type is selected, a specific sensor must be selected, as performed in the accelerometer selection section of this thesis. As done there, the designer must create sensor performance criteria and perform a market analysis to identify units meeting their performance needs at an acceptable cost. Common criteria for sensor performance and selection include frequency range for sampling and the resulting bandwidth, often higher frequency sensors can provide more information, but this will not always be useful information. Other metrics would be sensor accuracy, from resolution, noise and repeatability. Similar to the bandwidth higher accuracy can provide more information but a middle ground needs to be identified where there is enough information but not excessive detail that is adding increased system costs and data related burdens without supplying important information required for acceptable diagnosis accuracy [18].

To support the industrial aims related to this work, this sensor prototype will focus on creating a low-cost wireless sensor intended to be scaled up in future works. As a result, the design considerations may be different when compared to a high-end sensor intended for academic research. Instead of super high accuracy and very

high bandwidths, the ideal sensor for this scenario would be low-cost and accurate enough to identify changes and trends related to component wear.

3.1.2.1 TERAGO 5G mmWave Network at the MMRI

Shown in Figure 5 is the TERAGO 5G system map at the MMRI. This map shows the 5G core in a separate server room with fibre connections to a 4G LTE and 5G mmWave antenna on the ceiling of the MMRI, located above the main machine aisle. Since the core is in the building server room, an ethernet cable is routed to a local breakout port (LBO) to provide a direct 1 Gbps connection to the core from the MMRI shop floor.

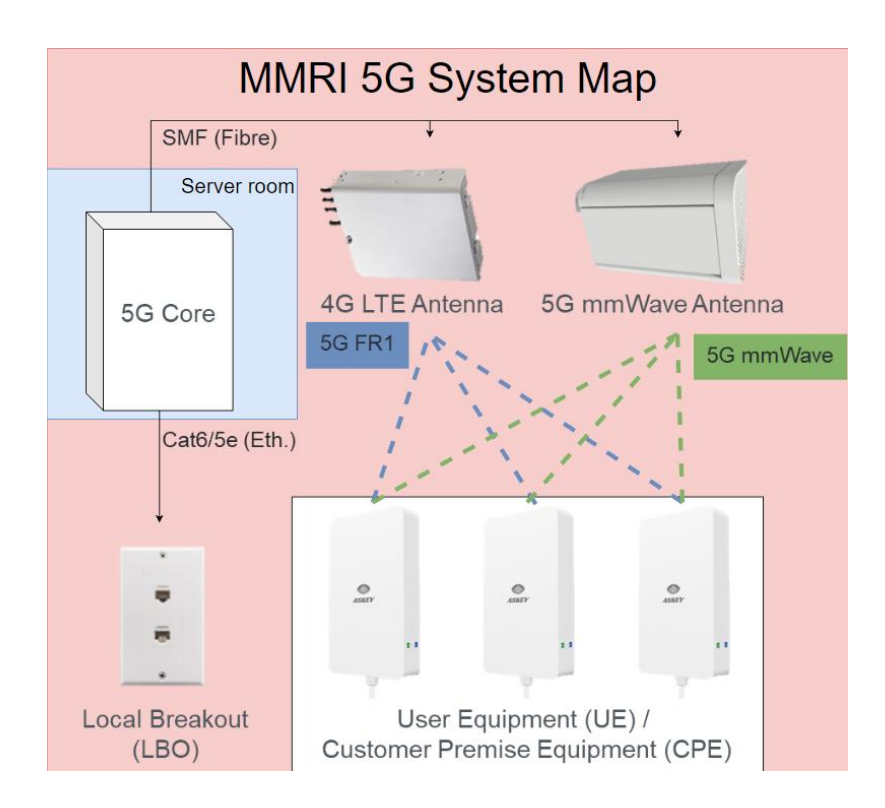


Figure 5: TERAGO 5G system map at the MMRI

The antennas connect to User Equipment (UEs) or Customer Premise Equipment (CPEs), to provide connectivity to the 5G mmWave network. This is shown in Figure 6, showing a sensor connected to the network via CPE. Currently these are the only way to connect to the 5G system, via an ethernet port, limiting the 5G sensor prototype to an external antenna to provide connectivity.

Devices connected to the core via the LBO must be configured with a static internet protocol (IP) address and gateway to connect to the CPEs then it gets routed to an IP address on the CPE subnet. When connecting to a CPE, the CPE will provide a valid IP address, and the connected device is able to communicate with devices connected via the LBO.

One limitation of the current implementation is that two CPE connected devices cannot communicate directly with one another, they can only communicate with devices connected via a wired connection. This can limit certain use cases but, as seen in Figure 6 below, for a WSN this limitation will not affect sensor design because the sensor can connect to 5G via the CPE and the receiver can be a server device with a wired connection.

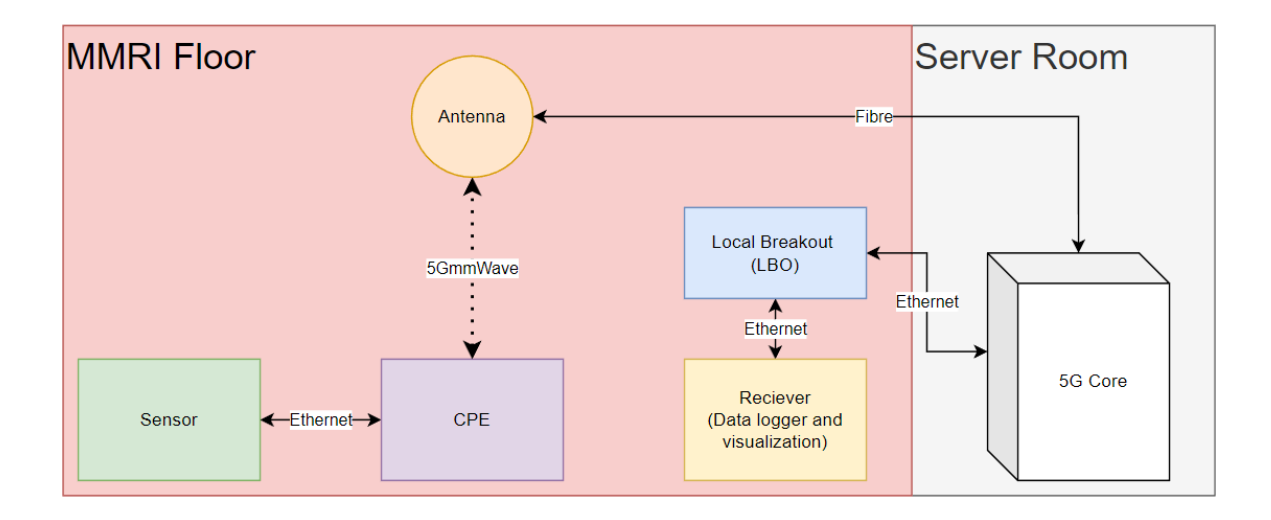


Figure 6: 5G sensor communication

3.2 Component Selection

Figure 7 demonstrates the key components making up the sensor system. The MMRI 5G section are the fixed parts required to connect to the 5G network. The left side shows the three main components for the sensor, the sensing accelerometer, the microcontroller or microcontroller unit (MCU) for connectivity and computing, and a battery to power both.

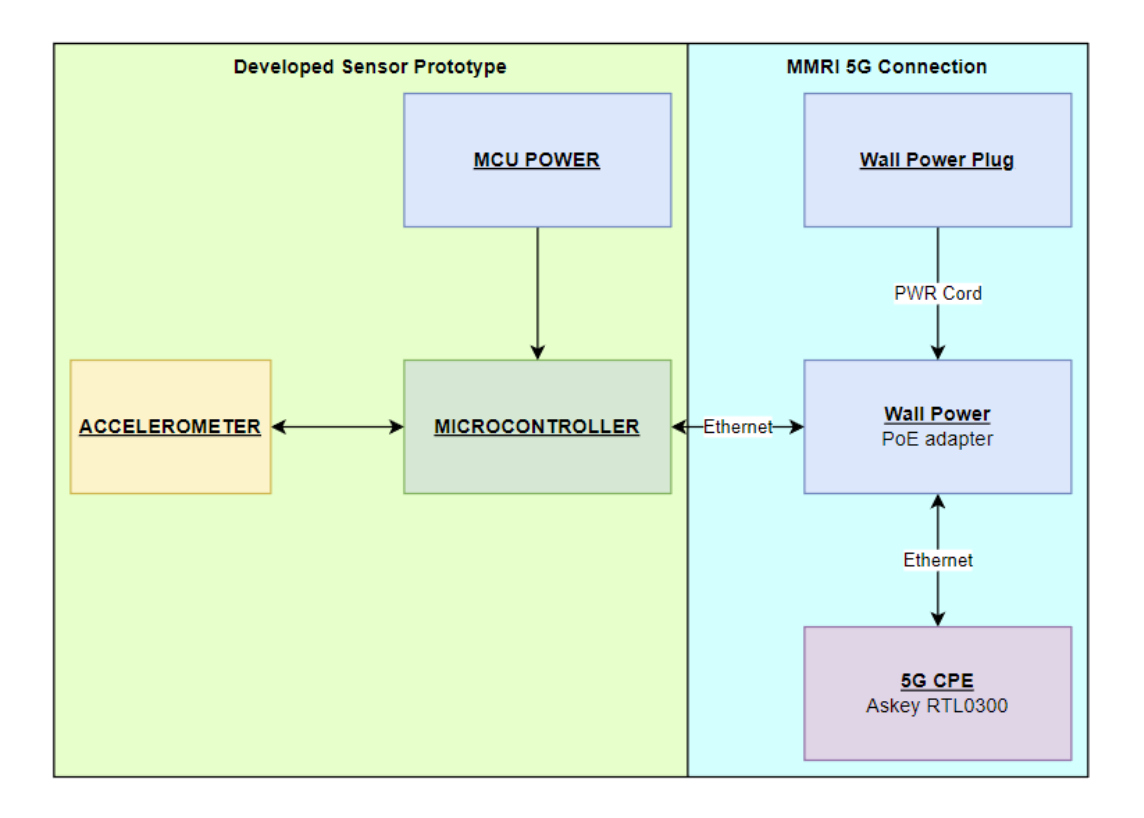


Figure 7: Sensor components

3.2.1 Accelerometer

3.2.1.1 Accelerometer Selection Criteria

Selecting a suitable accelerometer is a critical step in the development of a wireless vibration sensing system for CBM. The chosen sensor must balance performance, cost, and system compatibility while meeting the requirements for high-frequency industrial vibration monitoring. A comprehensive market analysis was conducted to evaluate a wide range of commercial accelerometers. The following criteria were used in the selection process:

Sensor Type:

- MEMS accelerometers are commonly used in wireless sensor systems due to their low cost, small size, and integration ease [52, 55, 72].
- Piezoelectric accelerometers generally offer superior dynamic performance (higher frequency range, lower noise) but are typically more expensive and require analog signal conditioning [29].

- Number of Axes:

 Single-axis sensors are sufficient for some applications, but triaxial sensors provide complete vibration profile information and allow flexibility in mounting orientation.

- Output Interface:

- Analog outputs are common in piezoelectric sensors but require ADC and signal conditioning.
- Digital outputs (e.g., Serial Peripheral Interface (SPI) or Interintegrated circuit (I²C)) simplify integration with microcontrollers and reduce signal noise, making them more suitable for embedded systems.

- Cost:

A major consideration, especially for scalable or deployable systems.
 MEMS devices typically provide a favorable balance of cost and performance.

- Measurement Range (±g):

 Must be appropriate for the vibration levels expected in the target machinery. For industrial rotating machinery, ±50 g is considered a suitable minimum maximum range [4].

- Sensitivity:

Defined in mV/g for analog sensors or LSB/g for digital sensors.
 Higher sensitivity improves resolution but must be balanced with range and noise floor [34, 35].

Sensor + ADC Resolution:

 Determines the smallest change in acceleration the sensor can detect. A higher resolution allows more precise measurements, especially at low amplitudes. The ADC and signal chain equipment can also limit the system's overall resolution [34].

- Bandwidth / Frequency Response:

The flat frequency response range (±3 dB) defines the usable bandwidth of the sensor [34, 35]. According to ISO 13373, the sensor should ideally capture 0.2× to 3.5× the frequencies of interest, typically extending up to 10 kHz for bearing or gear diagnostics [3-5].

- Noise Performance [32, 60]:
 - Two common specifications:
 - Root Mean Square (RMS) Noise: The total integrated noise over the bandwidth.
 - Noise Density: Typically expressed as µg/√Hz or µV/√Hz; used to estimate RMS noise using the square root of the bandwidth.
 - Low noise is essential for detecting early-stage faults and small amplitude signals.
- Cross-Axis Sensitivity (Transverse Sensitivity):
 - Measures the sensor's undesired response to motion along axes orthogonal to its intended measurement axis [34]. Expressed as a percentage, lower values (<5%) are preferred.
- Operating Temperature Range:
 - o Industrial environments may demand sensors with wide operational temperature ranges (e.g., −40 °C to +125 °C).
- Temperature Sensitivity:
 - Indicates how much the sensor's performance varies with temperature (typically %/°C).
- Maximum Shock Tolerance:
 - Important for installations in environments with potential for impact or high mechanical stress.

- Stability/Drift Over Time [3, 4]:

- MEMS accelerometers may exhibit long-term drift due to aging of mechanical elements, packaging stress, or environmental exposure.
- Piezoelectric accelerometers generally offer superior long-term
 stability but at a higher cost and with analog interface limitations.
- Lifetime stability is particularly important in wireless, hard-to-access installations where frequent recalibration or replacement is impractical.
- This parameter is typically assessed through metrics such as zero-g
 offset drift, sensitivity drift (% per year), and total bias stability.

3.2.1.2 Market Survey & Selections

A market survey was conducted to identify suitable MEMS accelerometers for CBM applications. In the survey, three distinct classes of MEMS accelerometers emerged based on performance characteristics, signal output type, and cost. The first group includes low-cost, low-performance options, such as the ADXL-345, offering tri-axial measurement at a minimal price (as low as \$4). Similar to the older generation MEMS evaluated by Albarbar and Teay [34, 35, 38, 42], these accelerometers have very high noise density, low resolution and low bandwidths compared to IEPE alternatives, making their use in CBM applications limited outside of basic implementations.

The second group is comprised of mid and upper tier digital MEMS accelerometers, such as the ADXL-355 and ADXL-357, which can offer higher

frequency response ranges with lower noise densities and with higher resolution outputs. The second group offers improved performance while retaining the digital output that makes the low-cost tier attractive, and at a moderate price increase (>\$100).

The third group of MEMS accelerometers identified offer the highest performance, with some models offering performance comparable to IEPE, with wider bandwidths (10kHz+) and noise densities approaching IEPE levels but not quite as low. This performance increase comes at a higher sensor cost, often only come in single axis variants, and requires an additional sensor stage to provide signal conditioning and an external ADC due to the removal of digital outputs.

The market survey included accelerometers of all three identified groups, but no group three accelerometers were selected for evaluation or implementation. The strongest sensor candidate from this group to replace IEPE systems, the ADXL-1001/2, has been widely used in existing research, but was skipped in this study due to two main reasons. The unit cost of the sensor, combined with requiring three to perform tri-axial measurements made the lowest possible cost for a wireless sensor employing this accelerometer to be quite high compared to digital options, even the choice with a tri-axial alternative, the 830M1 has a high unit cost. Having a sensor cost a few hundred dollars and requiring a custom signal conditioning and ADC developed would result in a sensor costing a few hundred dollars. Alternatively, works utilizing the lower performance MEMS with digital outputs can use sensors costing \$5 - \$80, making the minimum price much lower.

The second reason for focusing on the digital output accelerometers was that many works struggle while implementing even the lower bandwidth MEMS accelerometers with wireless transmissions. Therefore, these sensors provide a better starting point for sensor development, and the higher performance sensors can be utilized in a mid range sensor alternative if the performance requirements are higher and once the wireless transmission is proven using the cheaper alternatives.

For this study, the focus was on low-cost, digital output accelerometers and three models were selected for evaluation: the ADXL-345, ADXL-357, and ICM-42688-P. The ADXL-345 was chosen mostly due to its very low cost and widespread use in previous works [58, 73, 74]. The ADXL-357, untested in CBM literature, was selected for its superior noise performance (75 μg/√Hz at ±10 g) and high output data rate (ODR) up to 4 kHz, though its internal LPF limits usable bandwidth to about 1 kHz. After expanding the search to include IMUs, the ICM-42688-P emerged as a promising candidate, offering a frequency range up to 4 kHz (potentially 8 kHz with LPF disabled), noise density comparable to the ADXL-357, and an integrated gyroscope for potential multi-sensor applications at a lower cost than the ADXL-357.

Another promising sensor candidate, the ADXL-355, was initially passed over for testing due to it being characterized and used in other works [40, 49, 52, 54, 55, 74], unlike the ADXL-357. Although the ADXL-355 has better noise performance than the ADXL-357, the ADXL-357 also offers a higher measurement range than

any other sensor tested. Both sensors function almost identically, so it could easily be tested with the developed prototype if desired at a later stage.

After the ADXL-345 and ADXL-357 were integrated another interesting sensor candidate was identified. IMUs, which also offer a gyroscope, had been used in previous works [39, 66, 75] but often the MPU6050 or MPU9050 which has poor performance and is no longer available for purchase at their end-of-life phases. The ICM-42688-P was identified as a possible candidate for a higher frequency alternative to the ADXL-357. According to the datasheet [76], they have similar noise densities, but the ICM-42688-P has a frequency bandwidth of 4 kHz, possibly up to 8 kHz at 32 kHz ODR with the LPF disabled. This performance is much better than the last generation MPU options and is available at a much lower cost compared to the ADXL-357.

The ICM-42688-P also serves a dual purpose, as the ODR is much higher, it can be used to test the wireless accelerometer transmission capabilities, with higher data rates closer to those required of the higher performance and cost alternatives like the ADXL-1002 or 830M1.

Table 4 below summarizes some of the mentioned sensor alternatives with some important performance parameters, type of sensor and cost. The digital MEMS accelerometers with multiple ranges have settings to swap between the options listed, for analog MEMS and IEPE sensors the range is set per unit (no switching between ranges).

Table 4: Accelerometer candidate specifications

Accel	Туре	Output	Axis	Range (±g)	ADC Res. (Bits)	Highest Res.	Sampling Rate (kHz)	BW (±3dB) (kHz)	Noise Density (ug/√Hz)	Cost (CAD)
					10, 11,		(2)	(2)	290 (x,y),	
ADXL345	MEMS	Digital	3	2, 4, 8, 16		256 LSB/g	3.2	1.6		10.17
						_			25 (2g),	
ADXL355	MEMS	Digital	3	2, 4, 8	20	265000 LSB/g	4	1 (LPF)	34 (8g,est.)	98.39
									75 (10g),	
ADXL357	MEMS	Digital	3	10, 20, 40	20	51000 LSB/g	4	1 (LPF)	90 (40g)	109.57
ADXL1001	MEMS	Analog	1	100	N/A	20mV/g	N/A	11	30	98.21
ADXL1002	MEMS	Analog	1	50	N/A	40mV/g	N/A	11	25	98.21
805M1	PE	Analog	1	20	N/A	100mV/g	N/A	10	Not listed	184.64
820M1	PE	Analog	1	25	N/A	50mV/g	N/A	15	25	70.99
830M1	PE	Analog	3	25	N/A	50mV/g	N/A	15	25	210
MPU6050	MEMS	Digital	9	2, 4, 8, 16	16	16384 LSB/g	1	.26 (LPF)	400	(Obsolete)
MPU9250	MEMS	Digital	6	2, 4, 8, 16	16	16384 LSB/g	4	1.046	300	(Obsolete)
ICM42688-P	MEMS	Digital	6	2, 4, 8, 16	16	16384 LSB/g	32	8.4	65 (x,y), 70	8.12
352C03	PE	IEPE	1	500	N/A	10	N/A	15	4	By Quote
356A25	PE	IEPE	3	200	N/A	25	N/A	6.5	2	By Quote
8702B25/50/						200, 100, 50				
100	PE	IEPE	1	25, 50, 100	N/A	mV/g	N/A	8, 10, 10	Not listed	By Quote

As shown in Figure 8, only the highest-end MEMS accelerometers (e.g., ADXL-1001/2, 820M1 series) and traditional piezoelectric sensors (IEPE-type) meet or exceed the full bearing CBM recommendations of ±50 g max range and 10 kHz bandwidth. These devices, however, tend to be significantly more expensive and are often better suited to niche or high-end industrial use cases. The shaded pink region highlights a promising zone where lower-cost MEMS devices offer performance trade-offs that could be acceptable. While they may not fully reach the ideal specs for bandwidth or range, their small size, low power, and integration potential make them attractive for wireless sensor node deployments. For this reason, several digital MEMS sensors within this region were selected for deeper evaluation and testing in this project.

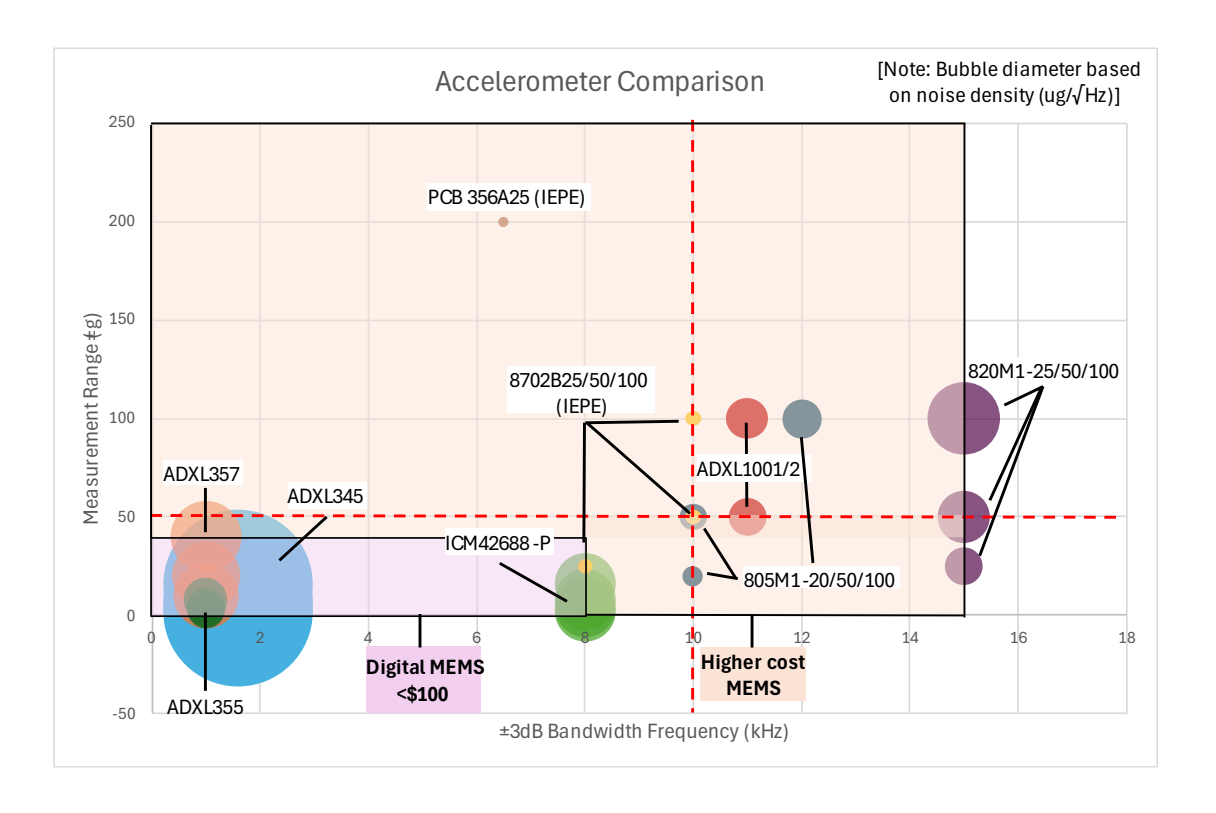


Figure 8: Accelerometer candidate comparison chart (based on [5])

3.2.1.3 ADXL-345

MEMS sensor, developed by Analog Devices with I²C and SPI outputs. The ADXL-345 is available in a variety of evaluation board forms, making it easy to test and integrate with the sensor system via SPI. The cheaper GY-291 board, shown in Figure 9, was used instead of the Analog Devices supplied EVAL-ADXL-345Z.

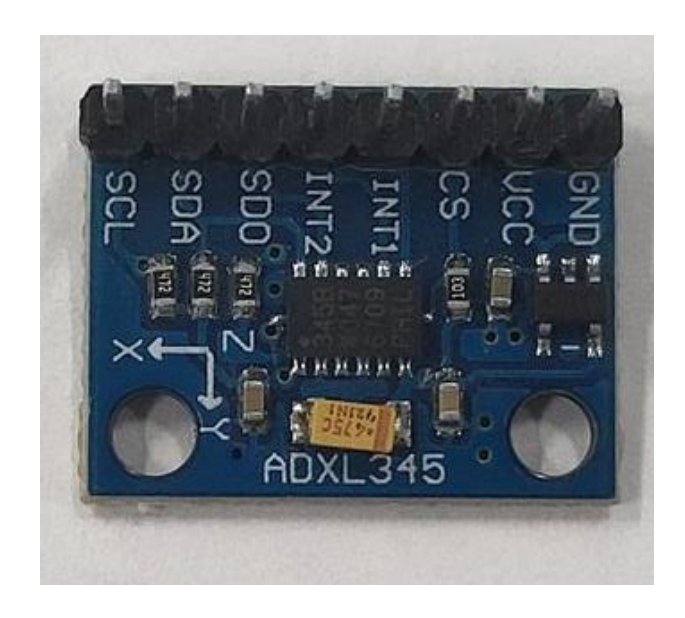
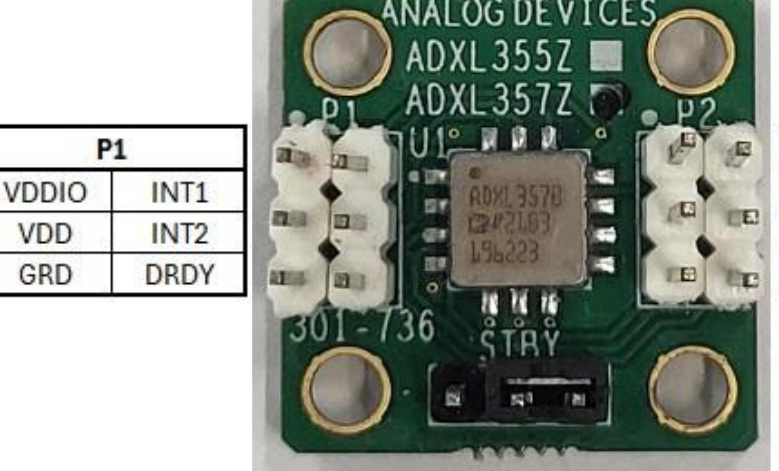


Figure 9: GY-291 / EVAL-ADXL-345 (20.4 mm x 15.2 mm)

3.2.1.4 ADXL-357

MEMS sensor, developed by Analog Devices with I²C and SPI outputs. Unlike the ADXL-345, the ADXL-357 has a non-bypassable on-board low-pass filter. So, although the sensor maximum ODR is 4 kHz, sensor bandwidth is limited to the 1 kHz cutoff frequency.

Like the ADXL-345, the ADXL-357 is available in an evaluation board form [77], as seen in Figure 10, except only from Analog Devices themselves. This board is more expensive compared to the more widely available ADXL-345, but is still affordable, and can be integrated with the sensor the same way as the other SPI evaluation board.



P2						
V1P8ANA	CS					
V1P8DIG	SCLK					
MISO	MOSI					

Figure 10: EVAL-ADXL-357Z PCB (0.8" x 0.8")

3.2.1.5 ICM-42688-P

Like the other two sensors tested, the ICM-42688-P is a MEMS sensor with digital I²C and SPI outputs. Unlike the other two sensors, it is a six-axis Inertial measurement unit (IMU) developed by TDK InvenSense.

Unlike Analog Devices evaluation boards, featuring the sensor chip and basic circuitry, TDK only offers the ICM-42688-P for evaluation as a development kit. The higher price of the development kits made it more economical to design a simple PCB, shown below in Figure 11, implementing the typical SPI operating circuit from the datasheet. Once ordered, these functioned the same as the other two evaluation boards, with the footprint matched to the ADXL-357 board so the two could share mounting hardware.



Figure 11: ICM-42688-P Evaluation PCB (0.8" x 0.8")

3.2.2 Microcontroller

The MCU is the central processing unit of the sensor, reading the data from the sensors and transmitting it over the network. The key requirements for this project were: an SPI interface, a Wi-Fi interface, low-cost, and an ethernet option had to be available for the 5G mmWave network connection.

MCU selection had to balance cost, processing capability and connectivity. Some examined alternatives and their information are included below in Table 5. Common options from past work includes the Arduino Uno, Raspberry Pi Pico, and ESP32. Other options, such as a Raspberry Pi 3, or BeagleBone Black were considered, but without a plan for performing edge compute on the sensor end,

low power consumption and cost were prioritized over the more draining but capable options.

Table 5: Controller board options

							ADC		Approx.
Board	Type	WiFi?	BT?	Eth?	Clock Speed	Cores	Res.	RAM	Price (\$)
Arduino Uno	MCU	n	n	Ext.	16 MHz	1	10	2 KB	10
Arduino Due	MCU	n	n	Ext.	84 MHz	1	12	96 KB	35
ESP8266	MCU	у	У	Ext.	80/160 MHz	1	10	32 KB	10
ESP32	MCU	у	У	y (\$20)	240 MHz	2	12	264 KB	10
Pi 3+	SBC	у	У	у	1.4 GHz	4	N/A	1 GB	50
BeagleBone Black	SBC	n	n	У	1 GHz	1?	12	512 MB	50
BeagleBone Black Wireless	SBC	у	У	n	1 GHz	1?	12	512 MB	100
Pi Zero	SBC	n	n	Ext.	1 GHz	1	N/A	512 MB	20
Pi Zero W	SBC	у	У	Ext.	1 GHz	1	N/A	512 MB	20
Pi Zero 2	SBC	n	n	Ext.	1 GHz	4	N/A	512 MB	20
Pi Zero 2 W	SBC	у	У	Ext.	1 GHz	4	N/A	512 MB	20
Pi Pico	MCU	n	n	Ext.	133 MHz	2	12	264 KB	5
Pi Pico W	MCU	у	У	Ext.	133 MHz	2	12	264 KB	10
Pi Pico 2	MCU	n	n	Ext.	150 MHz	2	12	520 KB	5
Pi Pico 2 W	MCU	у	У	Ext.	150 MHz	2	12	520 KB	10

The Arduino Uno is commonly used and offers simple integration options for SPI but lacks integrated network connectivity in regular configurations. The Raspberry Pi Pico is another low-cost option, and the Pico W has Wi-Fi and Bluetooth connectivity. But due to the combination of low-cost, high performance and a variety of package options, the ESP32, from Espressif Systems, was selected.

The ESP32 offers dual-core 240 MHz high performance processing to allow for the dual-thread producer-consumer software architecture, and supports high-speed SPI reads. As mentioned earlier, the power consumption is very low when compared to single board computer (SBC) options such as the Raspberry Pi 3, this will allow the sensor to collect the raw data for longer before needing to be charged.

Finally, the cost and options, it is often the lowest-cost dual core option, and an ethernet version is available to allow for 5G network integration.

Other ESP32 purchase options, such as an ESP32 with an external antenna and ESP32 with integrated 18650 battery hardware, also make for interesting future opportunities for sensor prototypes or alternatives.

3.2.3 Battery

Power management is a critical aspect of wireless sensors, with plenty of research into different power sources and methods for CBM systems, including batteries and self-powering sensors harnessing solar energy or other sources of energy like vibration from a manufacturing process [7, 58, 62, 78-81].

The selected ESP32 board operates at 3.3 V, drawing 80-200 mA in active mode. All of the selected accelerometers also operate with 3.3 V with very low current draws of ~30–140 μ A (ADXL-345), ~200 μ A (ADXL-357), and ~600 μ A (ICM-42688-P) at maximum ODR [76, 82]. Assuming 200 mA consumption during continuous operation and a 10-hour monitoring shift that would require $200 \ mA \times 10 \ h = 2000 \ mAh$.

Although the 5G version of the sensor will require wiring to the CPE which will be externally powered, the Wi-Fi version of the sensor will be tested with batteries to create a truly wireless sensor prototype. The battery will also allow the 5G version to operate with only an ethernet cable to the CPE instead of requiring power and ethernet run to the sensor. Another possible alternative to be considered in future

versions of the 5G prototype is changing to a power over ethernet (PoE) Ethernet ESP32, allowing the ethernet to carry both data and power. The PoE option was not integrated because future iterations of the MMRI 5G network should allow other 5G compatible devices to connect with a network SIM card and could remove the requirement for the CPE, allowing for a truly wireless 5G sensor if paired with an external battery.

Many battery types were considered for powering the sensor, compared based on cost efficiency, sizing and compatibility with the 3.3 V ESP32 sensor system.

Consumer USB battery packs or power banks provide a simple solution with high power capacities at a low cost. However, they are also large and heavy, especially at higher capacities, and can be subject to high losses. These often use internal lithium polymer (Li-Po) batteries, with output voltages from 3.2 V - 4.2 V and use regulators to provide a 5 V output. With the selected ESP32 requiring 3.3 V this means the battery voltage is converted from around 3.7 V to 5 V and back to 3.3 V by the ESP32 on-board power regulator. For example, a 26800 mAh USB power bank is about \$35 with 15.11 x 1.5 x 7.49 cm dimensions and weighing 350 g. Assuming 2000 mAh per day, this would provide about 13 days of run time, or around 10 days at 80% efficiency.

Alternatively, Li-Po batteries can be purchased themselves with a regulator. 18650, 18 x 65 mm length and diameter, Lithium-ion batteries are common and have 3.7 V output and capacities around 3300 mAh. This allows a single 18650 to be used

for 3.3 V power via a 3.3 V regulator and additional batteries can be added to add capacity, with one offering about a day and a half or two batteries offering around 3 shifts worth of run time.

Other options were considered, such as alkaline batteries and nickel-metal hydride (NiMH), but they are not as suitable as the lithium batteries chosen. Alkaline batteries are cheap but disposable and NiMH batteries have lower energy densities in comparison.

Both a USB power bank and 18650 batteries were purchased, with an adapter to provide regulation for the 18650s to 3.3 V. Both options have different pros and cons, with the larger, heavier USB power bank having a higher capacity and therefore longer sensor life while the 18650s are smaller, and more portable but at the cost of overall battery life. For a permanently installed sensor, the USB power bank offers longer time between charges and potentially a way to implement a swappable battery system when it dies. The 18650 would be more appropriate for a mobile sensor that is used to diagnose issues during a shift and can be removed at the end of the shift to recharge.

3.3 Electronics Design

The electronic hardware selection from this project was driven by three main objectives, minimizing sensor costs, maintaining maximum performance, and maintain design flexibility. The system was designed to allow for multiple accelerometers to be tested with minimal modifications to the system and presents

opportunities for easy integration of other sensor modalities, especially those with lower sampling rates and therefore data output requirements (such as temperature data).

All the selected accelerometers support SPI communication, at their maximum ODRs. This allows for the only major change between each sensor setup to be on the software end of integration. The SPI data communication also avoids a common ODR bottleneck of the ADXL-345 from literature, where the I²C bus is used instead, due to higher simplicity, but results in a maximum 1600 Hz ODR, compared to the 3200 Hz enabled with SPI. Lastly, this SPI connection could be expanded to work with analog sensors in the future via an external ADC with digital outputs, this could allow for analog sensors to be integrated with the existing prototype with higher performance compared to using the on-board ESP32 ADC.

Figure 12 and Figure 13 below show the difference between the Wi-Fi and 5G networked sensor units. The SPI connectivity allows any SPI accelerometer to be connected and tested if the appropriate software is available. This flexibility is a key feature of the modular sensor prototype, enabling future expansion to other sensor modalities beyond accelerometers. By maintaining a standardized SPI interface, the system can be easily adapted to support additional sensing technologies as needed.

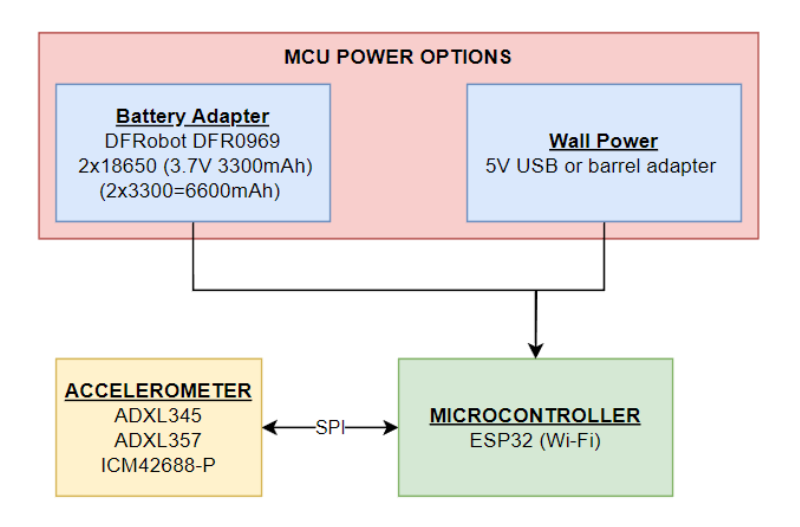


Figure 12: Wi-Fi sensor prototype electronics

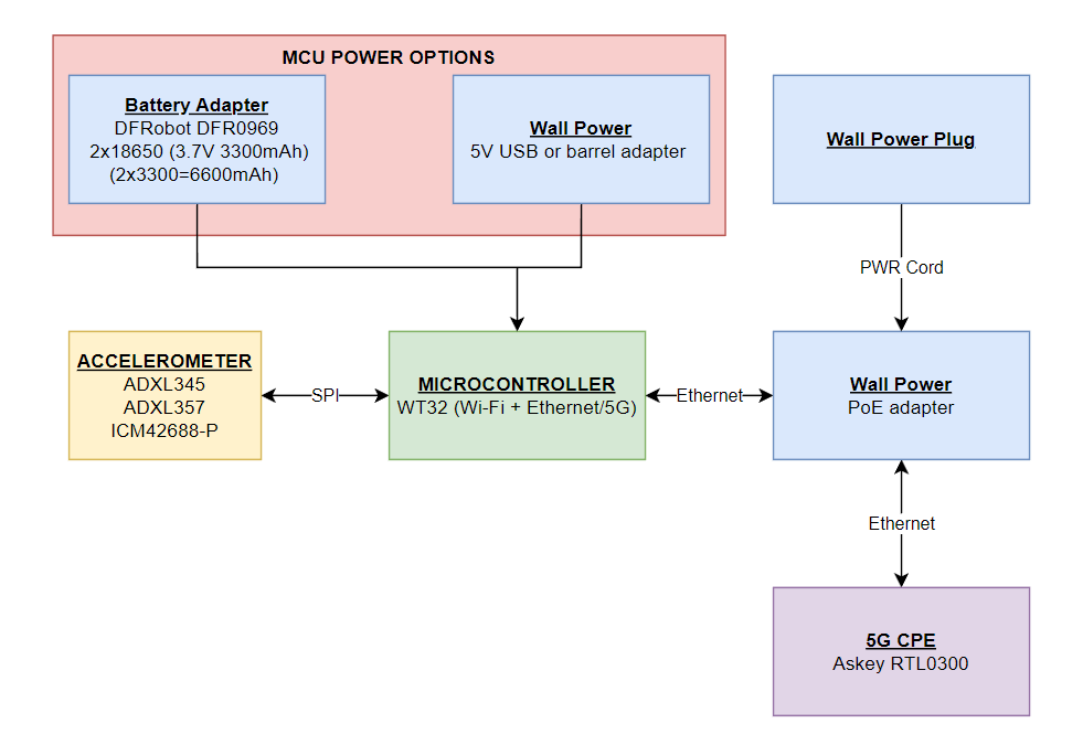


Figure 13: 5G sensor prototype electronics

3.4 Hardware Design

Since multiple accelerometers were tested with varying PCB dimensions, simple 3D printed accelerometer mounts were designed and used for testing. First, a screw mount adapter was made and used for the ADXL-345 and ADXL-357 in test 1. A magnetic case was designed to allow for easy sensor installation for test 2, and some shaker testing was redone with these mounts the see the change in performance. The design is similar to the clip-based mounts from PCB Piezotronics [83], without very tight mechanical coupling. These clips mounts are generally rated for around 1 - 3.5 kHz, so the current plastic mounts may only be acceptable for use with the lower frequency output ADXL-345 and ADXL-357.

Ideally, sensor mounts, and casing will both provide a rigid connection for vibration transfer and protect the MEMS sensor. To maintain sensor performance, the sensor mount resonant frequency should be over the frequency range of interest [83]. Therefore, these cheap plastic mounts should be replaced with a sturdier metal mount for future works using a single consistent accelerometer type throughout testing.

3.4.1 Sensor Prototype Costs

Below, Table 6 shows the costs for the Wi-Fi sensor variants using the regular ESP32, Table 7 shows the costs for the 5G compatible ethernet sensor versions. The miscellaneous section includes costs for filament for the cases/mounts and the wires for module connections. Both versions use a premade battery adapter

that could easily be replaced with a more affordable option in a final production design. Other than the adapter, the other costs would be the same for a more final sensor design, except for the added costs of any metal mount created for future versions.

The 5G CPE cost has not been included for the 5G sensor since the model used in testing is not available currently for purchase and is only used due to the MMRI 5G network connection requirements. However, the CPE cost, estimated at \$800 - 1000 USD per CPE, would significantly limit the scalability of the 5G solution. To deal with this, the CPE could be removed from a scalable system, replacing it and the ethernet connection with a 5G native MCU or other cheaper connection method. For example, a Waveshare Raspberry Pi 5G HAT with a 5G module is available for around \$330 USD, and the modules will only become more affordable as more are available on the market.

The current 5G ethernet sensor version can also lower the cost associated with the CPE by dividing it among multiple sensor nodes via a network switch. With multiple sensors connected, the performance will be split, but most of the sensor modalities mentioned only require a fraction of the bandwidth the CPE provides in testing. One example use case for this would be with multiple sensors on one machine, as if the sensors are too spread out and sharing a CPE, the wiring issues return.

These costs, while approximate for a production version sensor, are intended to demonstrate the potential cost savings of this strategy compared to using the

current standard equipment. They show that an entire wireless sensor can be made for about the cost of the high-end IEPE accelerometer, before accounting for any of the high cost IEPE acquisition equipment.

Table 6: Wi-Fi sensor costs

Wi-Fi Sensor Costs								
Component	Cost	QTY.						
ESP32	11.13	1						
Breadboard	6.66	1						
Battery								
Adapter	18.99	1						
18650 Battery	8.15	2						
ADXL-345	3.76	1						
ADXL-357	66.35	1						
ICM-42688-P	10.33	1						
Magnet	0.49	3						
Misc	~5.00	1						
TOTAL - 345	63.33							
TOTAL - 357	125.92							
TOTAL - ICM	73.66							

Table 7: 5G sensor costs

5G Sensor Costs								
Component	Cost	QTY.						
WT32 (Eth.)	27.25	1						
Battery								
Adapter	18.99	1						
18650 Battery	8.15	2						
ADXL-345	3.76	1						
ADXL-357	66.35	1						
ICM-42688-P	10.33	1						
Magnet	0.49	3						
Misc	~5.00	1						
TOTAL - 345	72.79							
TOTAL - 357	135.37							
TOTAL - ICM	83.12							

3.5 Software Design

3.5.1 Sensor Software

The sensor software, shown below in Figure 14, follows a dual-threaded producer-consumer architecture to manage data flow from the sensor to the network. This design prioritizes acquisition speed and code reusability to allow for high-speed data acquisition of multiple accelerometer types (and possibly other sensor types in the future) with minimal code changes.

The producer thread is an interrupt driven task triggered by each sensor's data-ready interrupt output. This output triggers each time the accelerometer has a new sample read to be read by the ESP32, each pulse triggers an SPI read of the accelerometer's data registers and the data is placed into a shared FreeRTOS queue. This queue allows the data read by this thread to be accessed by the consumer thread. This architecture ensures that the data collection (the producer) thread is always free for reading data when the data ready trigger occurs and since data collection occurs in this part of the code it is the only major modification needed between different sensor types.

The other thread, the consumer, reads the incoming data queued by the producer and processes it in batches, preparing the data for transmission. When a specified batch size is reached the consumer thread writes the accumulated data to the server via a Transmission Control Protocol (TCP) message to ensure no data is lost. This batching strategy minimizes the overhead compared to sending many small TCP messages, while maintaining timely delivery to the receiver.

The software design ensures that the data producer will read and queue all the sensor data if the data is read faster than the data ready signal is occurring, and the consumer task is able to send data off the device fast enough to maintain room in the shared data queue.

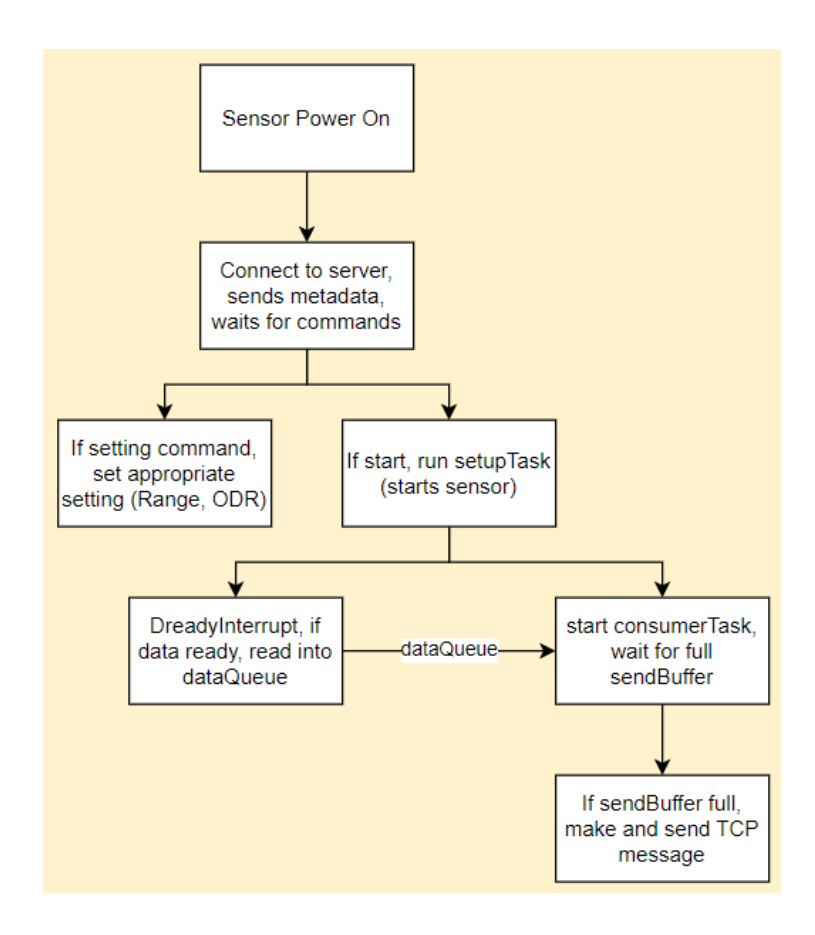


Figure 14: Sensor software basic functions

All accelerometers used the same producer-consumer software loop with some minimal changes for the different sensors. To allow for this, a library was used for each sensor to allow the appropriate settings to be controlled and data collected via SPI. The main challenge for supporting new accelerometer models is the requirement of a working library for SPI reads. For ADXL-345 this was simple as there are existing libraries to base the library on. For the others it was more complicated, the ADXL-357 has no public library, so one had to be created. An the existing ADXL-345 library and a public ADXL-355 library was used to create a custom ADXL-357 SPI library. The ICM-42688-P had an existing library, and this

was used to create a similar customized library, this allowed the function names to be matched with the ADXL-345 and ADXL-357 libraries used previously to allow for easy switching between the three. The file structure for pulling in the different sensor libraries is shown below in Figure 15.

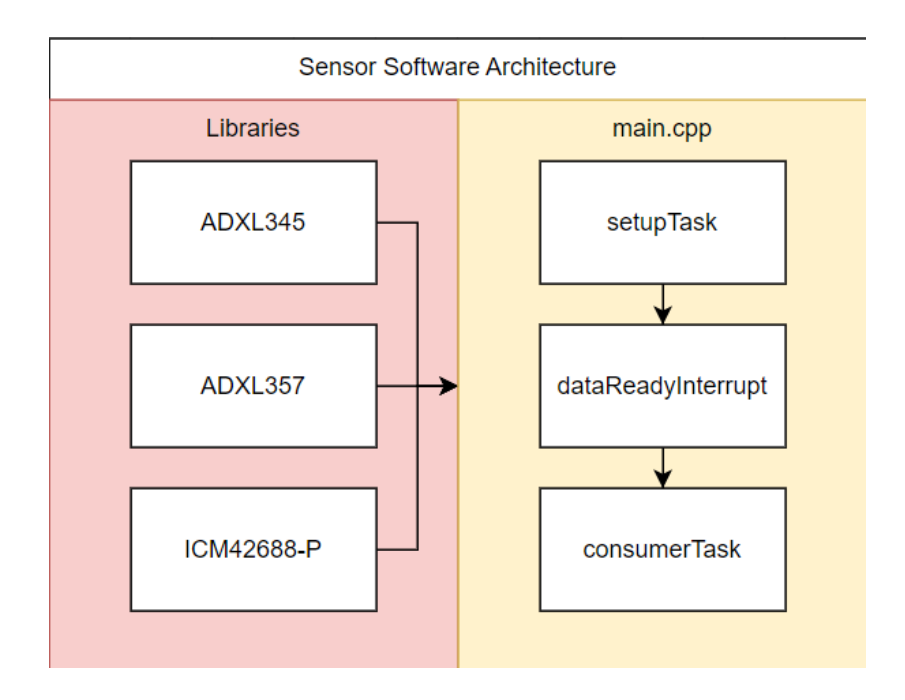


Figure 15: Sensor software file architecture

3.5.2 Receiver Software

The receiver software, mapped out in Figure 16, runs on the acquisition server or PC and is responsible for user controls, data visualization, data acquisition, and data logging. Currently it provides some data processing in the form of scaling the incoming sensor data.

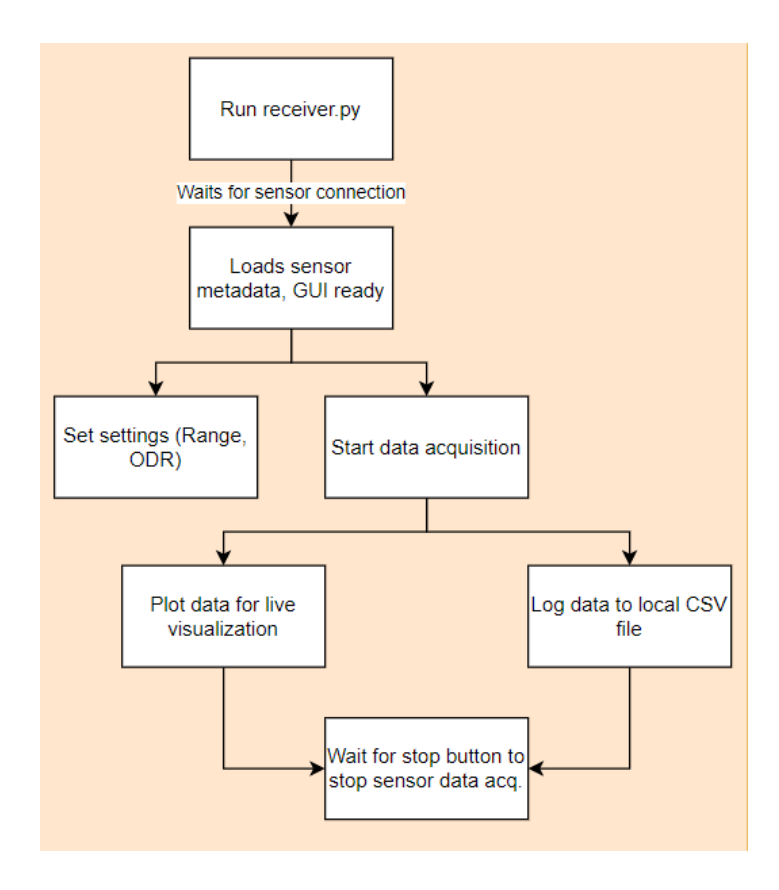


Figure 16: Receiver software basic functions

The Python based program provides a graphical user interface (GUI) to allow for acquisition control, once a sensor has been connected, the acquisition is controlled with start and stop buttons, each sending the respective command to the sensor.

Once acquisition has started, the GUI provides a live data visualization of X, Y, and Z sensor data. Currently the incoming data is written to a local comma separated values (CSV) file for future analysis.

3.5.3 Data formatting

Table 8 displays an example sensor sample message format with the byte sizing. Each sample records the change in time from the last sample (Delta_T), and

contains the raw binary XYZ axis data, all separated by commas and ended with a newline character (/n, 1 byte). The commas and newline take up 4 bytes per sample, with the time and data columns varying with sensor resolutions and ODR settings.

Table 8: Sensor sample data formatting (20-bit ADXL-357 XYZ data)

Structure:	Delta_T	,	X_DATA	,	Y_DATA	,	Z_DATA	/n	
Example:	250	,	±524287	,	±524287	,	±524287	/n	
Bytes:	3	1	7	1	7	1	7	1	28

Table 9 shows some of the selected sensors with the bytes per sample, ODR and calculated theoretical data rate in kbps, simply calculated by multiplying the maximum possible bytes per sample by ODR setting (samples per second). Usually, samples will be smaller than this because not all axes will be accelerating at the same time, for example a static sensor under gravity in Z-axis, X and Y should be about zero while Z has more data bytes, reducing the total data rate.

Table 9: Sensor output bit rates (Using maximum bytes per sample)

Sensor	Res. (bits)	XYZ Range	Max Bytes / sample	ODR (Hz)	Max Rate (kbps)
ADXL-345	13	±4095	22	3200	704
ADXL-357	20	±524287	28	4000	896
ICM42688	16	±32767	25	4000	800
ICM42688	16	±32767	27	32000	6912

In Table 9 the ICM4268-P is included at 4 kHz (the maximum ADXL-357 ODR) and its own 32 kHz maximum. Both were included to show the immense increase in

required data throughput as sampling rate is increased. The digital sensor options usually have ODR double for the next higher ODR setting so each increase in ODR (4 kHz to 8 kHz) doubles the data bitrate and requires additional data formatting and time information.

Chapter 4: Chapter 4: Testing

This chapter outlines testing methodology and results of experimental testing for both the MEMS sensors and the 5G network. Testing was performed to test the sensor performance against current SOTA IEPE systems and measurement was validated in both controlled and more industrial environments. Lastly, network performance was tested beyond sensor requirements to assess the capabilities of the network in various parts of the MMRI.

4.1 Testing Methodology

The testing methodology outlined in Figure 17 had three main objectives, each with an associated test. First, to test and validate sensor performance in a more controlled environment, a vibration calibration reference shaker was used for sensor benchmarks. This provided a known reference for sensor comparisons and for the MEMS performance to be validated before moving it into a test environment with more noise and error sources.

Second, the sensors were tested in a more realistic deployment environment on the linear axis testbed and compared to the existing IEPE sensor installation. Two wireless sensors were installed, one on a mobile carrier block and one on a static rail, to replicate a CBM system used in previous works [69-71]. This allows a direct comparison between the developed sensor prototype and a SOTA system in a real CBM use case.

Lastly, the network performance was tested beyond the sensor prototype requirements with the iPerf network testing tool. This tool allowed a separate test setup to be used to test network performance across various spots of the MMRI shop floor from both outside and inside the machines. The data allows for network performance evaluation of upload and download for both TCP and UDP traffic.

Together, these three tests provide a good baseline for the selected MEMS sensor performance with known and reliable test equipment, a direct comparison of the MEMS sensors to a SOTA measurement system in an industrial use case scenario, and 5G mmWave network performance information from an industrial setting to provide insight into usage opportunities.

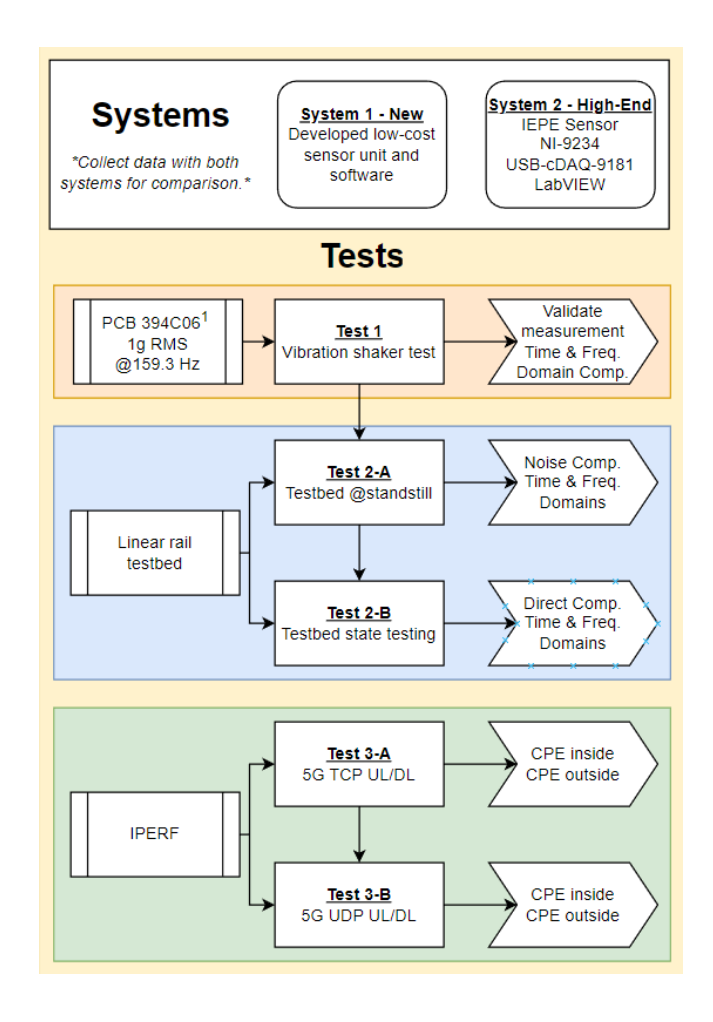


Figure 17: Testing plan

4.2 Accelerometer Test 1: Vibration Test Shaker

4.2.1 Test 1 Objectives and Setup

The first test was used to validate wireless sensor performance and to provide basic performance characteristics for comparison for the selected low-cost MEMS accelerometers and a high-performance IEPE reference sensor. A Model 394C06 Handheld Vibration Shaker [84] served as the vibration reference source for this

experiment, providing a known reference vibration source for comparing the various sensors.

The shaker is designed for system calibration and validation, delivering a stable output at 159.2 Hz with two selectable operation modes: 1 g RMS or 1 g peak. The device automatically compensates for sensor masses up to 210 g, seen in Figure 18 below with an internal reference sensor inside that maintains the set amplitude at the target frequency.

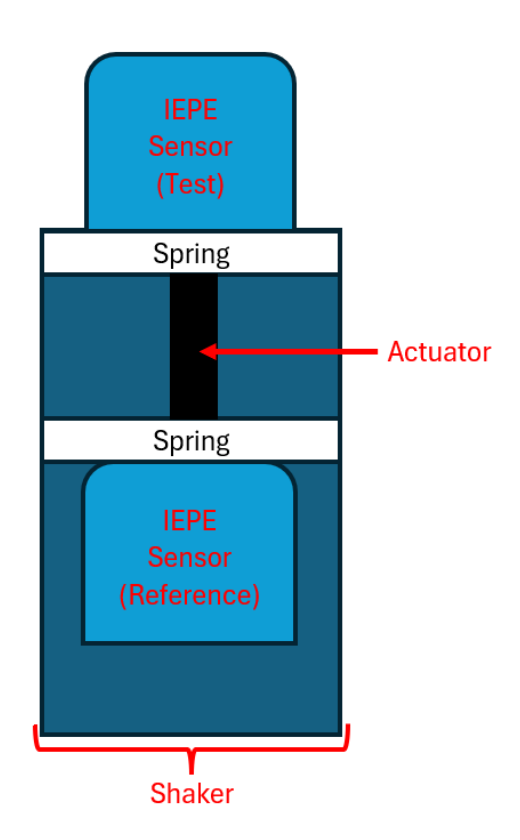


Figure 18: Cross-section of Handheld Vibration Shaker Head [84]

As seen in Figure 19 and Figure 20, each accelerometer was individually mounted on the shaker and tested, including a high-end IEPE sensor to provide a SOTA baseline for performance. Both Analog Devices MEMS accelerometers were tested

at their highest ODR and each of their respective measurement ranges. Since testing was performed later, the ICM-42688-P was tested at 4 kHz to match the ADXL-357 and IEPE reference. The IEPE sensor was set to 4 kHz to match the sampling rate of the original highest ODR MEMS accelerometer (ADXL-357). 15, 45 second data samples were collected for each sensor.







Figure 20: ADXL-357 mounted on shaker

The test consisted of 5 static samples, with the sensor mounted to the shaker but with the shaker powered off and 5 samples in each shaker operation mode (1 g RMS and 1 g peak). The static samples allowed for baseline noise and offset characteristics to be investigated, while the shaker data provided insight into dynamic performance.

The Analog Devices MEMS sensors (ADXL-345 and ADXL-357) were all tested using the Wi-Fi sensor variant, but for the ICM42688, the 5G sensor version was utilized for data collection (Figure 21 and Figure 22). Both sensor versions use the same receiver program for controls, data visualization and data logging to local CSV files. The IEPE reference accelerometer data was acquired using a typical wired data acquisition setup, consisting of a National Instruments (NI) cDAQ-9184 chassis, a NI-9234 IEPE acquisition card and captured with a LabVIEW program.

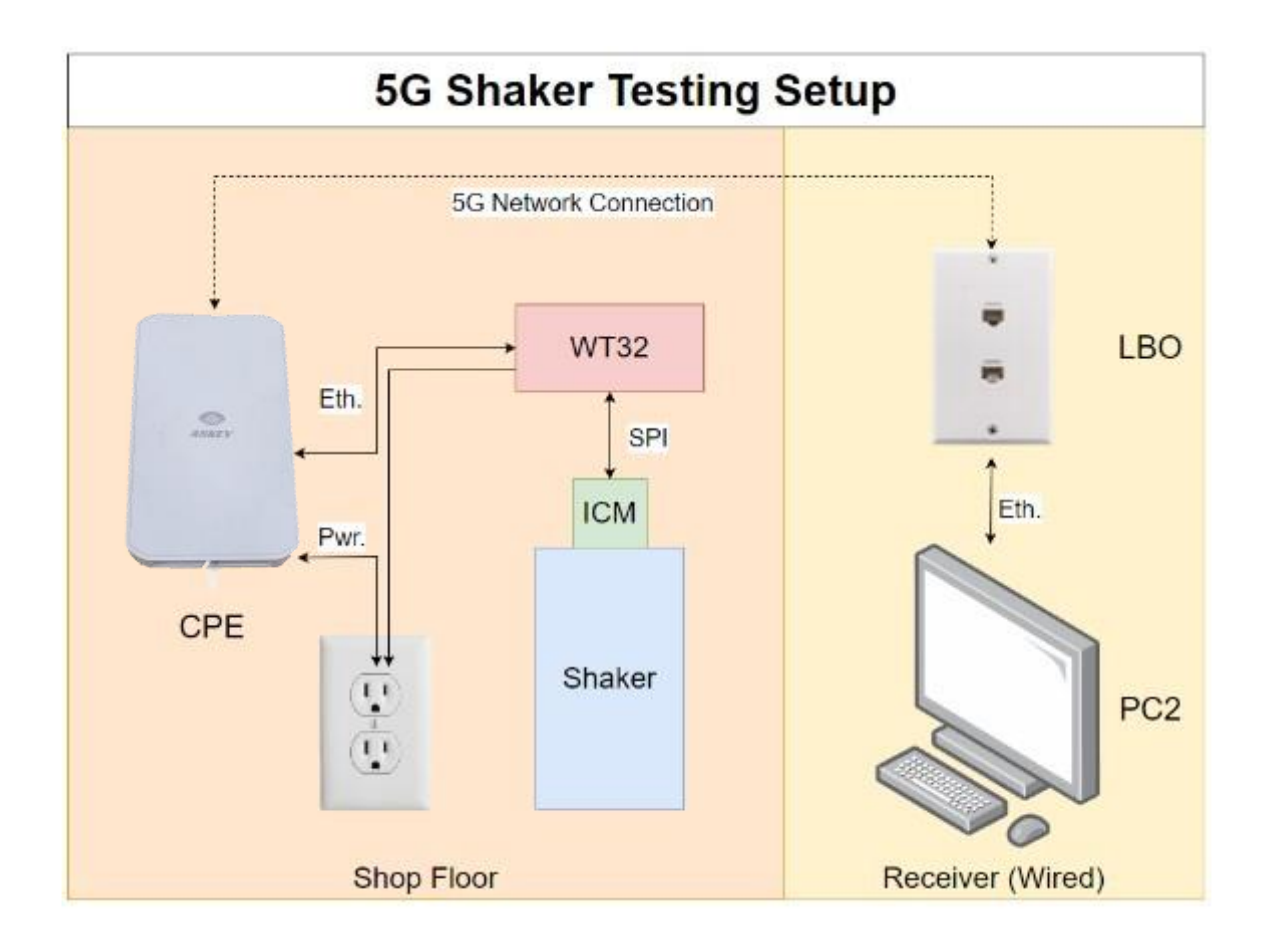


Figure 21: 5G Shaker testing setup diagram

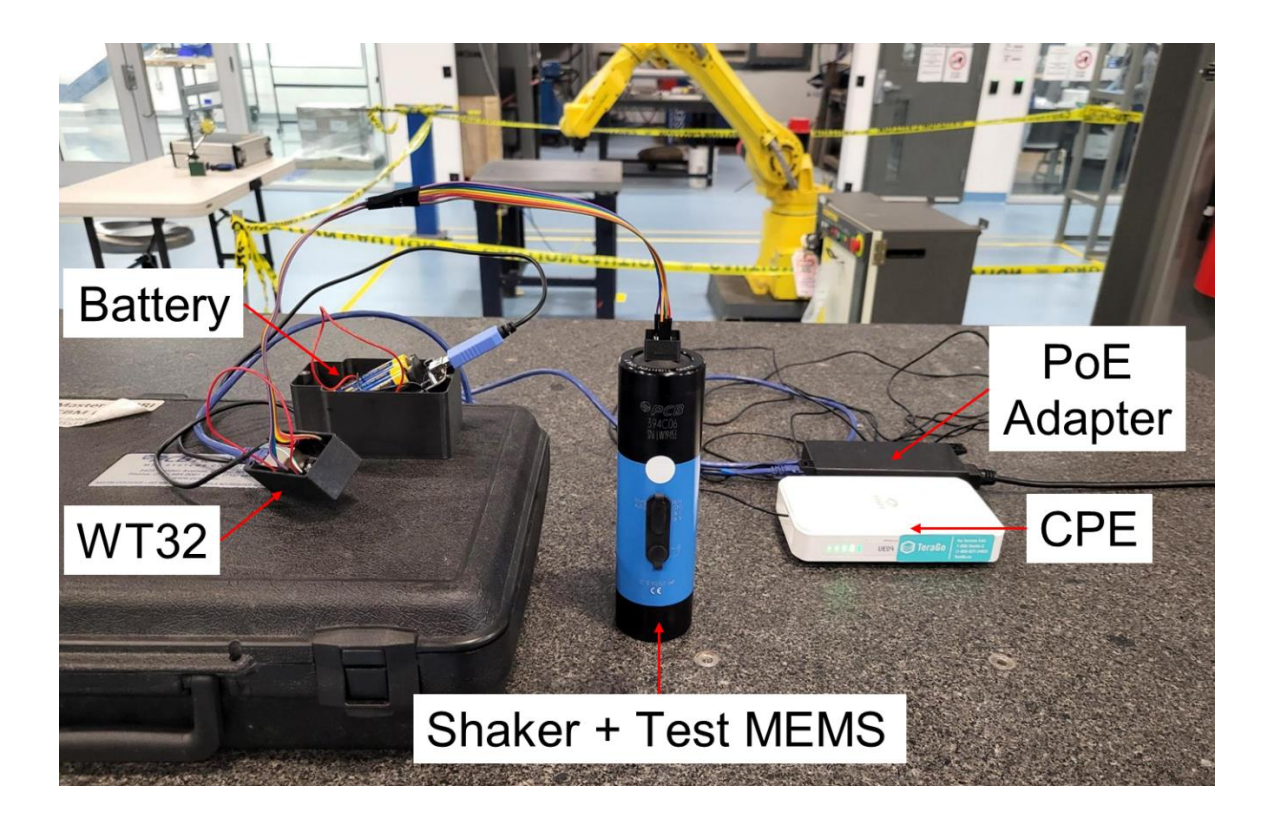


Figure 22: Test 1 setup, ICM-42688-P 5G

Table 10 contains a summary of all the tests performed using the shaker for test 1, showing the different sensors tested, ranges, ODRs and communication methods for each individual test.

Table 10: Summary of test 1 data collected

Test 1									
Sensor	Range	Mode	Power	ODR	Comm.				
ADXL-345	2 g	Static	USB	3200Hz	Wi-Fi				
ADXL-345	4 g	Static	USB	3200Hz	Wi-Fi				
ADXL-345	8 g	Static	USB	3200Hz	Wi-Fi				
ADXL-345	16 g	Static	USB	3200Hz	Wi-Fi				
ADXL-345	2 g	RMS	USB	3200Hz	Wi-Fi				
ADXL-345	4 g	RMS	USB	3200Hz	Wi-Fi				
ADXL-345	8 g	RMS	USB	3200Hz	Wi-Fi				
ADXL-345	16 g	RMS	USB	3200Hz	Wi-Fi				
ADXL-357	10 g	Static	USB	4000Hz	Wi-Fi				

ADXL-357	20 g	Static	USB	4000Hz	Wi-Fi
ADXL-357	40 g	Static	USB	4000Hz	Wi-Fi
ADXL-357	10 g	RMS	USB	4000Hz	Wi-Fi
ADXL-357	20 g	RMS	USB	4000Hz	Wi-Fi
ADXL-357	40 g	RMS	USB	4000Hz	Wi-Fi
PB352C03	500g	Static	NI-DAQ	4000Hz	Wired
PB352C03	500g	RMS	NI-DAQ	4000Hz	Wired
ADXL-357	10 g	Static	Battery	4000Hz	Wi-Fi
ADXL-357	20 g	Static	Battery	4000Hz	Wi-Fi
ADXL-357	40 g	Static	Battery	4000Hz	Wi-Fi
ADXL-357	10 g	RMS	Battery	4000Hz	Wi-Fi
ADXL-357	20 g	RMS	Battery	4000Hz	Wi-Fi
ADXL-357	40 g	RMS	Battery	4000Hz	Wi-Fi
ADXL-357	10 g	Peak	Battery	4000Hz	Wi-Fi
ADXL-357	20 g	Peak	Battery	4000Hz	Wi-Fi
ADXL-357	40 g	Peak	Battery	4000Hz	Wi-Fi
ICM42688	2 g	Static	Battery	4000Hz	5G
ICM42688	4 g	Static	Battery	4000Hz	5G
ICM42688	8 g	Static	Battery	4000Hz	5G
ICM42688	16 g	Static	Battery	4000Hz	5G
ICM42688	2 g	RMS	Battery	4000Hz	5G
ICM42688	4 g	RMS	Battery	4000Hz	5G
ICM42688	8 g	RMS	Battery	4000Hz	5G
ICM42688	16 g	RMS	Battery	4000Hz	5G
ICM42688	2 g	Peak	Battery	4000Hz	5G
ICM42688	4 g	Peak	Battery	4000Hz	5G
ICM42688	8 g	Peak	Battery	4000Hz	5G
ICM42688	16 g	Peak	Battery	4000Hz	5G

4.2.2 Test 1 Data Processing and Analysis

Figure 23 contains an outline of the data processing steps for test 1. During collection, the raw data was transmitted from the sensor to a receiving PC and logged to local CSV files on the receiving end. This raw data went through a multi-

step process before being compared. First, the data files were all validated for data completeness and sampling rate consistency. Second, the data files were cleaned, with sampling time intervals (ΔT) being equalized to account for any small variations in sampling frequency. Then the static data was used to calculate static axis offsets, ideally this allows static effects, such as gravity in the Z direction, to be removed. Lastly, the offset raw binary data value is scaled to g based on the sensor and range specific scaling factor.

From the static data samples collected for each accelerometer, noise density was calculated to characterize baseline performance. Noise density, expressed in $\mu g/\sqrt{Hz}$, was calculated by performing a Fast Fourier Transform (FFT) on the static time-series data, computing the Power Spectral Density (PSD), and averaging the noise floor across the sensor's bandwidth. This value was also compared to the noise density value from each accelerometer datasheet to validate performance.

From the dynamic data, many time-domain statistical features were calculated from each sampling and averaged out over the five sets. The features included:

- Mean (g): Indicates bias or offset, should be 0g for a sinusoidal shaker signal.
- Standard deviation (STD Dev g): Variation around the mean, should match RMS for a sinusoidal signal.
- Root mean square (RMS g): Should be 1 g for RMS mode, 0.707g for peak (Pk) mode

- Peak to Peak (Pk-Pk g): Range of minimum to maximum, for RMS mode should be around 2.828 g, for Pk mode ideally 2 g
- Excess kurtosis: Ideally -1.5 for a sinusoidal wave, higher than this means
 the data has sharper peaks than a sine wave and lower has flatter peaks.
 Sharp peaks could indicate noise or impulsive events while flat peaks could
 be the result of damping.
- Skewness: Should be 0 for a sine wave
- Median (g): The middle data value, for a sine wave this should be close to
 Og and can help tell if the mean is skewed
- Peak (Pk g): Should be 1.414 g for RMS mode, 1 g for Pk mode
- Crest Factor: Ratio of peak to RMS value, should be 1.414 for both shaker modes. Over 1.414 indicates sharp spikes or impulses and lower values are flatter than sinusoidal, indicating possible damping.

Additionally, frequency-domain analysis was performed via FFT to verify the spectral performance of the accelerometers, at low frequency (159.2 Hz).

The FFT plot for RMS data should ideally show a peak at 159.2 Hz with 1.414 g amplitude, or as calculated according to: $A_{peak} = A_{RMS} \times \sqrt{2}$, so with 1 g RMS at 159.2 Hz the corresponding peak would be $A_{peak} = 1g \times \sqrt{2} \approx 1.414 \ g$.

After the FFT was plotted, a Hanning window was applied to the FFT, making the peak more prominent and showing how simple data processing can be used to improve the outputs. A Hanning window was chosen because the samples taken

from the shaker do not all start and end at the same point of the wave, so a Hanning window can help smooth out the discontinuities from beginning to end. By reducing spectral leakage, the datasets all more clearly reveal the shaker's peak frequency.

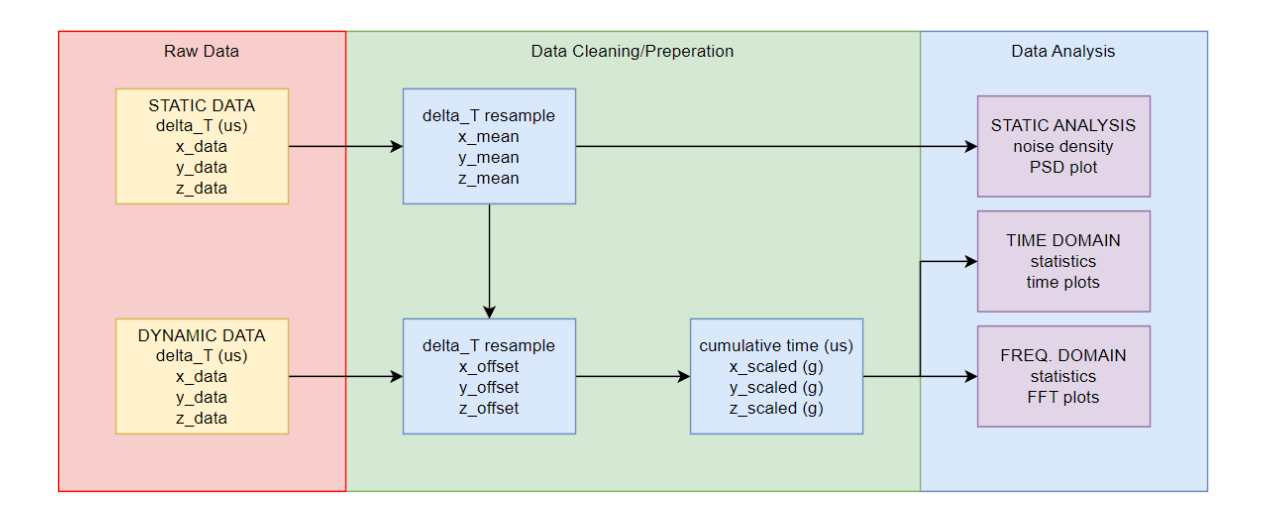


Figure 23: Data processing steps

4.2.3 Test 1 Static Shaker Test Results

4.2.3.1 ADXL-345 – Bolt Mounted, USB Powered

Figure 24 - Figure 26 contain the ADXL-345 static PSD for each axis individually, with Figure 27 combining all ranges and monitored axes into one plot. These show a consistent noise performance within each axis for all range settings, with the noise going down slightly as the frequency rises.

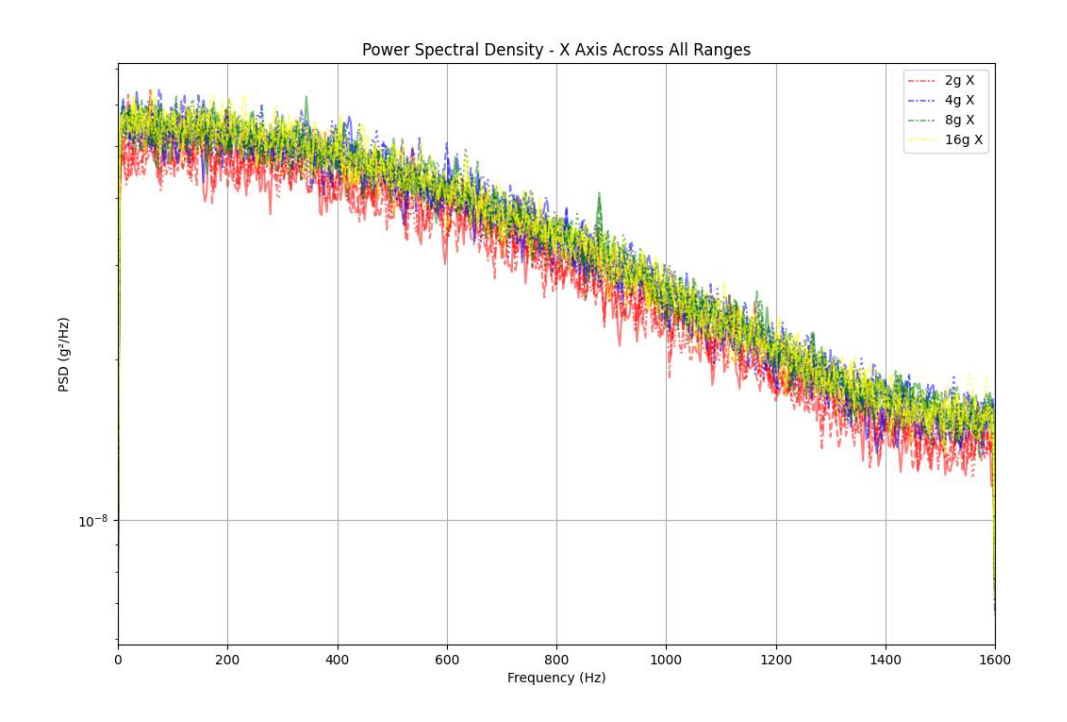


Figure 24: ADXL-345 x-axis PSD all ranges

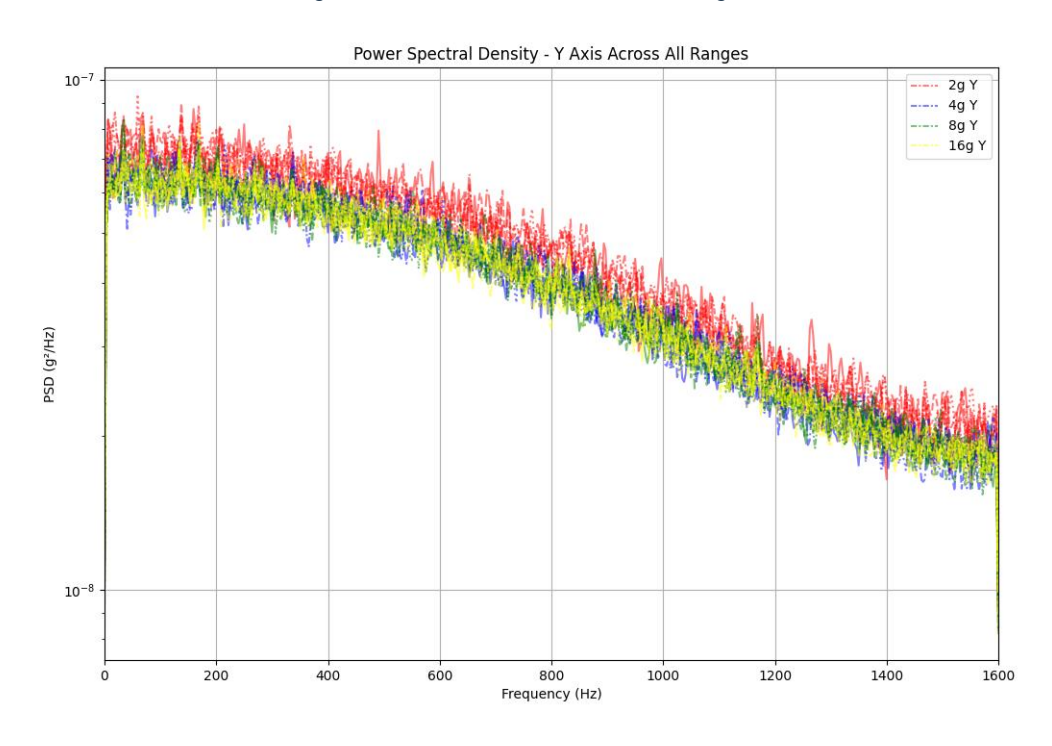


Figure 25: ADXL-345 y-axis PSD all ranges

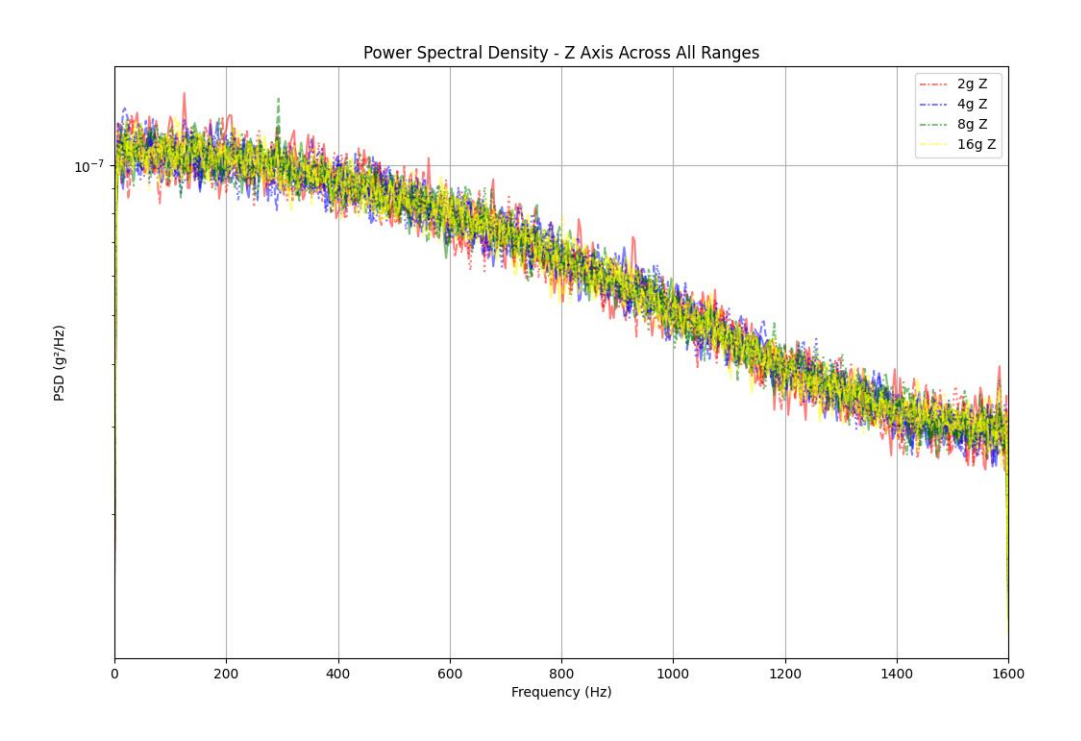


Figure 26: ADXL-345 z-axis PSD all ranges

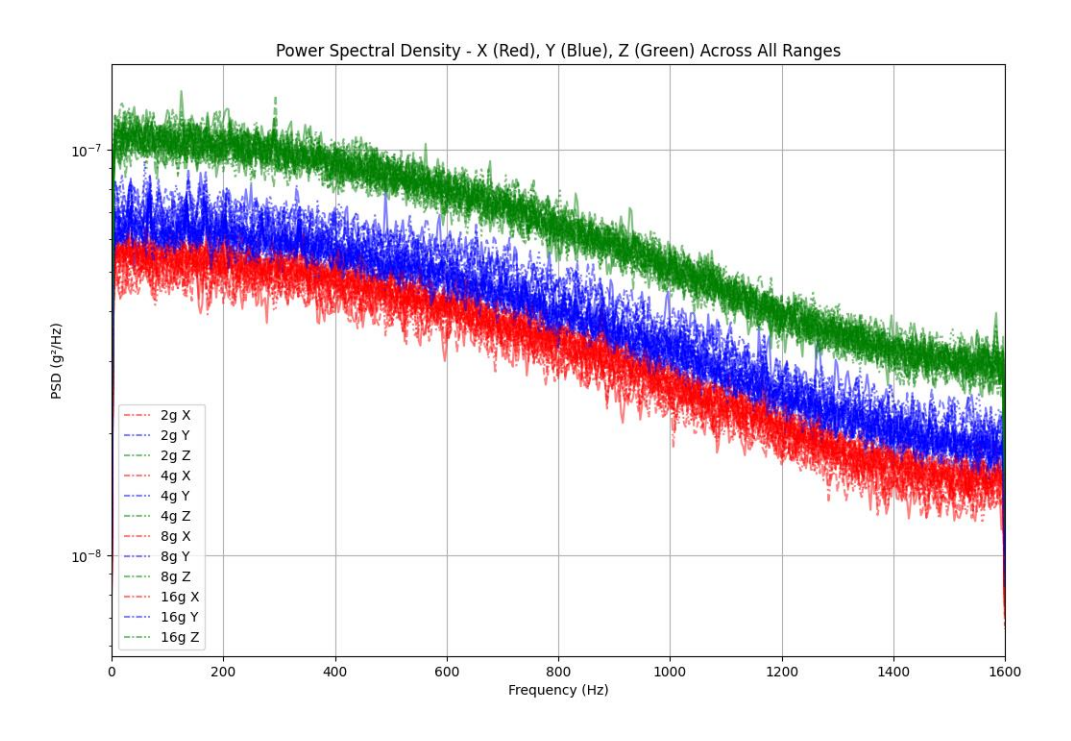


Figure 27: ADXL-345 XYZ PSD all ranges

Table 11 shows the noise densities calculated with the static data. The value shown is the average noise from the five data samples collected for each range setting. The ADXL-345 datasheet [85] specifies the ADXL-345 noise density as 290 μ g/ \sqrt{Hz} for the x-axis and y-axis and 430 μ g/ \sqrt{Hz} for the z-axis. The noise values from the test align with having a higher z-axis noise, and all ranges show slightly less noise than specified.

Table 11: ADXL-345 Average Noise Density results

ADXL-345 Noise Density (μg/√Hz)									
Range (±g)	X	Υ	Z						
2	207	250	301						
4	217	234	301						
8	217	234	302						
16	217	233	301						
Avg	214	238	301						
Datasheet [85]	290	290	430						

It should also be noted that the ADXL-345 tests were all performed at the maximum 3200 Hz ODR (normal power) to maximize frequency bandwidth. The ADXL-345 datasheet [85] shows that in normal power mode, output noise drops when switching to lower ODR settings down to 100 Hz. This could be useful for lowering output noise in applications with lower bandwidth requirements.

4.2.3.2 ADXL-357 – Bolt Mounted, USB Powered

Figure 28 - Figure 30 each contain PSDs for all ranges of each axis individually, with Figure 31 showing all axes for the 40 g range only, the range of the highest noise density. Unlike the ADXL-345, the plots clearly show an increase in noise

density when changing measurement range up from 10 g to 20 or 40 g ranges.

Overall, these PSDs show a lower noise density compared to the previously tested ADXL-345, as expected based on the datasheet parameters.

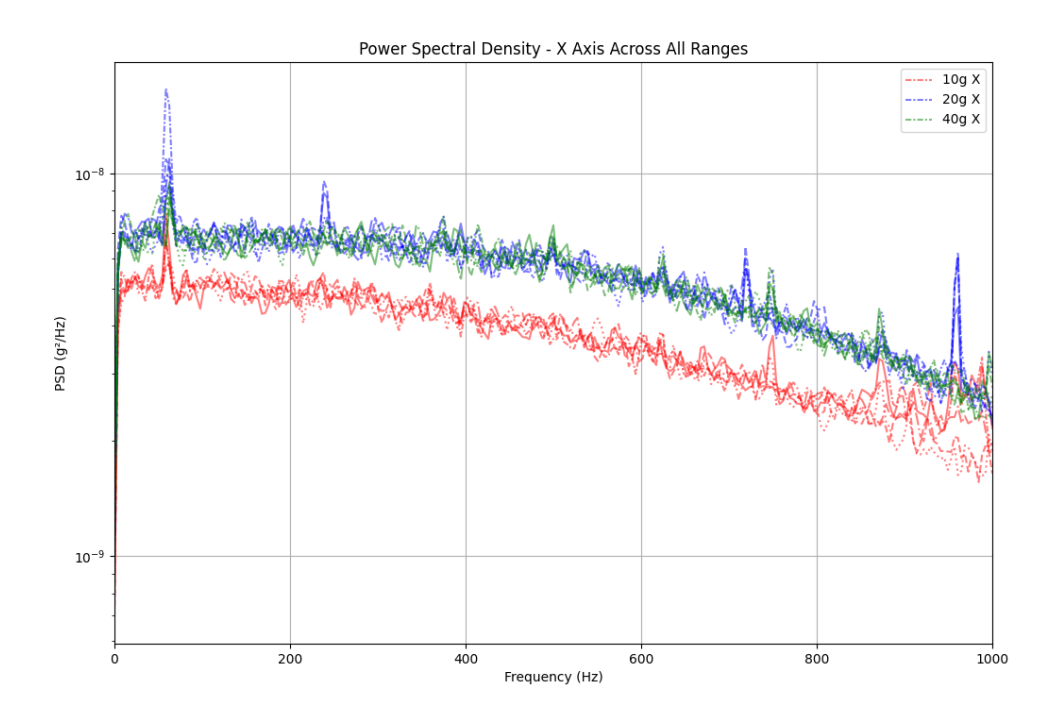


Figure 28: ADXL-357 x-axis PSD all ranges

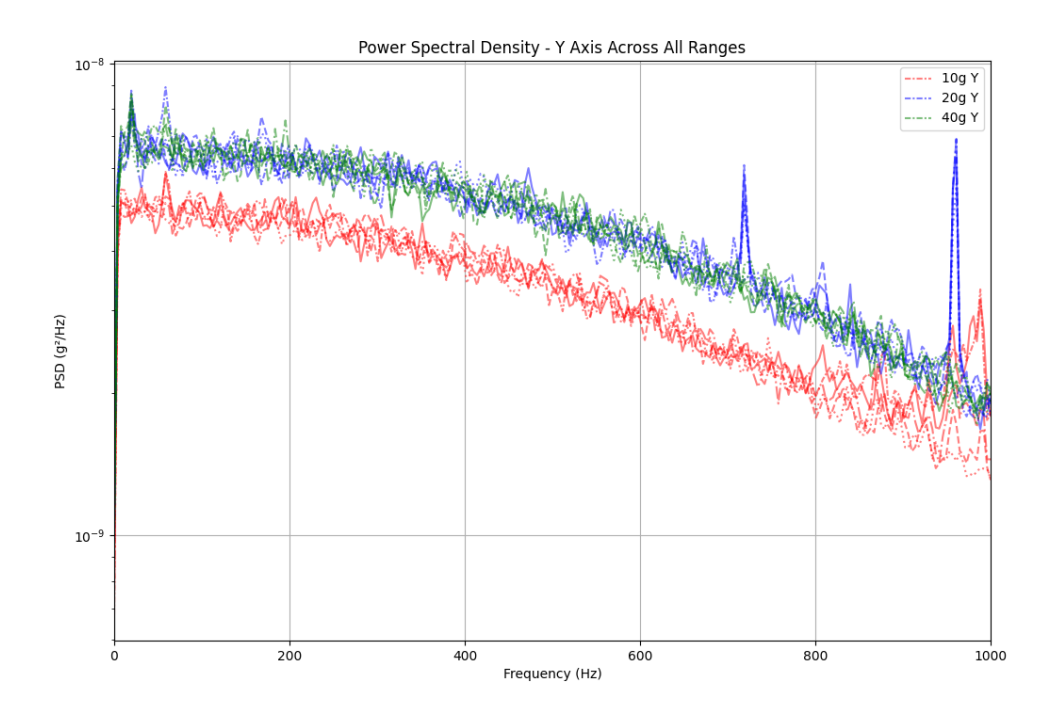


Figure 29: ADXL-357 y-axis PSD all ranges

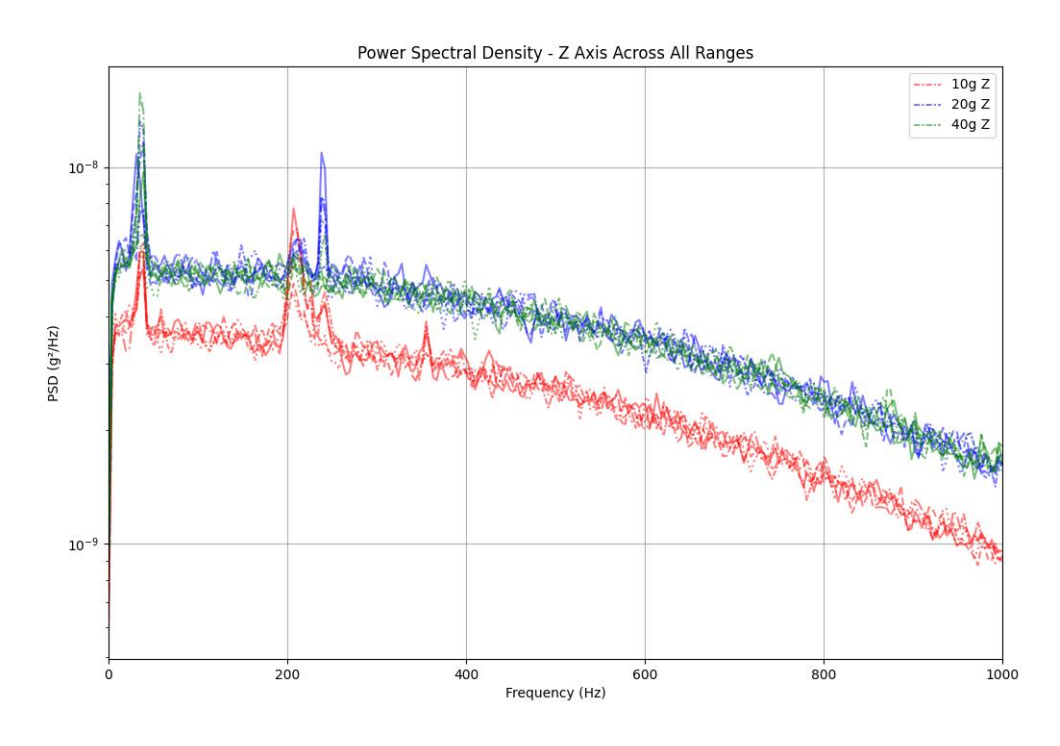


Figure 30: ADXL-357 z-axis PSD all ranges

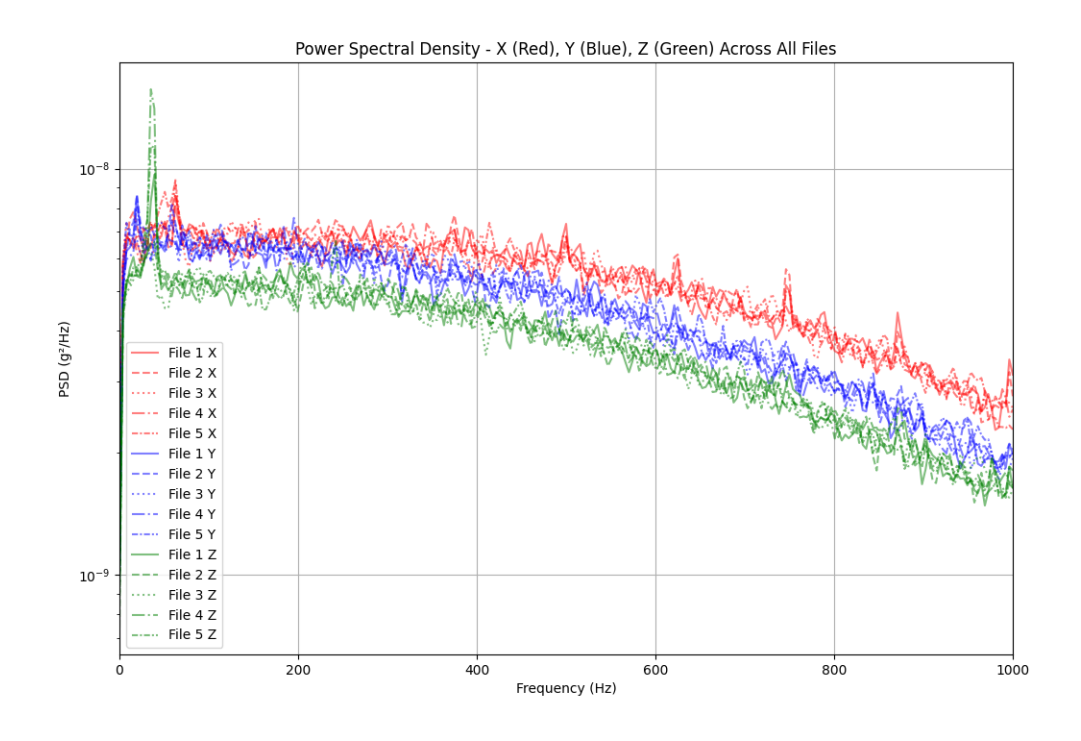


Figure 31: ADXL-357 XYZ PSD 40 g range

In Table 12, the ADXL-357 demonstrates a clear relationship between its full-scale range setting and the observed noise density. At the lowest range setting of ± 10 g, the average noise density is 57 μ g/ \sqrt{Hz} , which increases slightly to 68 μ g/ \sqrt{Hz} at both ± 20 g and ± 40 g ranges. This result aligns with the datasheet specifications, due to a difference in ADC architecture, the higher range settings introduce higher noise levels due to reduced sensitivity when changed. The measured values are consistent with or better than the datasheet noise densities, which report 75 μ g/ \sqrt{Hz} at ± 10 g 90 μ g/ \sqrt{Hz} at ± 40 g. Unfortunately, the datasheet has no ± 20 g value so it is not clear if the noise should change between the two higher settings, but they do not in the testing results.

In contrast, the ADXL-345 shows much higher noise densities across all range settings. Its average noise densities across the X, Y, and Z axes, which matched the expected result in the datasheet, are 214, 238, and 301 μ g/ \sqrt{Hz} , which are significantly above those of the ADXL-357.

Overall, the ADXL-357 offers significantly lower noise performance than the ADXL-345, particularly at the lowest range setting, making it more suitable for precision vibration measurements or condition-based monitoring applications requiring low noise.

Table 12: ADXL-357 Average Noise Density results

	ADXL-357 Noise Density (µg/√Hz)										
Power	Range (±g)	X	Υ	Z	Avg	Datasheet					
USB	10	61	58	51	57	75					
USB	20	74	68	62	68	N/A					
USB	40	73	68	62	68	90					

4.2.3.3 ADXL-357 – Magnet Mounted, Battery Powered (5V)

This testing was mainly to ensure noise performance was not changed when powered with the battery instead of via the USB cable. Figure 32 - Figure 34 contain the PSDs for X, Y and Z with the magnetic mount while Figure 35 shows XYZ for the 40 g range only. When compared to Figure 28 - Figure 31 with the bolt mount and USB power, no major differences were revealed.

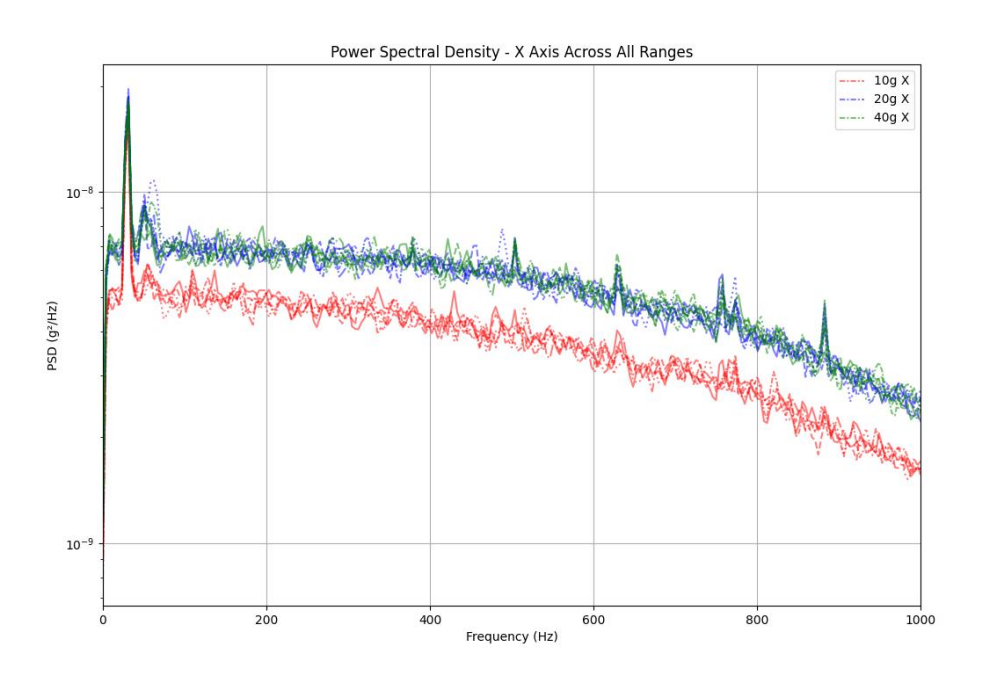


Figure 32: ADXL-357 magnet mount x-axis PSD all ranges

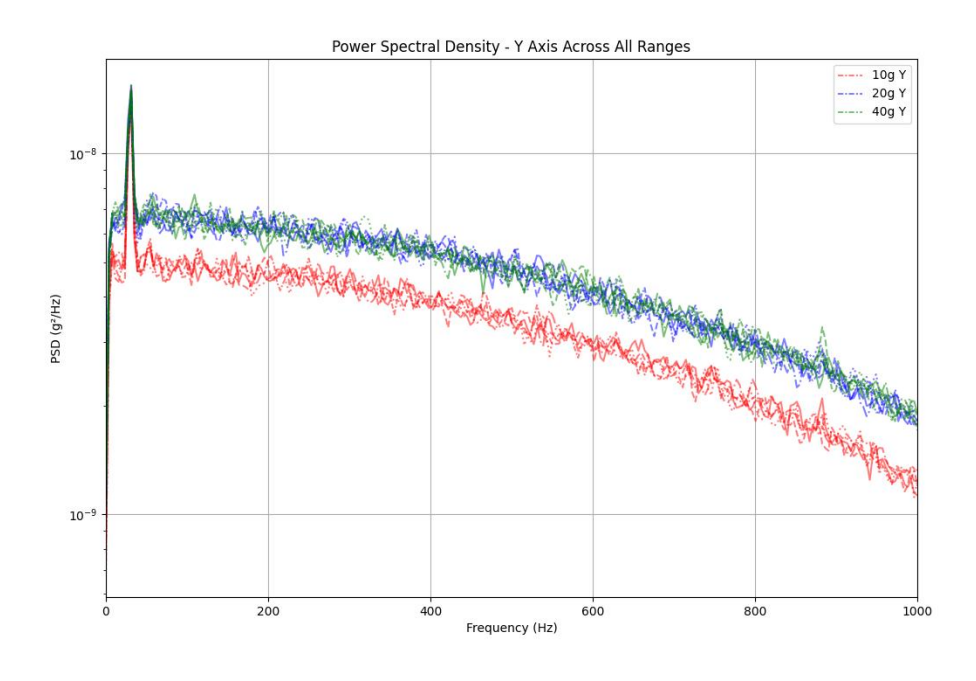


Figure 33: ADXL-357 magnet mount y-axis PSD all ranges

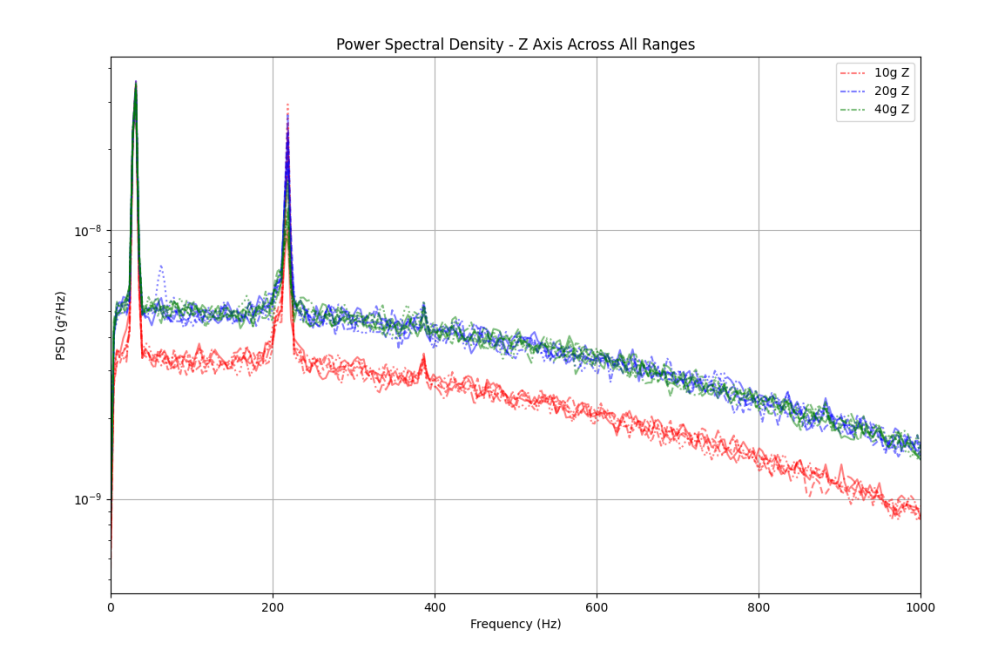


Figure 34: ADXL-357 magnet mount z-axis PSD all ranges

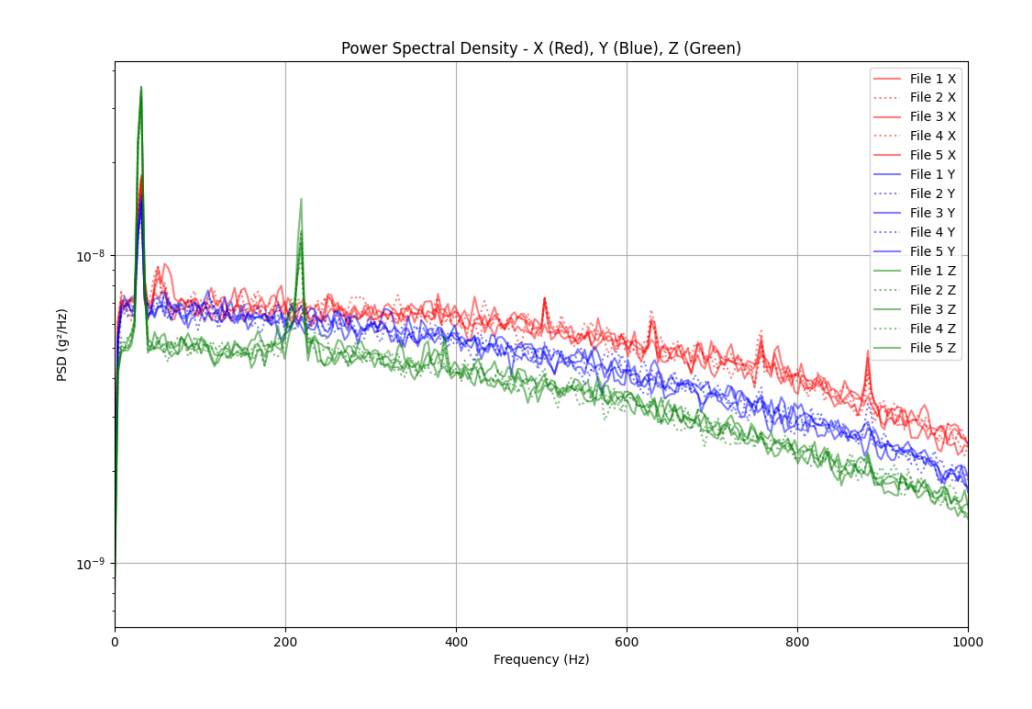


Figure 35: ADXL-357 magnet mount XYZ PSD 40 g range

The noise results in Table 13 show an identical resulting noise density when averaged across all axes for each range showing that the measurement performance was not affected by the power supply change.

Table 13: ADXL-357 noise comparison USB vs battery powered

A	ADXL-357 Noise Density (μg/√Hz)										
Mode	Range (±g)	X	Υ	Z	Avg						
USB	10	61	58	51	57						
Battery	10	62	58	52	57						
USB	20	74	68	62	68						
Battery	20	74	68	63	68						
USB	40	73	68	62	68						
Battery	40	74	68	63	68						

4.2.3.4 ICM-42688-P - Magnet Mounted, Battery Powered, 5G, 4 kHz ODR

Since the previous test with the ADXL-357 displayed similar results for both the screw mount and magnet mounted accelerometers, the ICM-42688-P was only tested with the magnet mount. A magnetic base was required for test 2 (due to a lack of mounting studs), so test 1 was performed with the mount planned to be used in further tests.

Figure 36 - Figure 39 contain the ICM-42688-P PSDs from test 1. They show a similar result as the ADXL-345 in the sense that the noise was consistent within a single axis even while switching measurement ranges. It was similar to the ADXL-357 results in terms of total noise density across the measured spectrum.

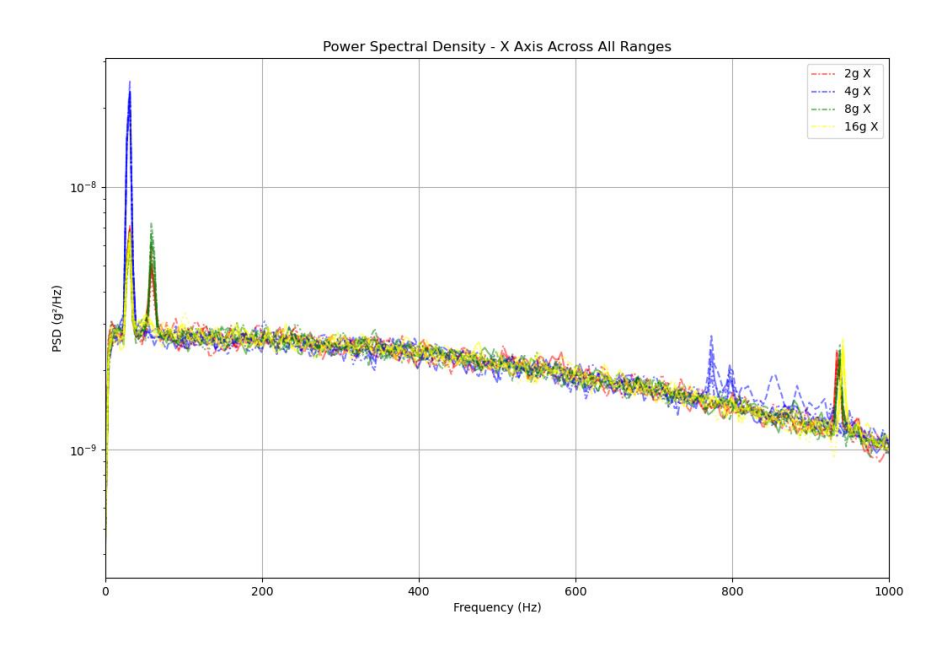


Figure 36: ICM-42688-P x-axis PSD all ranges

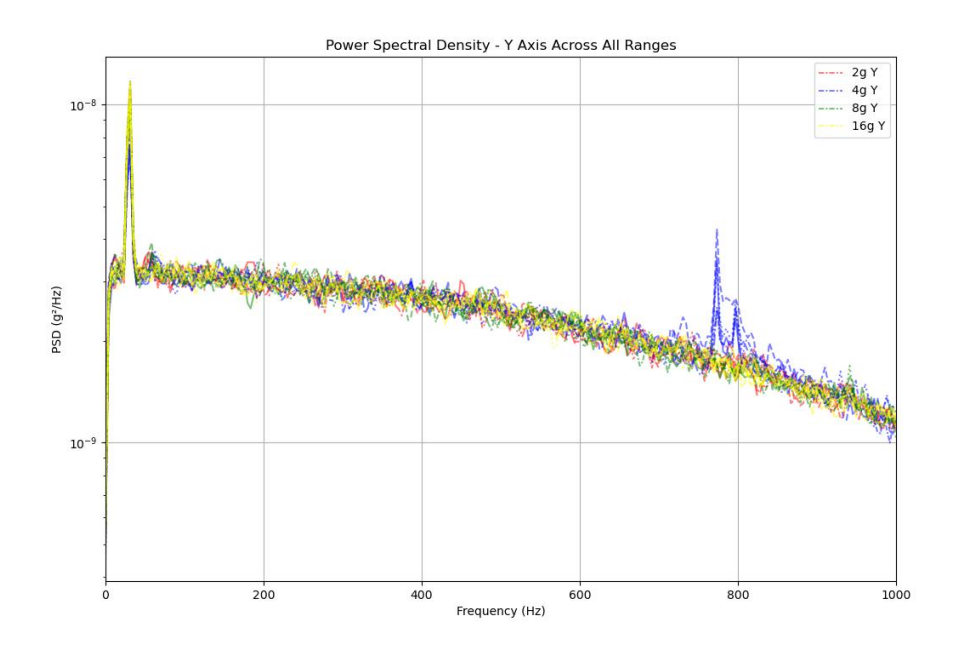


Figure 37: ICM-42688-P y-axis PSD all ranges

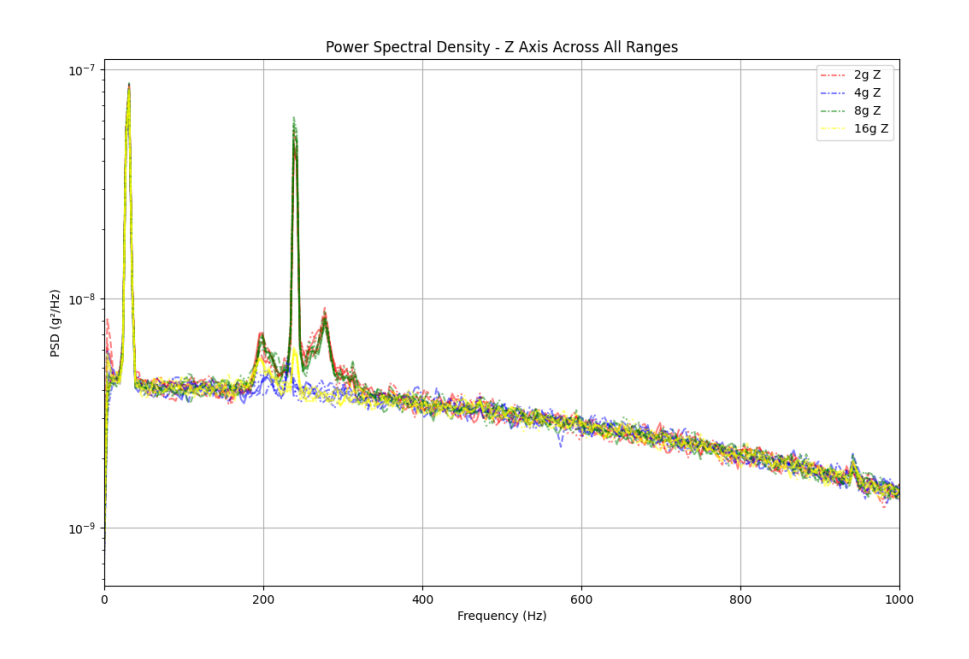


Figure 38: ICM-42688-P z-axis PSD all ranges

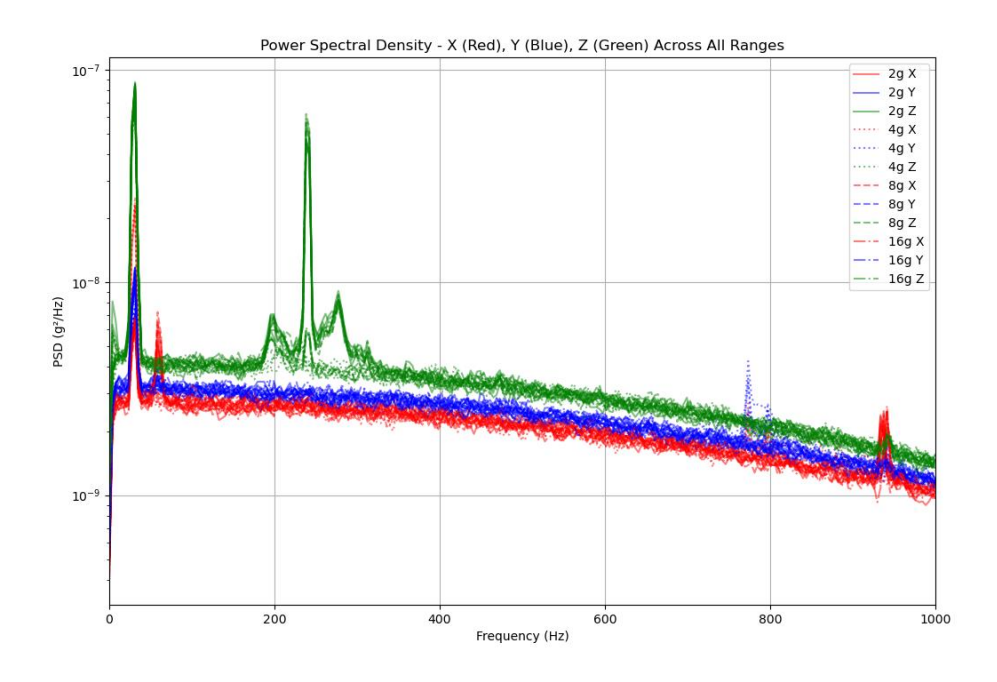


Figure 39: ICM-42688-P XYZ PSD all ranges

Table 14 below shows that the noise performance of the ADXL-357 and ICM-42688-P at 4 kHz ODR settings are similar up to 1 kHz, with the ICM-42688-P performing slightly better despite the appearance of some noise peaks on the PSD plot.

Table 14: ICM-42688-P Average Noise Density results

Noise Density (μg/√Hz)										
Power	Range (±g)	X	Υ	Ζ	Avg					
ADXL-357	10	62	58	52	57					
ADXL-357	20	74	68	63	68					
ADXL-357	40	74	68	63	68					
ADXL-357	Avg.	70	65	59	65					
ICM24688-P	2	46	49	64	53					
ICM24688-P	4	47	49	60	52					
ICM24688-P	8	46	49	65	53					
ICM24688-P	16	46	49	60	52					
ICM24688-P	Avg.	46	49	62	52					

4.2.3.5 IEPE Reference – PB352C03

Figure 40 shows the PSD for the IEPE reference sensor tested, showing the IEPE higher noise at low frequencies, falling as the frequency increases. 42.50 μ g/ \sqrt{Hz} average noise density was found, which is high for an IEPE sensor, due to both the high range of the IEPE sensor used and the low sampling rate, as IEPE noise falls with increased frequency, so the high frequency very low noise spectrum has been cutoff in this test result.

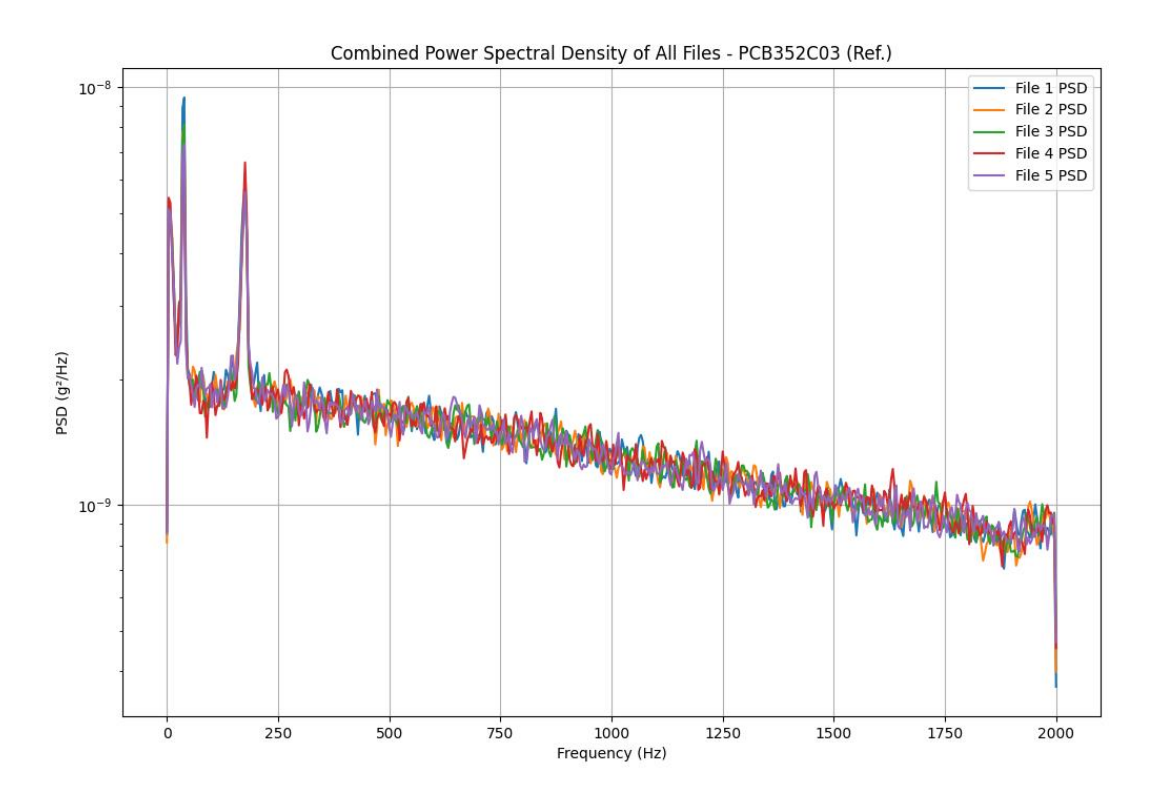


Figure 40: IEPE Reference PSD

4.2.3.6 Static Shaker Testing Summary

The static tests allowed noise density to be calculated for the different MEMS sensors and for different prototype configurations. The results showed that the USB and battery power show similar noise performance characteristics. The results were close to those from the datasheet specifications and the ADXL-357 and ICM-42688-P performed much better compared to the ADXL-345. While the ADXL-345 was useful for initial system testing and initial verification with a comparison to the datasheet, it will no longer be tested after test 1 to allow the two better performing options to be studied in test 2.

4.2.4 Test 1 Dynamic Shaker Test Results

4.2.4.1 RMS Mode – ADXL-345 vs ADXL-357 vs IEPE (PB352C03)

ADXL-345 and ADXL-357 were bolt mounted with a mounting adapter and powered via a USB cable for these tests, the IEPE reference was mounted with a magnetic mount.

This section provides a comparison of both Analog Devices MEMS sensors and a reference IEPE sensor.

Table 15 contains the time domain statistics calculated for the ADXL-357, ADXL-345 and the IEPE reference, with each MEMS being tested at each range setting.

All test results are for the 1 g RMS shaker mode.

All sensors tested show good agreement with both the expected values and with the IEPE reference sensor. The ADXL-345 at 2 g range cut-off the top peaks, resulting in slightly distorted results, for example the crest factor furthest from 1.44, and therefore the furthest from a pure sinusoidal result. The lower kurtosis and crest factor values suggest the ADXL-357 has less noise and produces an output closer to a pure sine wave.

The ideal peak value for 1 g RMS would be $\sqrt{2}*RMS$, therefore 1.414 g. This makes the Pk-Pk 1.414 * 2 = 2.828 g. The IEPE sensor comes closest to this ideal value, showing its superior performance, resulting in a cleaner symmetric signal with less noise than the MEMS alternatives.

Table 15: Test 1 dynamic result comparison, time domain

Sensor	Range (g)	Mean (g)	Std.	RMS	Pk-Pk (g)	Kurtosis	Skewness	Median	Peak	Crest
			Dev.	(g)					(g)	Factor
ADXL357	10g	-0.000148	1.0283	1.0283	2.9580	-1.4740	-0.0050	0.0030	1.4827	1.4418
ADXL357	20g	-0.000200	1.0262	1.0262	2.9559	-1.4727	-0.0052	0.0050	1.4822	1.4444
ADXL357	40g	0.000024	1.0147	1.0147	2.9153	-1.4774	-0.0022	0.0005	1.4597	1.4386
ADXL357	Avg	-0.000108	1.0231	1.0231	2.9431	-1.4747	-0.0042	0.0028	1.4749	1.4416
ADXL345	2g	-0.054662	0.9189	0.9205	2.5023	-1.5325	-0.1280	-0.0008	1.4539	1.5794
ADXL345	4g	0.002928	1.0080	1.0080	2.9719	-1.4652	-0.0016	0.0118	1.4946	1.4827
ADXL345	8g	0.002754	1.0046	1.0046	2.9719	-1.4673	0.0023	0.0039	1.4930	1.4862
ADXL345	16g	0.002787	1.0037	1.0038	2.9641	-1.4681	0.0027	0.0041	1.4869	1.4814
ADXL345	Avg	-0.011548	0.9838	0.9842	2.8525	-1.4833	-0.0312	0.0048	1.4821	1.5074
ADXL345	Avg (4-16)	0.002823	1.0054	1.0055	2.9693	-1.4669	0.0011	0.0066	1.4915	1.4834
IEPE Ref.	500g	0.001605	1.0052	1.0052	2.8592	-1.4993	-0.0015	0.0024	1.4304	1.4230

Table 16 contains the frequency domain statistical summary for the ADXL-345, ADXL-357 and IEPE reference. All sensors at all ranges detect the peak frequency around 159.2 Hz, showing agreement between the sensor results and the shaker parameters. All sensors measured a peak amplitude slightly below the ideal 1.414 g at 159.2 Hz.

Table 16: Test 1 dynamic result comparison, frequency domain

Sensor	Range	Peak	FFT Pk Peak		FFT Pk Amp.
	(g)	(Hz)	Amp. (g)	Windowed (Hz)	Windowed (g)
ADXL357	10g	159.2102	1.2068	159.2102	1.3380
ADXL357	20g	159.2236	1.3335	159.2192	1.4032
ADXL357	40g	159.2255	1.1368	159.2210	1.3105
ADXL357	Avg	159.2198	1.2257	159.2168	1.3505
ADXL345	2g	159.2544	1.1421	159.2544	1.2264
ADXL345	4g	159.1973	1.0920	159.1935	1.2933
ADXL345	8g	159.2220	1.2020	159.2220	1.3318
ADXL345	16g	159.2346	1.2343	159.2346	1.3429
ADXL345	Avg	159.2271	1.3669	159.2261	1.2986
IEPE Ref.	500g	159.2024	1.3669	N/A	N/A

4.2.4.2 RMS Mode – ADXL-357 Bolt Mounted vs Magnet Mounted

Table 17 contains the same statistical time domain results for ADXL-357 from the previous Table 15 but compares them to another ADXL-357 test. The original data comes from a bolt mounted, USB powered sensor. This test compares this original result to a test performed with the magnetic mount and the battery pack for powering the sensor in test 2.

All measurement ranges show a closer to the ideal 0 mean value, but also lower peak values with both Pk-Pk and RMS values being lower for the magnetic mounted sensor. Overall, a comparison reveals good agreement between the two sensors despite the small changes due to the new mounting and power supply.

Table 17: Test 1 dynamic results ADXL-357 mounting comparison, time domain

Setup	Range	Mean (g)	Std. Dev.	RMS (g)	Pk-Pk (g)	Kurtosis	Skewness	Median	Peak (g)	Crest Factor
	(g)									
Bolt, USB	10g	-0.000148	1.0283	1.0283	2.9580	-1.4740	-0.0050	0.0030	1.4827	1.4418
Mag, Bat.	10g	-0.000079	0.9667	0.9667	2.7866	-1.4744	-0.0061	0.0035	1.3965	1.3919
Differe	nce:	-0.000069	0.0617	0.0617	0.1714	0.0005	0.0011	-0.0005	0.0862	0.0499
Bolt, USB	20g	-0.000200	1.0262	1.0262	2.9559	-1.4727	-0.0052	0.0050	1.4822	1.4444
Mag, Bat.	20g	-0.000032	0.9502	0.9502	2.7302	-1.4782	-0.0017	0.0005	1.3678	1.4395
Differe	nce:	-0.000168	0.0760	0.0760	0.2257	0.0055	-0.0036	0.0045	0.1144	0.0049
Bolt, USB	40g	0.000024	1.0147	1.0147	2.9153	-1.4774	-0.0022	0.0005	1.4597	1.4386
Mag, Bat.	40g	0.000018	0.9486	0.9486	2.7263	-1.4793	-0.0011	-0.0001	1.3643	1.4382
Differe	nce:	0.000006	0.0661	0.0661	0.1891	0.0019	-0.0011	0.0006	0.0954	0.0004
Bolt, USB	Avg	-0.000108	1.0231	1.0231	2.9431	-1.4747	-0.0042	0.0028	1.4749	1.4416
Mag, Bat.	Avg	-0.000031	0.9552	0.9552	2.7477	-1.4773	-0.0030	0.0013	1.3762	1.4232
Differe	nce:	-0.000077	0.0679	0.0679	0.1954	0.0026	-0.0012	0.0015	0.0987	0.0184

Table 18 displays similar results as above, with lower FFT peak amplitudes for each of the magnetic sensors compared to the bolted version. However, it also shows the magnetic mounted sensors get a little closer to the 159.2 Hz peak frequency with all ranges having a slightly lower frequency peak than the first trials.

Table 18: Test 1 dynamic results ADXL-357 mounting comparison, frequency domain

Sensor	Range	Peak	FFT Pk	Peak	FFT Pk Amp.
	(g)	(Hz)	Amp. (g)	Windowed (Hz)	Windowed (g)
Bolt, USB	10g	159.2102	1.2068	159.2102	1.3380
Mag, Bat.	10g	159.2036	1.1976	159.2036	1.2889
Differe	nce:	0.0066	0.0092	0.0066	0.0491
Bolt, USB	20g	159.2236	1.3335	159.2192	1.4032
Mag, Bat.	20g	159.2034	1.1454	159.2034	1.2712
Differe	nce:	0.0203	0.1881	0.0159	0.1319
Bolt, USB	40g	159.2255	1.1368	159.2210	1.3105
Mag, Bat.	40g	159.1973	1.1098	159.2013	1.2431
Differe	ence:	0.0282	0.0269	0.0198	0.0674
Bolt, USB	Avg	159.2198	1.2257	159.2168	1.3505
Mag, Bat.	Avg	159.2014	1.1509	159.2027	1.2677
Differe	nce:	0.0184	0.0747	0.0141	0.0828

4.2.4.3 RMS and Pk Modes – ADXL vs ICM-42688-P

The dynamic shaker testing results in Table 19 - Table 24 show similar performance between the ADXL-357 and ICM-42688-P at the 4 kHz output setting. The ICM-42688-P is showing slightly better performance, with more accurate 1 g RMS for RMS mode and 2 g Pk-Pk for 1 g Pk mode. Additionally, the ICM-42688-P was closest to 1 g peak at 159.2 Hz for Pk mode after simple windowing for signal processing as outlined in the data processing and analysis section.

Table 19: Test 1 dynamic results ADXL-357 RMS and Pk modes, time domain

Mode	Range	Mean (g)	Std.	RMS	Pk-Pk (g)	Kurtosis	Skewness	Median	Peak	Crest
	(g)		Dev.	(g)					(g)	Factor
PK	10g	-0.000112	0.6788	0.6788	1.9504	-1.4807	-0.0015	-0.0002	0.9769	1.4392
PK	20g	-0.000040	0.6729	0.6729	1.9364	-1.4811	-0.0017	0.0000	0.9697	1.4410
PK	40g	-0.000049	0.6733	0.6733	1.9488	-1.4811	-0.0017	-0.0002	0.9803	1.4560
PK	Avg	-0.000067	0.6750	0.6750	1.9452	-1.4810	-0.0017	-0.0002	0.9756	1.4454
RMS	10g	-0.000079	0.9667	0.9667	2.7866	-1.4744	-0.0061	0.0035	1.3965	1.3919
RMS	20g	-0.000032	0.9502	0.9502	2.7302	-1.4782	-0.0017	0.0005	1.3678	1.4395
RMS	40g	0.000018	0.9486	0.9486	2.7263	-1.4793	-0.0011	-0.0001	1.3643	1.4382
RMS	Avg	-0.000031	0.9552	0.9552	2.7477	-1.4773	-0.0030	0.0013	1.3762	1.4232

Table 20: ICM-42688-P test 1 dynamic results (time domain)

Mode	Range	Mean (g)	Std.	RMS	Pk-Pk	Kurtosis	Skewness	Median	Peak	Crest
	(g)		Dev.	(g)	(g)				(g)	Factor
PK	2g	-0.004380	0.7144	0.7145	2.0016	-1.4953	-0.0210	0.0017	1.0377	1.4525
PK	4g	-0.000129	0.7168	0.7168	2.0650	-1.4771	-0.0051	0.0012	1.0353	1.4443
PK	8g	0.000027	0.7195	0.7195	2.0682	-1.4819	-0.0043	0.0018	1.0364	1.4405
PK	16g	-0.001494	0.7169	0.7169	2.0449	-1.4847	-0.0101	0.0016	1.0365	1.4457
RMS	2g	-0.082253	0.9103	0.9140	2.4184	-1.5498	-0.1728	0.0016	1.4546	1.5914
RMS	4g	-0.000112	1.0072	1.0072	2.8953	-1.4770	-0.0042	0.0017	1.4512	1.4408
RMS	8g	0.000033	1.0159	1.0159	2.9125	-1.4812	-0.0017	0.0005	1.4583	1.4356
RMS	16g	0.000100	1.0126	1.0126	2.9020	-1.4823	-0.0015	0.0004	1.4533	1.4351

Table 21: Test 1 dynamic results ADXL-357 RMS and Pk modes, frequency domain

Mode	Range	Peak	FFT Pk	Peak	FFT Pk Amp.
	(g)	(Hz)	Amp. (g)	Windowed (Hz)	Windowed (g)
PK	10g	159.2030	0.7964	159.2030	0.9007
PK	20g	159.2048	0.7768	159.2007	0.9109
PK	40g	159.2048	0.7768	159.2048	0.8812
PK	Avg	159.2042	0.7834	159.2028	0.8976
RMS	10g	159.2036	1.1976	159.2036	1.2889
RMS	20g	159.2034	1.1454	159.2034	1.2712
RMS	40g	159.1973	1.1098	159.2013	1.2431
RMS	Avg	159.2014	1.1509	159.2027	1.2677

Table 22: ICM-42688-P test 1 dynamic results (frequency domain)

Mode	Range (g)	Peak	FFT Pk	Peak Windowed	FFT Pk Amp.
		(Hz)	Amp. (g)	(Hz)	Windowed (g)
PK	2g	159.2116	0.9417	159.2116	0.9765
PK	4g	159.2109	0.8478	159.2109	0.9585
PK	8g	159.1964	0.9358	159.1964	0.9841
PK	16g	159.2185	0.8834	159.2185	0.9660
RMS	2g	159.2143	1.2442	159.2143	1.2590
RMS	4g	159.2077	1.2143	159.2077	1.3522
RMS	8g	159.1977	1.2057	159.1977	1.3437
RMS	16g	159.1889	1.3207	159.1889	1.3967

Table 23: ADXL-357 vs ICM-42688-P average result test 1 dynamic comparison (time domain)

Sensor	Mode	Mean (g)	Std.	RMS	Pk-Pk	Kurtosis	Skewness	Median	Peak	Crest
			Dev.	(g)	(g)				(g)	Factor
ICM42688-P	PK (Avg 4-16g)	-0.000532	0.7177	0.7177	2.0594	-1.4812	-0.0065	0.0015	1.0360	1.4435
ADXL357	PK (Avg 10-40g)	-0.000067	0.6750	0.6750	1.9452	-1.4810	-0.0017	-0.0002	0.9756	1.4454
ICM42688-P	RMS (Avg 4-16g)	0.000007	1.0119	1.0119	2.9033	-1.4802	-0.0025	0.0009	1.4543	1.4372
ADXL357	RMS (Avg 10-40g)	-0.000031	0.9552	0.9552	2.7477	-1.4773	-0.0030	0.0013	1.3762	1.4232

Table 24: ADXL-357 vs ICM-42688-P average result test 1 dynamic comparison (frequency domain)

Sensor	Mode	Peak	FFT Pk	Peak Windowed	FFT Pk Amp.	
		(Hz)	Amp. (g)	(Hz)	Windowed (g)	
ICM42688-P	PK (Avg 4-16g)	159.2086	0.8890	159.2086	0.9696	
ADXL357	PK (Avg 10-40g)	159.2042	0.7834	159.2028	0.8976	
ICM42688-P	RMS (Avg 4-16g)	159.1981	1.2469	159.1981	1.3642	
ADXL357	RMS (Avg 10-40g)	159.2024	1.1509	159.2027	1.2677	

4.2.5 Test 1 Conclusions

First, static testing verified system performance compared to sensor datasheets, confirming the superior performance of ADXL-357 and ICM-42688-P compared to the ADXL-345. This led to the decision to stop using this option in testing moving forward.

The static and dynamic testing both showed similar performance resulting from the ADXL-357 and ICM-42688-P. Therefore, both sensors will be used in test 2 for comparison, with the ADXL-357 providing a fixed 4 kHZ ODR option with the 1 kHz LPF, and the ICM-42688-P offering the chance to test higher acquisition frequencies.

4.3 Accelerometer Test 2: Linear Motion Testbed

For the second test, the MMRI linear axis testbed (MLAT), was used to compare sensor prototype performance to the high-end IEPE used in previous works at the MMRI [69-71]. This testbed was developed to simulate testing of linear axis, which are a common major subsystem of computer numerical control (CNC) machines, driving and guiding axis movements [69].

Similar linear axis testbeds have also been used for sensor testing in previous studies, including Koene [52] who had compared the ADXL-355 to an IEPE sensor [55], Vogl [9, 19-22], and Uhlmann [50, 51, 86] uses an axis test rig to generate vibration data of different ball screw failure conditions.

4.3.1 Test 2 Objectives and Setup

After comparing sensor performance in a relatively controlled setting with the vibration shaker, another test was performed to evaluate sensor performance in a more industrial equivalent environment. This test used a pair of wireless sensor nodes to compare with an existing CBM system on a linear axis testbed, monitoring a linear rail as shown in Figure 41. The best performing MEMS accelerometers from test 1, the ADXL-357 and ICM-42688-P, will be compared with the existing IEPE accelerometer setup used in previous CBM research performed at the MMRI.

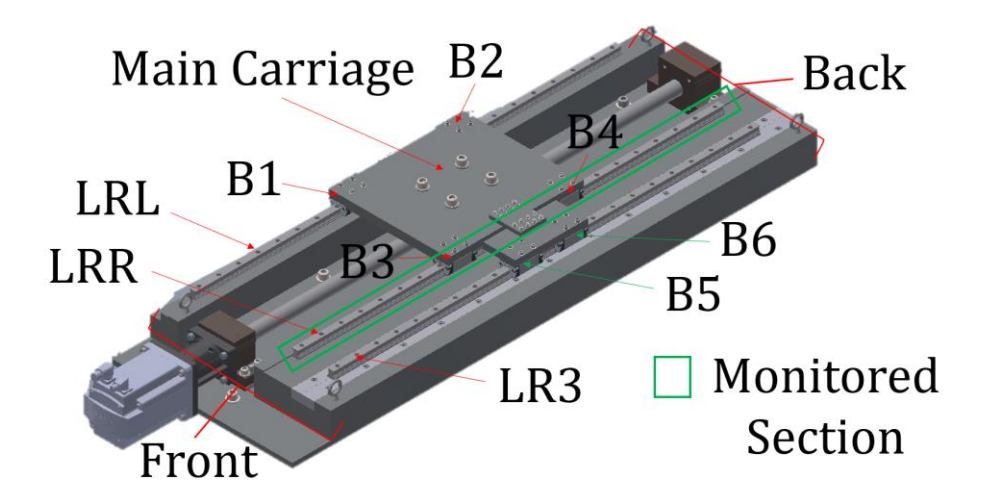


Figure 41: Linear testbed component naming conventions

As seen in Figure 42 and Figure 43, one sensor node was used to monitor the carrier block (B3) and was compared to a tri-axial IEPE accelerometer (PCB356A25). The other sensor was installed to monitor one of the linear rails (LRR) and compared to a mono-axial IEPE accelerometer (Kistler 8702B50).

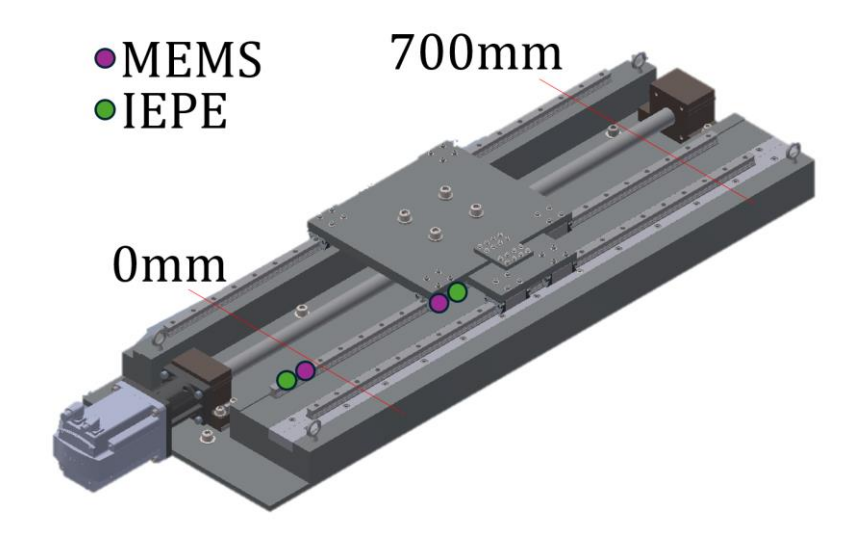


Figure 42: Test 2 sensor placements

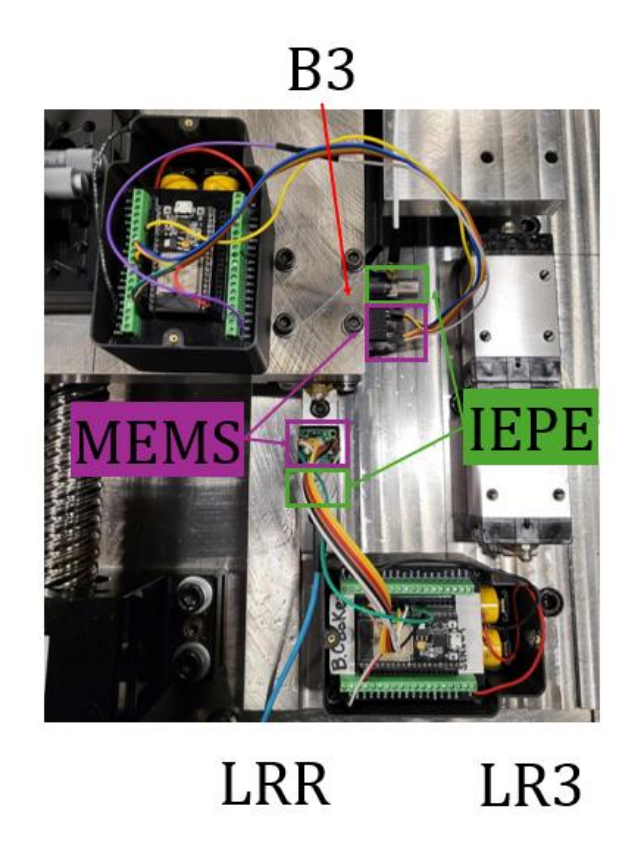


Figure 43: Test 2 sensor installation

The ADXL-357 wireless sensor data was collected using the Wi-Fi version of the wireless sensor node, as the performance of both Wi-Fi and 5G versions was sufficient to support the 4 kHz ODR. The higher frequency ICM-42688-P was tested using the 5G network connection as the Wi-Fi connection of the ESP32 could not keep up with the 16 kHz data output rate ICM-42688-P, the highest setting that would work via regular SPI reads and without redoing the sensor code to read from the sensor FIFO.

Only one sensor location was used for the 5G sensor testing due to the sensor setup requirements for the current 5G system, but future work includes a multi-

sensor 5G setup for the current MMRI 5G system and another for a future upgraded network. Therefore, only the B3 location is monitored for these tests, the higher network performance was taken advantage of, with both MEMS and IEPE sampled at 16 kHz instead of the 4 kHz used for the ADXL-357 Wi-Fi tests.

First, static measurements were retaken on the testbed to compare to the shaker results. To try to segment possible noise sources, the static tests were performed with the testbed powered down and then repeated with the testbed powered on and in engaged mode (energized and ready for movement commands). Then, as shown in Table 25, three different speed settings were tested on the linear axis testbed, with each measurement repeated five times, for a total of 15 runs over the three speeds. Each run included five back and forth movements of the carriage, with one second of idle time separating each direction change.

Table 25: Testbed operational parameters for test 2

Test Setting	Velocity (mm/s)	Acceleration (mm/s²)	Position (mm)	Idle Time (s)
Low	110	±3000	0 - 700	1
Medium	300	±3000	0 - 700	1
High	700	±3000	0 - 700	1

4.3.2 Test 2 Data Processing and Analysis

Data processing for test 2 was very similar to test 1, following the same processing steps for data preparation including data validation, cleaning, application of static offsets and data scaling.

Analysis was also like test 1, with similar plots and statistic features calculated for sensor comparisons. Unlike test 1, the second test data contained higher frequency data, so the MEMS built in LPF altered the results. To allow for a direct comparison, both the raw data and post filtered IEPE data has been compared. The ADXL-357 has a built-in LPF at ¼ ODR, so for the 4 kHz sampling rate used for that test it has a 1 kHz LPF, this means the IEPE raw data contains high frequency components filtered out of the MEMS data even though they have the same sampling rate and could be more susceptible to aliasing.

Due to the LPF on the ADXL-357, some frequency content above 1 kHz was suppressed, with content tapering off around the 1 kHz cutoff frequency. Since this test contained more higher frequency content, above 1 kHz, this information was more impactful on the data collected with the IEPE sensor (compared to the oversampled result from test 1). As a result, the ADXL-357 data appeared cleaner or less peaky/energetic. The FFT of the IEPE included higher magnitudes over 1 kHz and appeared spikier. In the time domain, the MEMS was smoother and less jittery since high frequency noise and vibrations were filtered out. On the other hand, without an LPF, the IEPE data appeared more detailed but also potentially had higher noise due to real or aliased high frequency content as content over 2 kHz (4 kHz/2) could have been aliased. For statistical analysis, the LPF impacted results by making the IEPE have higher expected values, due to the inclusion of more of the higher frequency content.

The ICM-42688-P has a built-in LPF like the ADXL-357, but it can be bypassed. The test settings used no low pass filter for the ICM-42688-P to get a more balanced comparison between the MEMS and IEPE, both sampled at 16 kHz. However, the 16 kHz ODR setting recommended anti-aliasing filter cutoff frequency is around 4 kHz so the performance after that may not be recommended. Additionally, with the high frequency sampling rate and no filtering, the sensors could have been susceptible to high frequency aliasing. Lastly, the MEMS mounts, made from plastic, may have introduced some noise damping, resonance, phase shift or other data issues due to poor coupling between the sensor and monitored surface.

4.3.3 Test 2 Static Test Results

4.3.3.1 ADXL-357 4 kHz ODR – Wi-Fi

Figure 44 - Figure 47 show that the increase in noise when turned on mostly only effects the sensor mounted on the carrier block, with the LRR sensors seeing a small noise increase. With the testbed powered off both the LRR and B3 sensor prototypes exhibit about the same noise levels as captured during the static shaker testing. With the testbed powered on and the motor in an engaged state the LRR sensor shows almost no change in noise density. B3 shows something different, with higher noise values, especially in the Y-axis. Since the other sensor did not exhibit the same behavior, and the major noise change being in the direction of carriage travel (Y-axis is aligned with carriage movement), this is believed to be caused by the sensor motor attempting to compensate for any changes in position.

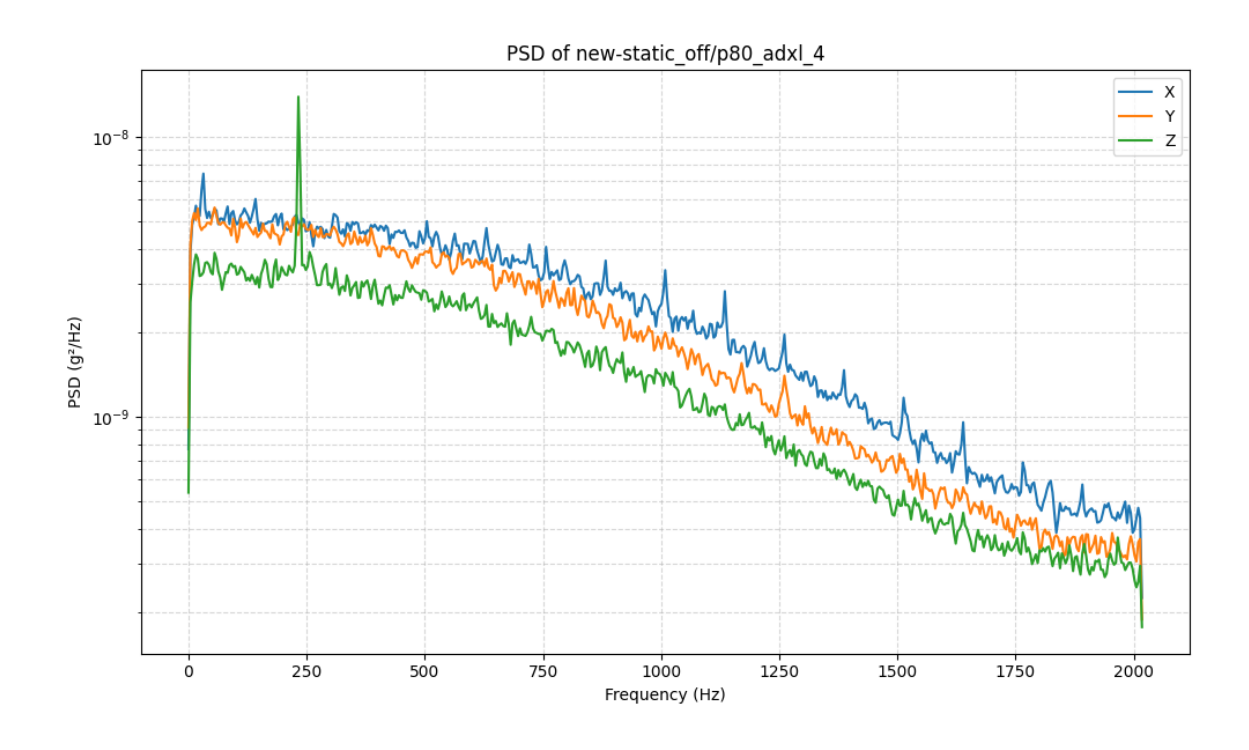


Figure 44: ADXL-357 10 g, B3 sensor, static noise testbed powered off

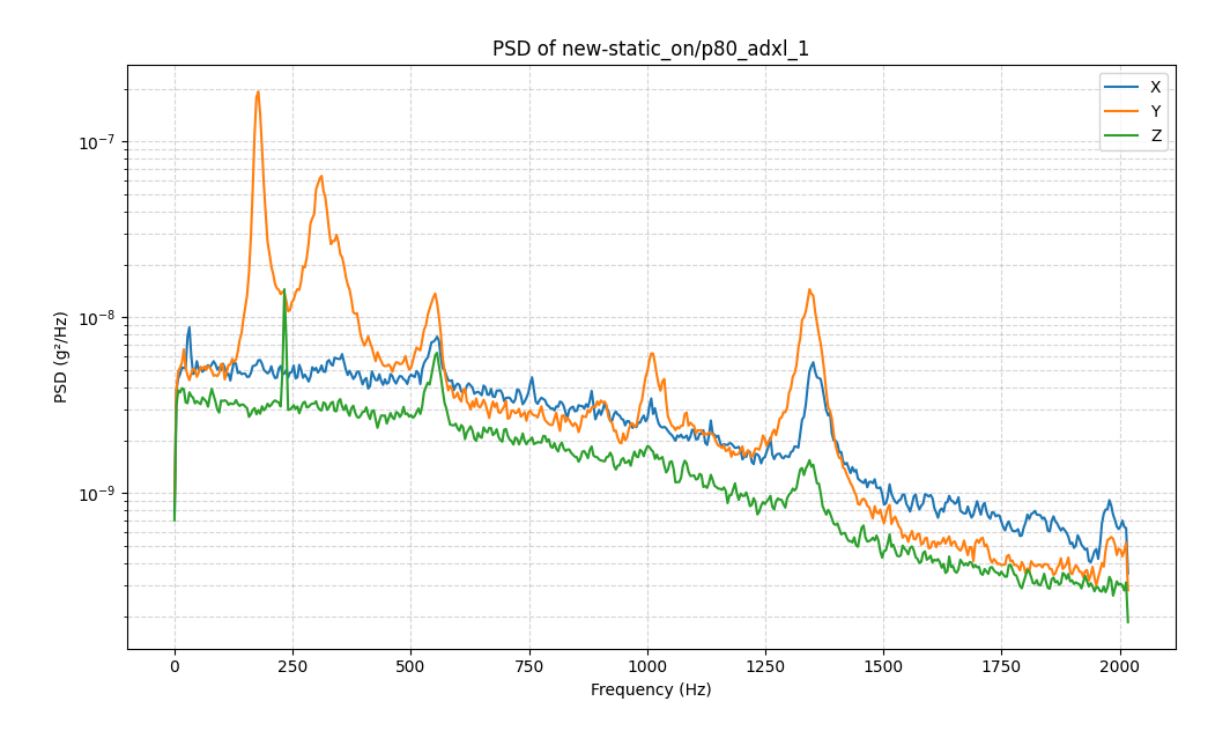


Figure 45: ADXL-357 10 g, B3 sensor, static noise testbed powered on

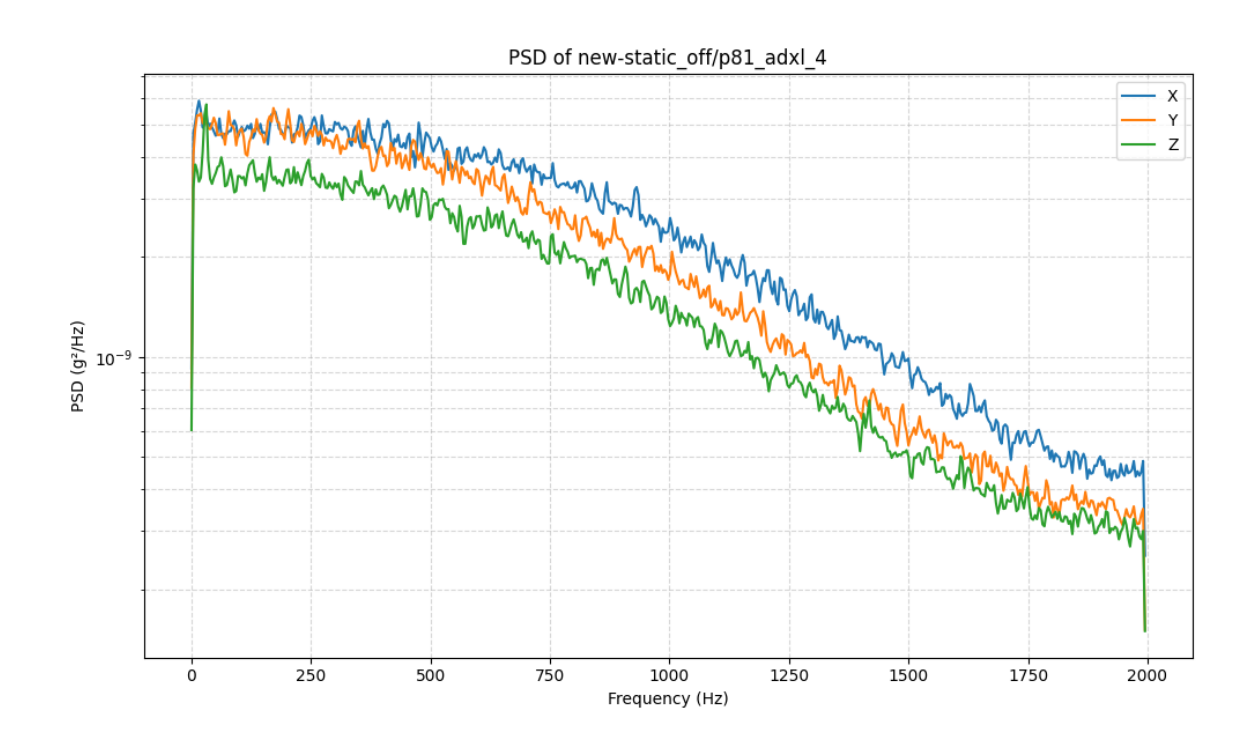


Figure 46: ADXL-357 10 g, LRR sensor, static noise testbed powered off

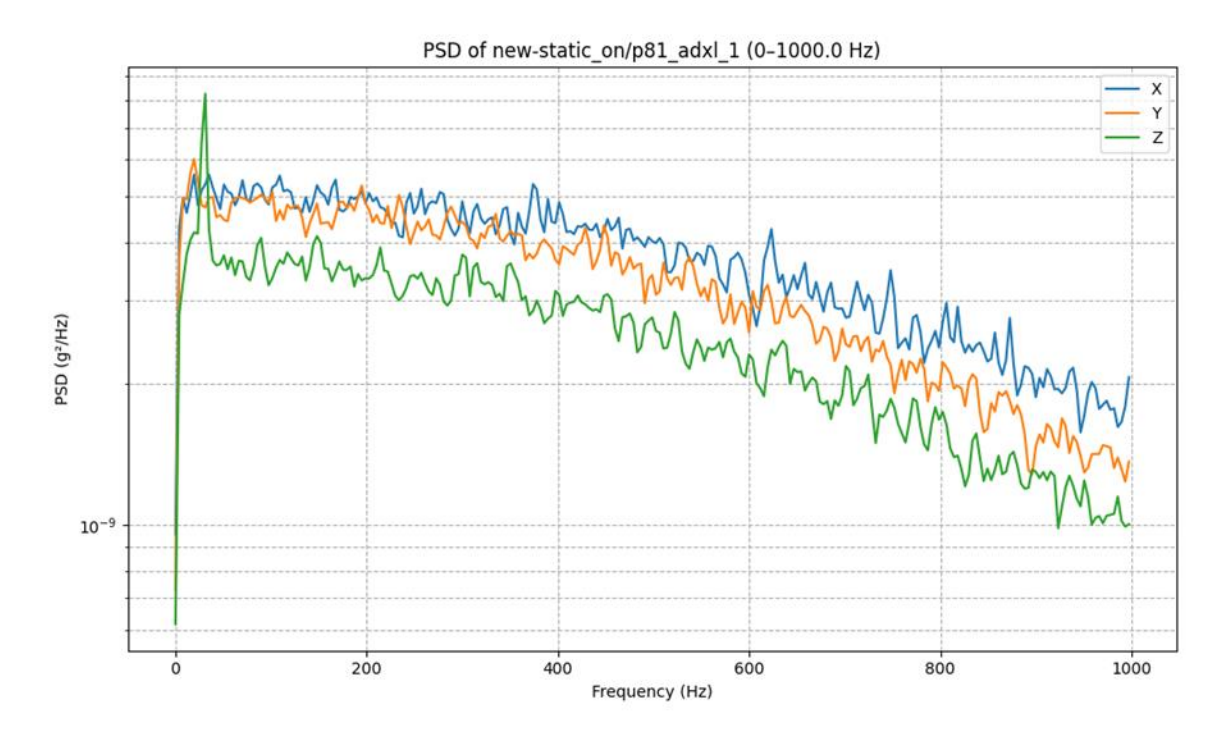


Figure 47: ADXL-357 10 g, LRR sensor, static noise testbed powered on

4.3.3.2 ICM-42688-P 16 kHz ODR - 5G

All measurements for ICM-42688-P data are taken only from B3 location.

In Figure 48 - Figure 52, the ICM-42688-P static data shows an interesting aspect of MEMS sensors compared to the IEPE accelerometers, the IEPE sensor noise decreases as frequency increases, but the 8 kHz PSD shows the rising noise for the MEMS sensor once it reaches over the recommended cutoff frequency for 16 kHz ODR of 4 kHz.

In the powered-on data, similar noise spikes can be seen for both sensors mounted to the carrier block, with two Y axis peaks around 250 Hz, all three axes peaking after 500 Hz and again around 1300 Hz.

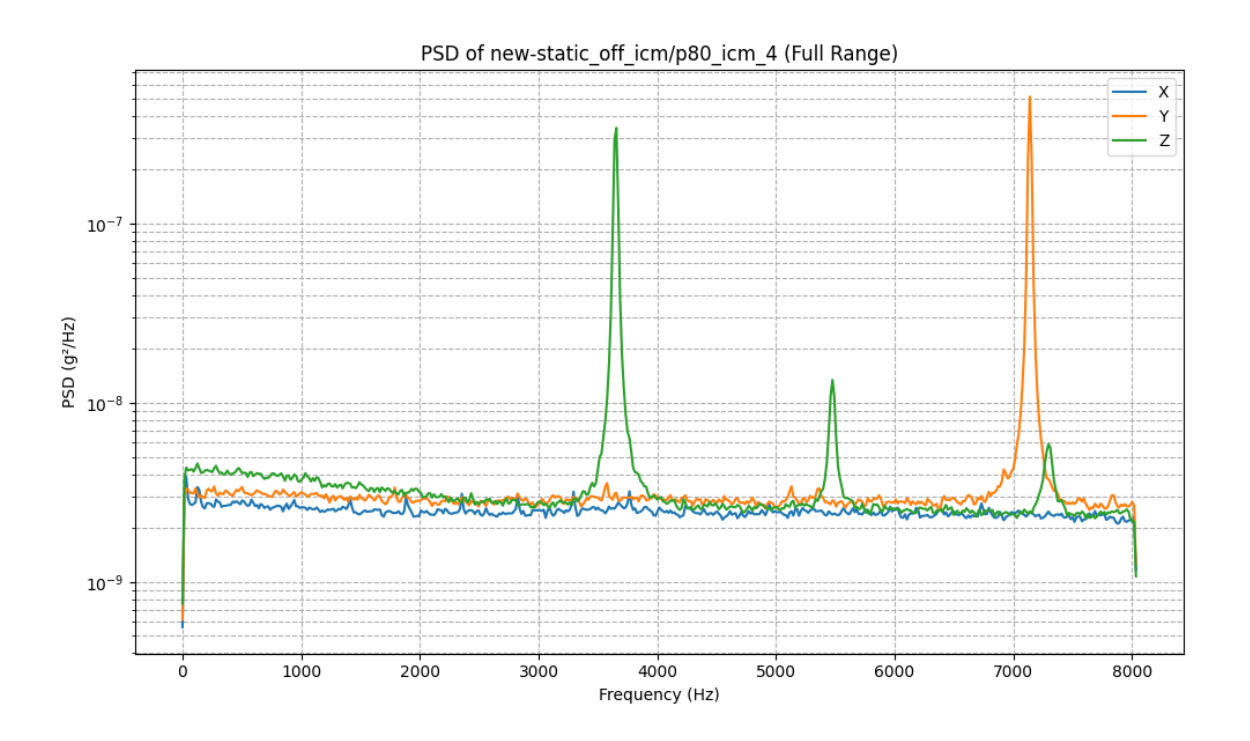


Figure 48: ICM-42688-P static noise testbed powered off

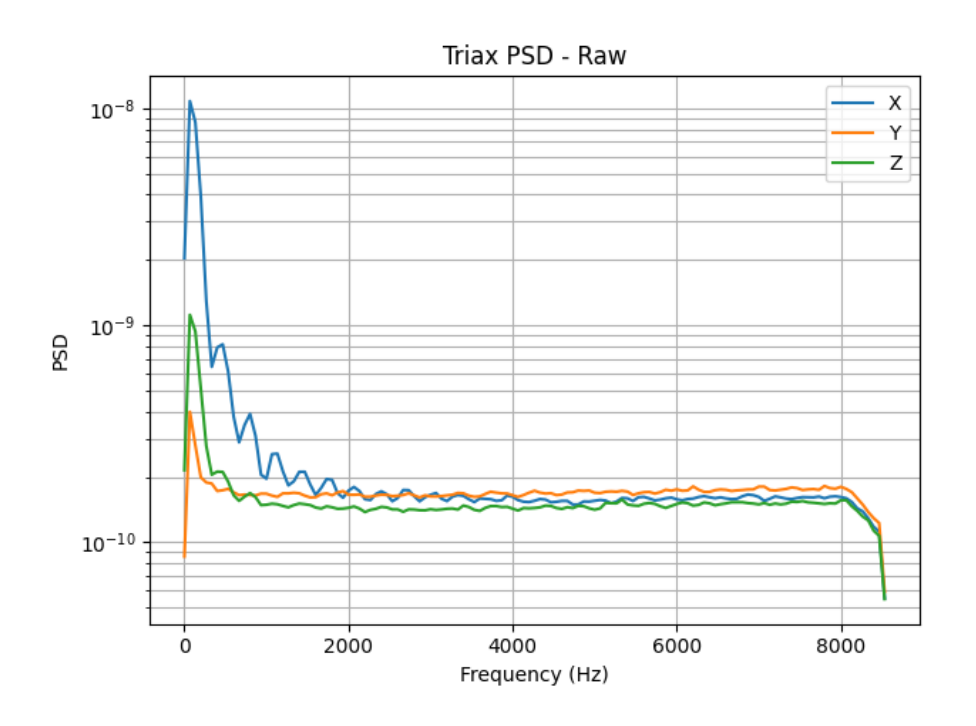


Figure 49: IEPE B3 static noise testbed powered off

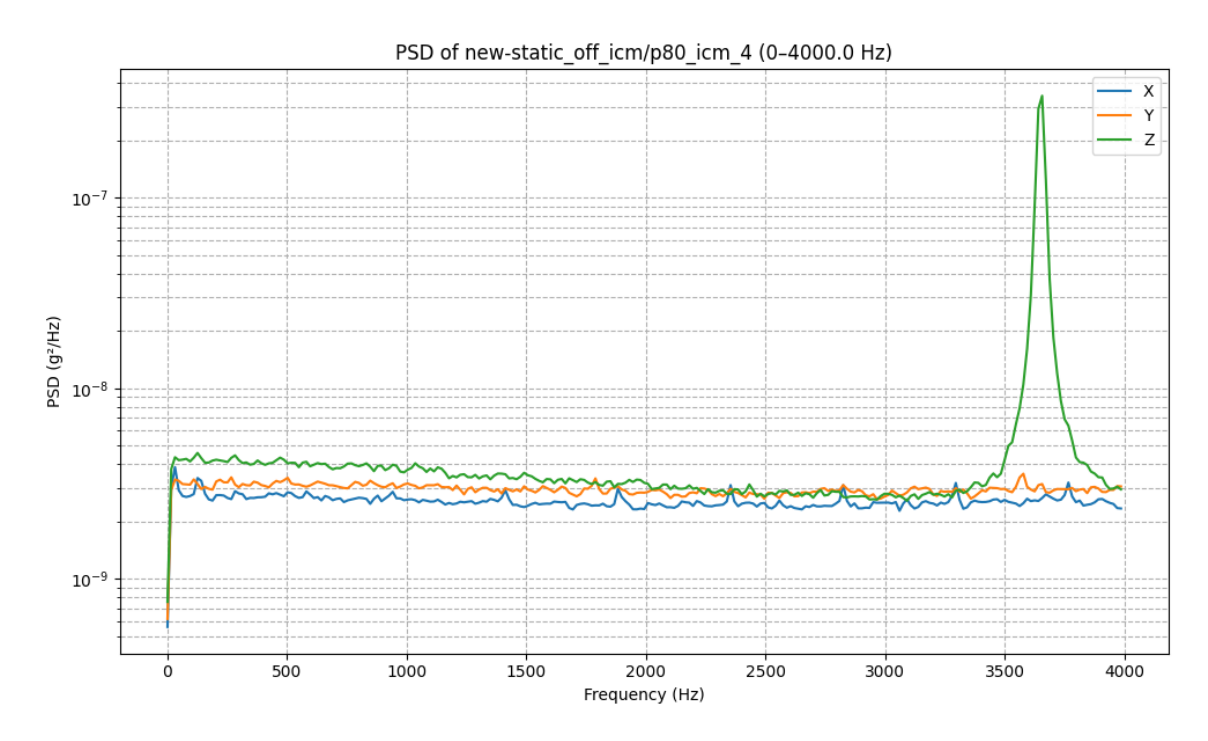


Figure 50: ICM-42688-P static noise, testbed powered off (4 kHz cutoff)

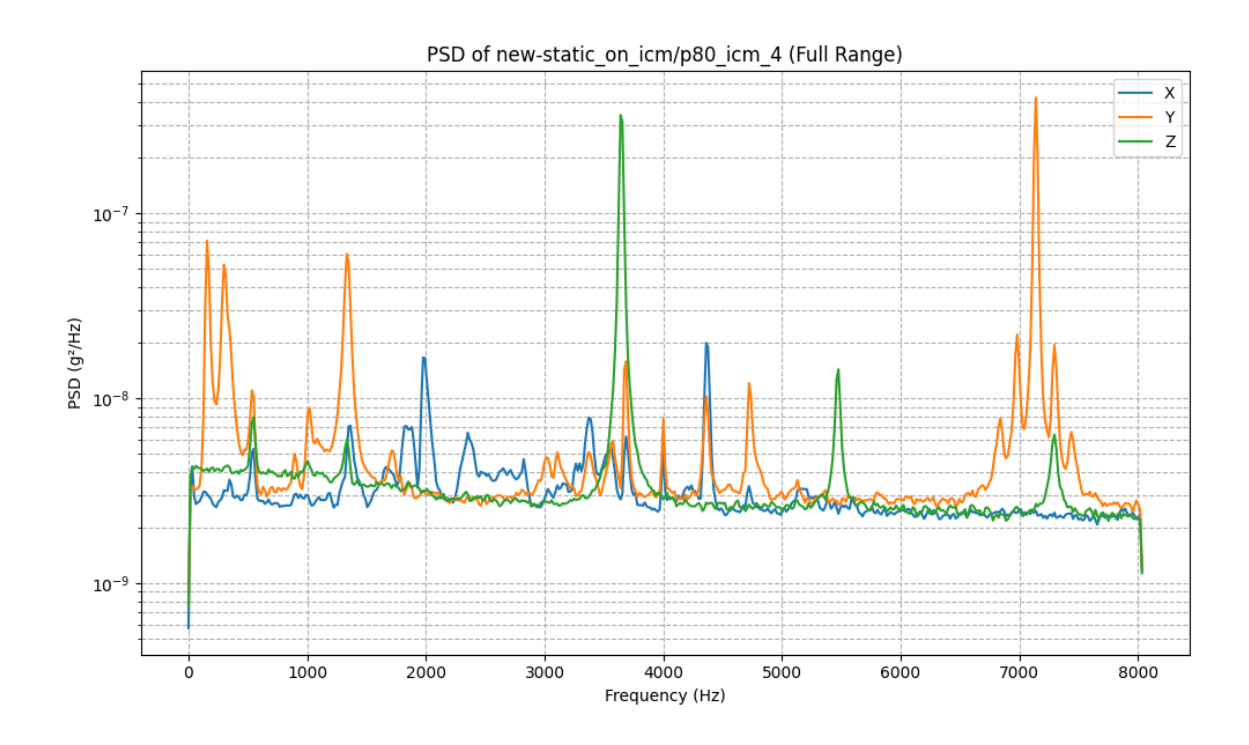


Figure 51: ICM-42688-P static noise, testbed powered on

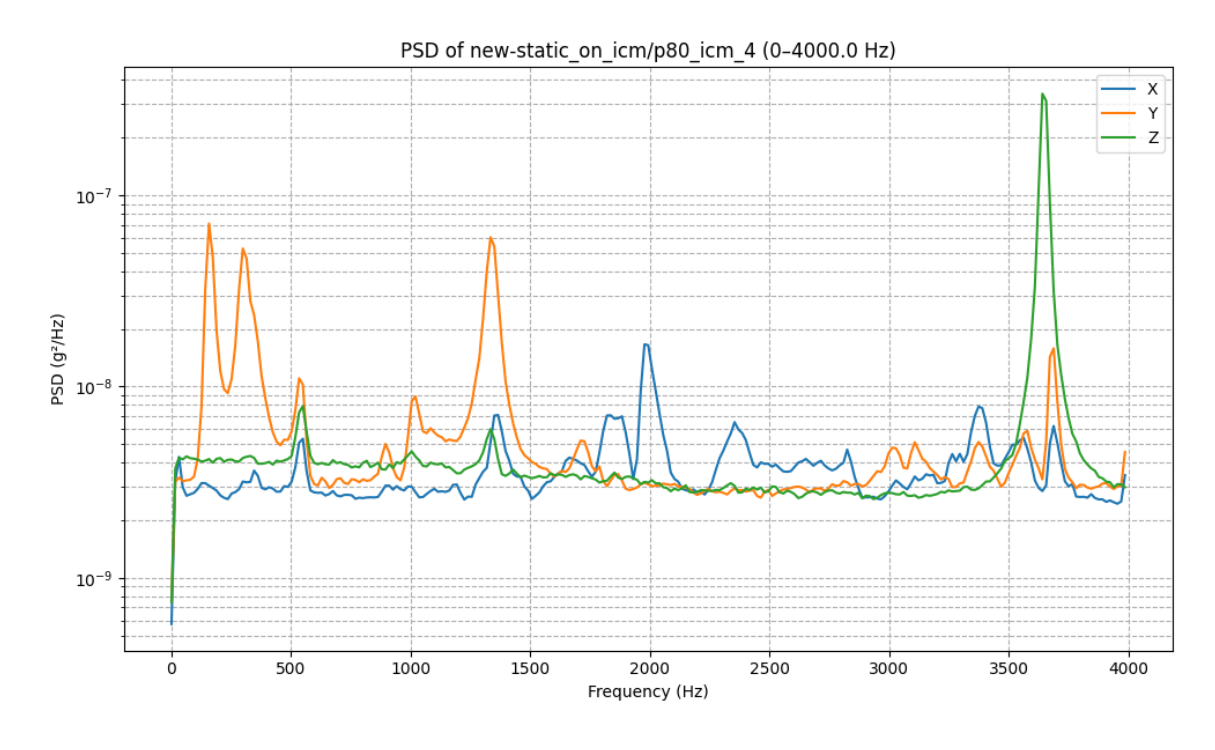


Figure 52: ICM-42688-P static noise, testbed powered on (4 kHz cutoff)

4.3.3.3 Conclusions

Static testing on the testbed allowed validation of sensor performance compared to the more isolated testing environment of the vibration reference shaker. Both sensors showed similar noise performance with the testbed powered off, showing the sensors were good to proceed in the test procedure.

The power cycling in this test was originally intended to isolate possible noise sources from the testbed by introducing power sources and other sources of noise in the second sampling. With the testbed powered on both sensors mounted on the carrier block exhibited more noise, but most was not noise and instead the carriage motor self correcting the position. However, the LRR ADXL sensor saw little additional noise when powered on without being mounted on the moving section.

In this case, with the static data containing motor movement information, the static data offset for dynamic testing was generated using the static data collected with the testbed powered off.

4.3.4 Test 2 Dynamic Test Results

Due to issues with the wired IEPE sensor cabling on the moving carriage, the low and medium speed testing data will be focused on for comparison to give the most accurate comparison. The high-speed plots are included below in the appendix for reference.

The high-speed IEPE data has some spikes, mainly noticeable in Z axis data, from an unknown cause that could not be fixed during testbed testing. (Tried changing DAQs, cables, sensors, but could not get consistent clean data)

4.3.4.1 ADXL-357 4 kHz ODR - Wi-Fi

Table 26 - Table 28 contain the statistical results from the ADXL-357 low speed tests. As expected, the RMS value for the IEPE sensor was higher due to containing the higher frequency content with no low pass filter.

As expected due to the low pass filter, the IEPE data in Figure 54 matches the MEMS well until around 1 kHz when the filter us suppressing the higher frequency content. This is most noticeable in the X and Z directions. These additional high frequency components are seen in Figure 53 where the IEPE magnitude is higher than the ADXL-357.

Table 26: Test 2 ADXL-357 dynamic test B3 statistical results, low speed

	Summary - LOW									
		RMS	S (mg)	Pea	k (mg)	Crest				
Sensor	Axis	mean std		mean	std	mean	std			
A (MEMS)	Χ	5.730	0.070	32.840	2.710	5.735		0.492		
A (MEMS)	Υ	23.330	0.220	263.920	10.890	11.311		0.403		
A (MEMS)	Z	4.890	0.060	27.930	0.980	5.713		0.206		
B (IEPE)	Χ	7.370	0.130	45.120	3.410	6.124		0.427		
B (IEPE)	Υ	23.240	0.260	256.910	10.200	11.054		0.368		
B (IEPE)	Z	6.120	0.100	34.440	3.250	5.629		0.516		

Table 27: Test 2 ADXL-357 dynamic test B3, low speed (MEMS – IEPE)

Summary - LOW (A-B)										
	RMS (mg) Peak (mg) Crest									
Axis	mean	std	mean	std	mean	std				
Χ	-1.640	-0.060	-12.280	-0.700	-0.388	0.065				
Υ	0.090	-0.040	7.010	0.690	0.258	0.035				
Z	-1.230	-0.040	-6.510	-2.270	0.083	-0.311				

Table 28: Test 2 ADXL-357 dynamic test B3, low speed (MEMS – IEPE, as percentage)

Summary - LOW (AvsB %diff)										
	RMS (%) Peak (%) Crest (%)									
Axis	mean std		mean	std	mean	std				
Χ	-25.04	-60.00	-31.50	-22.88	-6.54	14.20				
Υ	0.39	-16.67	2.69	6.54	2.30	9.19				
Z	-22.34	-50.00	-20.88	-107.33	1.47	-86.02				

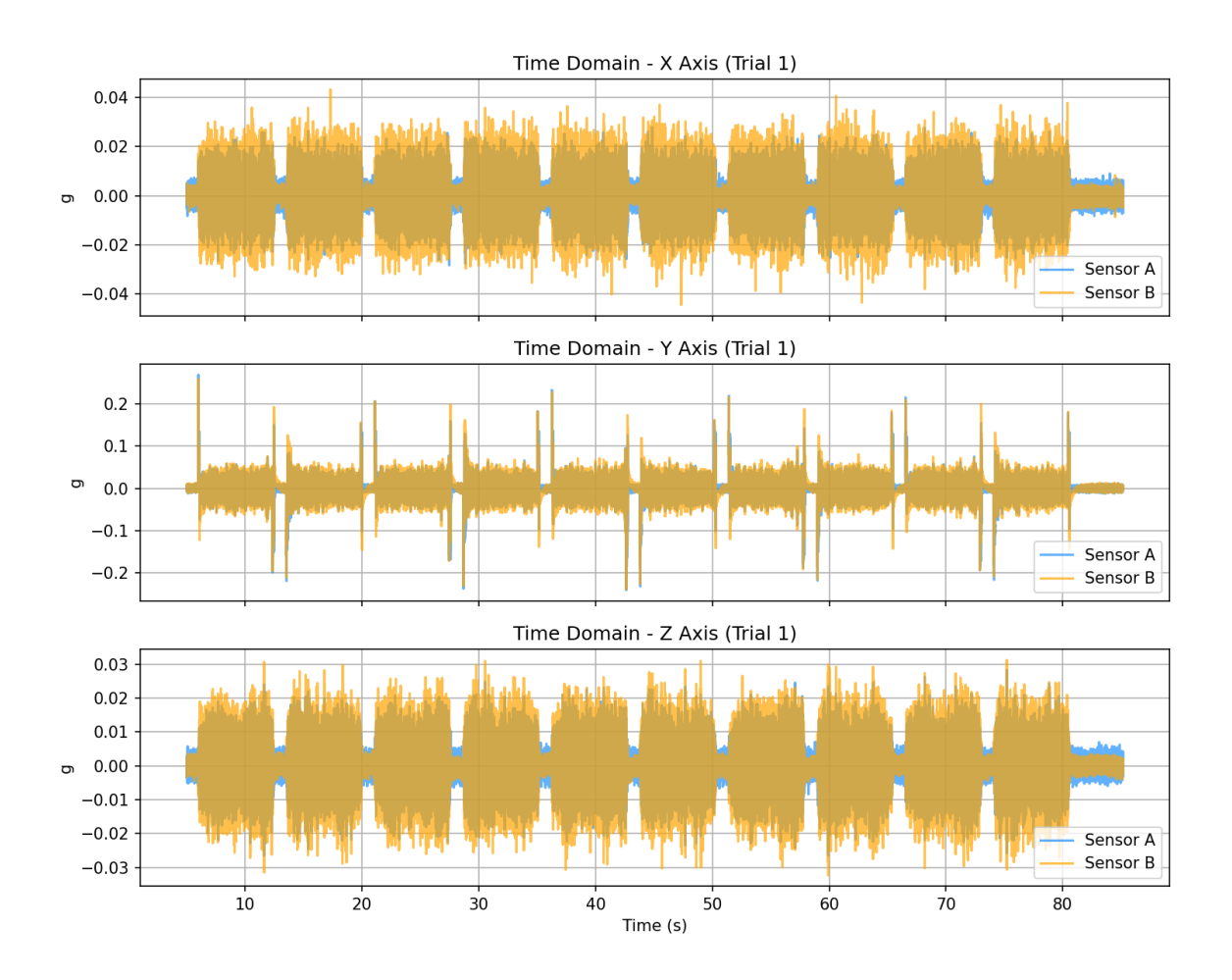


Figure 53: Time domain B3 ADXL-357 (Blue) vs IEPE (Yellow), low speed

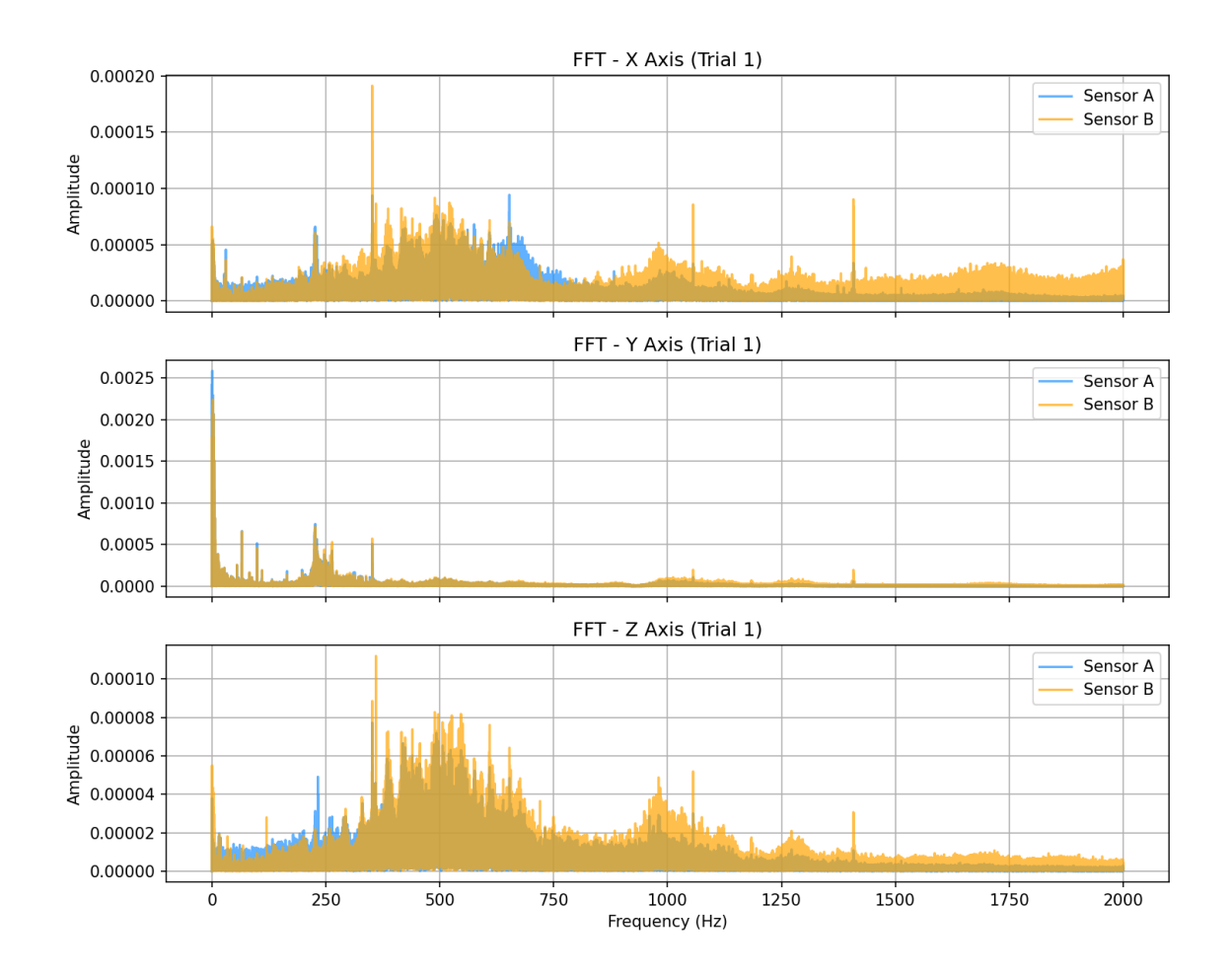


Figure 54: FFT B3 ADXL-357 (Blue) vs IEPE (Yellow), low speed

Once again, Figure 55 and Figure 56 show the sensors with similar results up to 1 kHz. Even after that they have similar shapes and peaks, but IEPE has higher magnitude due to the lack of filtering. The higher speed introduces more high frequency content which is why the comparison in Table 29 - Table 31 looks further off compared to the previous low speed results (Table 26).

Table 29: Test 2 ADXL-357 dynamic test B3 statistical results, medium speed

	Summary - MED											
		RMS	(mg)	Pea	k (mg)	Crest						
Sensor	Axis	mean	std	mean	std	mean	std					
A (MEMS)	Χ	12.280	0.120	82.850	4.130	6.747	0.	.340				
A (MEMS)	Υ	46.300	0.410	265.450	11.360	5.734	0.	.250				
A (MEMS)	Z	10.070	0.090	64.720	6.690	6.432	0.	.698				
B (IEPE)	Χ	23.830	0.460	207.500	30.010	8.725	1.	.377				
B (IEPE)	Υ	46.470	0.850	311.440	15.490	6.705	0.	.370				
B (IEPE)	Z	14.730	0.240	104.380	9.440	7.095	0.	.721				

Table 30: Test 2 ADXL-357 dynamic test B3, medium speed (MEMS – IEPE)

	Summary - MED (A-B)									
	RMS	(mg)	Peak	(mg)	Crest					
Axis	mean	std	mean	std	mean	std				
Χ	-11.550	-0.340	-124.650	-25.880	-1.978	-1.037				
Υ	-0.170	-0.440	-45.990	-4.130	-0.971	-0.121				
Z	-4.660	-0.150	-39.660	-2.750	-0.663	-0.023				

Table 31: Test 2 ADXL-357 dynamic test B3, medium speed (MEMS – IEPE, as percentage)

	Summary - MED (A vs B %diff)										
	RMS	(%)	Peal	k (%)	Crest (%)						
Axis	mean	std	mean std		mean	std					
Χ	-64	-117	-85.9	-152	-25.6	-121					
Υ	-0.37	-69.8	-15.9	-30.8	-15.6	-39					
Z	-37.6	-90.9	-46.9	-34.1	-9.8	-3.25					

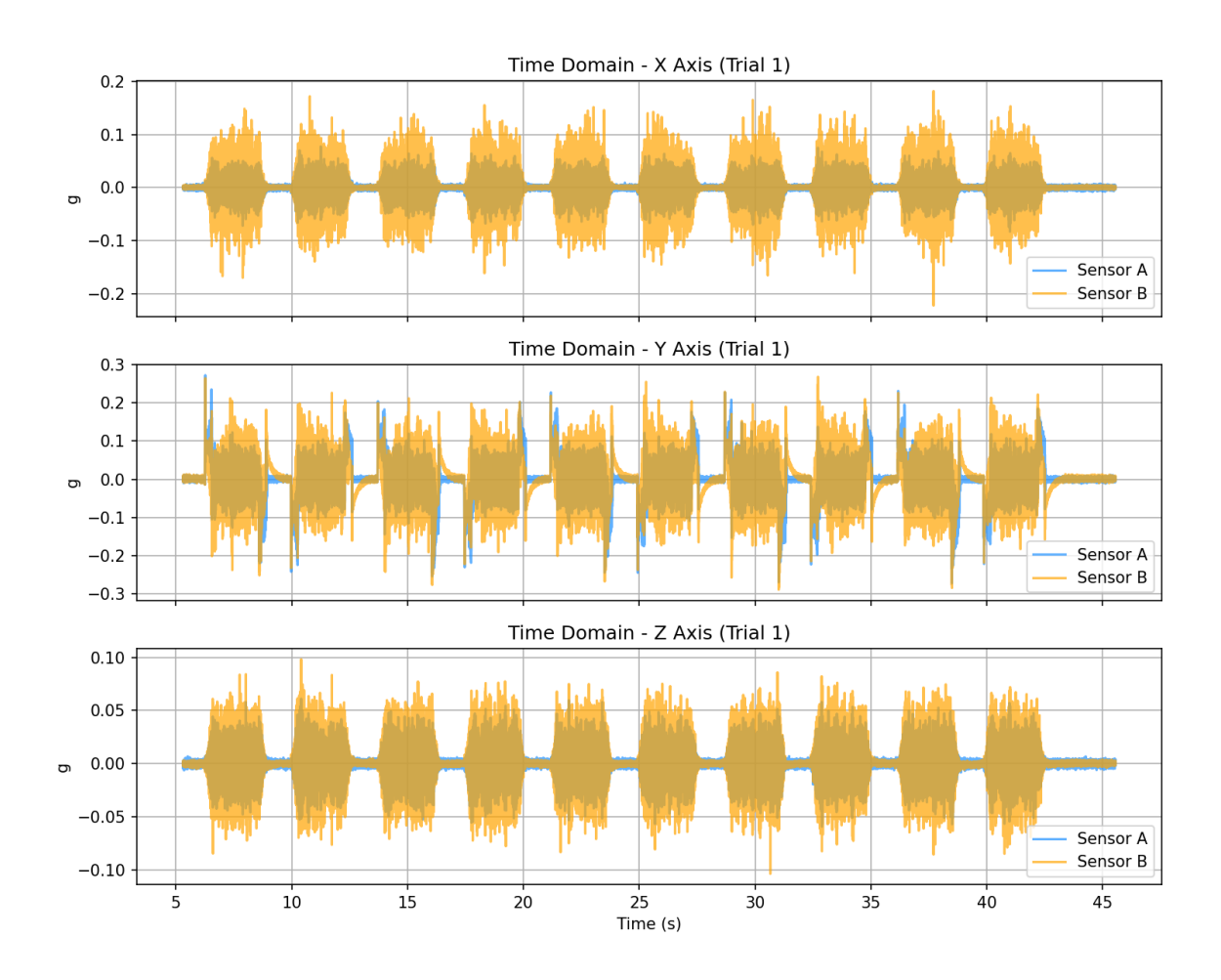


Figure 55: Time domain B3 ADXL-357 (Blue) vs IEPE (Yellow), medium speed

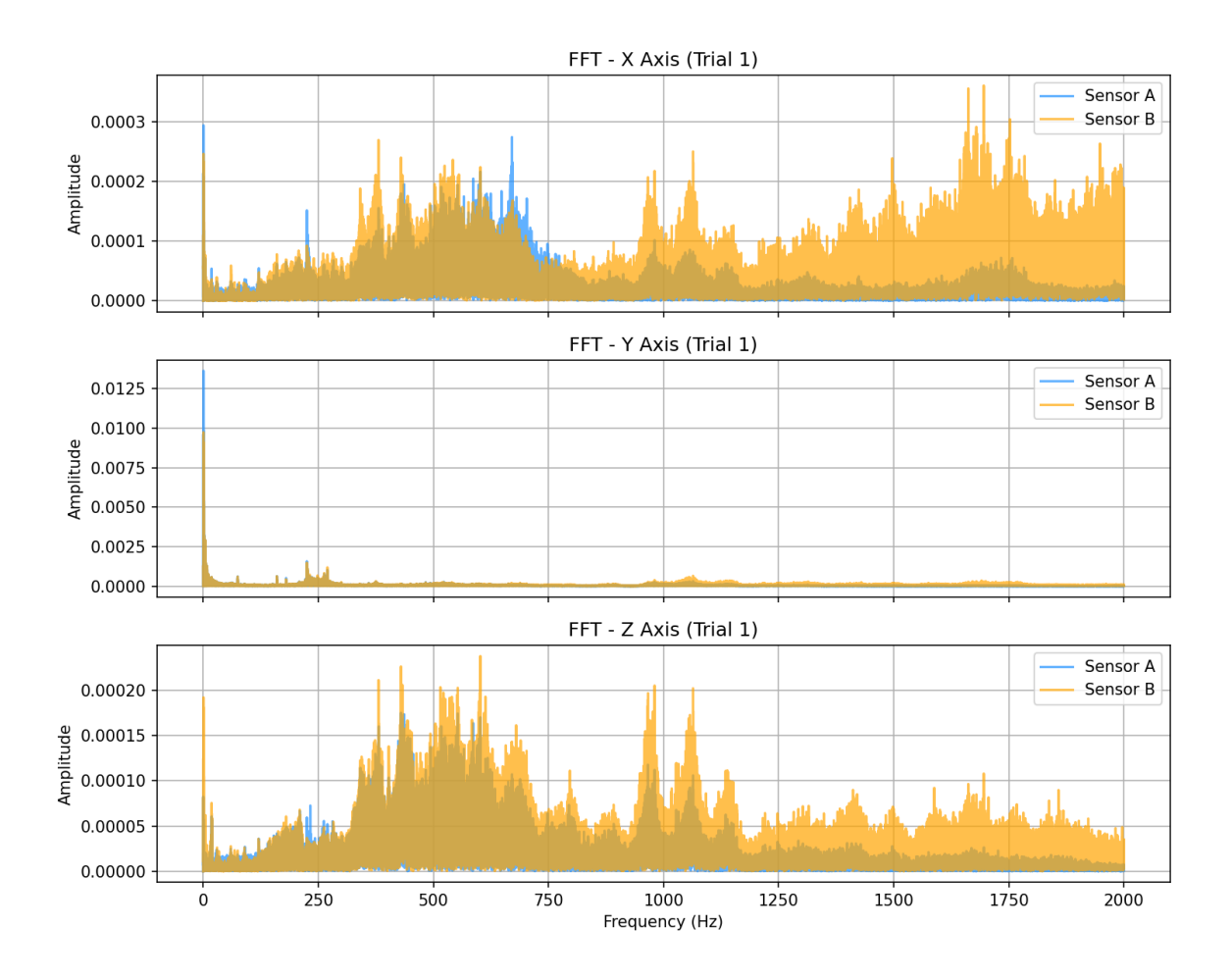


Figure 56: FFT B3 ADXL-357 (Blue) vs IEPE (Yellow), medium speed

The Table 32 and Figure 57 - Figure 58 LRR sensor results only have an IEPE comparison for the Z-axis direction. X and Y axis results from the MEMS sensor have been included to show that the Z axis result for the MEMS is basically identical to the X and Y results.

For comparison, the static results from the LRR sensors are shown in Figure 59. When comparing the low speed to the static or between XY and Z from low speed, the MEMS sensor is too noisy to pickup the much lower amplitude vibrations seen

on the rail. The IEPE sensor, less noisy in the figure below, can pickup the smaller vibration data.

Table 32: Test 2 ADXL-357 dynamic test LRR statistical results, low speed

	Summary										
		RMS		Pea	ak	Cre	Crest				
Sensor	Axis	mean	std	mean	std	mean	std				
A (MEMS)	Χ	0.00205	0.00001	0.01070	0.00064	5.20827	0.31739				
A (MEMS)	Υ	0.00190	0.00001	0.00959	0.00036	5.04960	0.17958				
A (MEMS)	Z	0.00195	0.00001	0.01091	0.00064	5.58436	0.32151				
B (IEPE)	Z	0.00229	0.00001	0.01306	0.00044	5.69361	0.18911				
A-B	Z	-0.00034	0.00000	-0.00215	0.00020	-0.10925	0.13240				

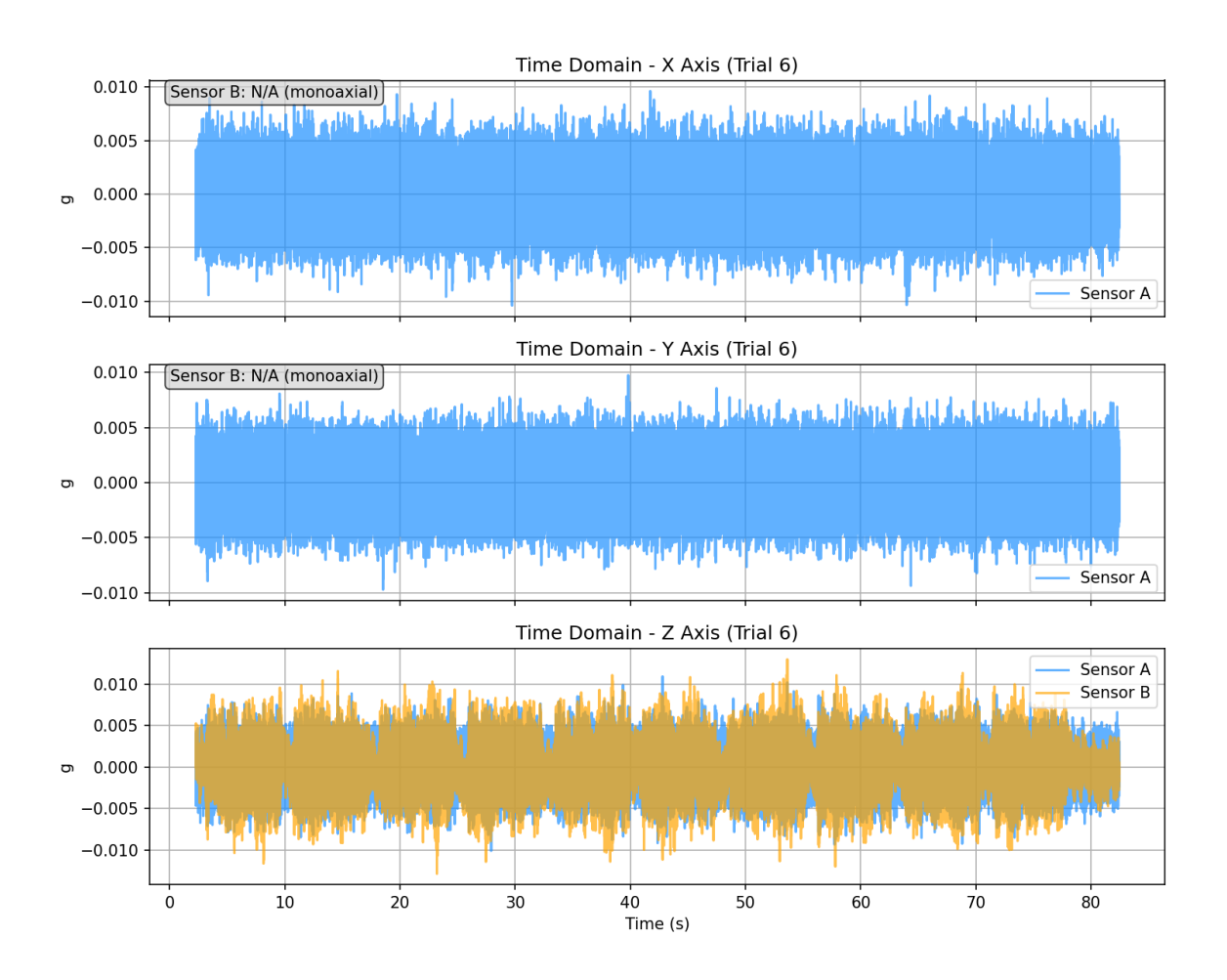


Figure 57: Time domain LRR ADXL-357 (Blue) vs IEPE (Yellow), low speed

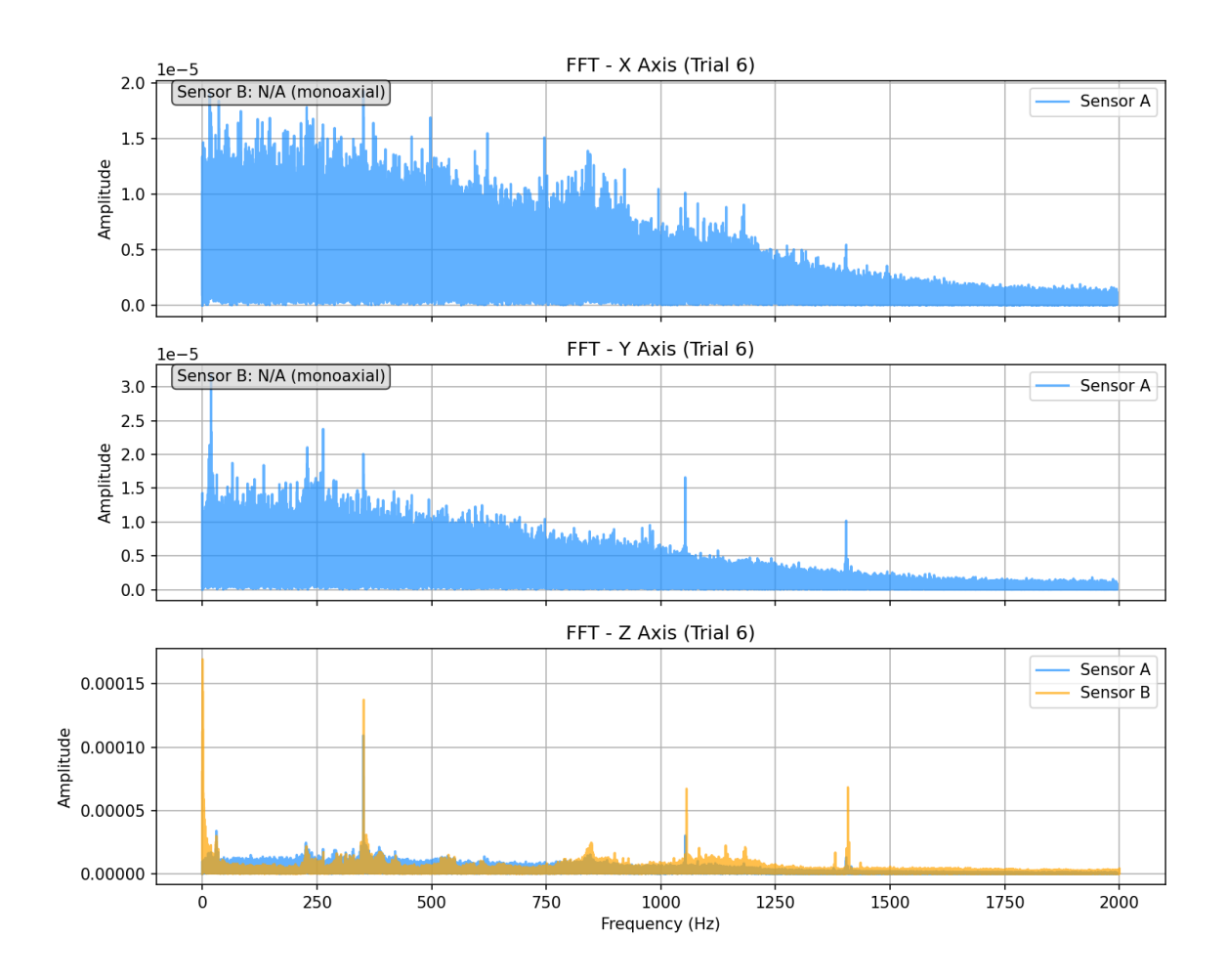


Figure 58: FFT LRR ADXL-357 (Blue) vs IEPE (Yellow), low speed

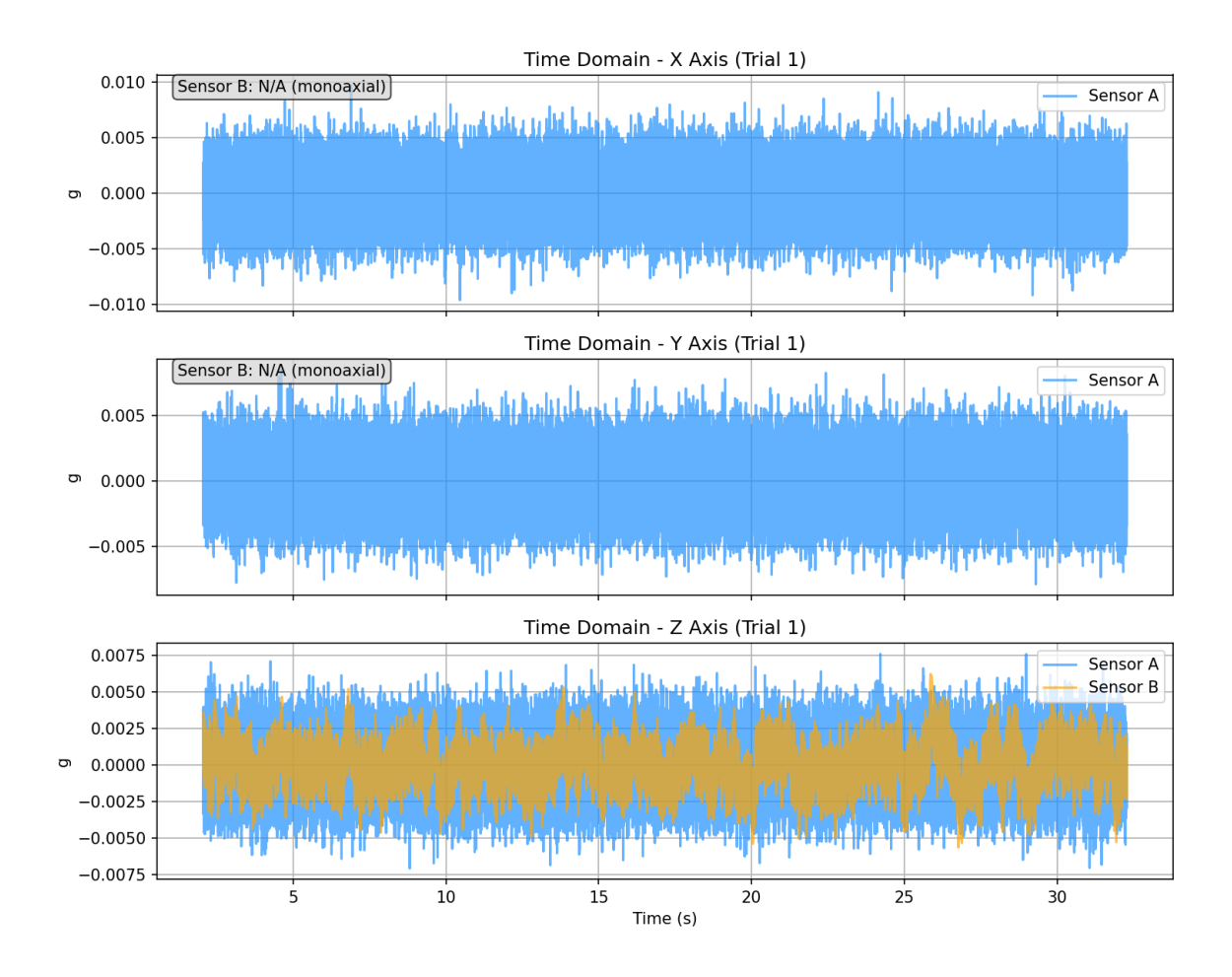


Figure 59: Time domain LRR ADXL-357 (Blue) vs IEPE (Yellow), static

At medium speeds, the LRR results in Table 33, Figure 60, and Figure 61 show the vibration magnitude higher, overcoming the noise levels of the ADXL-357. Like the B3 sensor, the frequency domain shows good agreement, with the magnitude of the MEMS starting to be lower than IEPE around the 1 kHz filtered range.

Table 33: Test 2 ADXL-357 dynamic test LRR statistical results, medium speed

	Summary										
		RN	RMS		ak	Cro	Crest				
Sensor	Axis	mean	std	mean	std	mean	std				
A (MEMS)	Χ	0.00272	0.00004	0.01807	0.00263	6.63605	0.92498				
A (MEMS)	Υ	0.00217	0.00001	0.01163	0.00073	5.36833	0.34698				
A (MEMS)	Z	0.00292	0.00004	0.01969	0.00108	6.74607	0.42416				
B (IEPE)	Z	0.00493	0.00006	0.03608	0.00231	7.31555	0.49771				
A-B	Z	-0.00201	-0.00002	-0.01639	-0.00123	-0.56948	-0.07355				

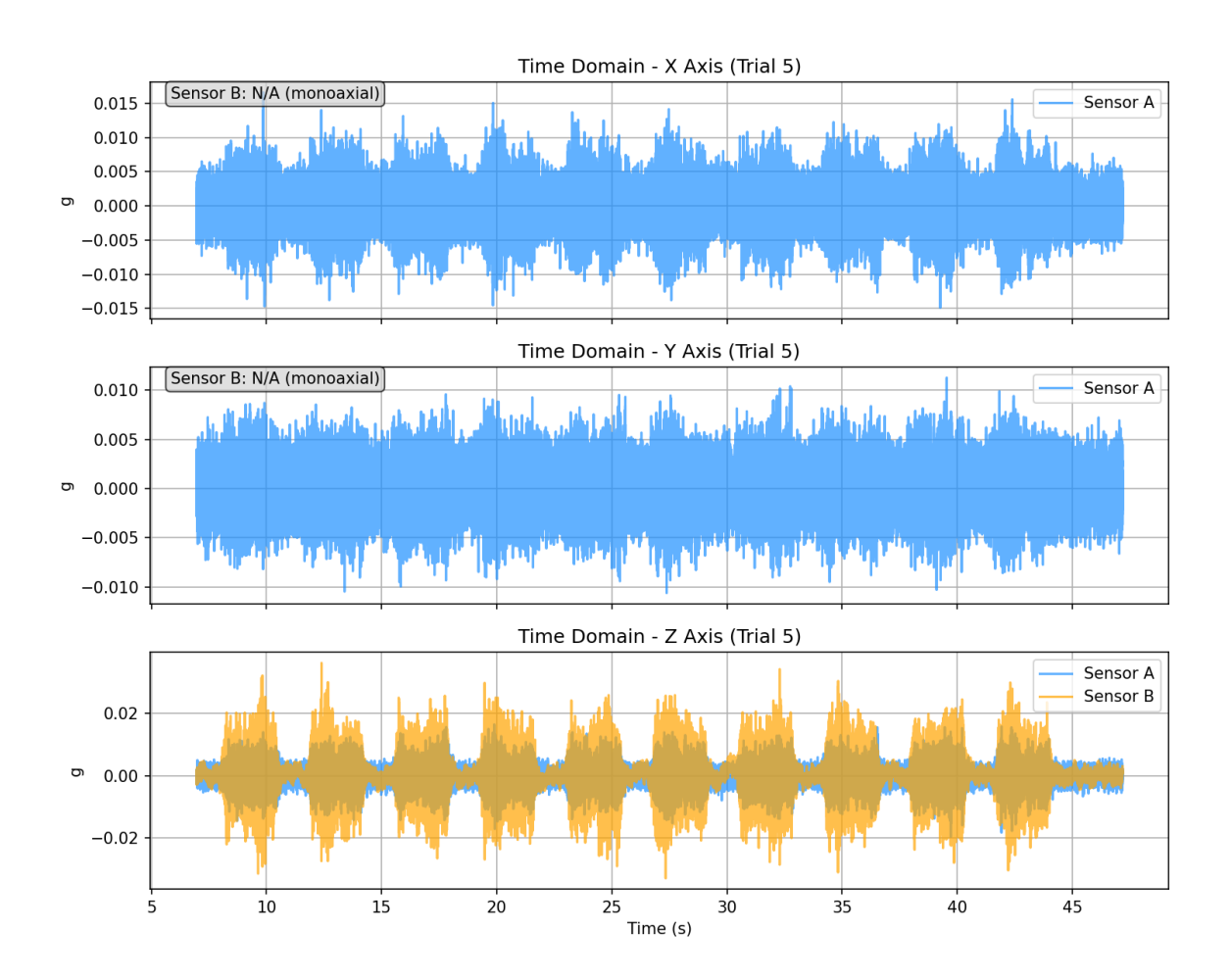


Figure 60: Time domain LRR ADXL-357 (Blue) vs IEPE (Yellow), medium speed

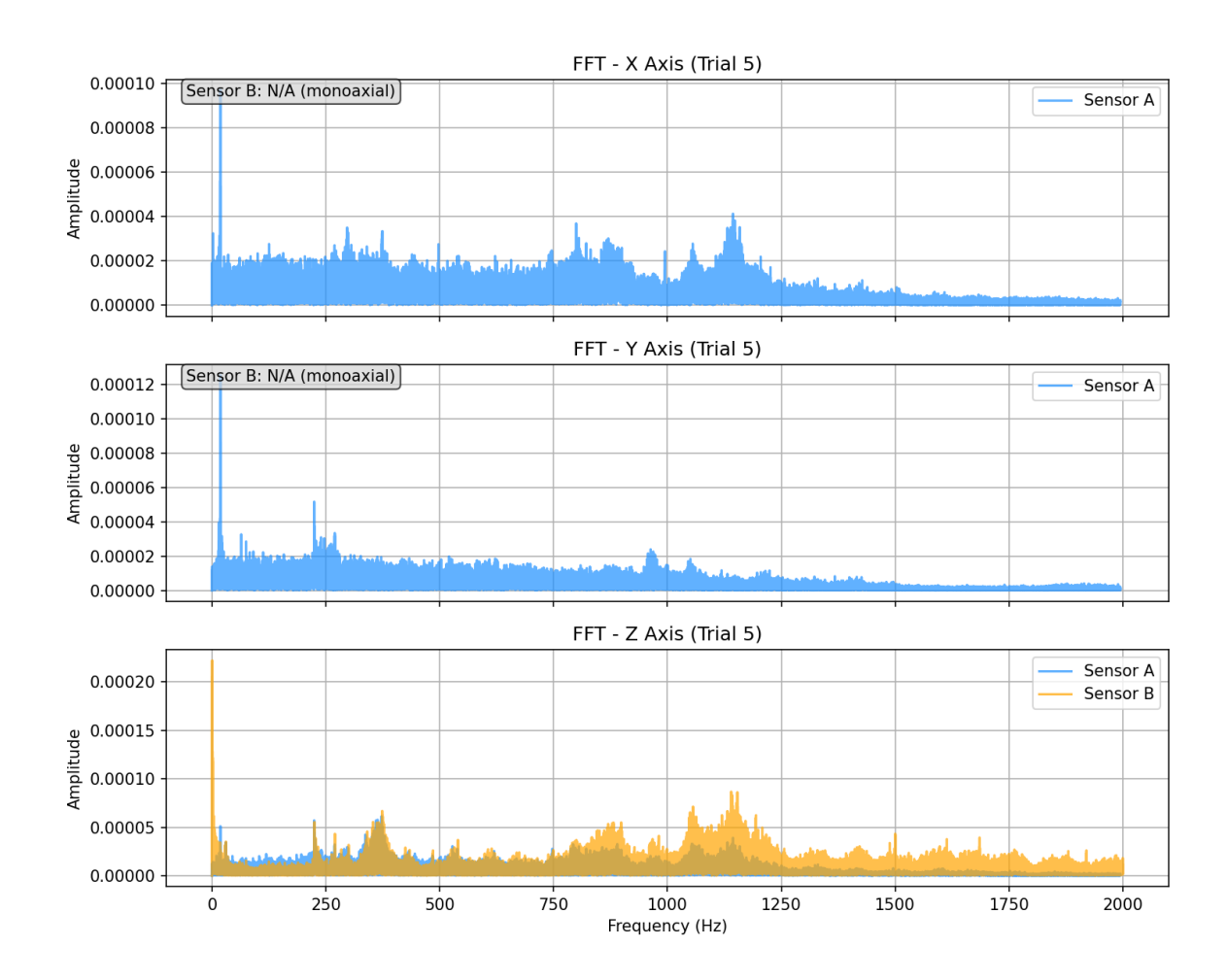


Figure 61: FFT LRR ADXL-357 (Blue) vs IEPE (Yellow), medium speed

4.3.4.2 ICM-42688-P 16 kHz ODR - 5G

The ICM-42688-P low speed test, with the statistical results in Table 34 - Table 36 and shown in Figure 62 and Figure 63, was collected at 16 kHz with unfiltered data. The higher frequency, unfiltered data looks much noisier than the ADXL-357 results due to the high frequency content.

The time domain and FFT show better consistency between the MEMS and IEPE results in the X and Y directions. This may be due to the higher frequency content contained in the Z axis data (as shown in Figure 63) and the better coupling for the

IEPE mount compared to the plastic magnet mount used for the ICM-42688-P sensor.

Table 34: Test 2 ICM-42688-P dynamic test statistical results, low speed

	Summary – LOW										
		RMS	RMS (mg)		(mg)	Cre	st				
Sensor	Axis	mean	std	mean	std	mean	std				
A (MEMS)	Χ	21.040	0.390	425.070	55.560	5.735	0.492				
A (MEMS)	Υ	33.950	0.300	411.230	78.850	11.311	0.403				
A (MEMS)	Z	9.530	0.050	104.430	23.160	5.713	0.206				
B (IEPE)	Χ	21.120	0.290	501.560	46.330	6.124	0.427				
B (IEPE)	Υ	29.400	0.270	378.390	65.090	11.054	0.368				
B (IEPE)	Z	12.210	0.140	244.040	34.090	5.629	0.516				

Table 35: Test 2 ICM-42688-P dynamic test, low speed (MEMS – IEPE)

	Summary - LOW (A-B)									
	RMS	(mg)	Peak	(mg)	Crest					
Axis	mean	std	mean	std	mean	std				
Χ	-0.080	0.100	-76.490	9.230	-0.388	0.065				
Υ	4.550	0.030	32.840	13.760	0.258	0.035				
Z	-2.680	-0.090	-139.610	-10.930	0.083	-0.311				

Table 36: Test 2 ICM-42688-P dynamic test, low speed (MEMS – IEPE, as percentage)

	Summary - LOW (A vs B %diff)										
	RMS	(%)	Peak	(%)	Crest (%)						
Axis	mean	std	mean std		mean	std					
Χ	-0.38	29.41	-16.51	18.12	-16.05	26.01					
Υ	14.36	10.53	8.32	19.12	-6.05	5.58					
Z	-24.66	-94.74	-80.13	-38.18	-58.32	-9.12					

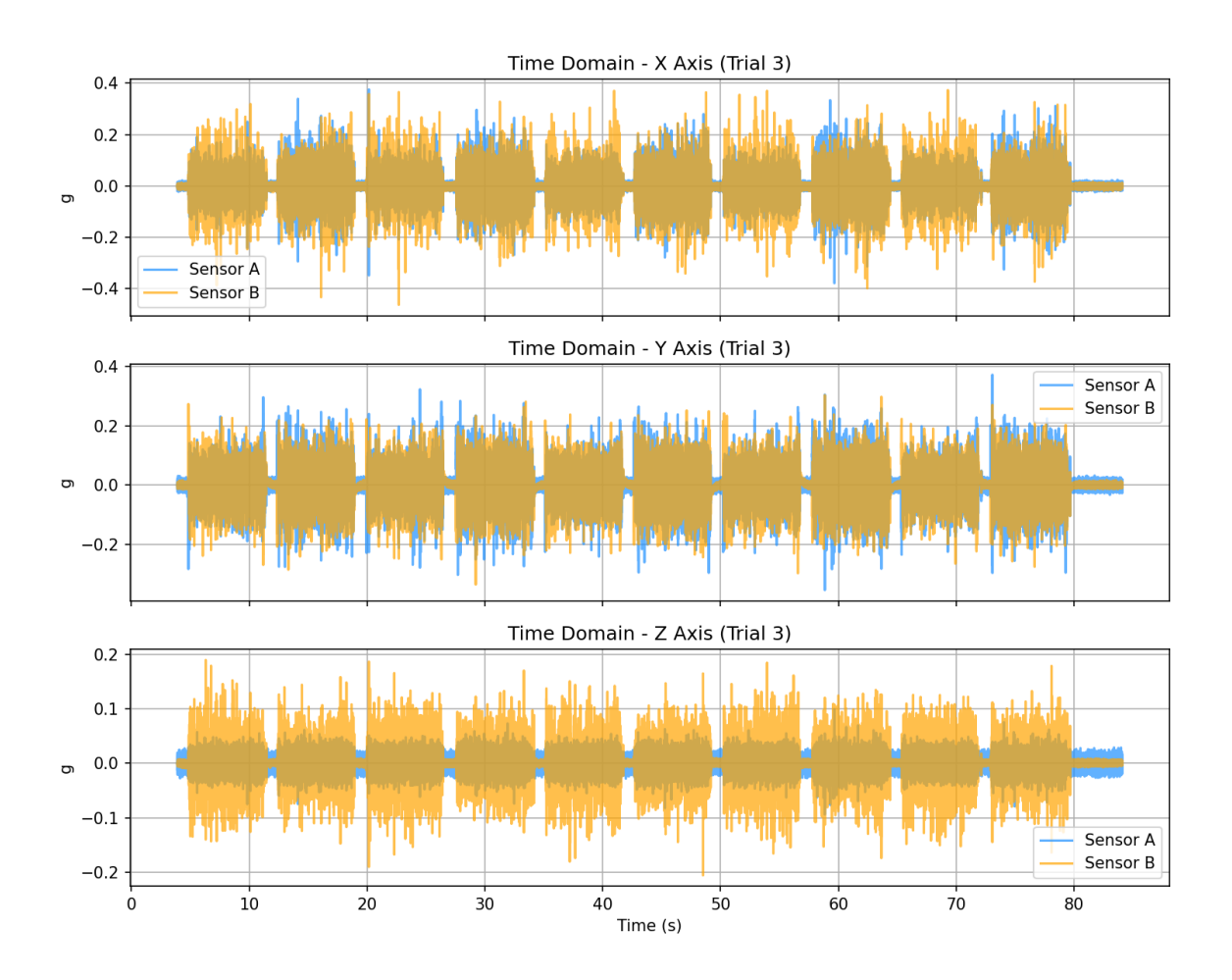


Figure 62: Time domain B3 ICM-42688-P (Blue) vs IEPE (Yellow), low speed

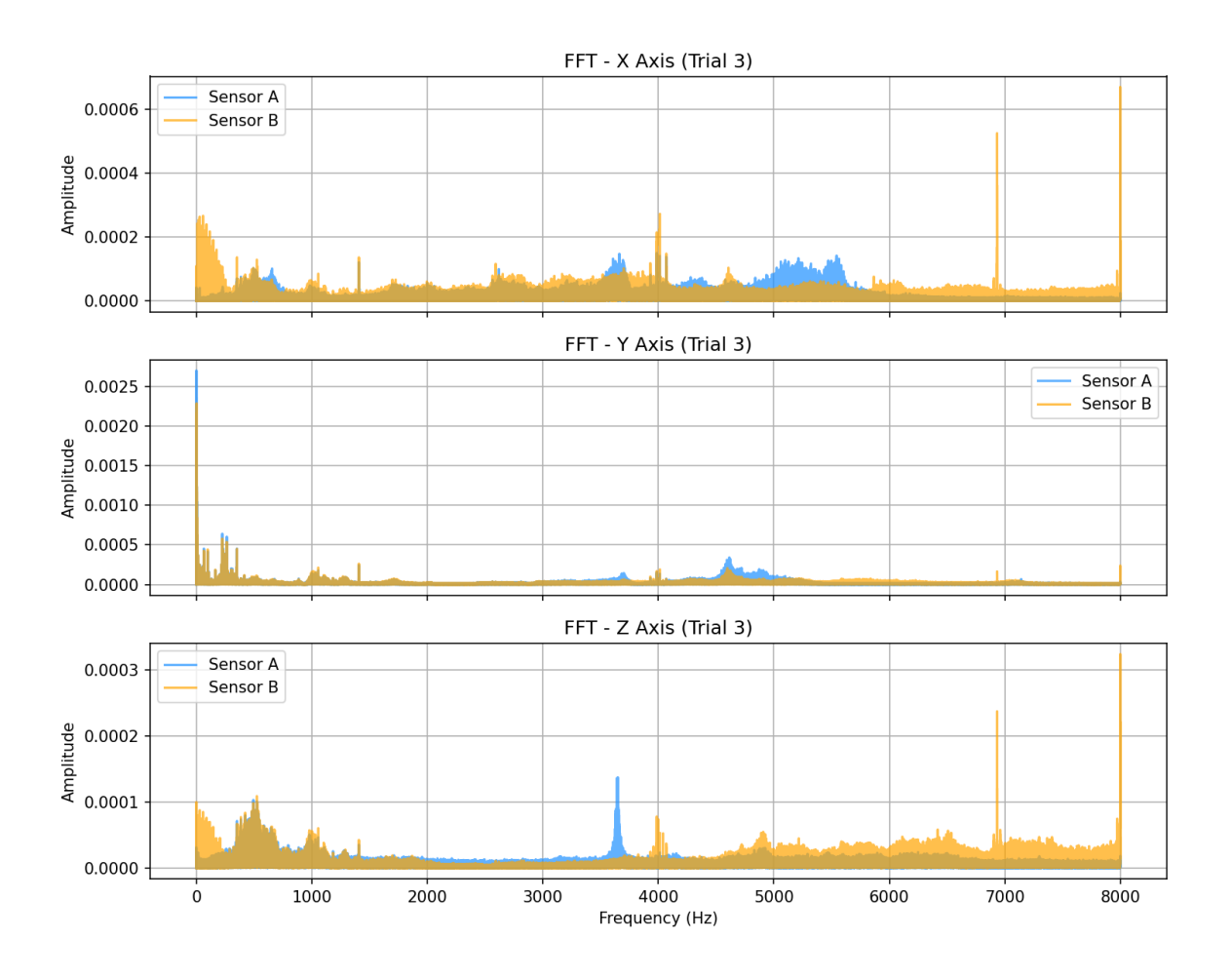


Figure 63: FFT B3 ICM-42688-P (Blue) vs IEPE (Yellow), low speed

The medium speed testing results for the ICM-42688-P, in Table 37 - Table 39, Figure 64, and Figure 65, show a similar result as the low speed. The X and Y data are closer between the two sensors and the higher frequency Z axis data is detected better by the IEPE sensor.

In both low and medium speed tests, the FFT shows better agreement between X and Y with Z being further apart. For X and Y moist major peaks under 4 kHz can be identified, and while the Z data looks similar both low and medium speed MEMS results have the 4 kHz Z peak at a lower frequency. The X axis peak around 4 kHz

shows as the same for both sensors so this is probably due to the mount being less stiff and well coupled for the MEMS sensor.

Table 37: Test 2 ICM-42688-P dynamic test statistical results, medium speed

	Summary - MED										
		RMS (mg)		Peak	(mg)	Crest					
Sensor	Axis	mean	std	mean	std	mean	std				
A (MEMS)	Χ	229.620	1.470	2568.260	124.110	6.747	0.340				
A (MEMS)	Υ	230.930	1.650	2578.300	184.770	5.734	0.250				
A (MEMS)	Z	34.100	0.180	402.900	46.530	6.432	0.698				
B (IEPE)	Χ	234.960	0.930	3568.870	926.440	8.725	1.377				
B (IEPE)	Υ	171.210	0.640	2028.090	97.260	6.705	0.370				
B (IEPE)	Z	85.630	2.010	9804.060	4871.960	7.095	0.721				

Table 38: Test 2 ICM-42688-P dynamic test, medium speed (MEMS – IEPE)

	Summary - MED (A-B)									
	RMS	(mg)	Peak	(mg)	Crest					
Axis	mean	std	mean std		mean	std				
Χ	-5.340	0.540	-1000.610	-802.330	-1.978	-1.037				
Υ	59.720	1.010	550.210	87.510	-0.971	-0.121				
Z	-51.530	-1.830	-9401.160	-4825.430	-0.663	-0.023				

Table 39: Test 2 ICM-42688-P dynamic test, medium speed (MEMS – IEPE, as percentage)

	Summary - MED (A vs B %diff)									
	RMS	6 (%)	Peal	k (%)	Crest (%)					
Axis	mean	std	mean std		mean	std				
Χ	-2.30	45.00	-32.61	-152.74	-30.33	-152.19				
Υ	29.70	88.21	23.89	62.06	-5.92	34.40				
Z	-86.08	-167.12	-184.21	-196.22	-162.30	-189.83				

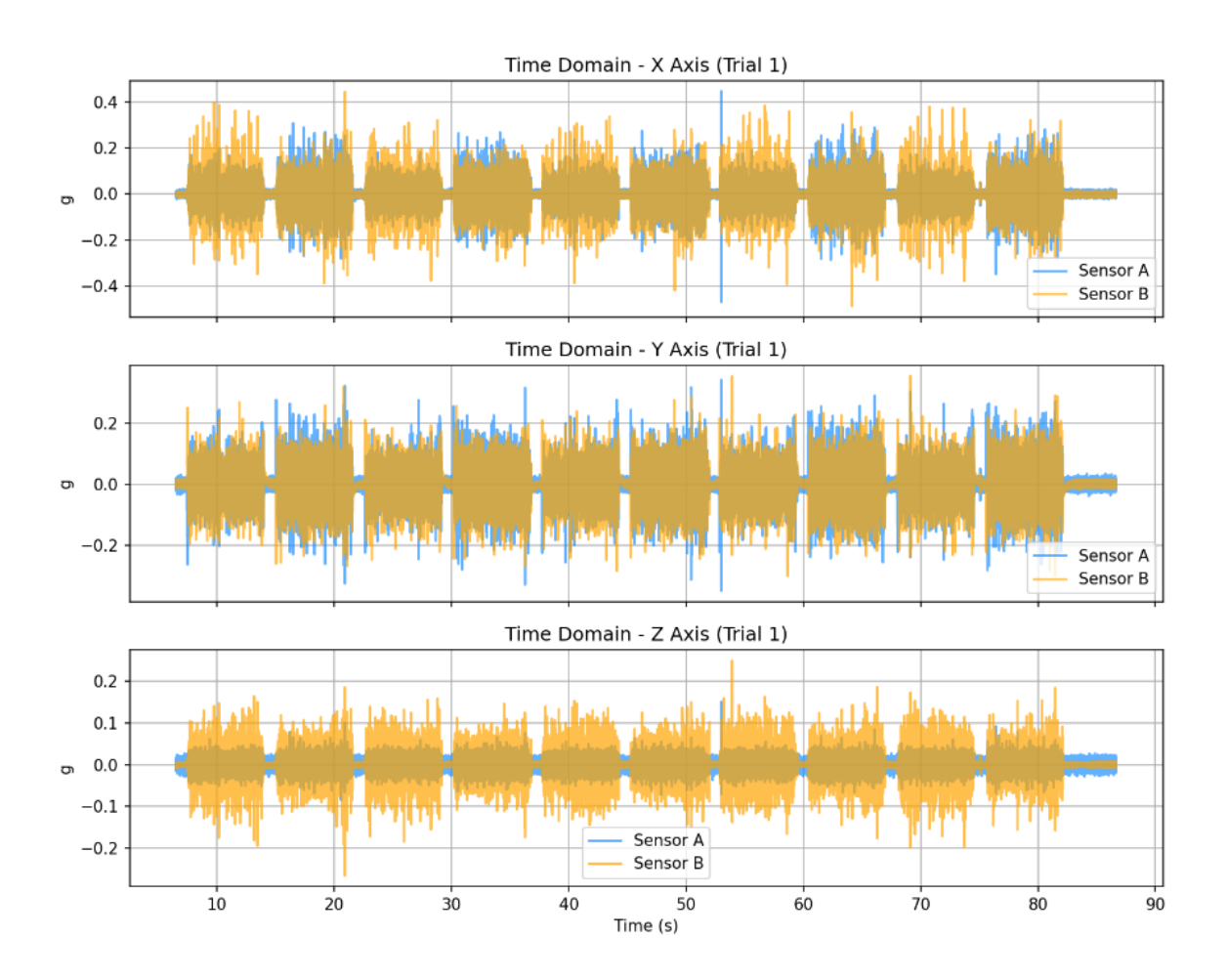


Figure 64: Time domain B3 ICM-42688-P (Blue) vs IEPE (Yellow), medium speed

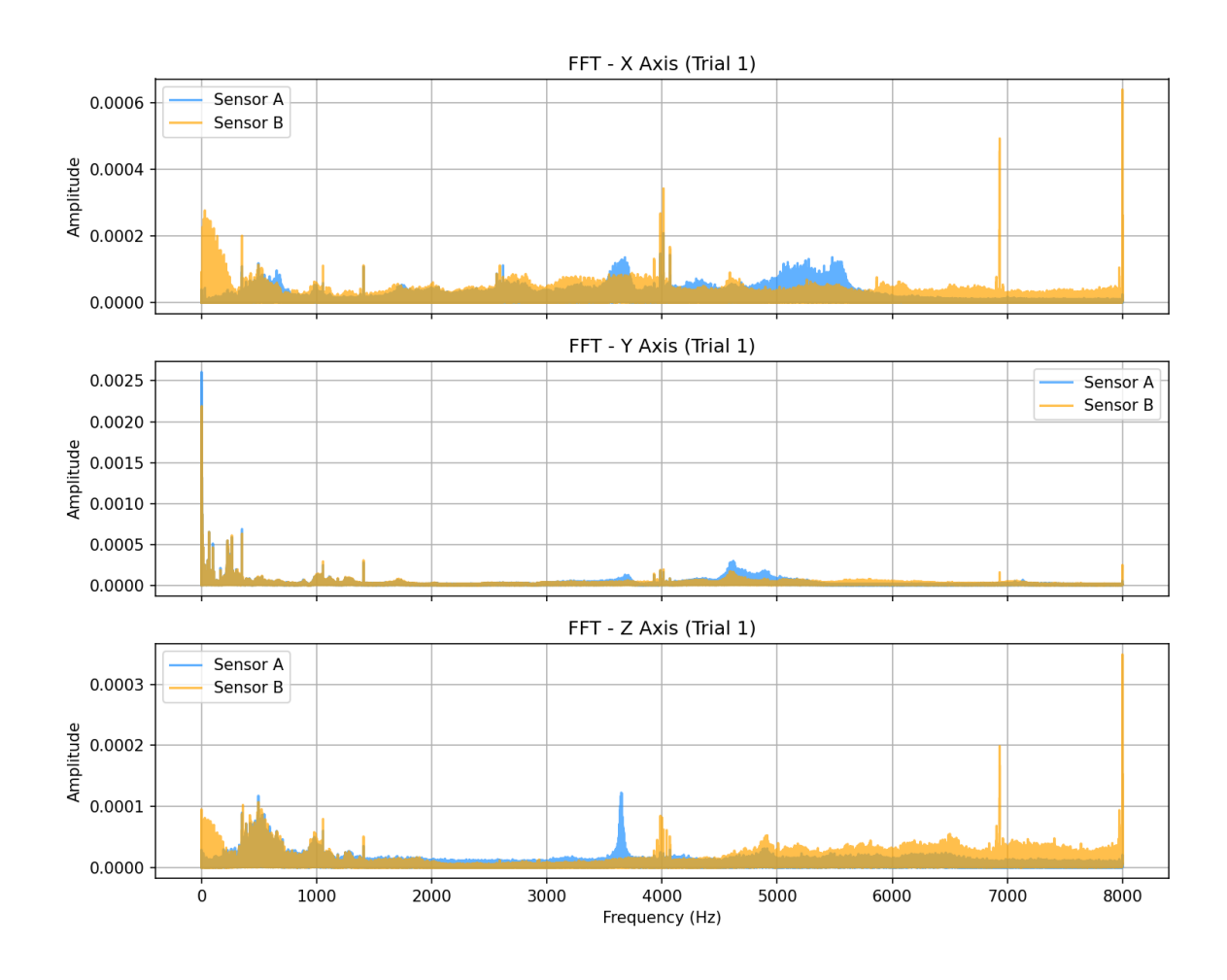


Figure 65: FFT B3 ICM-42688-P (Blue) vs IEPE (Yellow), medium speed

4.4 Test 3: 5G mmWave Network Performance

In addition to the sensor-based testing, networking performance in the MMRI was also evaluated with Iperf. This network testing tool allowed the limits of the 5G mmWave system to be tested beyond the data transmission requirements of just the accelerometer. Iperf is a standard, open-source network performance measurement tool, used to generate traffic between a client and server and measure multiple network performance metrics, including throughput and latency for TCP traffic, and additionally packet loss plus jitter for UDP traffic. These

performance metrics will allow for evaluation of 5G mmWave performance, and its ability to serve high throughput, low latency applications.

For this study, two computers were equipped with 10 Gbps Network Interface cards (NICs) and used during testing to ensure that the end devices were not a bottleneck for performance. One PC remained in one location, wired to the 5G core via the LBO, creating a direct ethernet wired connection from the core to the PC. The second PC, with a 5G network connection supplied from a CPE, was positioned in multiple locations across the facility to assess network performance in different areas. For each placement, test data was collected with the CPE both inside and outside each CNC machine to provide a comparison of performance with a clear line of sight (LOS) compared to a disrupted LOS from inside the machine, allowing CPE placement options to be accessed (shown in Figure 66).

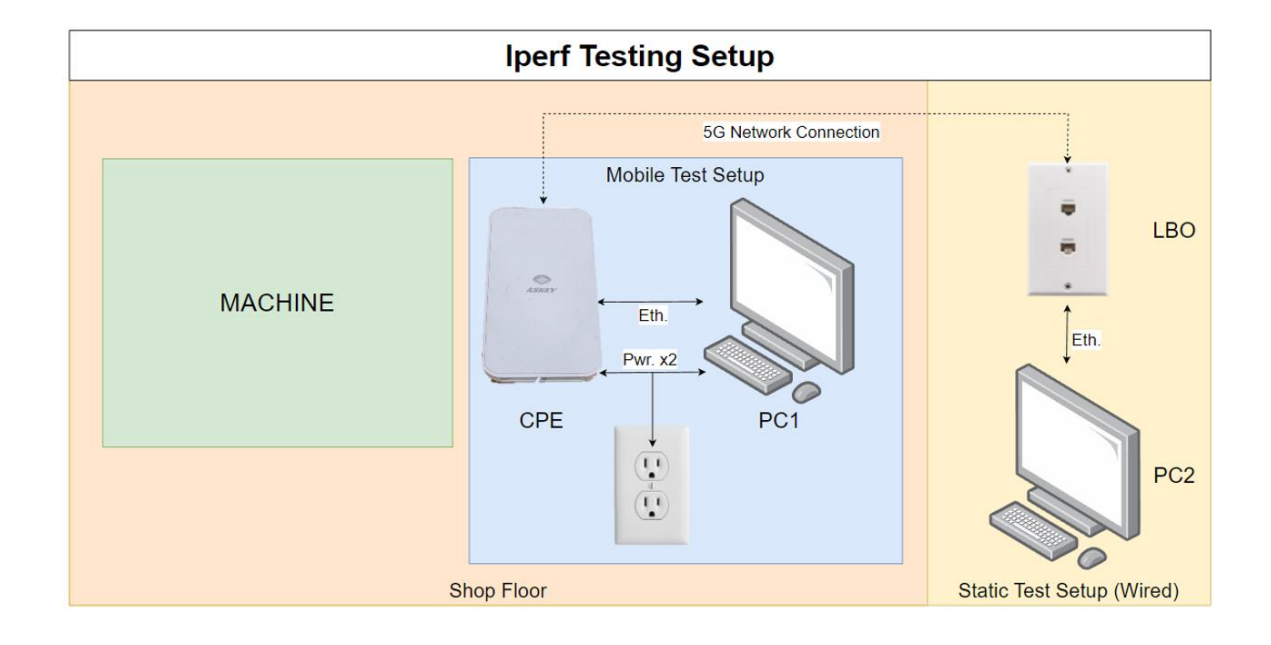


Figure 66: Iperf 5G network testing setup

At each test location, as shown in Figure 67, TCP and UDP tests were performed in both upload and download directions to provide a full picture of networking performance.

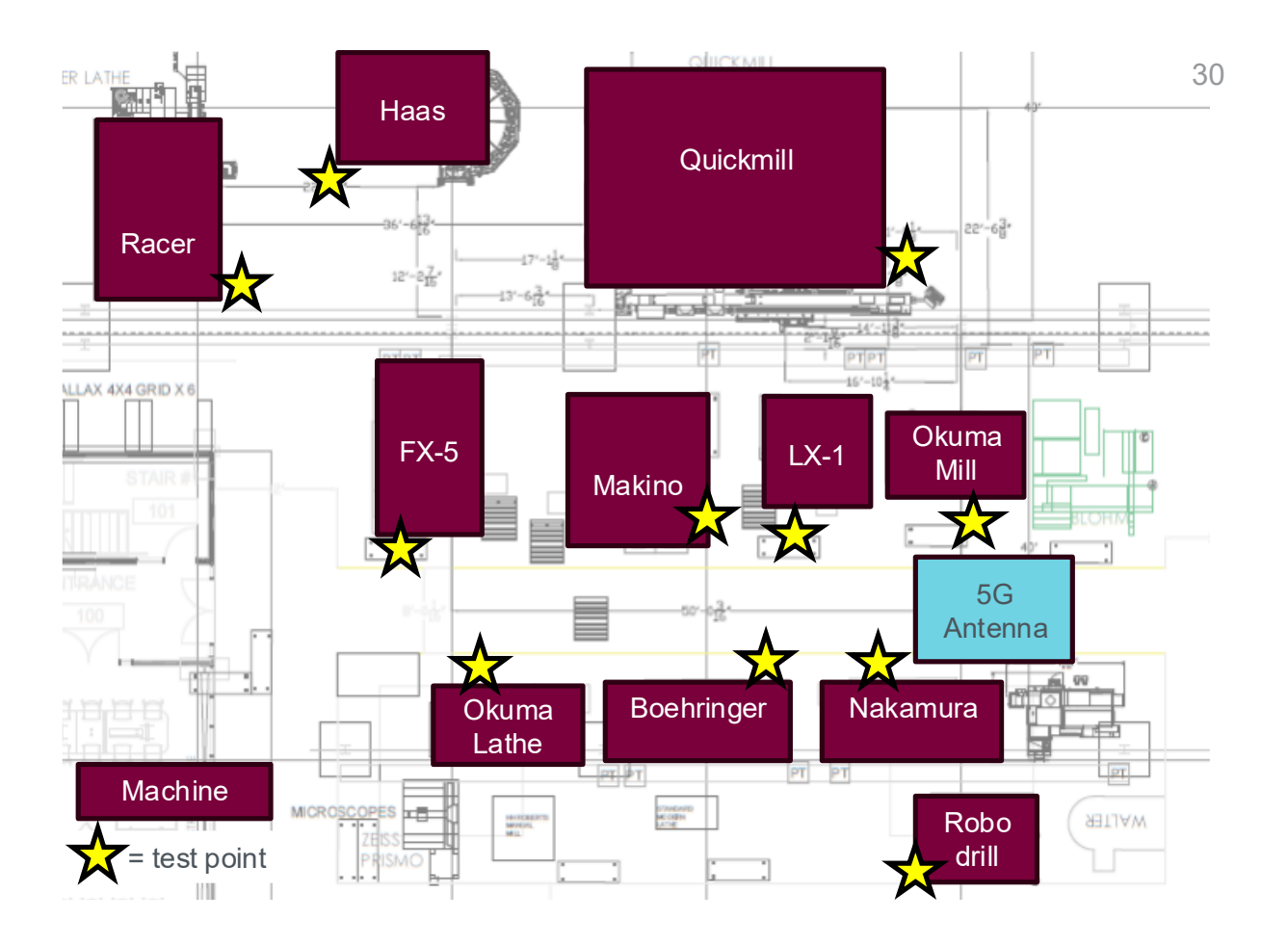


Figure 67: 5G mmWave test points

The UDP download (DL) testing results in Table 41 show the potential of 5G, it almost saturates the 1 Gbps limit with very low jitter and data loss. TCP results in Table 40 are much slower due to the two-way communication nature of TCP compared to the send and forget nature of UDP. The UDP results show the

potential of the system, but UDP networking for sensors could result in lost samples, ruining the potential for frequency analysis.

The results showed good coverage of the middle machine aisle of the MMRI, with similar performance results throughout the aisle, with lower performance and failed tests becoming more prevalent when tested at machines outside of this main aisle with worse LOS to the main roof mounted antennas.

The drawbacks of this system are the connection method and the network upload/download (UL/DL) ratio. The connection method limitations requiring a CPE limit the ability to implement a fully wireless 5G sensor node until the network is upgraded. Similarly, the ratio of the incoming upgraded system has more control options, with a closer to 50/50 UL/DL split available. This will result in the superior performance of 5G without the current drawbacks of the specific system at the MMRI.

Table 40: Average 5G TCP test results

		TCP Speed	(Mbps	5)		
	l	JPLOAD		DO	WNLOAD	
Machine	Desk	In Machine	Desk		In Machine)
FX-5	65.1	N/A		50.9	N/A	
Makino	74.8	75.9		56.5		58.4
LX-1	55.3	39.3		65.6		47.4
Okuma Mill	83.8	37.5		67.4		43.9
Okuma Lathe	68.4	6.6		65		47.1
Boehringer	71.4	53.6		75.2		58.1
Nakamura	64.8	32.6		66.3		44.6
Robodrill	47.7	N/A		55.8	N/A	
Racer	7.54	N/A		45	N/A	
Quickmill	26.9	N/A		55.9	N/A	
Haas	3.88	N/A		40.5	N/A	

Table 41: Average 5G UDP test results

UDP Speed (Mbps)								
	UPLOAD		DOWNLOAD					
Machine	Desk	In Machine	Desk In Machine					
FX-5	155.54	N/A	958.32	N/A				
Makino	121.2	40.2	965.3	958.34				
LX-1	106.69	59.5	962.29	765.51				
Okuma Mill	201.6	21.51	964.87	649.23				
Okuma Lathe	158.34	12.7	959.87	493.17				
Boehringer	194.2	32.68	962.00	957.37				
Nakamura	199.35	35.7	962.51	970.22				
Robodrill	14.21	N/A	945.74	N/A				
Racer	15.12	N/A	944.77	N/A				
Quickmill	17.01	N/A	940.89	N/A				

Table 42 compares the 5G results with three Wi-Fi speed tests conducted at the MMRI, the Wi-Fi speeds are not intended to be an overall performance benchmark for these networking types, but to provide a comparison of the technologies within the MMRI. The 5G download speed of almost 1 Gbps far exceeds the bandwidth reached by any of the Wi-Fi versions and the lower latency highlights the capabilities that make 5G networking so attractive for some use cases.

Table 42: 5G test results vs Wi-Fi

	Wi-Fi 6	Wi-Fi 5	Wi-Fi 4	5G
TCP UL Speed (Mbps)	110	135	24.7	70
TCP DL Speed (Mbps)	110	119	25.6	65
UDP UL Speed (Mbps)	190	192	20.9	200
UDP UL Jitter (ms)	0.77	0.387	4.291	0.9
UDP UL Loss (%)	0.29	0.94	0	0.65
UDP DL Speed (Mbps)	178	180	16.5	967
UDP DL Jitter (ms)	0.468	0.551	3.921	0.091
UDP DL Loss (%)	0.36	1.1	83	0.22

Chapter 5: Discussion

5.1 Accelerometer Performance

The first test, using the low frequency reference shaker, displayed the potential of MEMS accelerometers as a replacement for the more expensive IEPE alternative. Although the low cost ADXL-345, common from the literature review, had high noise levels it could still identify the peak frequency. The ADXL-357 and ICM-42688-P both also could identify the key frequency peaks. They also performed better than the ADXL-345, with closer statistical analysis results when compared to the IEPE.

The second test showed some of the limitations of MEMS accelerometers. The ADXL-357 had good agreement with the IEPE reference, but the built in low pass filter prevents data from over 1 kHz to be accurately sampled, possibly restricting its potential use to lower frequency applications. Over 1 kHz the frequency spikes could be seen at lower magnitudes, so potentially this sensor could be used for up to 2 kHz range of interest if accounting for the LPF effects on the higher frequency magnitudes (as we are only interested in overall trends and patterns to identify anomalies, repeatability matters more than getting an exact precise measurement).

The ICM-42688-P showed its ability to measure higher frequency data compared to the ADXL-357. However, these tests highlighted the shortcomings of a plastic

mount for monitoring higher frequency ranges, especially in the Z axis where it was the least rigidly mounted.

Due to the potential for higher frequency monitoring with a similar noise density, all at a lower unit cost, the ICM-42688-P sensor makes the most sense for integration in future sensor work.

5.2 Network Performance

The 5G mmWave network testing results both displayed the high potential value and performance of this technology while also showing some of the current limitations and drawbacks.

Many of the current limitations are a result of the current 5G mmWave test network setup and should be solved as the technology and equipment matures. An example of this is the upload and download speed differences, instead of mature technology tuned to industrial needs, the current network hardware being used was made to service cellphones. This results in much higher download speeds, as this use case demands more data downloads than uploads. This is the inverse of most industrial use cases, but especially for CBM sensor networks, which primarily produce and upload data to the network.

Even with these limitations, the 5G mmWave performance results showed that it is a promising technology for future wireless industrial networks with high performance compared to the current alternatives. The low latency and ultra high reliability of 5G networks enables new use cases for wireless networking in

industry, both replacing wired networks being used for their reliability, but also entirely new use cases. The new use cases will be ones reliant on the high speed and reliability of wired networks but require the flexibility of wireless networks.

Overall, the network testing showed the potential of 5G mmWave networking for industrial use cases, especially around the main aisle where there is clear direct LOS between the device and the 5G antenna.

Chapter 6: Conclusion and Future Work

6.1 Conclusions

Overall, the first test proved to be the most effective for benchmarking accelerometer performance and comparing the MEMS sensors to the reference IEPE alternatives. Test 1 provided constant excitation and a controlled environment, allowing for fair and meaningful comparisons, but was limited by the low frequency of the shaker. The second test revealed important areas for improvement, especially regarding higher bandwidth performance and mounting stability. However, due to the difference in filtering for the ADXL-357 and mounting for the ICM-42688-P it was limited in usefulness for overall comparisons.

This work demonstrated the potential of MEMS accelerometers as replacements for traditional IEPE sensors, particularly for lower bandwidth applications, and highlighted current limitations of available digital MEMS options in high-frequency conditions. The resulting sensor prototypes with an approximate price of \$150 is much more appropriate for scaling up compared to the \$5000 system traditionally used. This would allow ten machines to be monitored with a tri-axial accelerometer for about \$1500 in sensor costs, leaving a lot more budget for the wireless networking portion. In comparison, this would allow for \$3500 in other costs before reaching the price of a single traditional system, much less the \$50000 price of ten traditional monitoring systems plus wired networking costs.

6.2 Research Contributions

This research aimed to address two main challenges for CBM implementation that are driving the cost too high for wide scale use, the high sensor costs, and the high networking costs. This was done by investigating low-cost sensor alternatives, and evaluating 5G networks as a wireless alternative to wired while overcoming the current limitations of wireless alternatives.

These objectives were achieved through three main contributions. The first was through research into existing low-cost sensor alternatives, integration of two untested sensor alternatives (ADXL-357 and ICM-42688-P) and providing performance benchmarks for both. This work introduces the ICM-42688-P as a very low-cost sensor with superior performance when compared with other digital MEMS sensors from literature. Second was to evaluate the real-world performance of a 5G mmWave network inside an industrial environment, showing the real potential and the current limitations of 5G private networks for manufacturing use cases. The last contribution was development of a low-cost wireless sensor prototype, a flexible, modular sensor architecture that is compatible with the current MMRI 5G network and could be easily altered for most sensor modalities.

Together, these three contributions demonstrate the feasibility of deploying affordable wireless sensors for CBM instead of relying on expensive systems. By enabling more widespread and scalable machine monitoring, this approach has the potential to significantly reduce unplanned downtime and productivity losses.

In the long term, it could help manufacturers improve operational efficiency, enhance competitiveness, and support more sustainable practices by minimizing scrap, reducing energy waste, and extending the life of equipment through improved maintenance strategies.

6.3 Future Work

6.3.1 Further ICM-42688-P Work

One limitation of test 2 for the ICM-42688-P was the 16 kHz sampling rate compared to the 32 kHz max sampling rate. 16 kHz was the fastest working sampling rate for the current SPI read library without rewriting the code to access the sensors internal data buffer. Now that the future focus will be on this sensor, it makes sense to make these changes to gather data at the maximum ODR.

Further testing can be completed to verify and possibly improve the understanding of the ICM-42688-P performance. First, 32 kHz testing to verify the top ODR. Second, testing can try different low pass filter and high pass filter settings using the internal sensor filters. For example, noise performance could be improved compared to the test 2 results from this work by using the LPF. At 32 kHz ODR the maximum recommended bandwidth is about 4 kHz, this could be compared to IEPE again but this time using LPFs during acquisition for a better comparison that avoids the aliasing caused by applying the LPF post acquisition.

Lastly, for these high frequency tests, if a sensor module has been selected it now makes sense to invest in creating a metal mount to replace the cheaper rapid prototyping plastic mount. This will improve the rigidity of the system and make the high frequency content more accurate and in line with the IEPE sensor results.

6.3.2 Multi 5G Wireless Sensor Setup

The test 2 setup for the ethernet based 5G ICM-42688-P sensor only used one sensor on B3, skipping the LRR sensor. However, in a real monitoring scenario if multiple sensors were needed to monitor a machine this could currently be done in two ways. The first simple way is to connect each sensor to a dedicated CPE, but this is limited by the number of CPES (and cost of each), and each requires a dedicated outlet. The second way is seen in Figure 68, adding a switch between the CPE and sensors, however then the CPE capabilities are split between the two sensors, providing less peak performance for each.

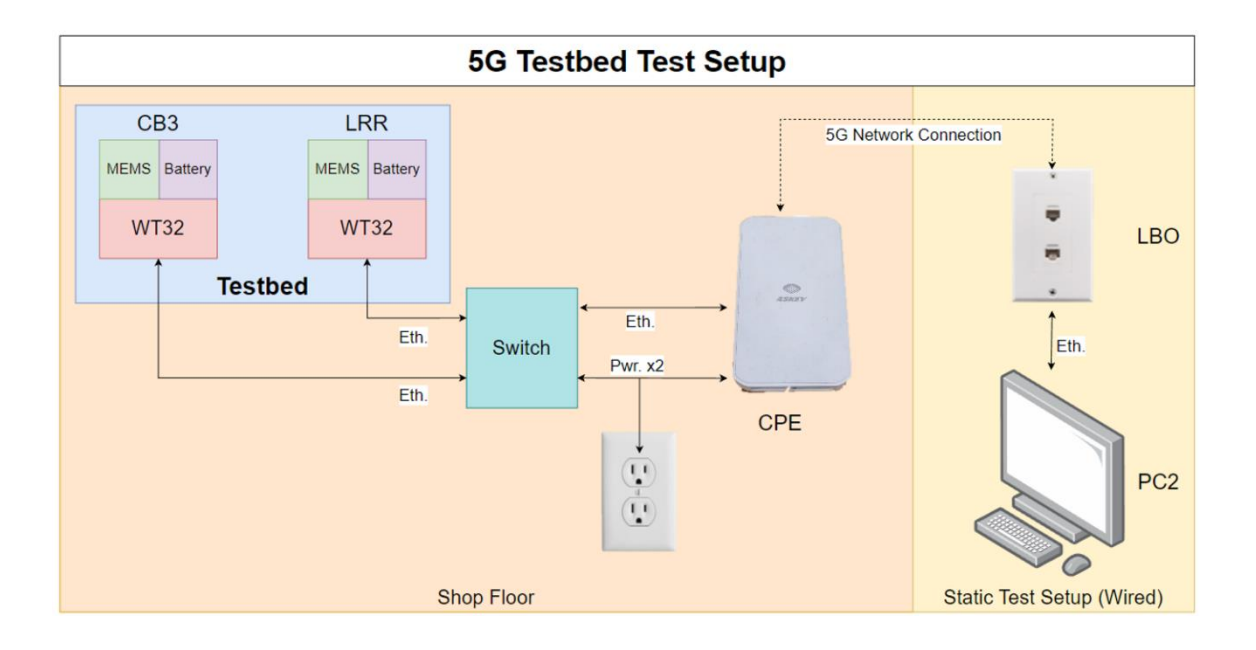


Figure 68: Multi 5G sensor testbed setup

6.3.3 5G Native Microcontroller

One limitation of the current work is the requirement of the ethernet to CPE connection to enable 5G connectivity. The next generation of the MMRI TERAGO 5G network is planned to fix this issue, taking advantage of their new partnership with Ericsson to utilize the Ericsson EP5G system, making wireless connectivity available more widely via greater device support.

This will allow the wired external CPE equipment to be removed from the system and replaced with an on-board 5G networking connection. Like how the current ESP32 Wi-Fi prototype operates but with the ability to connect to the 5G network. Once the network is updated this capability could be achieved via a 5G add on attachment or by using a 5G compatible MCU as an ESP32 replacement.

6.3.4 Accelerometer Array

For applications where noise density requirements are very demanding, such as displacement measurement, there is a strategy utilizing multiple MEMS accelerometers to lower the noise compared to a single sensor [39, 87, 88]. By using multiple accelerometers at the same time, any random noise can be reduced by averaging out readings across the multiple accelerometers. This strategy is common for IMU sensors used for displacement measurement but could be used as a strategy to create a high-performance alternative to IEPE sensors for other applications.

Theoretically, an IMU array of size N will see noise reduced by \sqrt{N} times from the noise of a single IMU [89]. Table 43 below shows the theoretical number of sensors required to meet the 10 μ g/ \sqrt{Hz} noise requirement, resultant theoretical noise density and total cost of the sensors.

Table 43 below shows that while not all sensors are practical for an array of this kind, due to a combination of the high count required and unit cost (ADXL-357), some sensors could be practical for implementation. The table does not include the extra cost and complexity of implementing this type of array. All the sensors must be synchronized, read simultaneously, and have the data averaged out, all on-board the sensor device. Still, this would be an interesting area to further develop these kinds of low-cost sensors for more demanding low-noise applications.

Table 43: Sensor array Noise Density (ND) vs cost

Sensor	Single ND (μg/√Hz)	Count req.	Array ND (μg/√Hz)	Price per	Total cost
ICM42688	70	49	10.00	3.33	163.17
ADXL-355	25	7	9.45	11	77
ADXL-357	75	57	9.93	57	3249

6.3.5 Accelerometer Alternatives

Another route for future work to improve sensor performance, other than an array of the low cost, poorer performance digital MEMS accelerometers, would be exploring the higher cost analog MEMS accelerometers. Some of these are common in literature but were avoided for the first sensor iteration to test out the best of the lowest cost option (digital MEMS) to benchmark the sensor before moving on.

In the case a higher performance sensor is needed, and cost is less important of a consideration, some higher performance MEMS accelerometers exist. Of the options available the ADXL-100X series from Analog Devices and the 820/30M1 from TE Connectivity appear to be the most promising candidates. The ADXL-1001/2 are common in literature. The 820/830M1 could not be found used in a CBM sensor paper.

Both options offer higher bandwidths and lower noise but are considerably more expensive compared to the very cheap ICM-42688-P chip. Additionally, unlike the

ICM-42688-P chip which requires a cheap and simple PCB, the analog sensors require a more complex integration, adding more cost.

6.3.6 Database Integration

The currently implemented data receiver is limited to logging incoming sensor data in local MS Excel CSV files. While this approach is simple and acceptable for smaller scale testing, it does not scale up well for large deployments, restricting real-time data accessibility, remote analysis, and access across an organization.

However, the existing receiver software has been designed to allow integration with more scalable data management solutions. The CSV logging function can easily be replaced with a structured query Language (SQL) database, or a time-series database logging function. These could support larger-scale deployments, enable efficient querying, and centralize data for visualization or machine learning pipelines.

This upgrade could also be designed to provide a link for future 5G based WSNs to existing IT infrastructure, seen below in Figure 69. In such a setup, all sensor nodes could transmit data directly to a central receiver server over the 5G network. The receiver server could be connected to both the dedicated sensor 5G network and the general-purpose enterprise IT network. This dual network arrangement would allow sensor data to be securely stored and accessed by workers through the database, without exposing the 5G sensor network to broader internet or internal office traffic. This separation improves security and reduces the risk of

network congestion while still enabling data access, analytics, and integration with exiting IT systems.

Implementing a standardized database logging mechanism would be an important next step for making the system suitable for deployment in real industrial environments instead of just for smaller scale lab use. Even within an academic setting, a database could allow sensor data to be saved and documented more thoroughly and in a standardized format, which could allow it to be more widely used for future work.

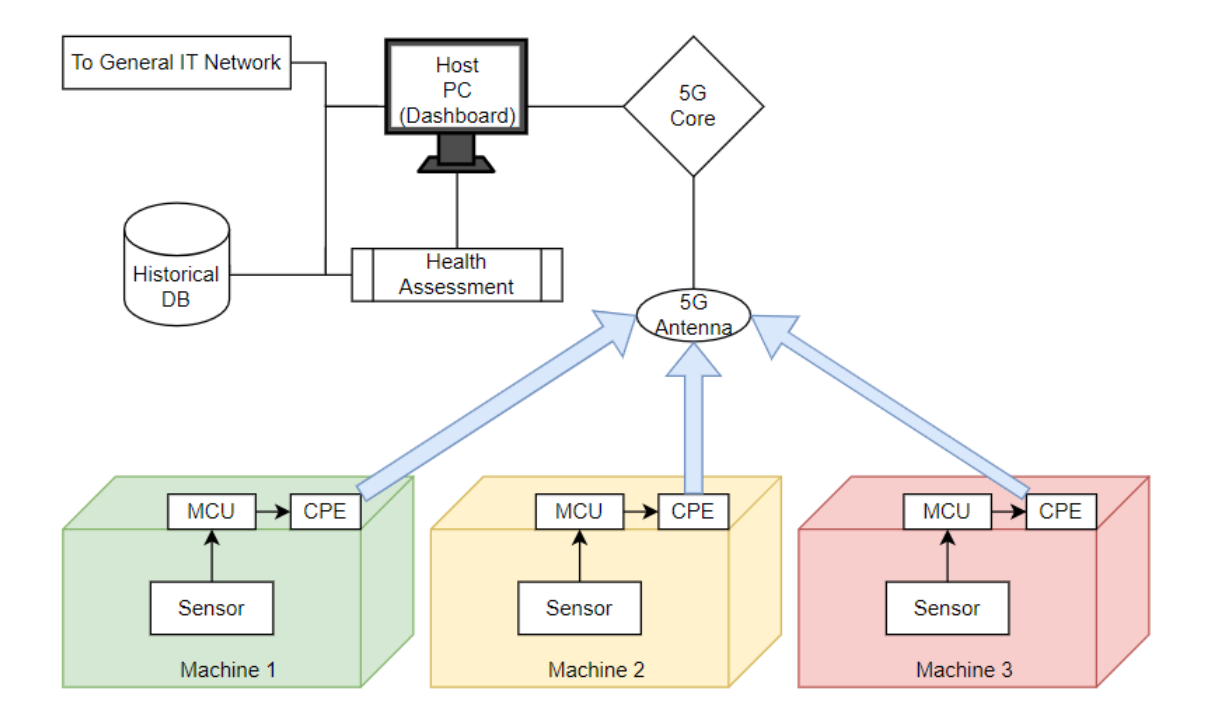


Figure 69: Network diagram, 5G sensors with server and database

Chapter 7: References

- 1. Thomas, D.S. and B. Weiss, *Maintenance Costs and Advanced Maintenance Techniques: Survey and Analysis*. International Journal of Prognostics and Health Management, 2021. **12**(1).
- 2. Tritschler, N.B., DEVELOPING A DEVICE FOR AUTOMATIC MONITORING OF ROLLING ELEMENT BEARING CONDITIONS, in Mechanical Engineering. 2019, Georgia Institute of Technology.
- 3. Ompusunggu, A.P., K. Janssen, and V. Dzyuba, *<Ompusunggu et al. -* 2019 Long-term vibration monitoring of induction motors.pdf>. HAL Open Science, 2019.
- 4. Ompusunggu, A.P., et al., Automated Bearing Fault Diagnostics with Cost-Effective Vibration Sensor, in Asset Intelligence through Integration and Interoperability and Contemporary Vibration Engineering Technologies. 2019. p. 463-472.
- 5. Ompusunggu, A.P., K. Eryılmaz, and K. Janssen, *Condition monitoring of critical industrial assets using high performing low-cost MEMS accelerometers*. Procedia CIRP, 2021. **104**: p. 1389-1394.
- 6. Failing, J.M., et al., A Tool Condition Monitoring System Based on Low-Cost Sensors and an IoT Platform for Rapid Deployment. Processes, 2023. **11**(3).
- 7. Chung, T.K., et al., An Attachable Electromagnetic Energy Harvester Driven Wireless Sensing System Demonstrating Milling-Processes and Cutter-Wear/Breakage-Condition Monitoring. Sensors (Basel), 2016. **16**(3): p. 269.
- 8. Zhou, C.a., et al., Development and testing of a wireless rotating triaxial vibration measuring tool holder system for milling process. Measurement, 2020. **163**.
- 9. Vogl, G.W., B.A. Weiss, and M.A. Donmez, *A Sensor-Based Method for Diagnostics of Machine Tool Linear Axes.* 2015.
- Nunes, P., J. Santos, and E. Rocha, Challenges in predictive maintenance

 A review. CIRP Journal of Manufacturing Science and Technology, 2023.

 40: p. 53-67.
- 11. Caroff, T.B., S.; Faucon, A.; Boness, A.; Arrizabalaga, A.S.; Ellinger, J., Ultra low power wireless multi-sensor platform dedicated to machine tool condition monitoring, in 30th International Conference on Flexible Automation and Intelligent Manufacturing (FAIM2021). 2020: Athens, Greece.
- 12. Xu, K., et al., *Advanced Data Collection and Analysis in Data-Driven Manufacturing Process*. Chinese Journal of Mechanical Engineering, 2020. **33**(1).

- 13. Mohamed, A., et al., *Tool Condition Monitoring for High-Performance Machining Systems-A Review.* Sensors (Basel), 2022. **22**(6).
- Mohanraj, T., et al., Tool condition monitoring techniques in milling process
 — a review. Journal of Materials Research and Technology, 2020. 9(1): p.
 1032-1042.
- 15. Nath, C., Integrated Tool Condition Monitoring Systems and Their Applications: A Comprehensive Review. Procedia Manufacturing, 2020. **48**: p. 852-863.
- 16. Pimenov, D.Y., et al., *Application of measurement systems in tool condition monitoring of Milling: A review of measurement science approach.*Measurement, 2022. **199**.
- 17. Shokrani, A., et al., Sensors for in-process and on-machine monitoring of machining operations. CIRP Journal of Manufacturing Science and Technology, 2024. **51**: p. 263-292.
- 18. Hassan, I.U., K. Panduru, and J. Walsh, *An In-Depth Study of Vibration Sensors for Condition Monitoring*. Sensors (Basel), 2024. **24**(3).
- 19. Vogl, G.W., B.C. Galfrond, and N.J. Jameson, *Bearing Metrics for Health Monitoring of Machine Tool Linear Axes*, in *ASME 2019 14th International Manufacturing Science and Engineering Conference*. 2019, American Society of Mechanical Engineers: Erie, Pennsylvania, USA.
- 20. Vogl, G.W. and M.E. Sharp, *Diagnostics of machine tool linear axes via separation of geometric error sources*, in *ANNUAL CONFERENCE OF THE PROGNOSTICS AND HEALTH MANAGEMENT SOCIETY*. 2017.
- 21. Vogl, G.W., et al., *Inertial Measurement Unit for On-Machine Diagnostics of Machine Tool Linear Axes*, in *Annual Conference of the PHM Society*. 2016.
- 22. Vogl, G.W., et al., A Sensor-based Method for Diagnostics of Geometric Performance of Machine Tool Linear Axes. Procedia Manufacturing, 2016. **5**: p. 621-633.
- 23. Ali, A. and A. Abdelhadi, *Condition-Based Monitoring and Maintenance:* State of the Art Review. Applied Sciences, 2022. **12**(2).
- 24. Wakiru, J.M., et al., *A review on lubricant condition monitoring information analysis for maintenance decision support.* Mechanical Systems and Signal Processing, 2019. **118**: p. 108-132.
- 25. Soto-Ocampo, C.R., et al., *Optimization of Low-Cost Data Acquisition Equipment Applied to Bearing Condition Monitoring.* Mathematics, 2023. **11**(16).
- 26. Marcocchio, A.V., Wireless Vibration Sensing with Local Signal Processing for Condition Monitoring within a Gas Turbine Engine, in Department of Automatic Control and Systems Engineering UTC. 2018, University of Sheffield.
- 27. Soto-Ocampo, C.R., et al., Low-Cost, High-Frequency, Data Acquisition System for Condition Monitoring of Rotating Machinery through Vibration Analysis-Case Study. Sensors (Basel), 2020. **20**(12).

- 28. Ahmed, H.E., et al., *Application of MEMS Accelerometers in Dynamic Vibration Monitoring of a Vehicle.* Micromachines (Basel), 2023. **14**(5).
- 29. Addabbo, T., et al., A Characterization System for Bearing Condition Monitoring Sensors, a Case Study with a Low Power Wireless Triaxial MEMS Based Sensor, in 2020 IEEE International Workshop on Metrology for Industry 4.0 & IoT. 2020: Roma, Italy.
- 30. Romanssini, M., et al., *A Review on Vibration Monitoring Techniques for Predictive Maintenance of Rotating Machinery.* Eng, 2023. **4**(3): p. 1797-1817.
- 31. Wu, T., et al., Research Status and Development Trend of Piezoelectric Accelerometer. Crystals, 2023. **13**(9).
- 32. Augustyn, D. and M. Fidali, *Identification and evaluation of the characteristics of a selected commercial mems based vibration sensor for the machine condition monitoring*. Diagnostyka, 2023. **24**(4): p. 1-8.
- 33. Bismor, D., Analysis and Comparison of Vibration Signals from Internal Combustion Engine Acquired Using Piezoelectric and MEMS Accelerometers. Vibrations in Physical Systems, 2019.
- 34. Albarbar, A., et al., Suitability of MEMS Accelerometers for Condition Monitoring: An experimental study. MPDI Sensors, 2008(8): p. 784-799.
- 35. Albarbar, A. and S.H. Teay, MEMS Accelerometers: Testing and Practical Approach for Smart Sensing and Machinery Diagnostics, in Advanced Mechatronics and MEMS Devices II. 2017. p. 19-40.
- 36. D'Emilia, G. and E. Natale, *Use of MEMS sensors for condition monitoring of devices: discussion about the accuracy of features for diagnosis.*International Journal of Metrology and Quality Engineering, 2021. **12**.
- 37. Lynch, J.P., et al., *Design of Piezoresistive MEMS-Based Accelerometer* for Integration with Wireless Sensing Unit for Structural Monitoring. Journal of Aerospace Engineering, 2003. **16**(3): p. 108-114.
- 38. Albarbar, A., et al., *Performance evaluation of MEMS accelerometers*. Measurement, 2009. **42**(5): p. 790-795.
- 39. Komarizadehasl, S., et al., *Development of a Low-Cost System for the Accurate Measurement of Structural Vibrations*. Sensors (Basel), 2021. **21**(18).
- 40. Hasani, H., et al., A Wireless Data Acquisition System Based on MEMS Accelerometers for Operational Modal Analysis of Bridges. Sensors (Basel), 2024. **24**(7).
- 41. Varanis, M., et al., *MEMS accelerometers for mechanical vibrations analysis: a comprehensive review with applications.* Journal of the Brazilian Society of Mechanical Sciences and Engineering, 2018. **40**(11).
- 42. Teay, S.H. and A. Albarbar, *Adoption of MEMS technology in e-maintenance systems for rotating machinery.* Insight Non-Destructive Testing and Condition Monitoring, 2017. **59**(12): p. 659-668.
- 43. Bleicher, F., et al., Sensor and actuator integrated tooling systems. CIRP Annals, 2023/01/01. **72**(2).

- 44. Instuments, N. Acquiring an Analog Signal: Bandwidth, Nyquist Sampling Theorem, and Aliasing. 2025; Available from:

 https://www.ni.com/en/shop/data-acquisition/measurement-fundamentals/analog-fundamentals/acquiring-an-analog-signal-bandwidth--nyquist-sampling-theorem-.html.
- 45. Stakhova, A., *Analysis of the influence of final resolution on ADC accuracy.* 2023.
- 46. Kistler. Sampling rate and aliasing effect. Available from: https://www.kistler.com/US/en/sampling-rate-and-aliasing-effect/C00000151.
- 47. Instruments, N. *Anti-Aliasing Filters and Their Usage Explained*. 2025; Available from: https://www.ni.com/en/shop/data-acquisition/measurement-fundamentals/analog-fundamentals/anti-aliasing-filters-and-their-usage-explained.html.
- 48. Pachchigar, M. *Increase Dynamic Range of SAR ADCs Using Oversampling*. 2015; Available from:
 https://www.analog.com/en/resources/technical-articles/increase-dynamic-range-of-sar-adcs-using-oversampling.html.
- 49. Di Zeo, A.T., *A Wireless Sensor Network for Machine Dynamics Performance Monitoring*. 2019, Delft University of Technology.
- 50. Uhlmann, E., et al., *Decentralized Data Analytics for Maintenance in Industrie 4.0.* Procedia Manufacturing, 2017. **11**: p. 1120-1126.
- 51. Uhlmann, E., et al., SMART WIRELESS SENSOR NETWORK AND CONFIGURATION OF ALGORITHMS FOR CONDITION MONITORING APPLICATIONS. Journal of Machine Engineering, 2017. **17**(2): p. 45-55.
- 52. Koene, I., V. Klar, and R. Viitala, *IoT connected device for vibration analysis and measurement*. HardwareX, 2020. **7**: p. e00109.
- 53. Crognale, M., et al., *Developing and Testing High-Performance SHM Sensors Mounting Low-Noise MEMS Accelerometers.* Sensors (Basel), 2024. **24**(8).
- 54. Caballero-Russi, D., et al., *Design and Validation of a Low-Cost Structural Health Monitoring System for Dynamic Characterization of Structures*.

 Applied Sciences, 2022. **12**(6): p. 2807.
- 55. Koene, I., R. Viitala, and P. Kuosmanen, *Internet of Things Based Monitoring of Large Rotor Vibration With a Microelectromechanical Systems Accelerometer.* IEEE Access, 2019. **7**: p. 92210-92219.
- 56. Hsiao, S.-J., *Employing a Wireless Sensing Network for AloT Based on a 5G Approach.* Electronics, 2022. **11**(5).
- 57. Kurfess, T.R., et al., A Review of Modern Communication Technologies for Digital Manufacturing Processes in Industry 4.0. Journal of Manufacturing Science and Engineering, 2020. **142**(11): p. 1-38.
- 58. Tang, X., et al., Energy Harvesting Technologies for Achieving Self-Powered Wireless Sensor Networks in Machine Condition Monitoring: A Review. Sensors (Basel), 2018. **18**(12).

- 59. Wang, S., et al., Wireless Sensor Network Technology for Vibration Condition Monitoring of Mechanical Equipment. Electrica, 2023.
- 60. Jakobsen, M.O., Low cost MEMS accelerometer and microphone based condition monitoring sensor, with LoRa and Bluetooth Low Energy radio. HardwareX, 2024. **18**: p. e00525.
- 61. Zhang, X.Y., et al., *A multi-sensor based online tool condition monitoring system for milling process.* Procedia CIRP, 2018. **72**: p. 1136-1141.
- 62. Niestoruk, L., et al., A Simplified Protocol for Energy Self-Sufficient Sensors in an IEEE 802.15.4/ZigBee WSN. 2009.
- 63. Varga, P., et al., 5G support for Industrial IoT Applications Challenges, Solutions, and Research gaps. Sensors (Basel), 2020. **20**(3).
- 64. Ludwig, S., et al., A 5G Architecture for The Factory of the Future. 2018.
- 65. Sachs, J. and K. Landernas, Review of 5G capabilities for smart manufacturing, in 2021 17th International Symposium on Wireless Communication Systems (ISWCS). 2021. p. 1-6.
- 66. Rodrigues, J.V.O., et al., *Performance evaluation of accelerometers ADXL345 and MPU6050 exposed to random vibrational input.* Research, Society and Development, 2021. **10**(15).
- 67. Schiavi, A., et al., Calibration of a multicomponent MEMS sensor for vibration monitoring of rolling bearings: broad-band and amplitude traceability up to 20 kHz, in 2022 IEEE International Workshop on Metrology for Industry 4.0 & IoT (MetroInd4.0&IoT). 2022. p. 229-233.
- 68. Sharma, G., et al., *MEMS Approach for Rolling Bearing Fault Diagnosis Using Vibration Signal Analysis.* Journal of Vibration Engineering & Technologies, 2025. **13**(1).
- 69. Hurtado Carreon, A., et al., *CNC linear axis condition-based monitoring: a statistics-based framework to establish a baseline dataset and case study.*Journal of Intelligent Manufacturing, 2024.
- 70. Hurtado Carreon, A., J.M. DePaiva, and S.C. Veldhuis, *Comprehensive health assessment of faulty and repaired linear axis components through multi-sensor monitoring.* The International Journal of Advanced Manufacturing Technology, 2024. **132**(11-12): p. 5487-5501.
- 71. Hurtado Carreon, A., J.M. DePaiva, and S.C. Veldhuis, *Linear Axis Guide Rail Misalignment Detection and Localization Using a Novel Signal Segmentation Analysis Technique.* Applied Sciences, 2024. **14**(6).
- 72. Koene, I., et al., On-Shaft Wireless Vibration Measurement Unit and Signal Processing Method for Torsional and Lateral Vibration. IEEE/ASME Transactions on Mechatronics, 2022. **27**(6): p. 5857-5868.
- 73. Ghazali, M.H.M. and W. Rahiman, Real-Time Vibration Monitoring Using MEMS Vibration Sensors, in Proceedings of the 11th International Conference on Robotics, Vision, Signal Processing and Power Applications. 2022. p. 356-362.
- 74. Holovatyy, A., et al., *Development of a system for monitoring vibration accelerations based on the raspberry pi microcomputer and the ADXL345*

- accelerometer. Eastern-European Journal of Enterprise Technologies, 2017. **6**(9 (90)): p. 52-62.
- 75. Kumaravel, B.T., et al., Development of an Internet of Things enabled Manufacturing system for tool wear characterization, in 2017 IEEE 3rd International Symposium on Robotics and Manufacturing Automation (ROMA). 2017.
- 76. InvenSense, T., ICM-42688-P Datasheet. 2023, TDK InvenSense.
- 77. Devices, A., *EVAL-ADXL356/EVAL-ADXL357 User Guide*. 2019, Analog Devices.
- 78. Villarroel, A., G. Zurita, and R. Velarde, *Development of a Low-Cost Vibration Measurement System for Industrial Applications*. Machines, 2019. **7**(1).
- 79. Ostasevicius, V., et al., *Monitoring the condition of the cutting tool using self-powering wireless sensor technologies.* The International Journal of Advanced Manufacturing Technology, 2016. **88**(9-12): p. 2803-2817.
- 80. Ostasevicius, V., et al., *Self-powering wireless devices for cloud manufacturing applications*. The International Journal of Advanced Manufacturing Technology, 2015. **83**(9-12): p. 1937-1950.
- 81. Ostasevicius, V., et al., *Cutting tool vibration energy harvesting for wireless sensors applications.* Sensors and Actuators A: Physical, 2015. **233**: p. 310-318.
- 82. Devices, A., *Data Sheet ADXL356/ADXL357/ADXL357B*. 2024, Analog Devices.
- 83. *Guidelines for Mounting Test Accelerometers*. [cited 2025 4/07/25]; Available from: https://www.pcb.com/resources/technical-information/mounting.
- 84. Piezoelectronics, P., *Model 394C06 Installation and Operating Manual*. 2018, Analog Devices.
- 85. Devices, A., Data Sheet ADXL345. 2022, Analog Devices.
- 86. Uhlmann, E., et al., *Condition Monitoring in the Cloud.* Procedia CIRP, 2015. **38**: p. 53-57.
- 87. Xuan, J., et al., A Review on the Inertial Measurement Unit Array of Microelectromechanical Systems. Sensors, 2024. **24**(22): p. 7140.
- 88. Blocher, L., et al. *Purely Inertial Navigation with a Low-Cost MEMS Sensor Array.* in 2021 IEEE International Symposium on Inertial Sensors and Systems (INERTIAL). 2021. IEEE.
- 89. Wang, L., et al., *Improving the Navigation Performance of the MEMS IMU Array by Precise Calibration*. IEEE Sensors Journal, 2021. **21**(22): p. 26050-26058.

Chapter 8: Appendix

8.1 Test 1 Graphs

Below, the appendix includes the plots from test 1 for each sensor and measurement range. Each figure includes the five samples in the time domain, the corresponding frequency spectrum obtained using an FFT, a zoomed-in view around the first frequency peak, and another zoomed-in view but with a Hanning windowed FFT.

8.1.1 ADXL-345 – Bolt Mounted, USB Powered, 1 g RMS

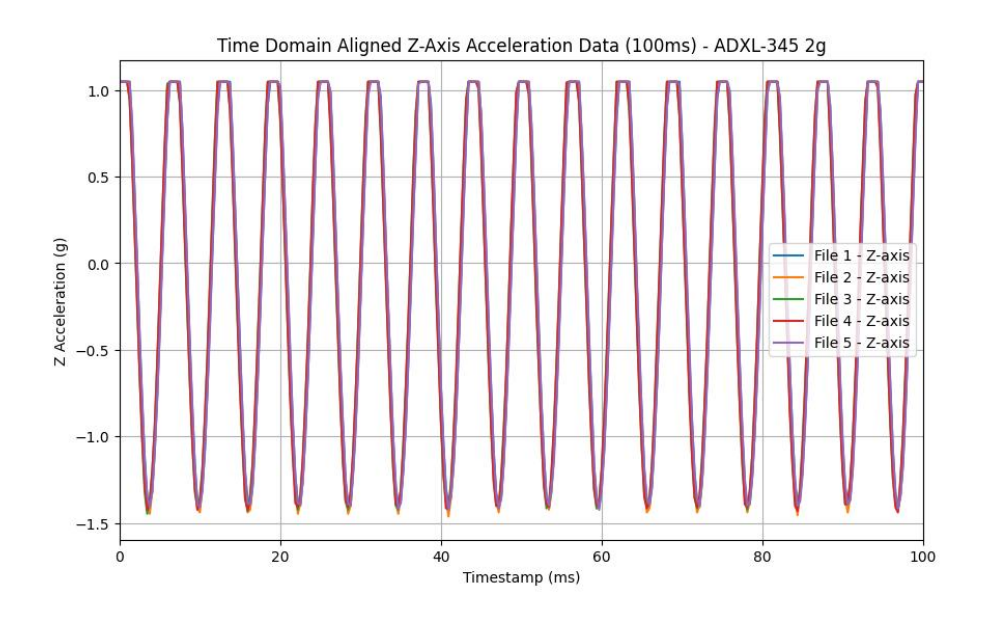


Figure 70: ADXL-345 2 g Time-domain plot

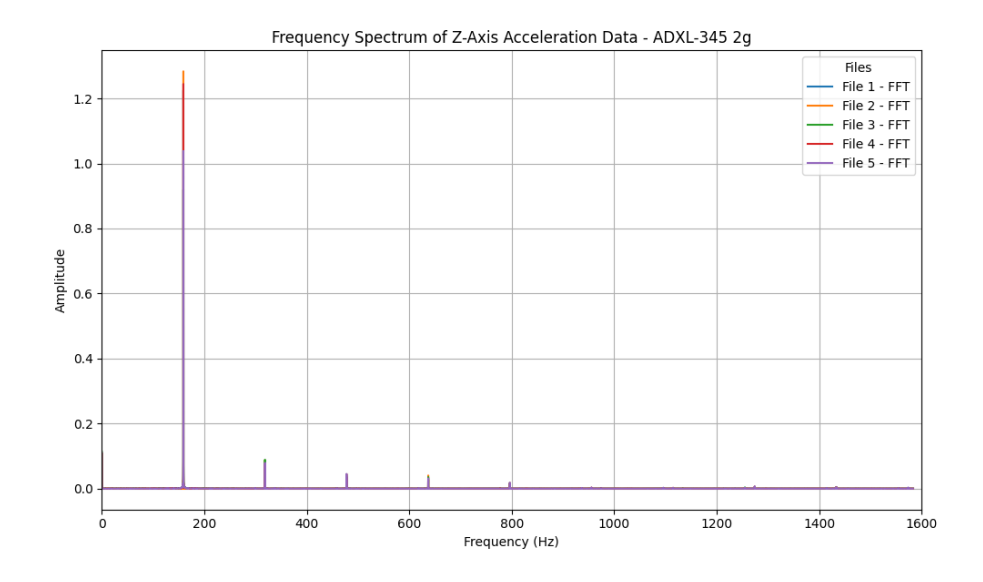


Figure 71: ADXL-345 2 g Frequency-domain plot

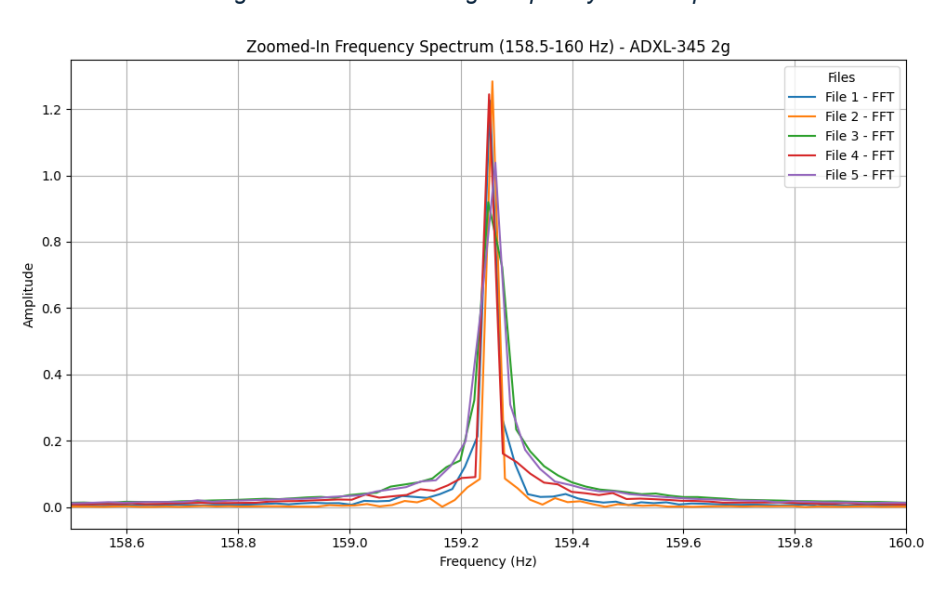


Figure 72: ADXL-345 2 g Frequency-domain plot peak

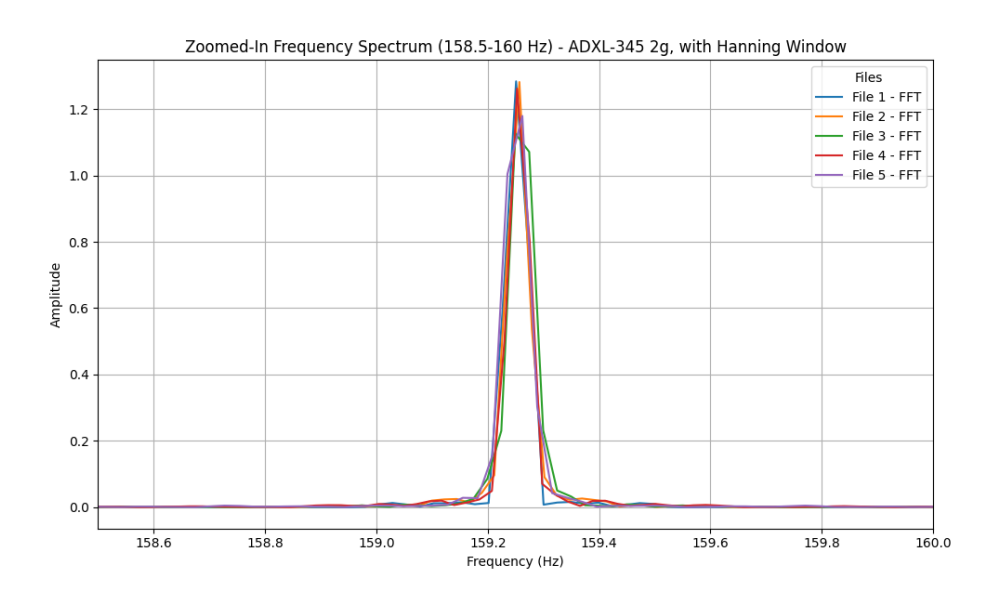


Figure 73: ADXL-345 2 g Frequency-domain plot peak windowed

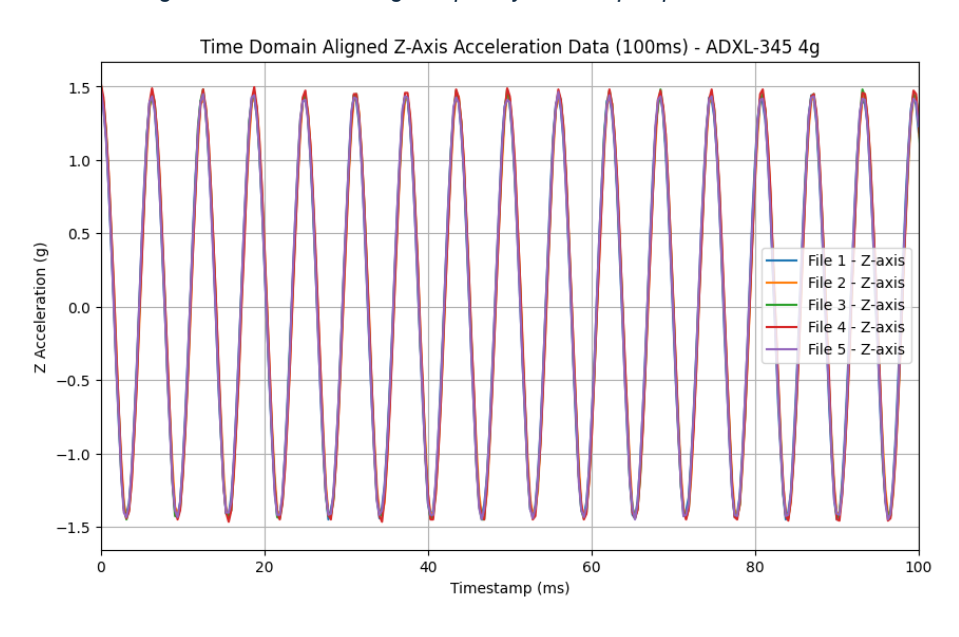


Figure 74: ADXL-345 4 g Time-domain plot

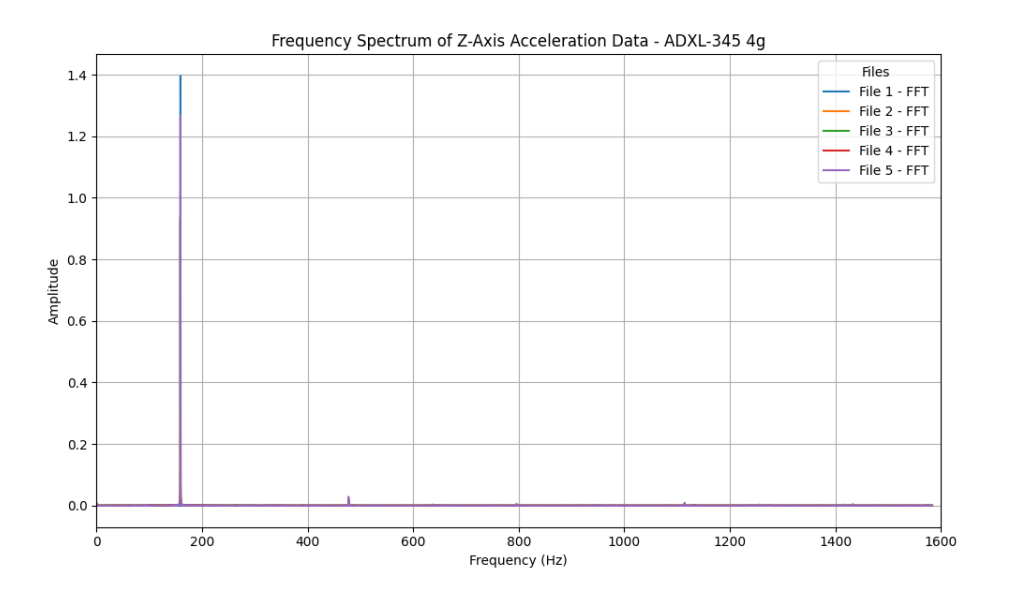


Figure 75: ADXL-345 4 g Frequency-domain plot

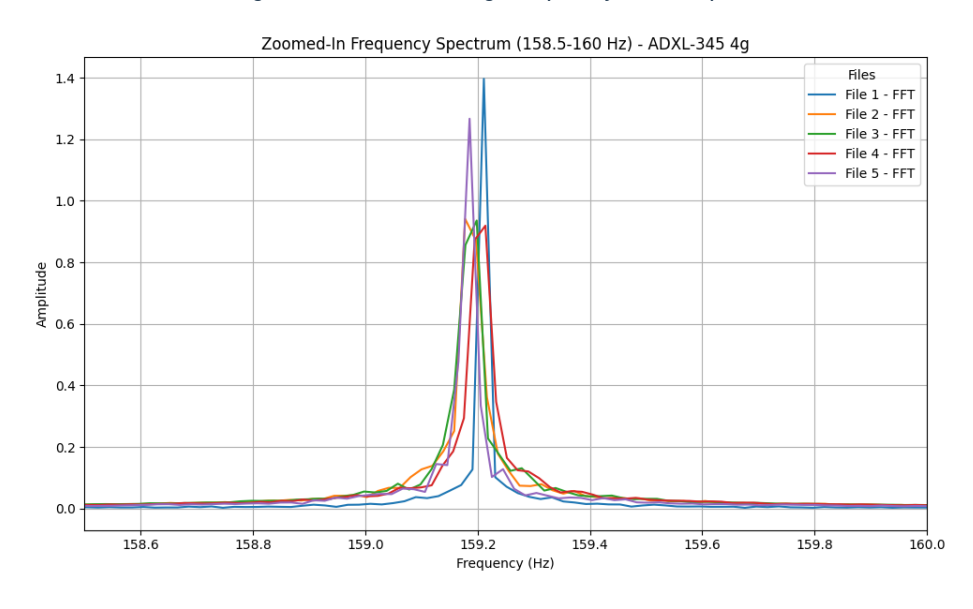


Figure 76: ADXL-345 4 g Frequency-domain plot peak

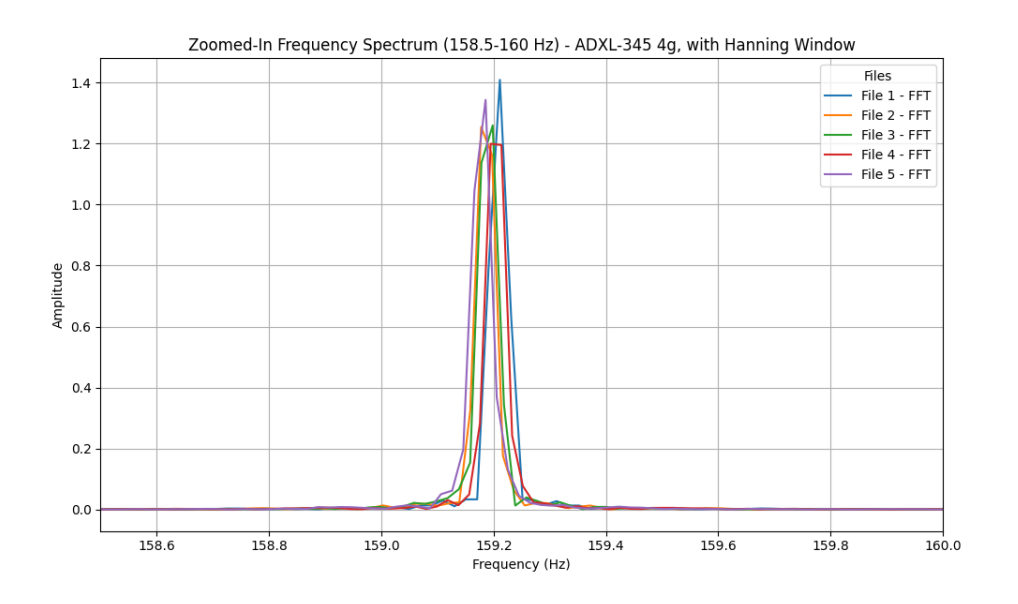


Figure 77: ADXL-345 4 g Frequency-domain plot peak windowed

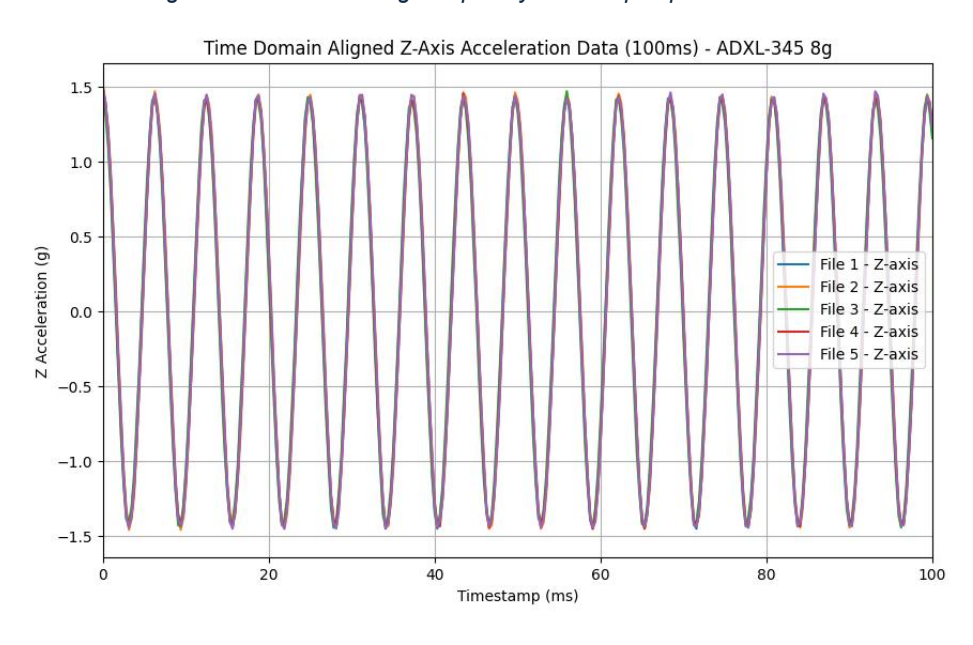


Figure 78: ADXL-345 8 g Time-domain plot

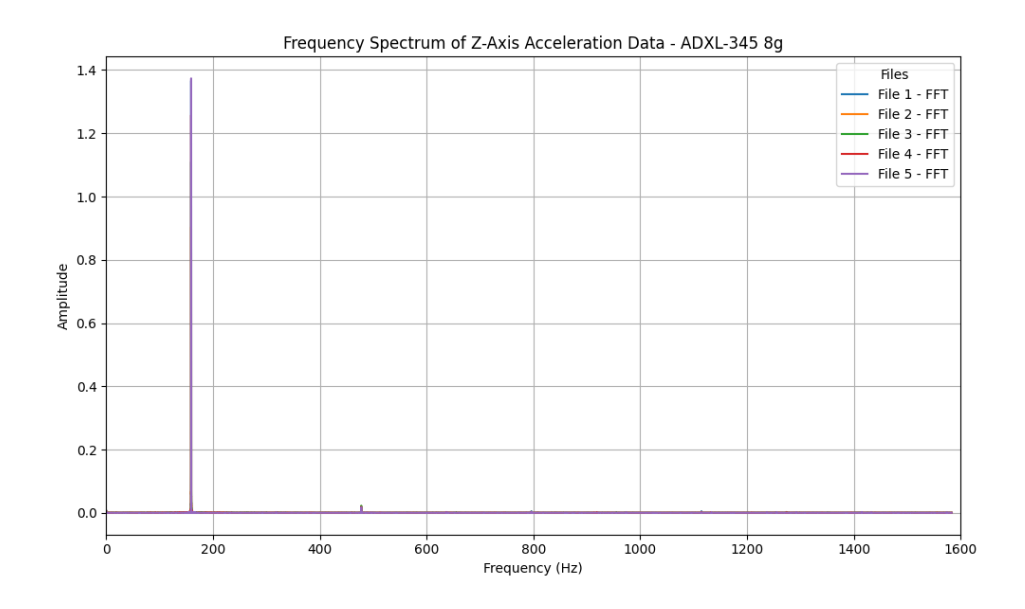


Figure 79: ADXL-345 8 g Frequency-domain plot

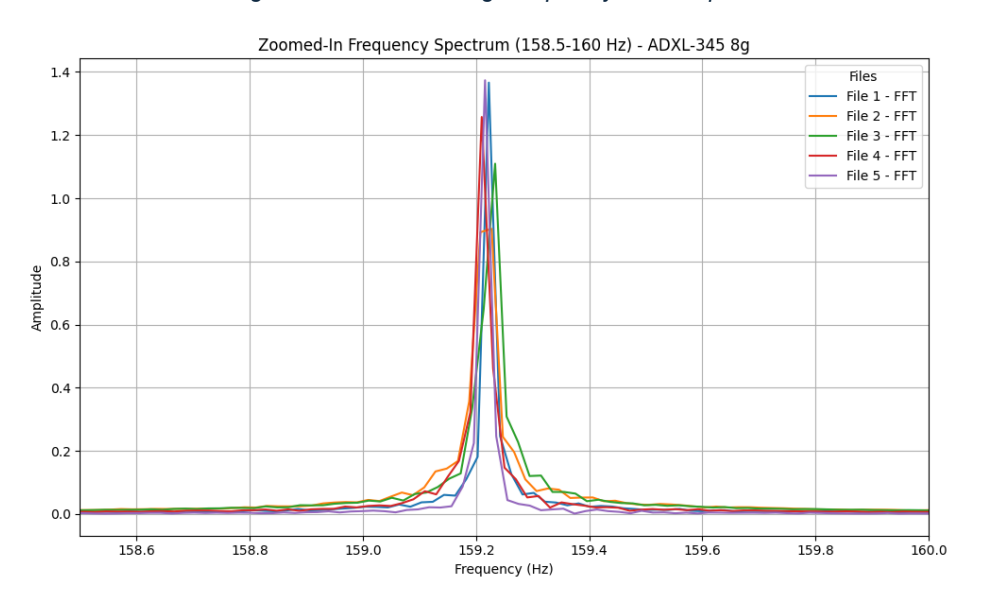


Figure 80: ADXL-345 8 g Frequency-domain plot peak

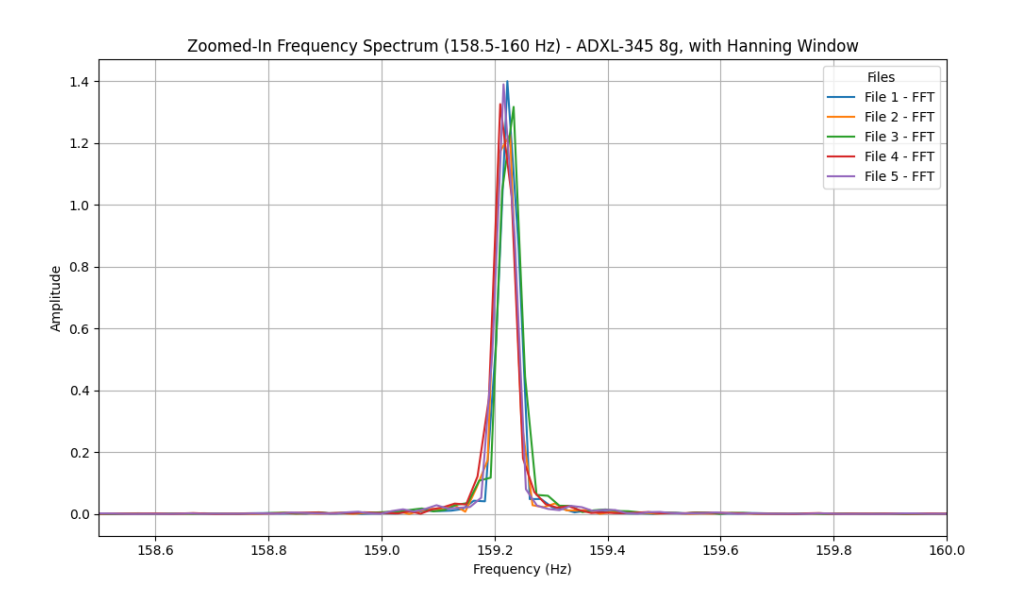


Figure 81: ADXL-345 8 g Frequency-domain plot peak windowed

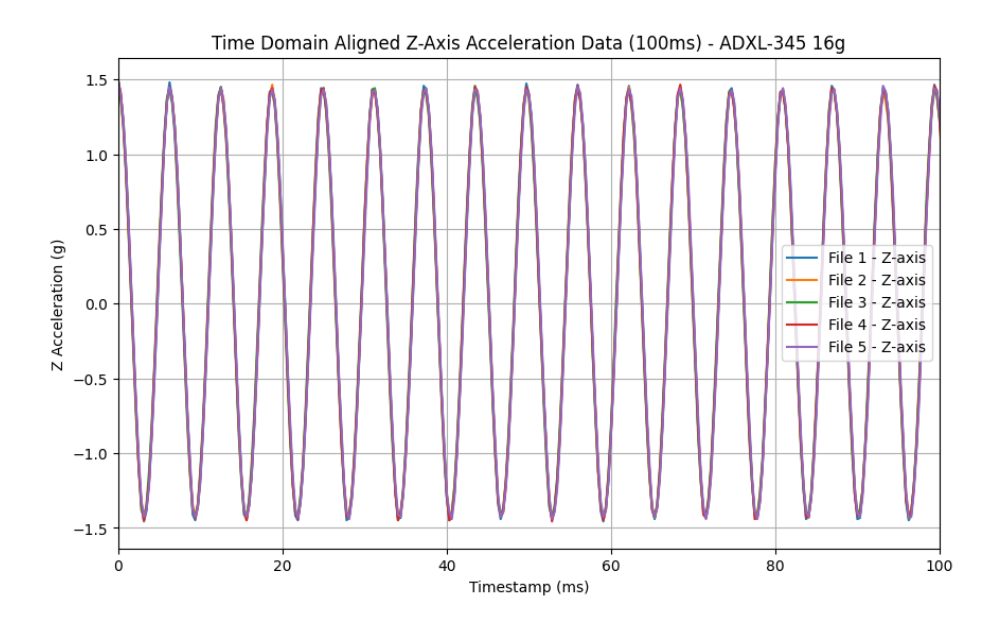


Figure 82: ADXL-345 16 g Time-domain plot

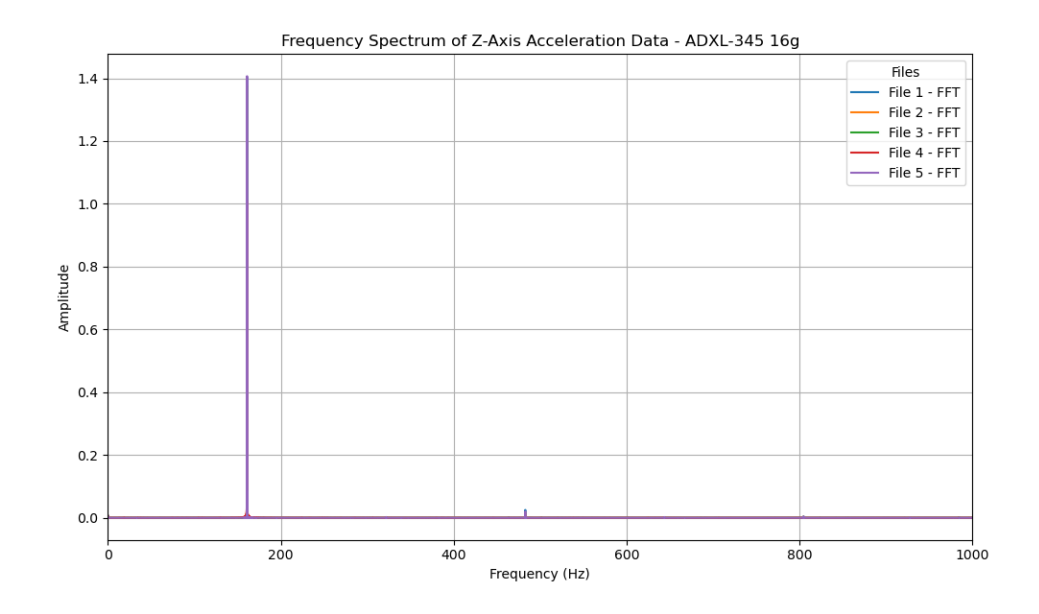


Figure 83: ADXL-345 16 g Frequency-domain

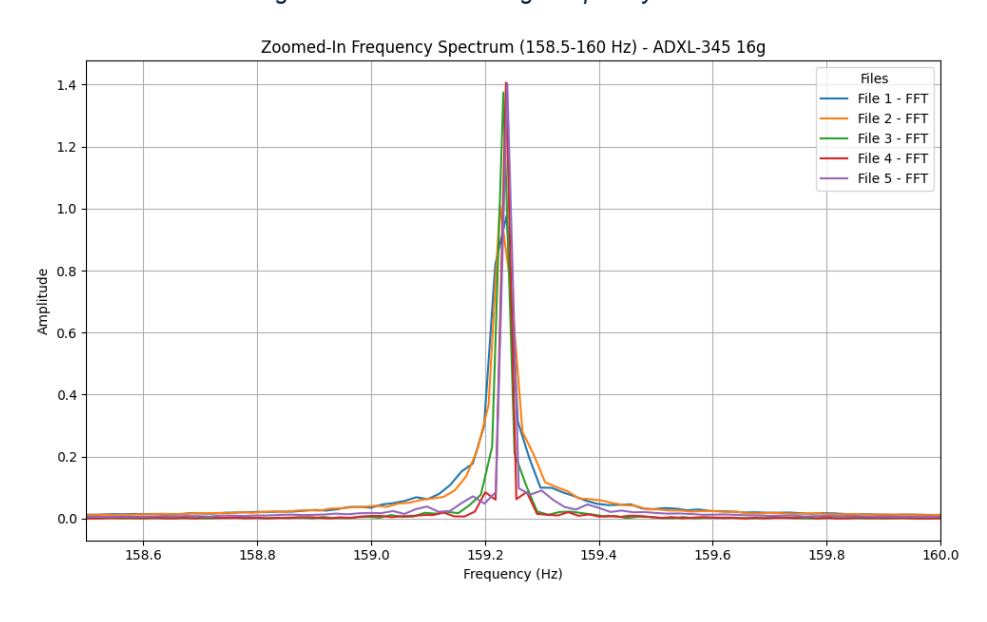


Figure 84: ADXL-345 16 g Frequency-domain plot peak

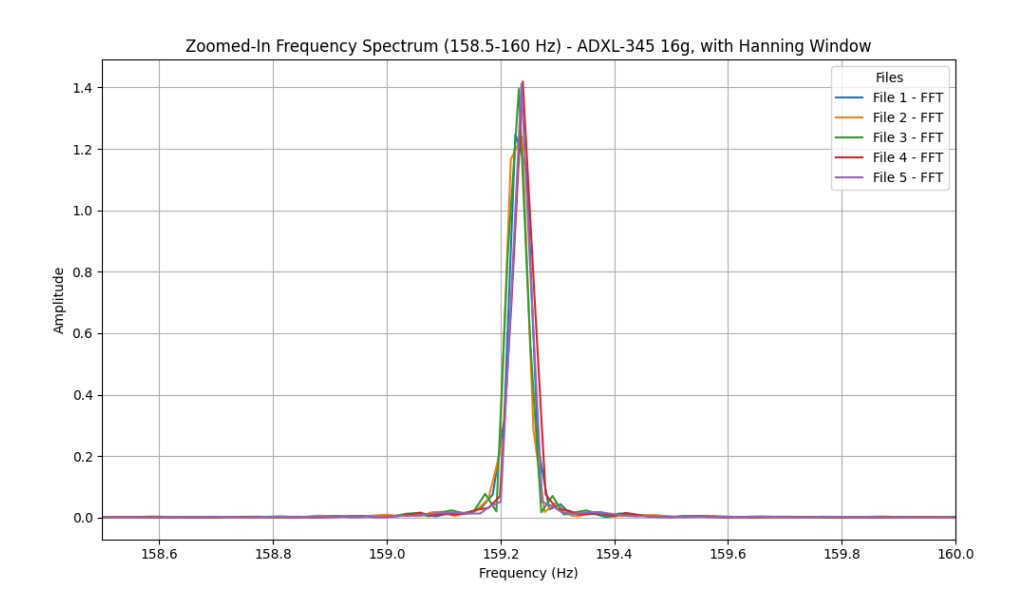


Figure 85: ADXL-345 16 g Frequency-domain plot peak windowed

8.1.2 ADXL-357 - Bolt Mounted, USB Powered, 1 g RMS

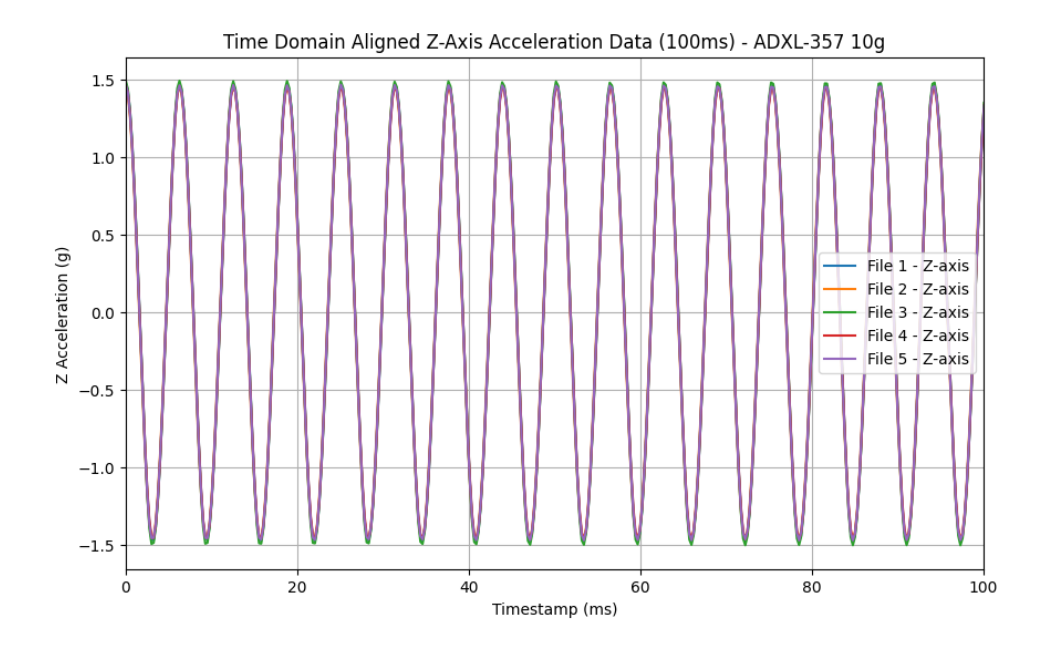


Figure 86: ADXL-357 10 g Time-domain plot

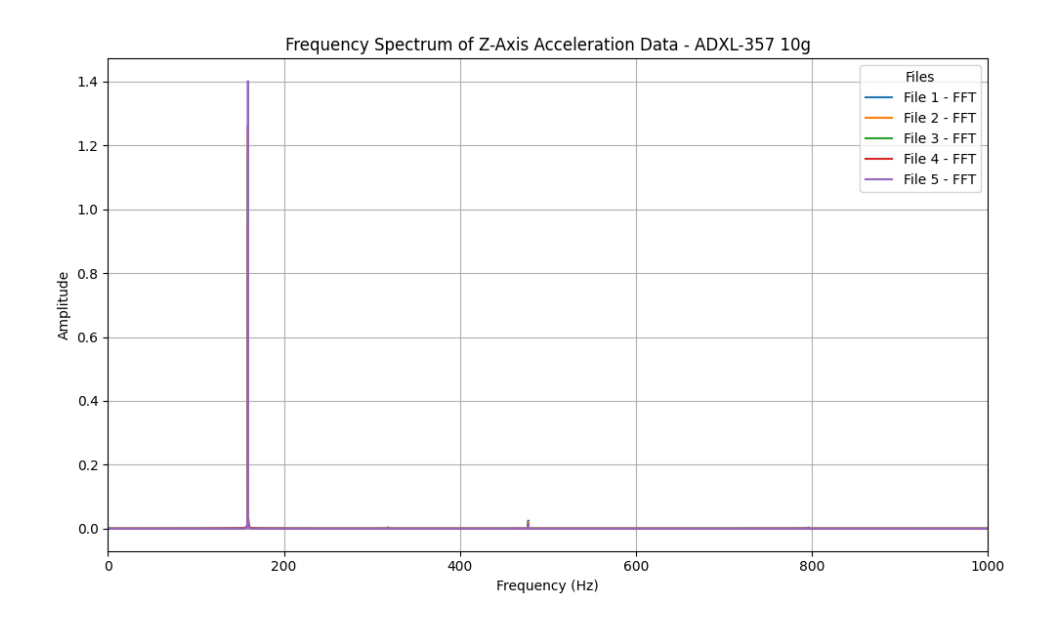


Figure 87: ADXL-357 10 g Frequency-domain plot

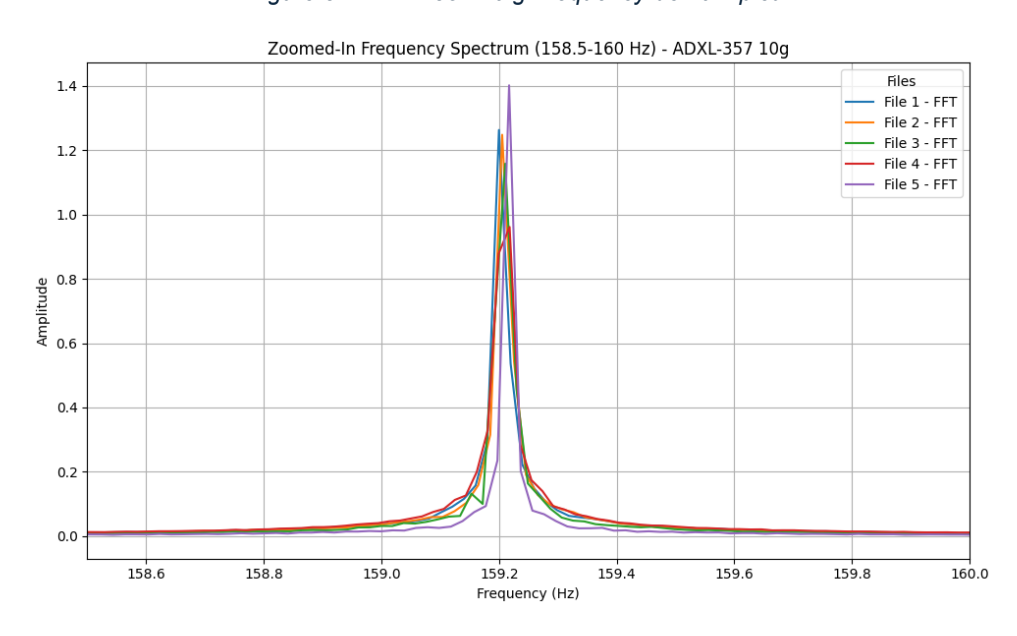


Figure 88: ADXL-357 10 g Frequency-domain plot peak

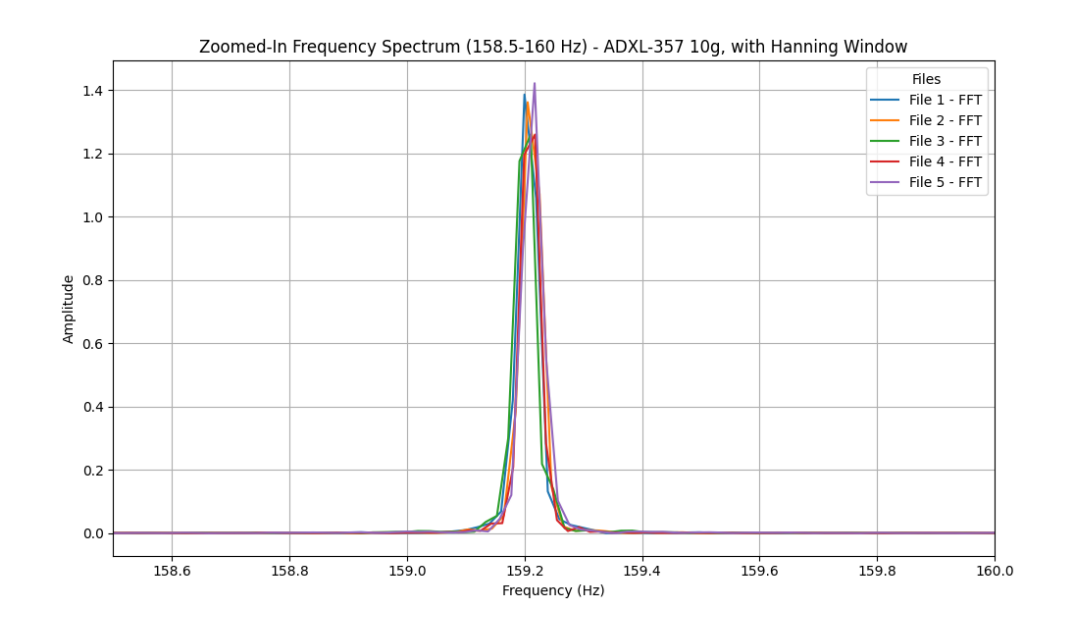


Figure 89: ADXL-357 10 g Frequency-domain plot peak windowed

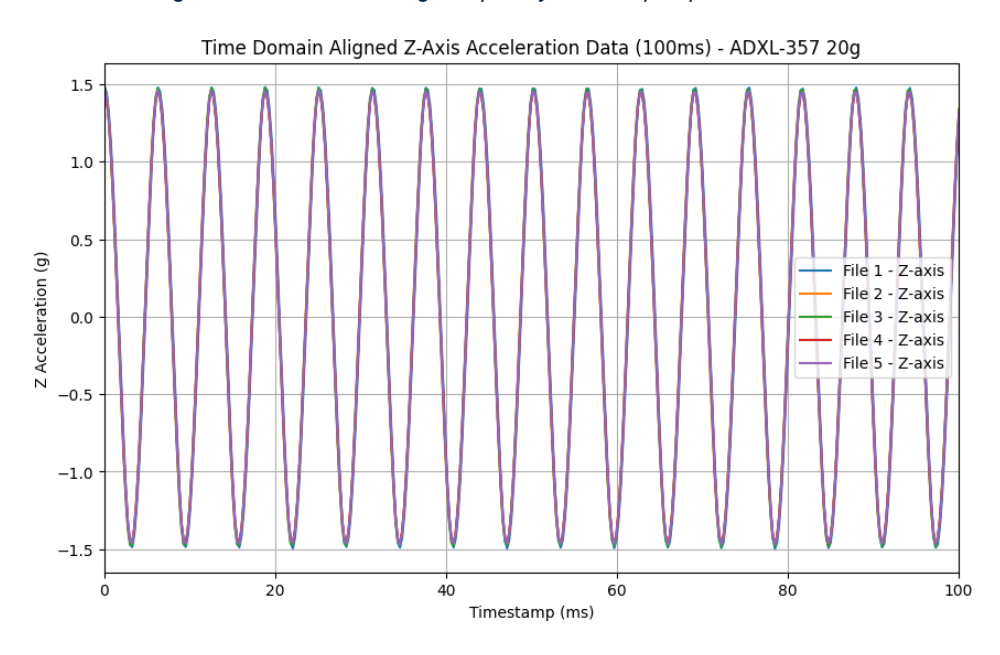


Figure 90: ADXL-357 20 g Time-domain plot

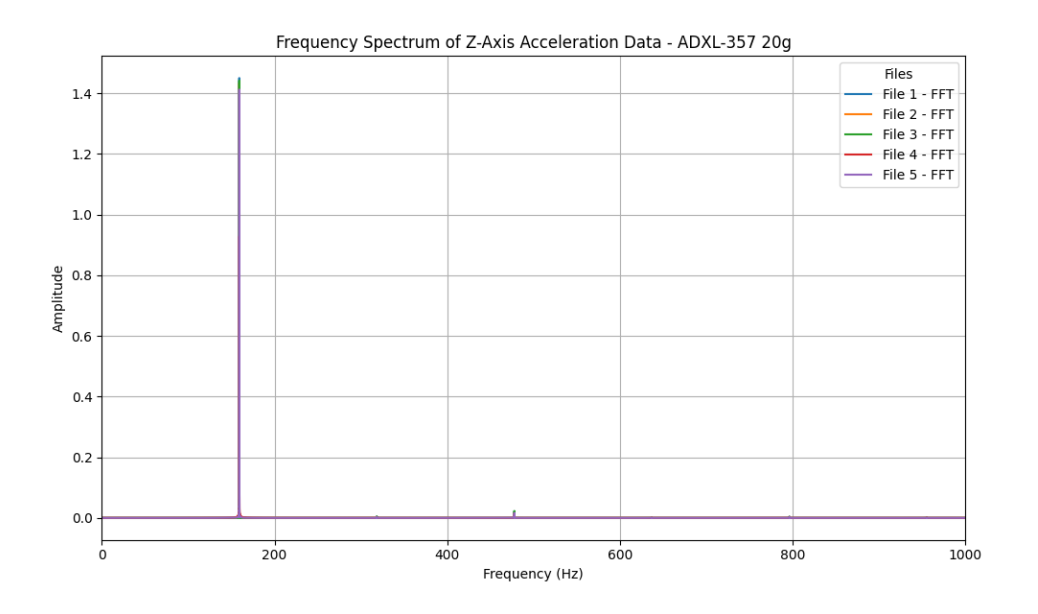


Figure 91: ADXL-357 20 g Frequency-domain plot

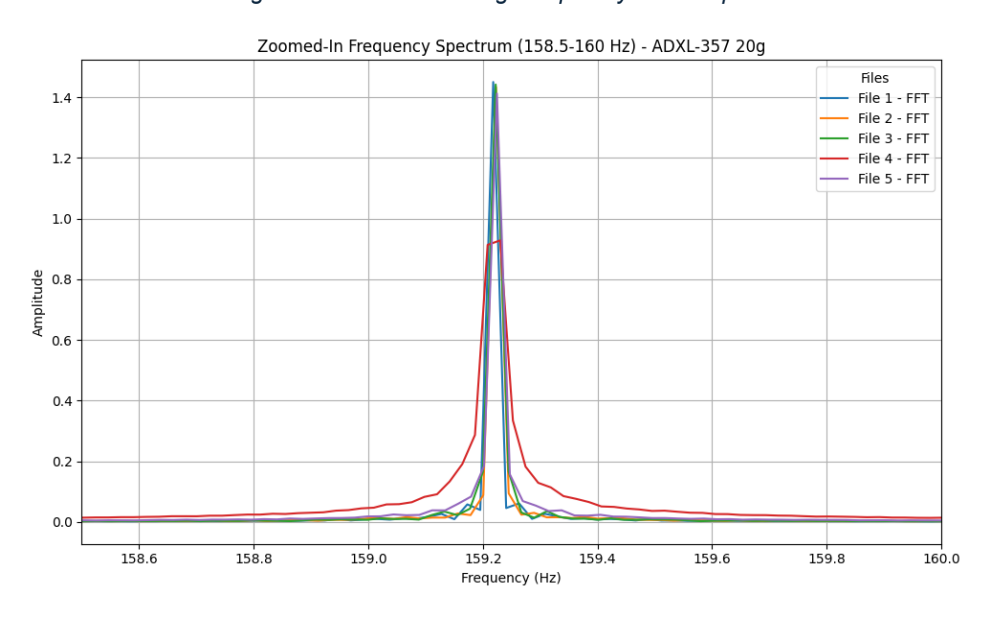


Figure 92: ADXL-357 20 g Frequency-domain plot peak

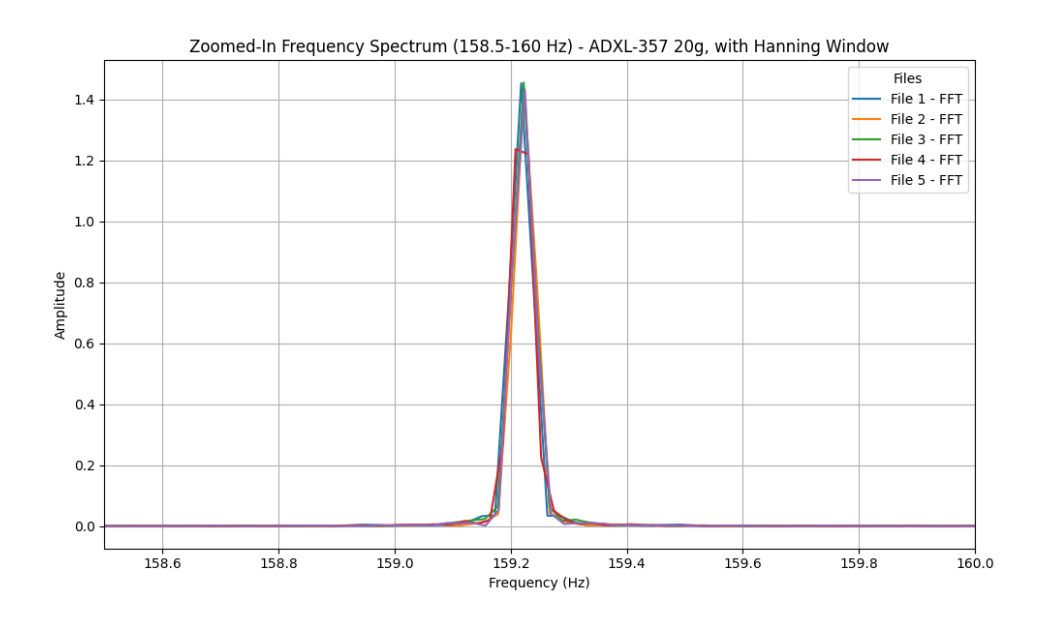


Figure 93: ADXL-357 20 g Frequency-domain plot peak windowed

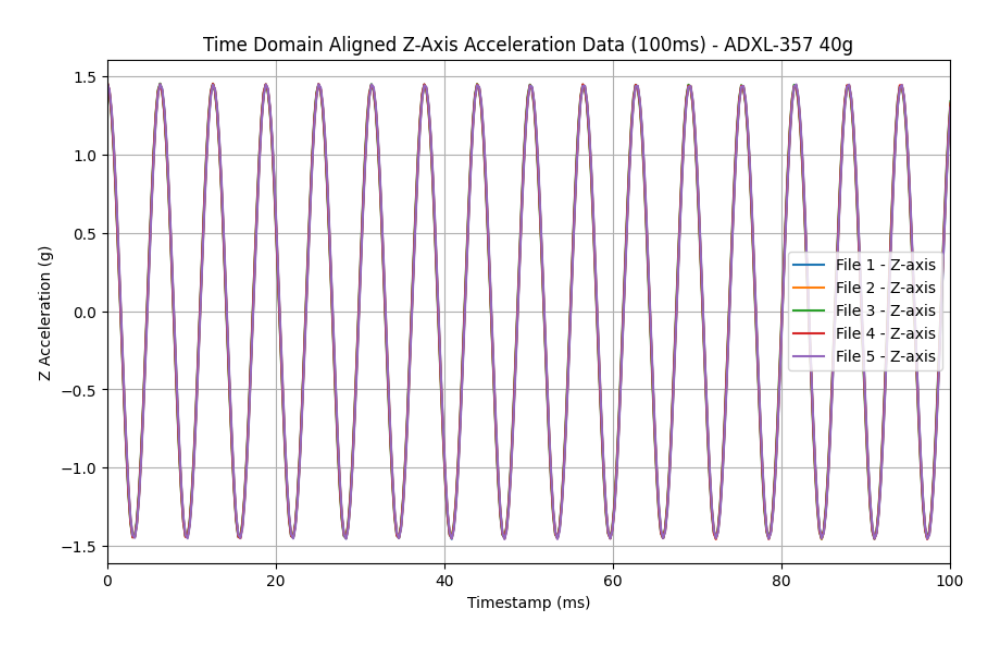


Figure 94: ADXL-357 40 g Time-domain plot

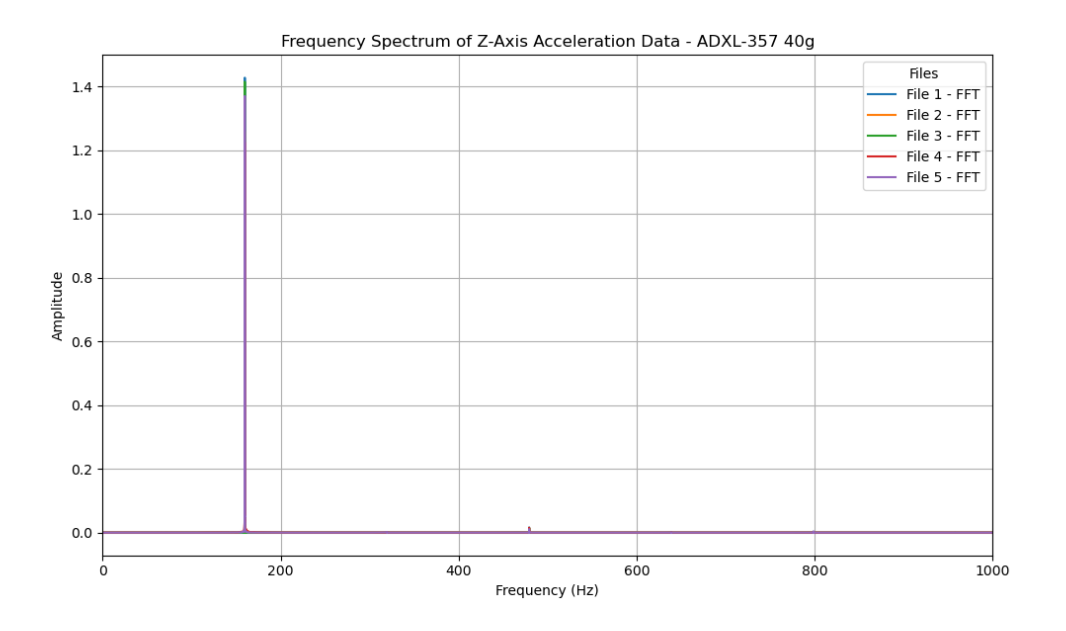


Figure 95: ADXL-357 40 g Frequency-domain plot

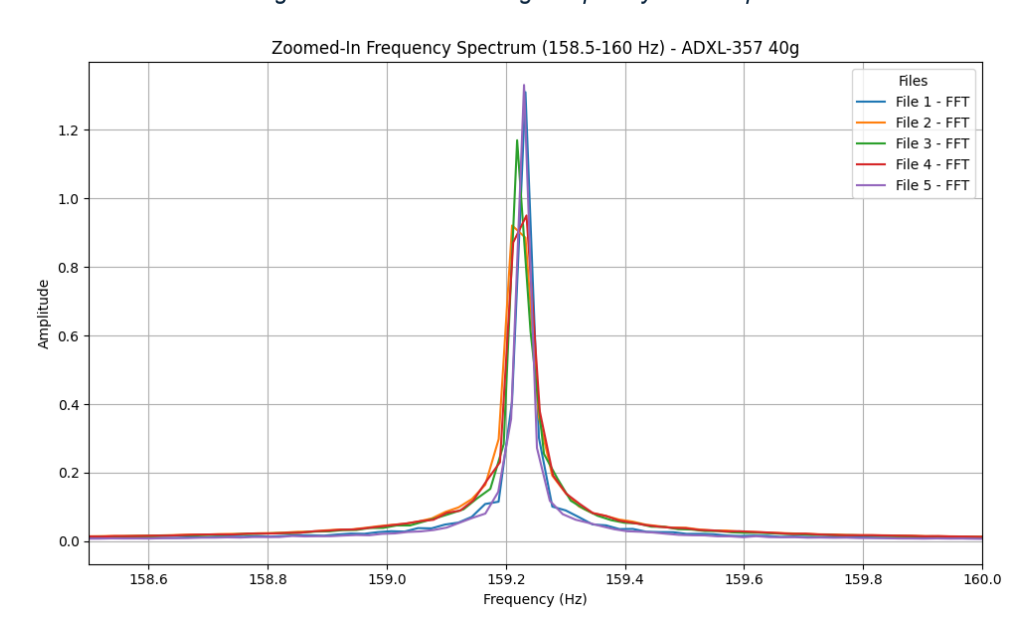


Figure 96: ADXL-357 40 g Frequency-domain plot peak

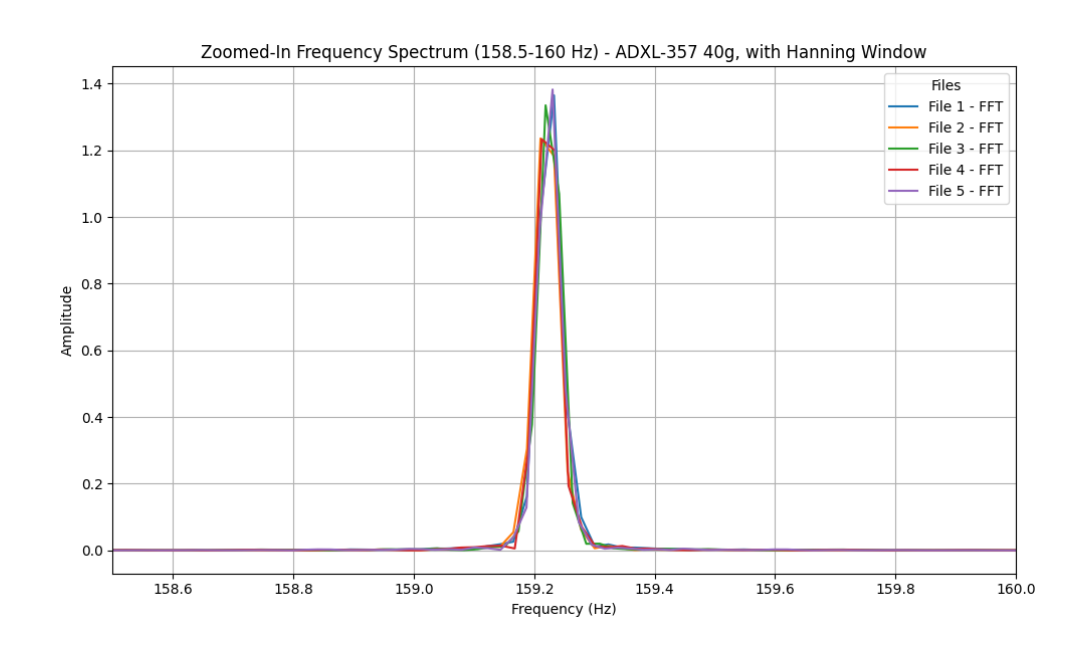


Figure 97: ADXL-357 40 g Frequency-domain plot peak windowed

8.1.3 ADXL-357 – Magnet Mounted, Battery Powered

8.1.3.1 1 g RMS

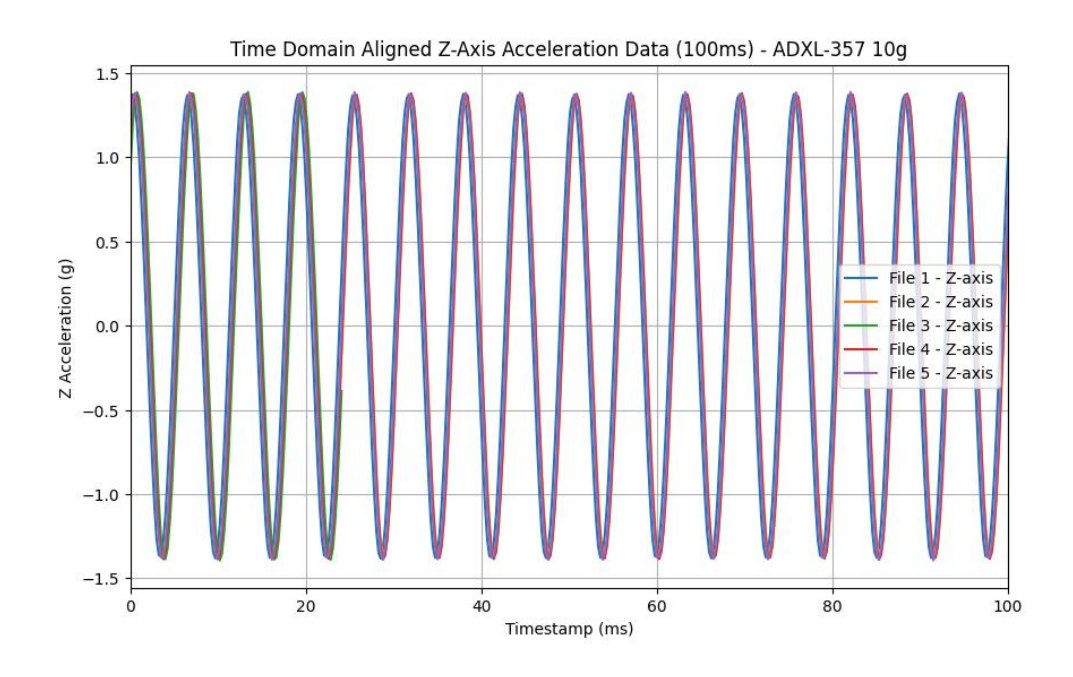


Figure 98: ADXL-357 magnet mounted 10 g Time-domain plot 1 g RMS

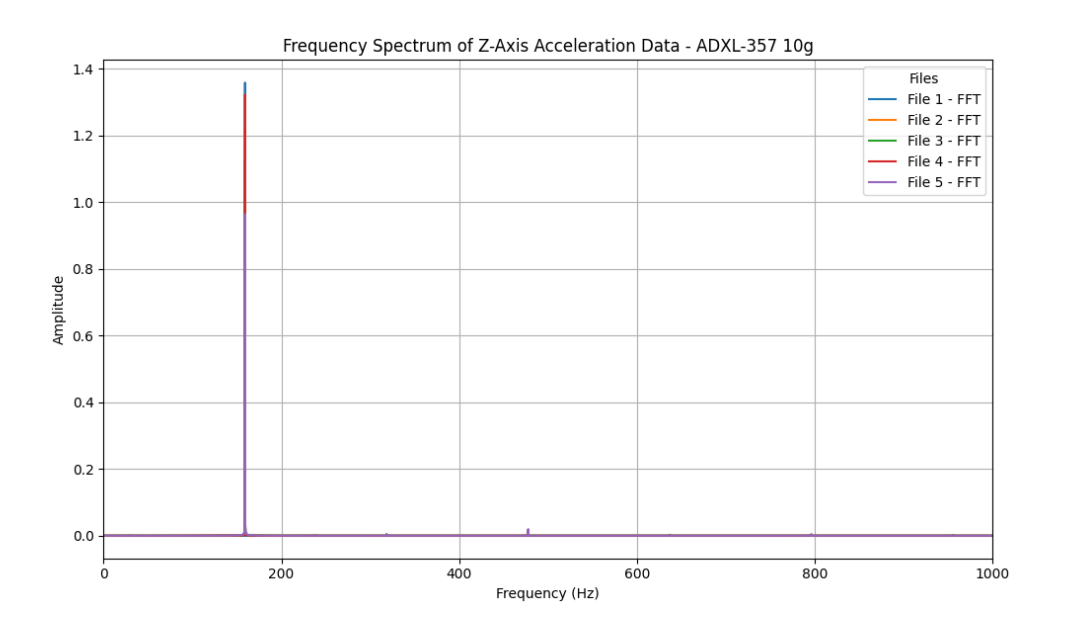


Figure 99: ADXL-357 magnet mounted 10 g Frequency-domain plot 1 g RMS

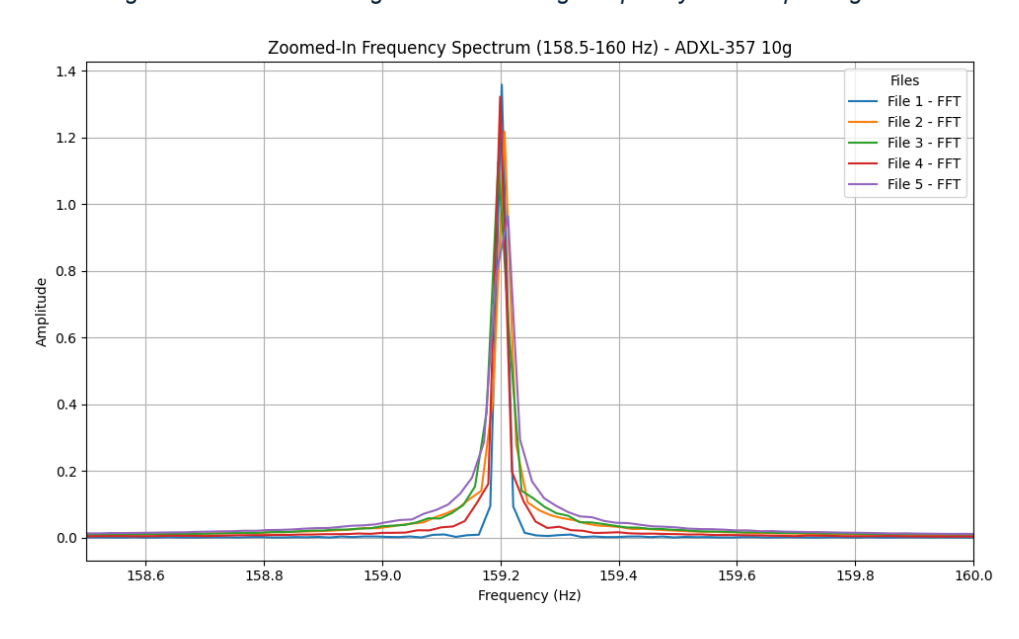


Figure 100: ADXL-357 magnet mounted 10 g Frequency-domain plot peak 1 g RMS

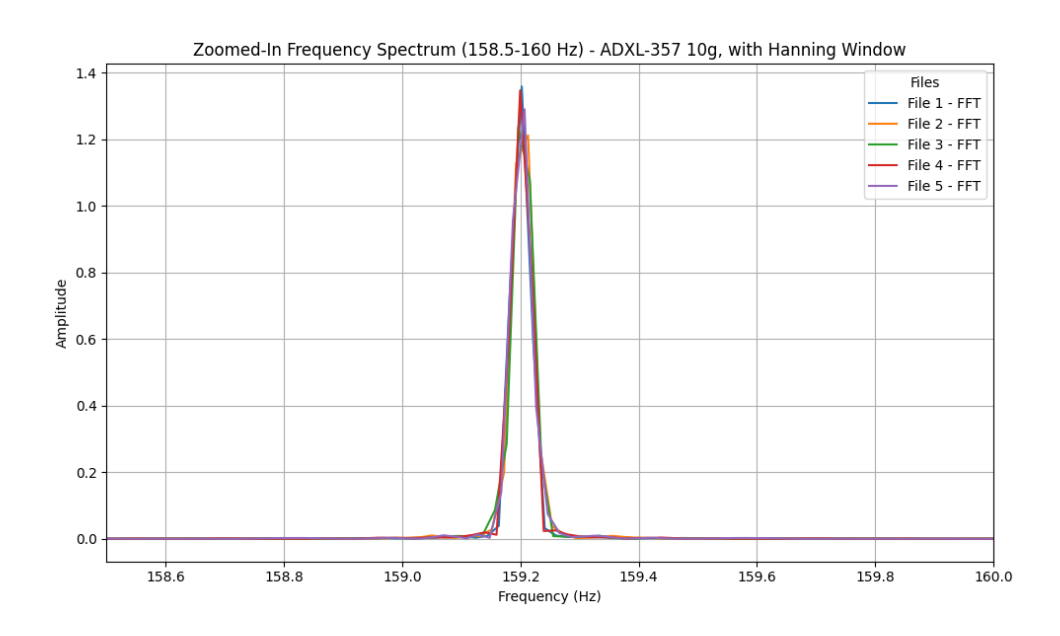


Figure 101: ADXL-357 magnet mounted 10 g Frequency-domain plot peak windowed 1 g RMS

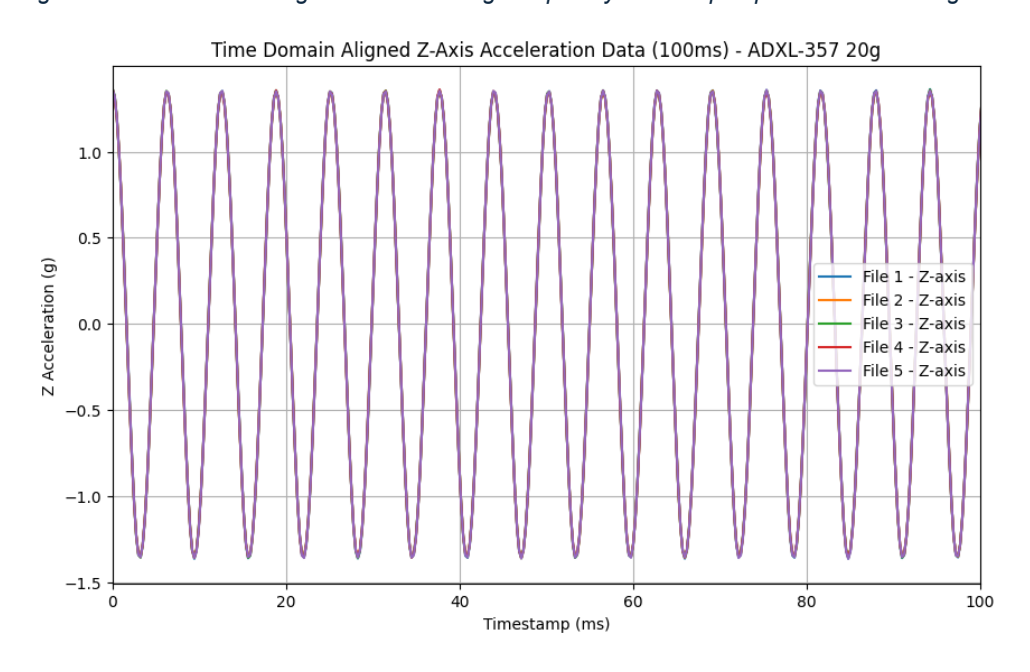


Figure 102: ADXL-357 magnet mounted 20 g Time-domain plot 1 g RMS

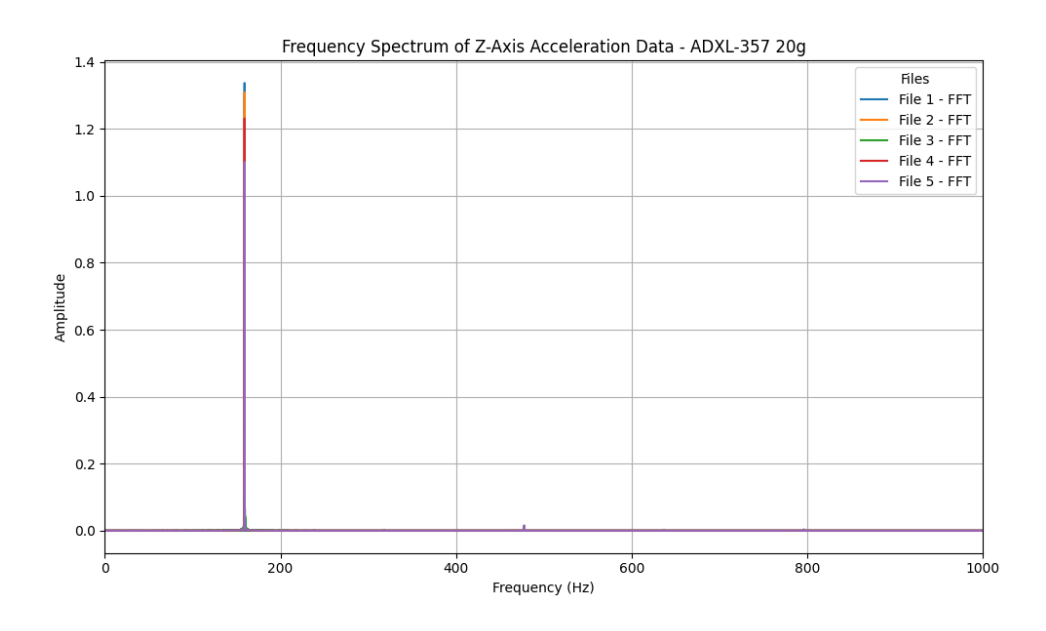


Figure 103: ADXL-357 magnet mounted 20 g Frequency-domain plot 1 g RMS

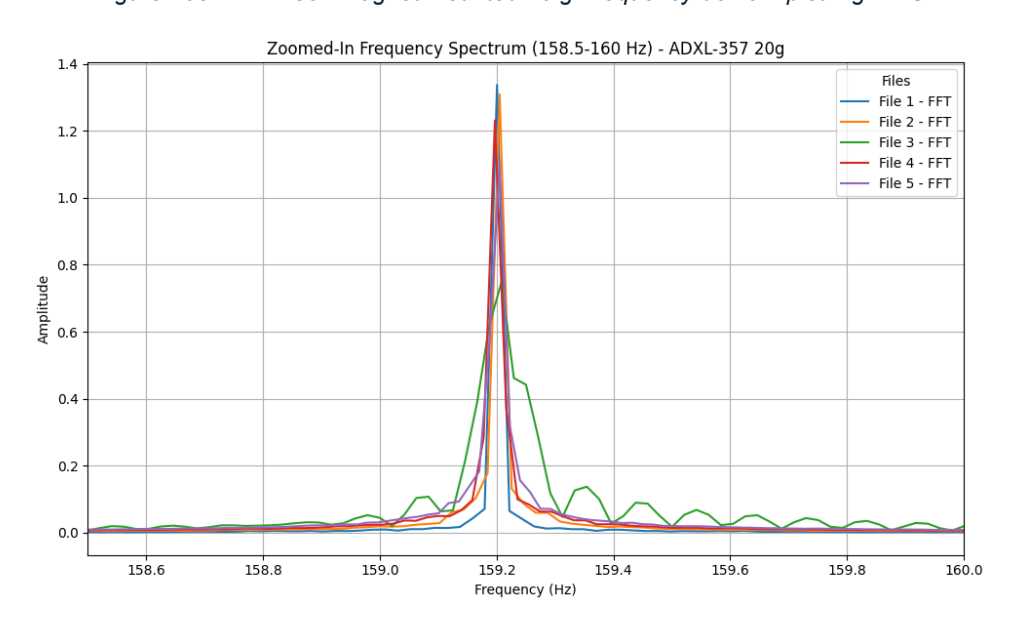


Figure 104: ADXL-357 magnet mounted 20 g Frequency-domain plot peak 1 g RMS

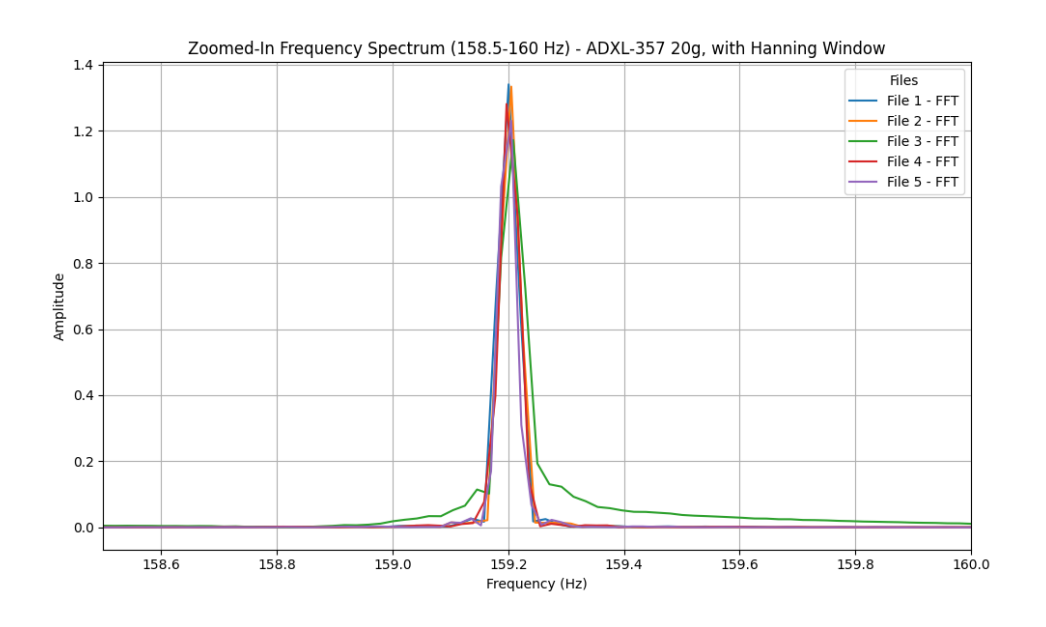


Figure 105: ADXL-357 magnet mounted 20 g Frequency-domain plot peak windowed 1 g RMS

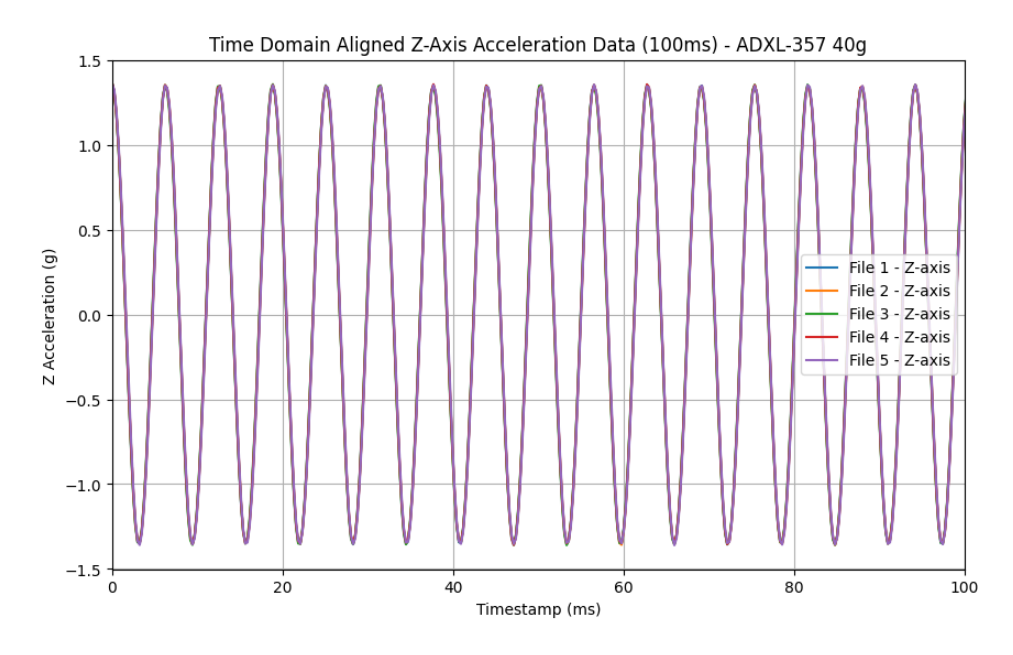


Figure 106: ADXL-357 magnet mounted 40 g Time-domain plot 1 g RMS

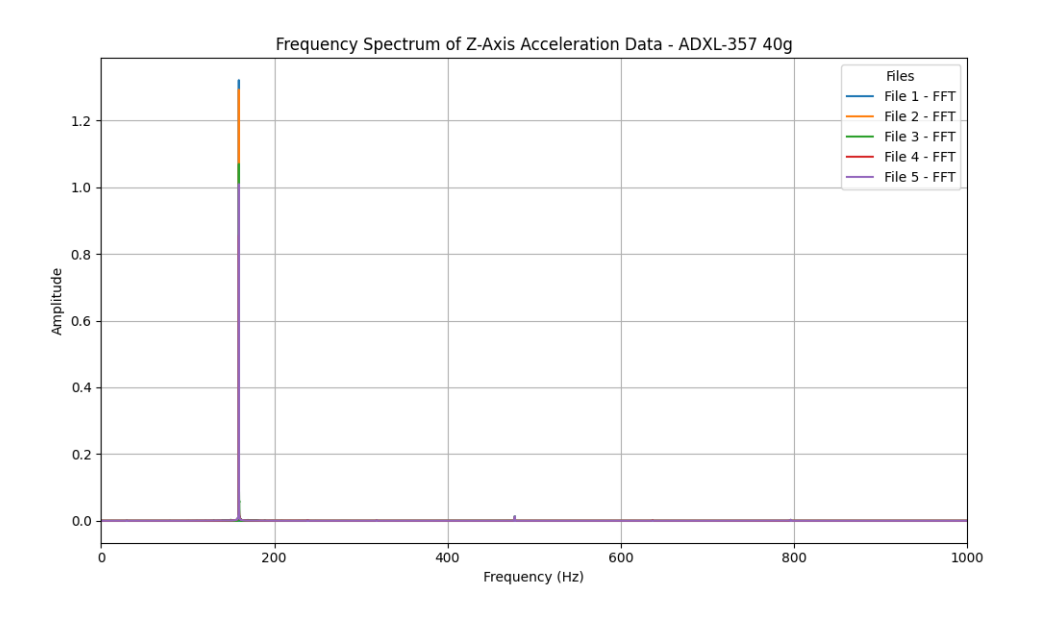


Figure 107: ADXL-357 magnet mounted 40 g Frequency-domain plot 1 g RMS

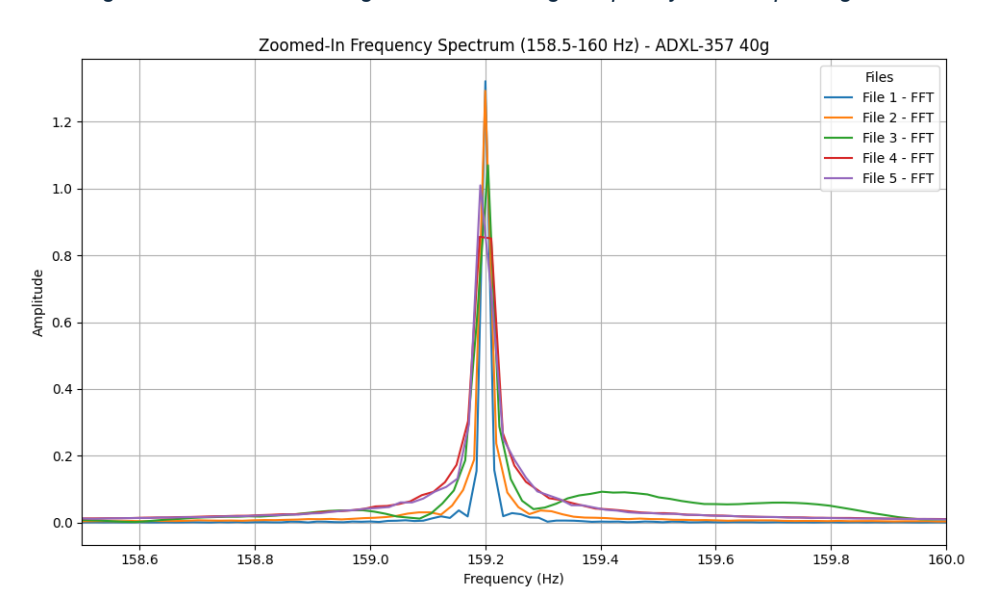


Figure 108: ADXL-357 magnet mounted 40 g Frequency-domain plot peak 1 g RMS

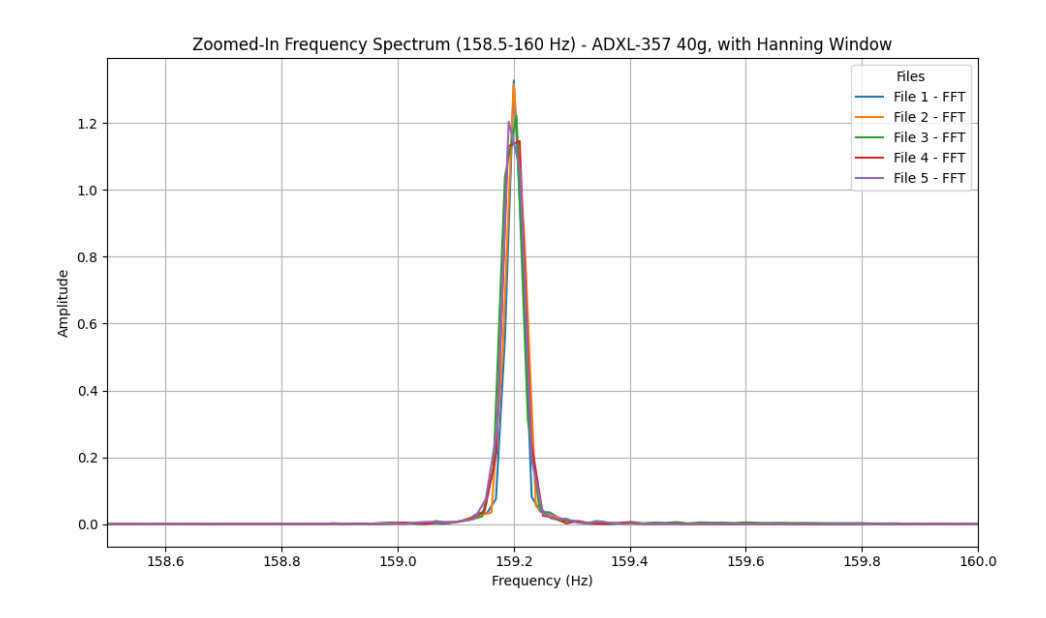


Figure 109: ADXL-357 magnet mounted 40 g Frequency-domain plot peak windowed 1 g RMS 8.1.3.2 1 g Pk

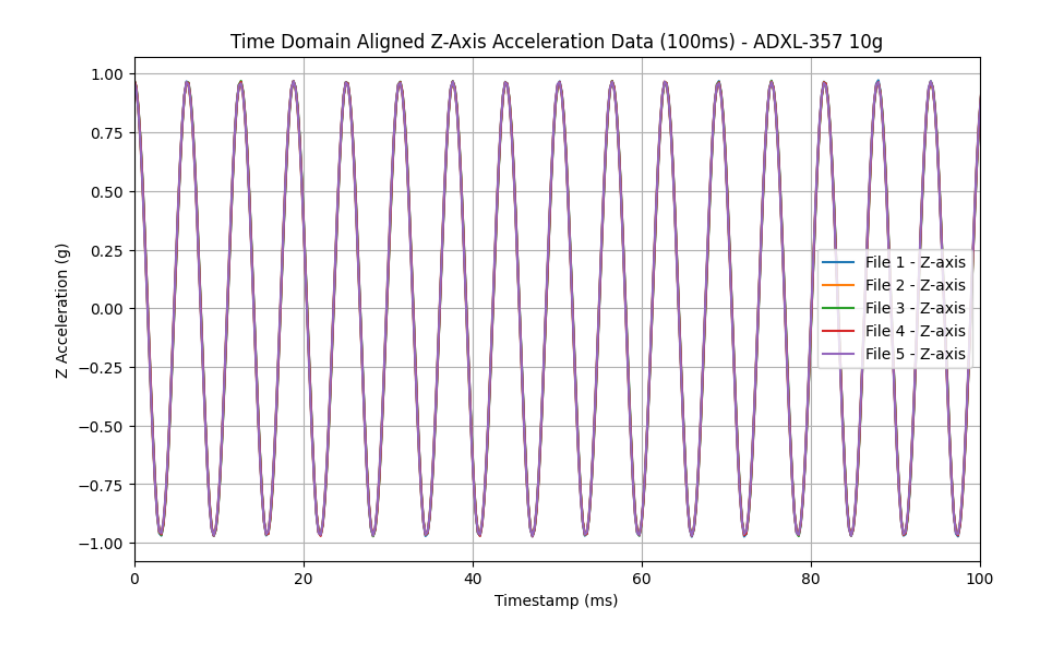


Figure 110: ADXL-357 magnet mounted 10 g Time-domain plot 1 g Pk

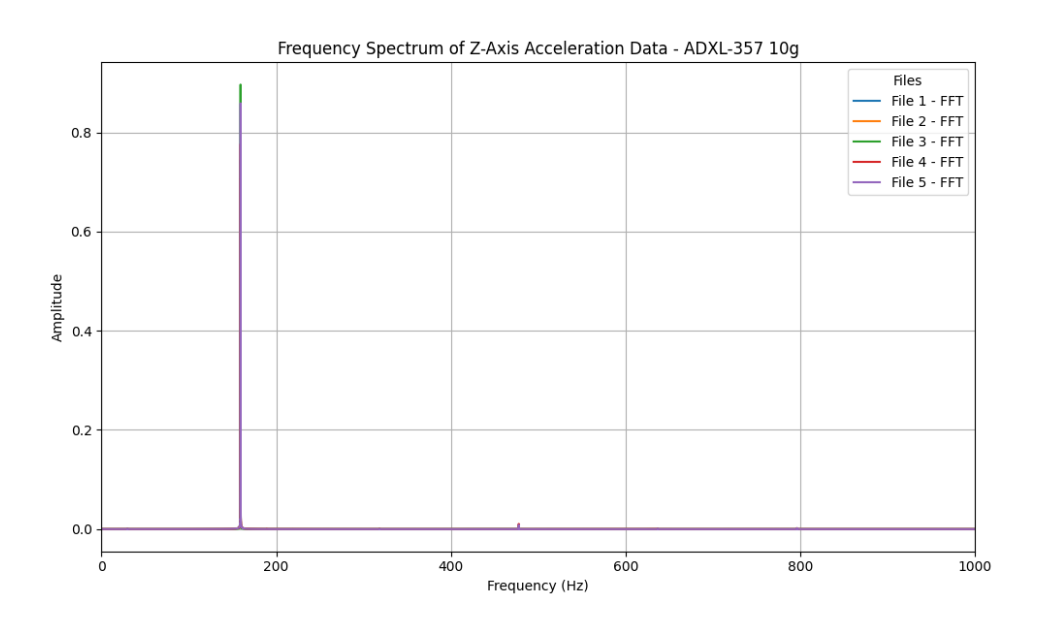


Figure 111: ADXL-357 magnet mounted 10 g Frequency-domain plot 1 g Pk

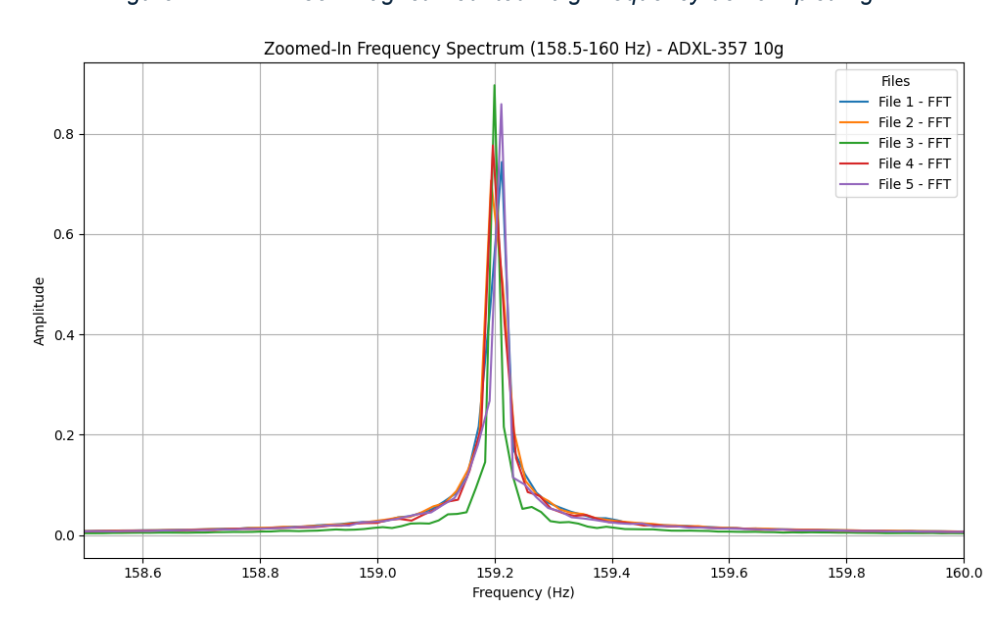


Figure 112: ADXL-357 magnet mounted 10 g Frequency-domain plot peak 1 g Pk

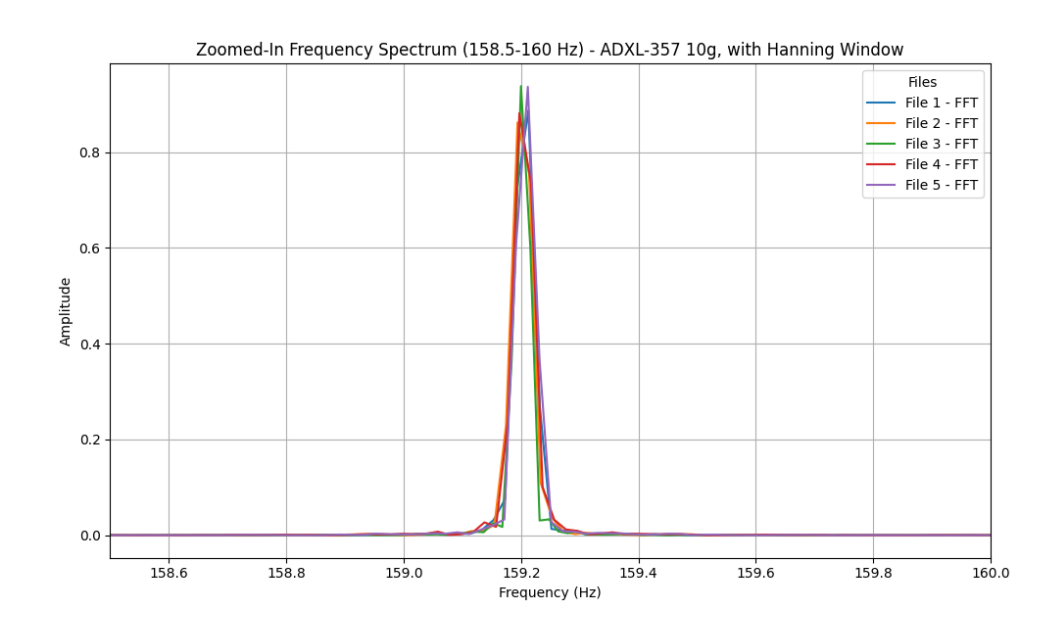


Figure 113: ADXL-357 magnet mounted 10 g Frequency-domain plot peak windowed 1 g Pk

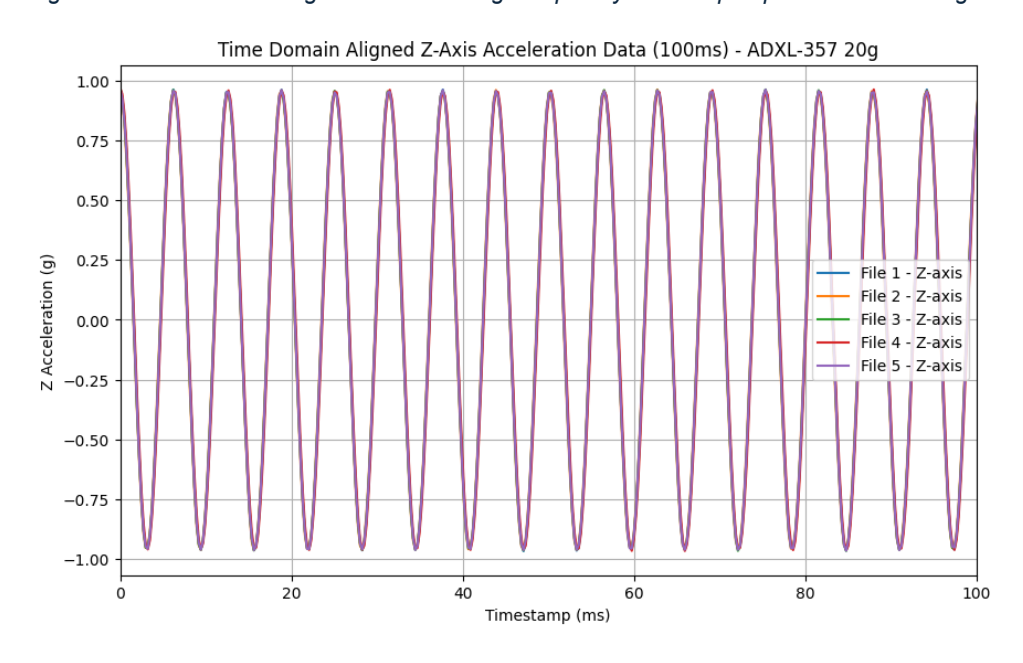


Figure 114: ADXL-357 magnet mounted 20 g Time-domain plot 1 g Pk

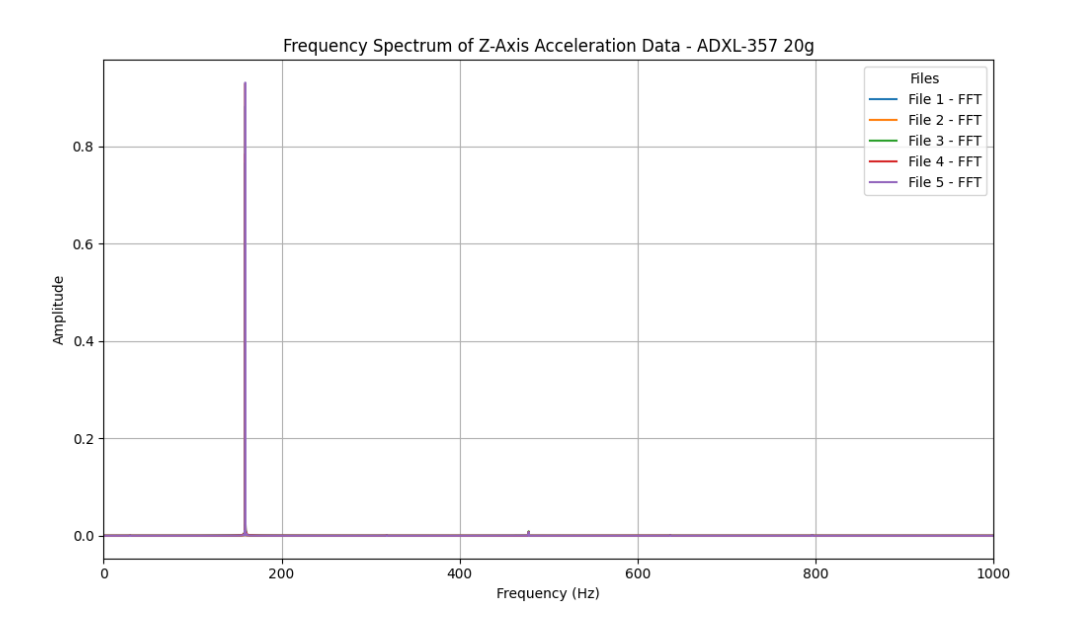


Figure 115: ADXL-357 magnet mounted 20 g Frequency-domain plot 1 g Pk

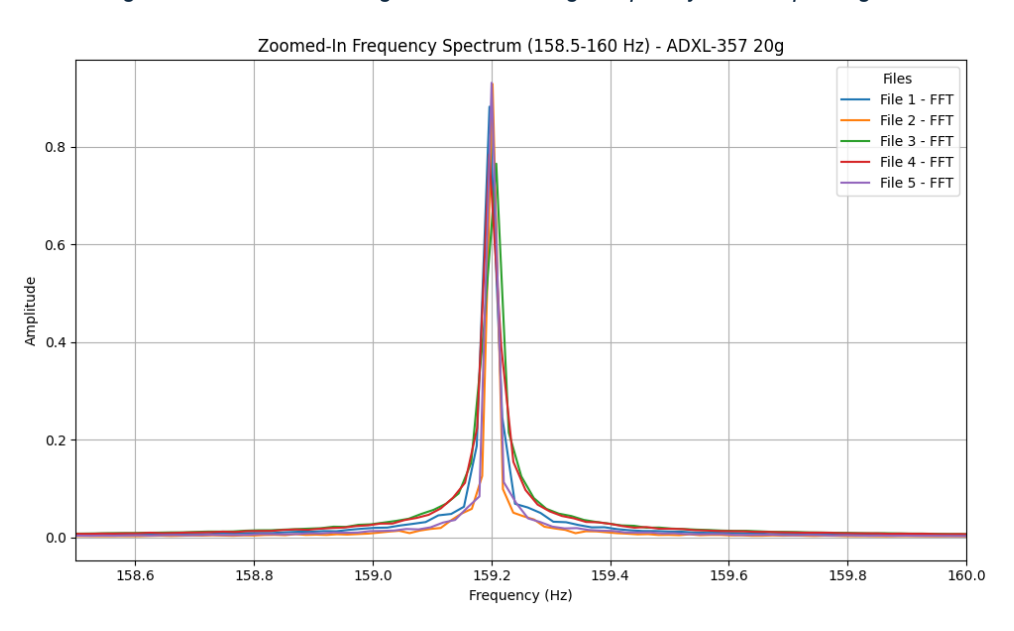


Figure 116: ADXL-357 magnet mounted 20 g Frequency-domain plot peak 1 g Pk

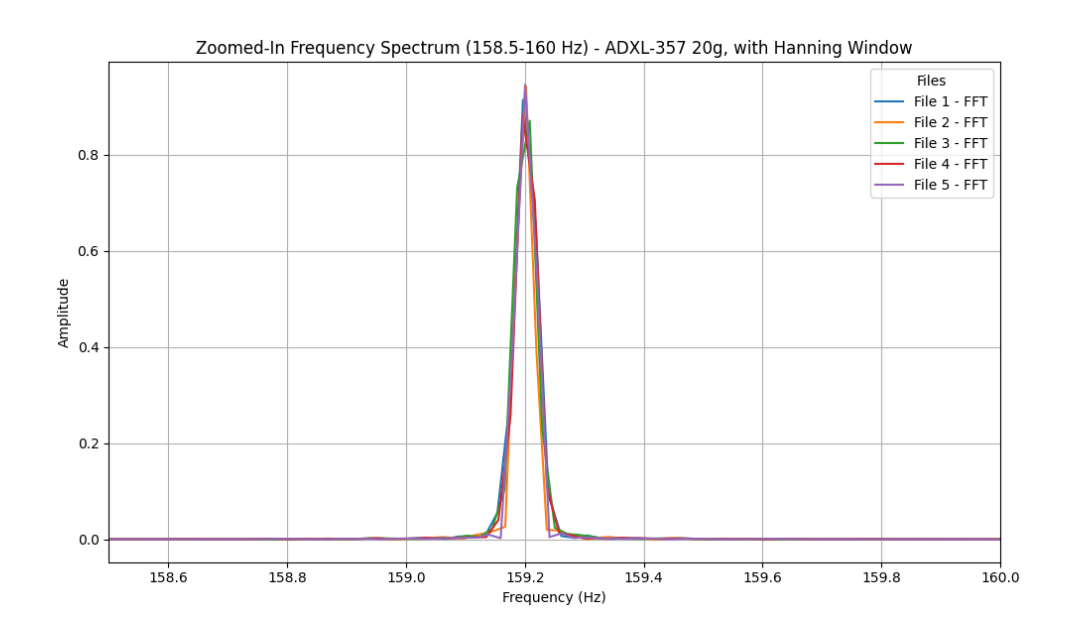


Figure 117: ADXL-357 magnet mounted 20 g Frequency-domain plot peak windowed 1 g Pk

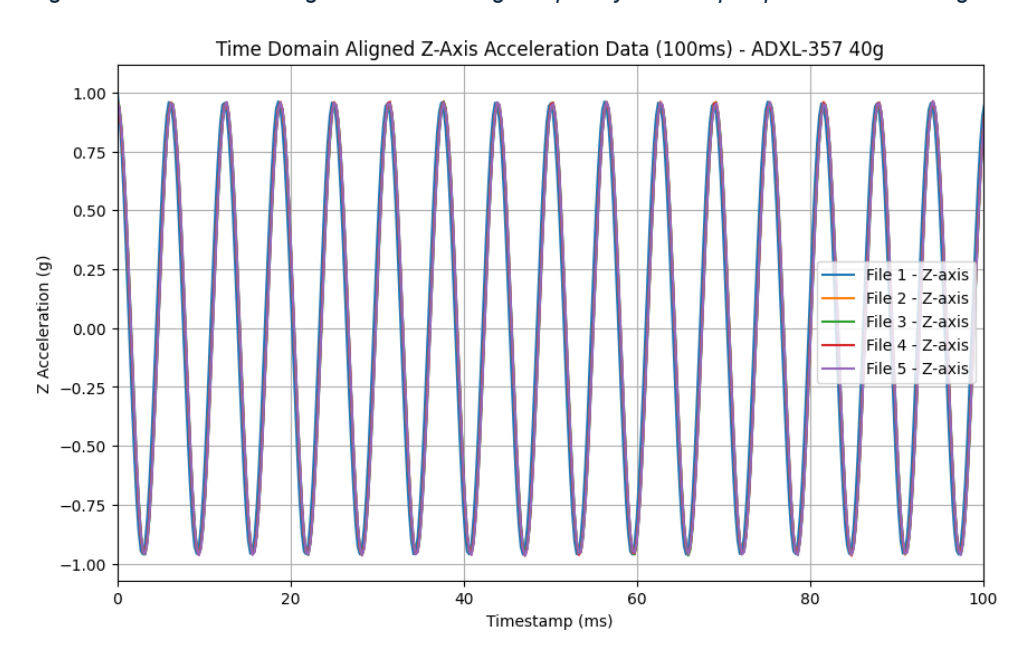


Figure 118: ADXL-357 magnet mounted 40 g Time-domain plot 1 g Pk

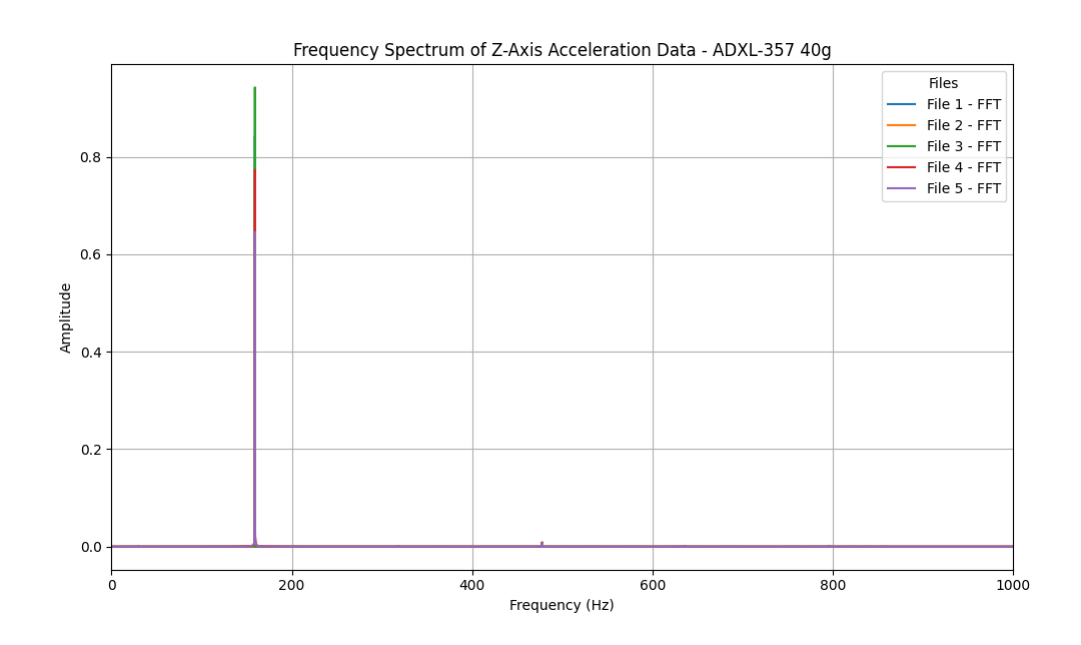


Figure 119: ADXL-357 magnet mounted 40 g Frequency-domain plot 1 g Pk

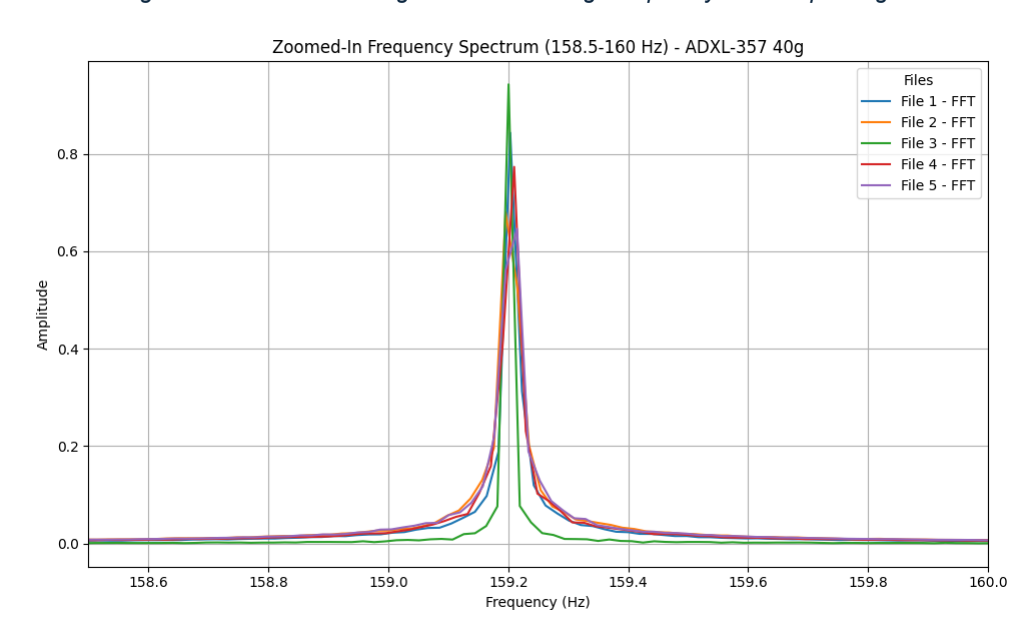


Figure 120: ADXL-357 magnet mounted 40 g Frequency-domain plot peak 1 g Pk

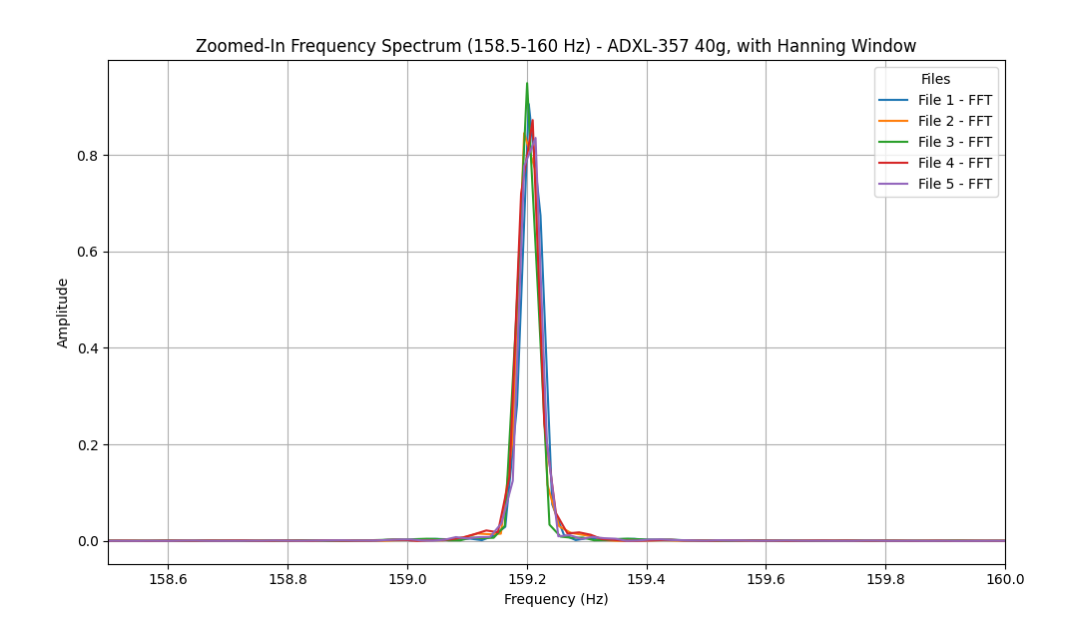


Figure 121: ADXL-357 magnet mounted 40 g Frequency-domain plot peak windowed 1 g Pk

8.1.4 ICM-42688-P – Magnet Mounted, Battery Powered, 5G, 4 kHz ODR

8.1.4.1 1 g RMS

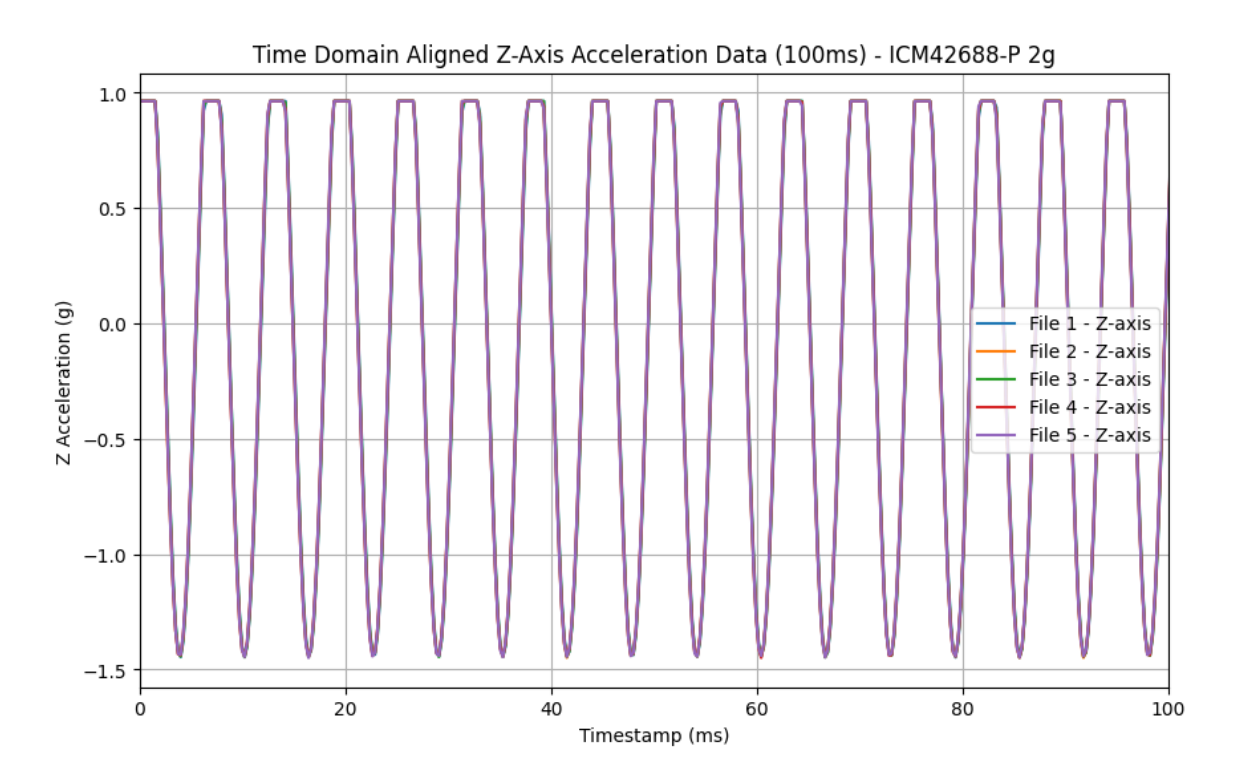


Figure 122: ICM-42688-P magnet mounted 2 g Time-domain plot 1 g RMS

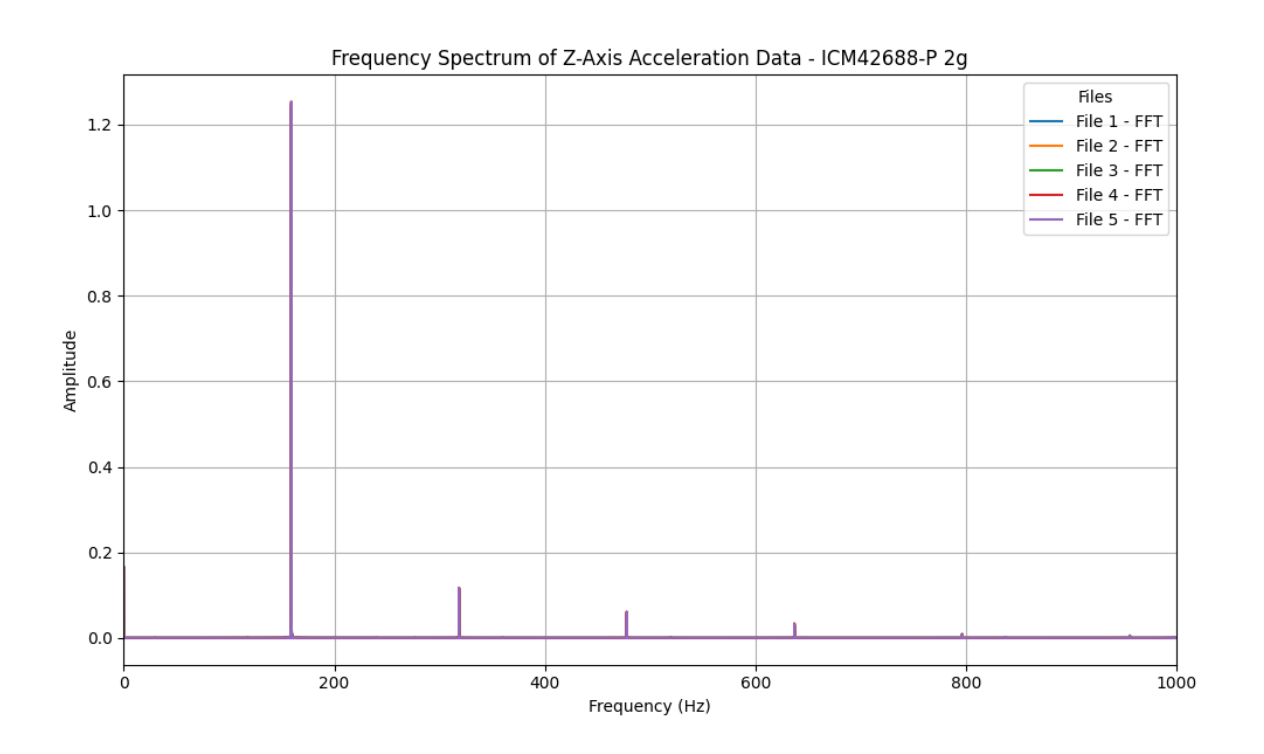


Figure 123: ICM-42688-P magnet mounted 2 g Frequency-domain plot 1 g RMS

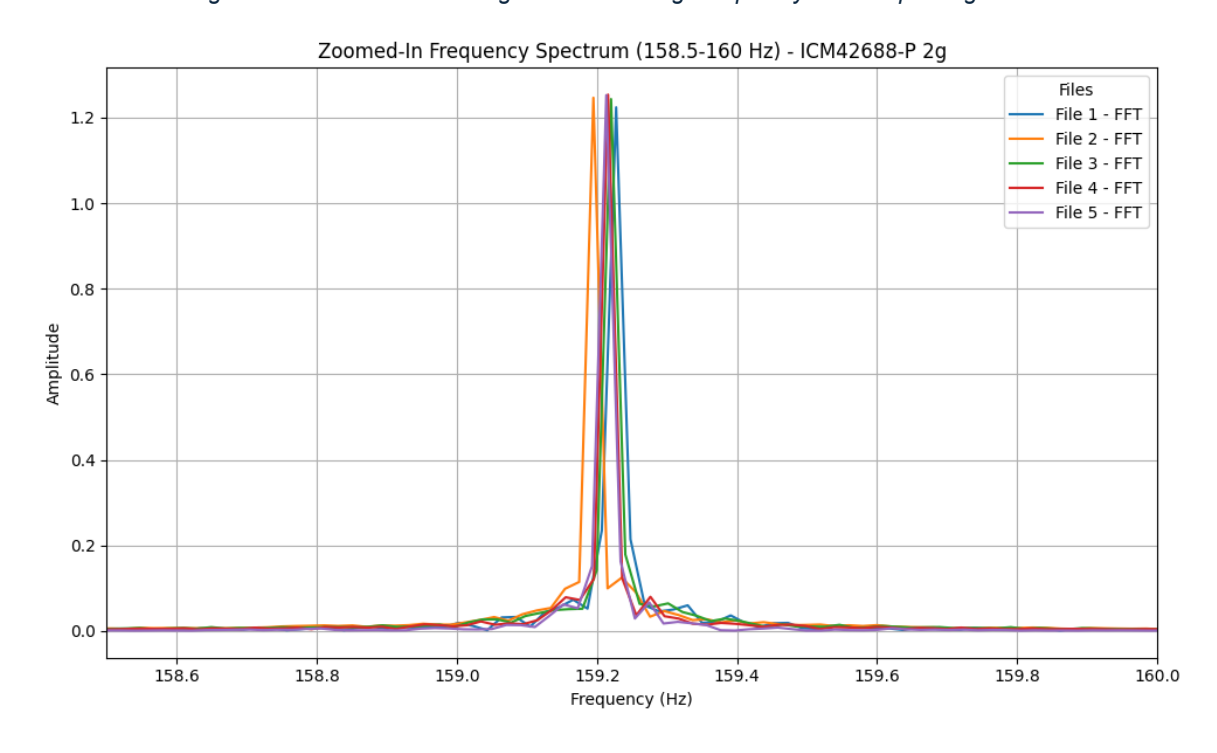


Figure 124: ICM-42688-P magnet mounted 2 g Frequency-domain plot peak 1 g RMS

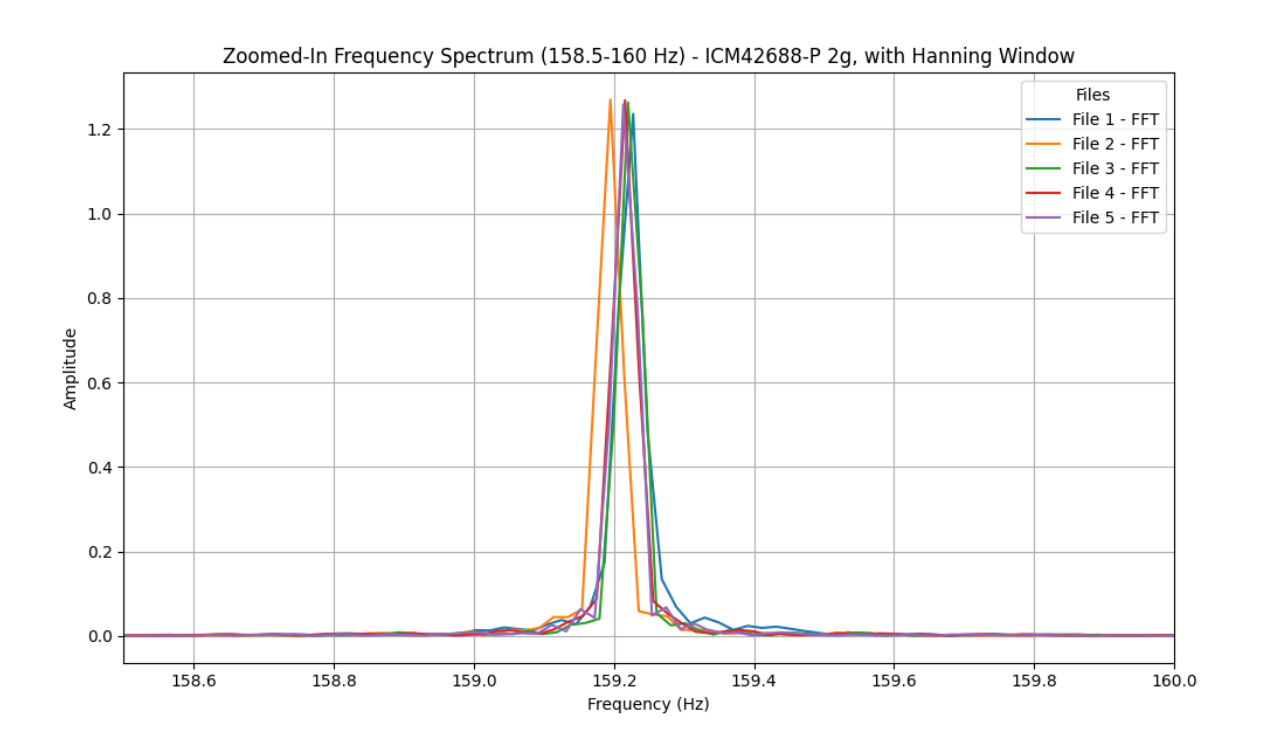


Figure 125: ICM-42688-P magnet mounted 2 g Frequency-domain plot peak windowed 1 g RMS

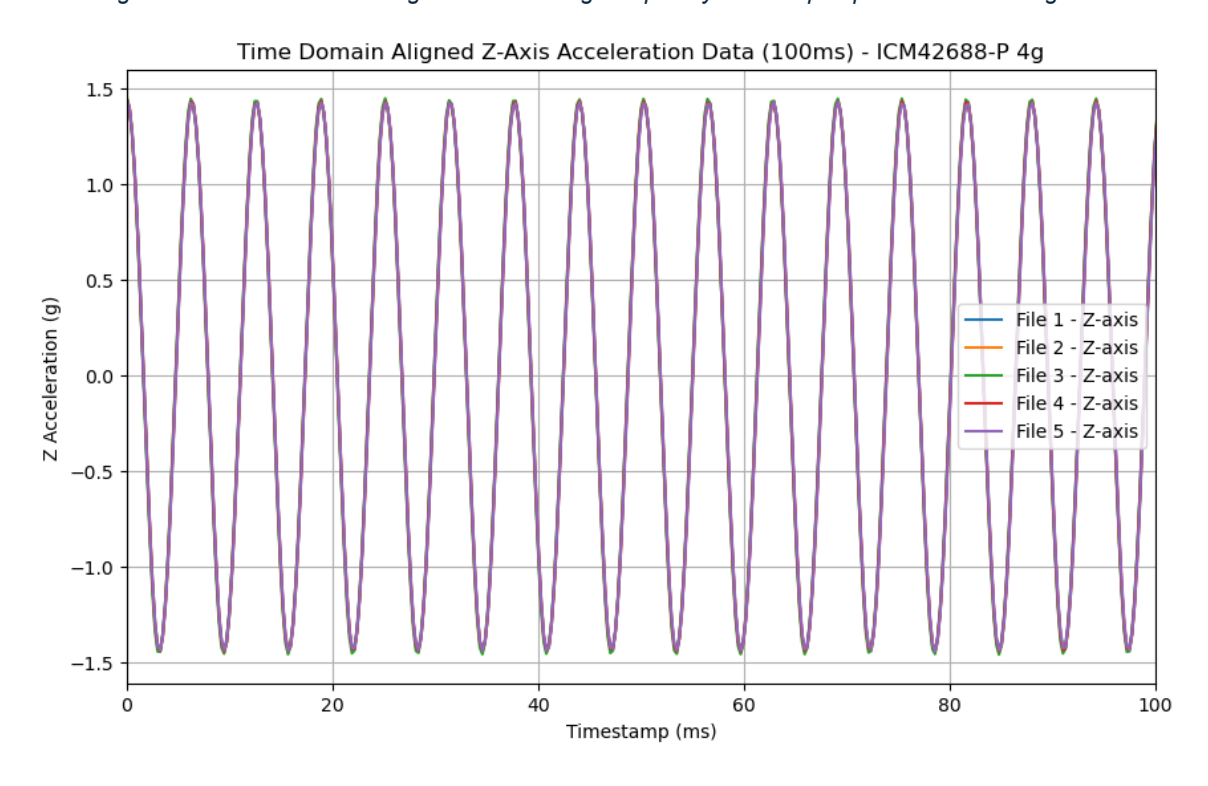


Figure 126: ICM-42688-P magnet mounted 4 g Time-domain plot 1 g RMS

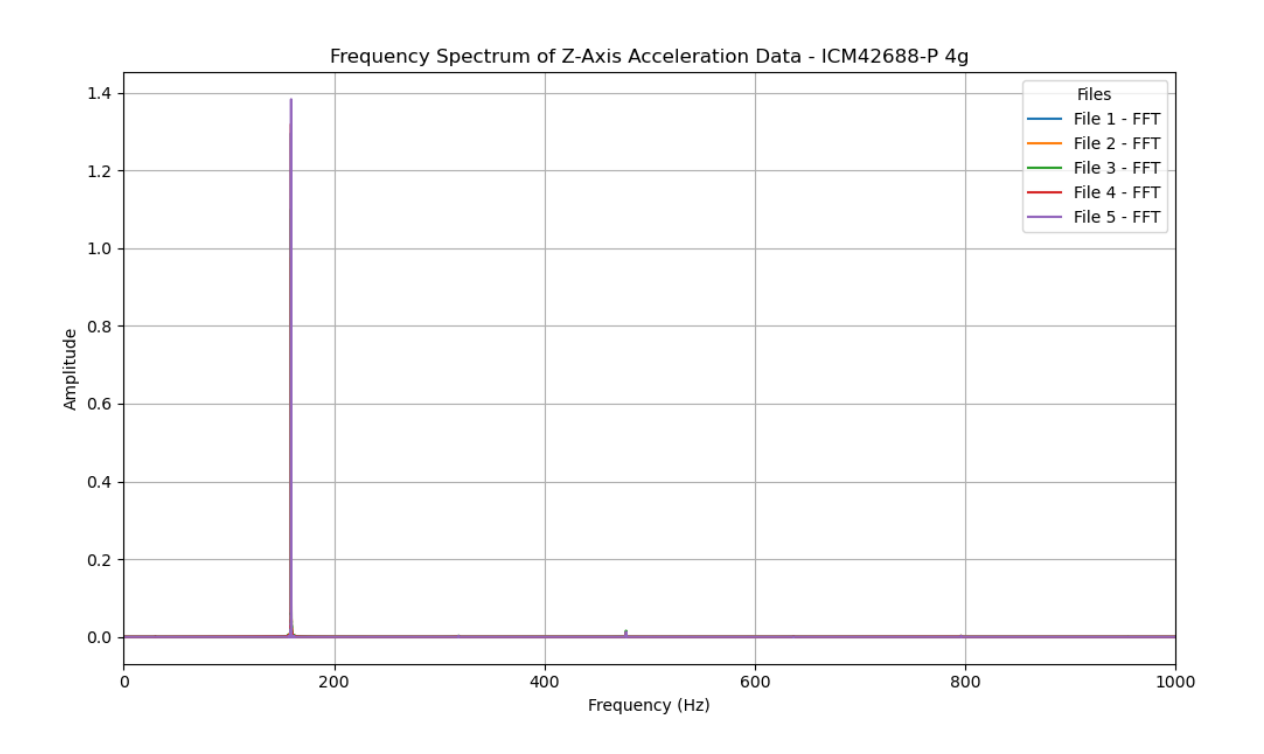


Figure 127: ICM-42688-P magnet mounted 4 g Frequency-domain plot 1 g RMS

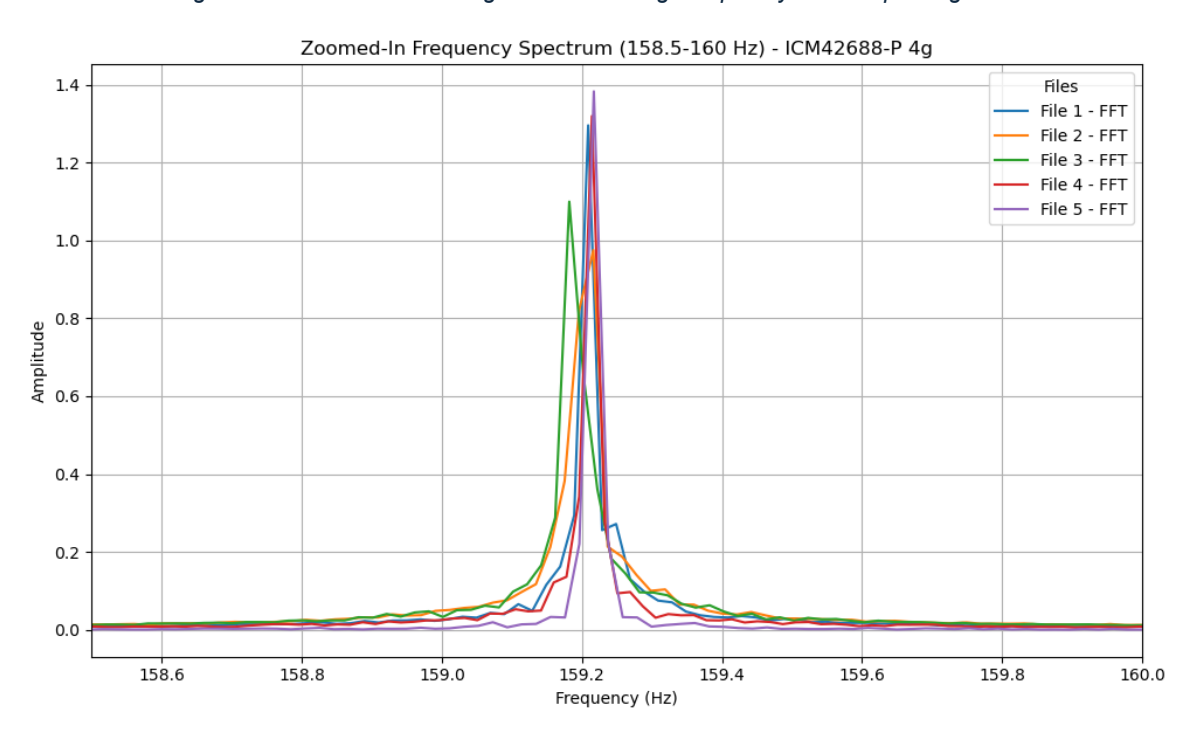


Figure 128: ICM-42688-P magnet mounted 4 g Frequency-domain plot peak 1 g RMS

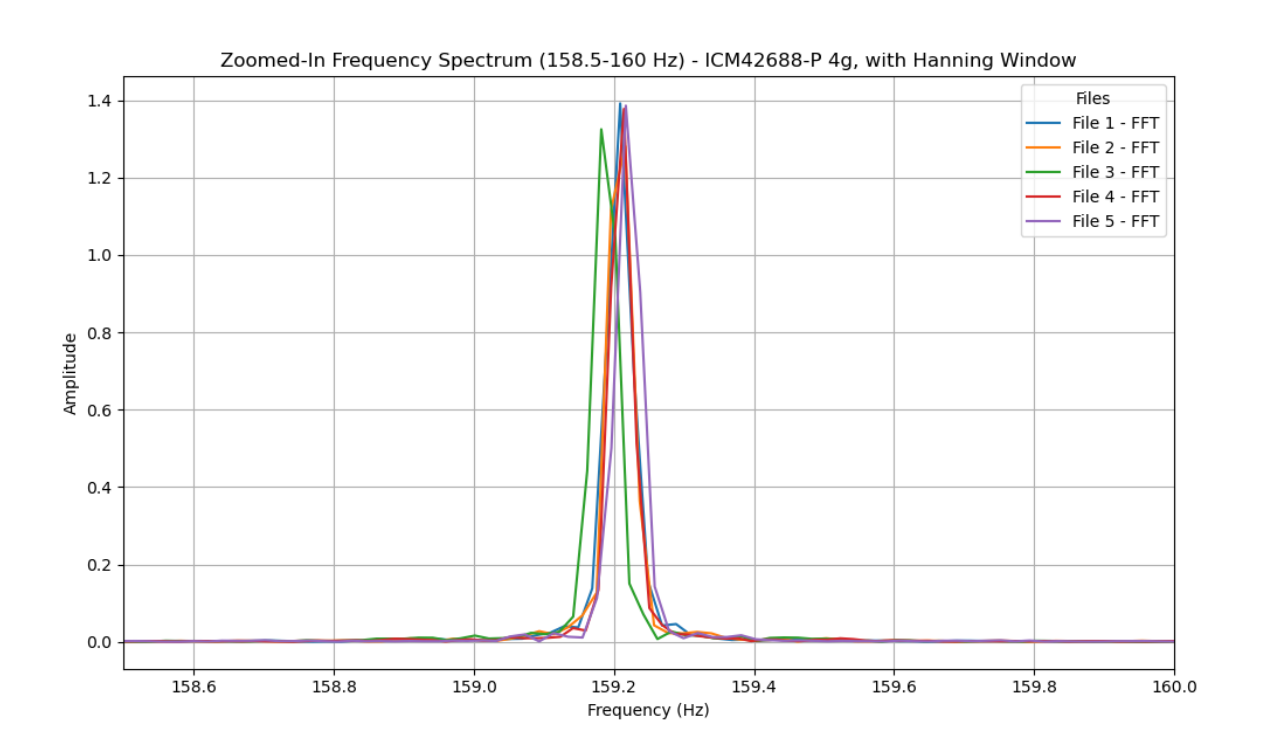


Figure 129: ICM-42688-P magnet mounted 4 g Frequency-domain plot peak windowed 1 g RMS

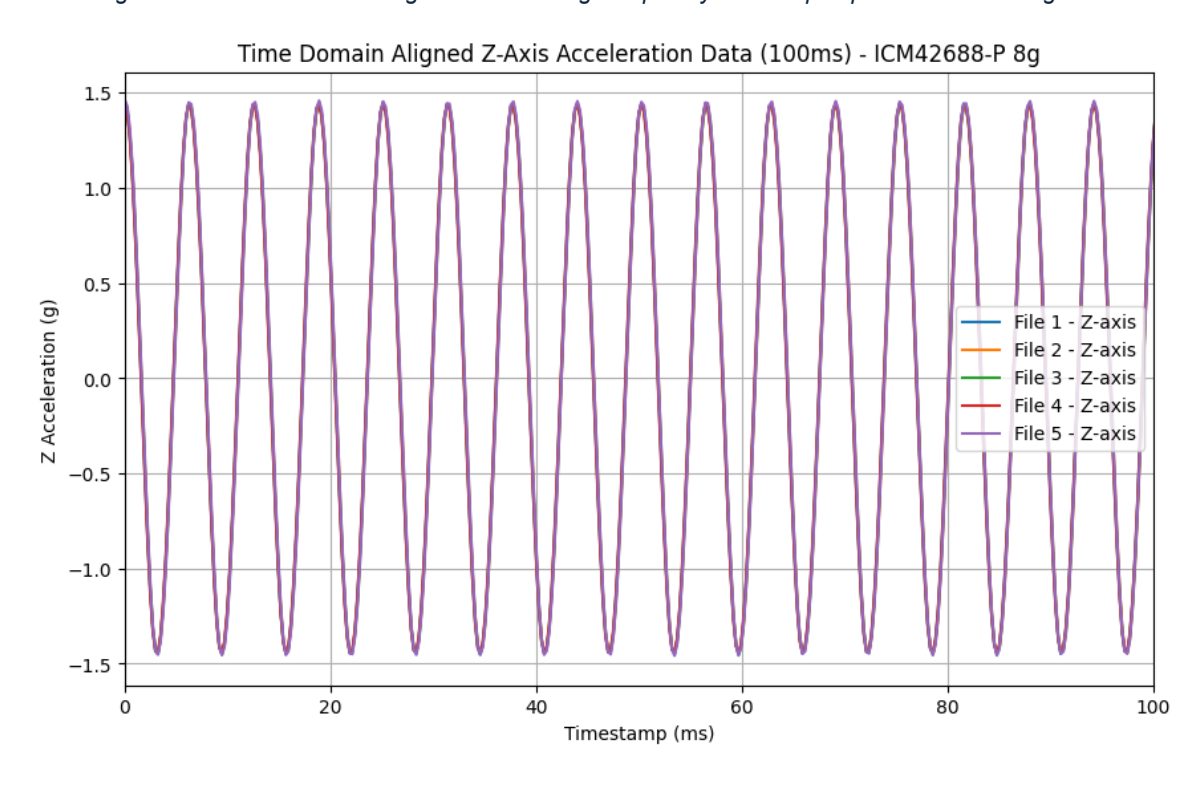


Figure 130: ICM-42688-P magnet mounted 8 g Time-domain plot 1 g RMS

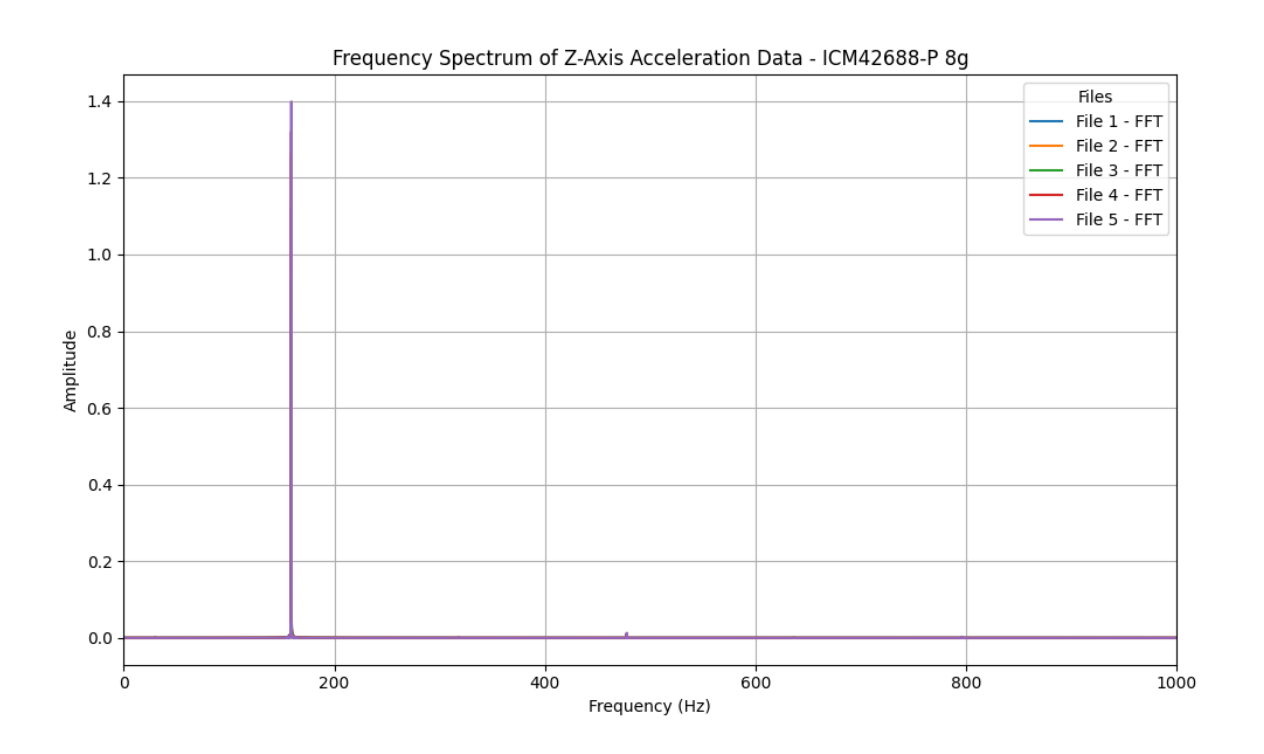


Figure 131: ICM-42688-P magnet mounted 8 g Frequency-domain plot 1 g RMS

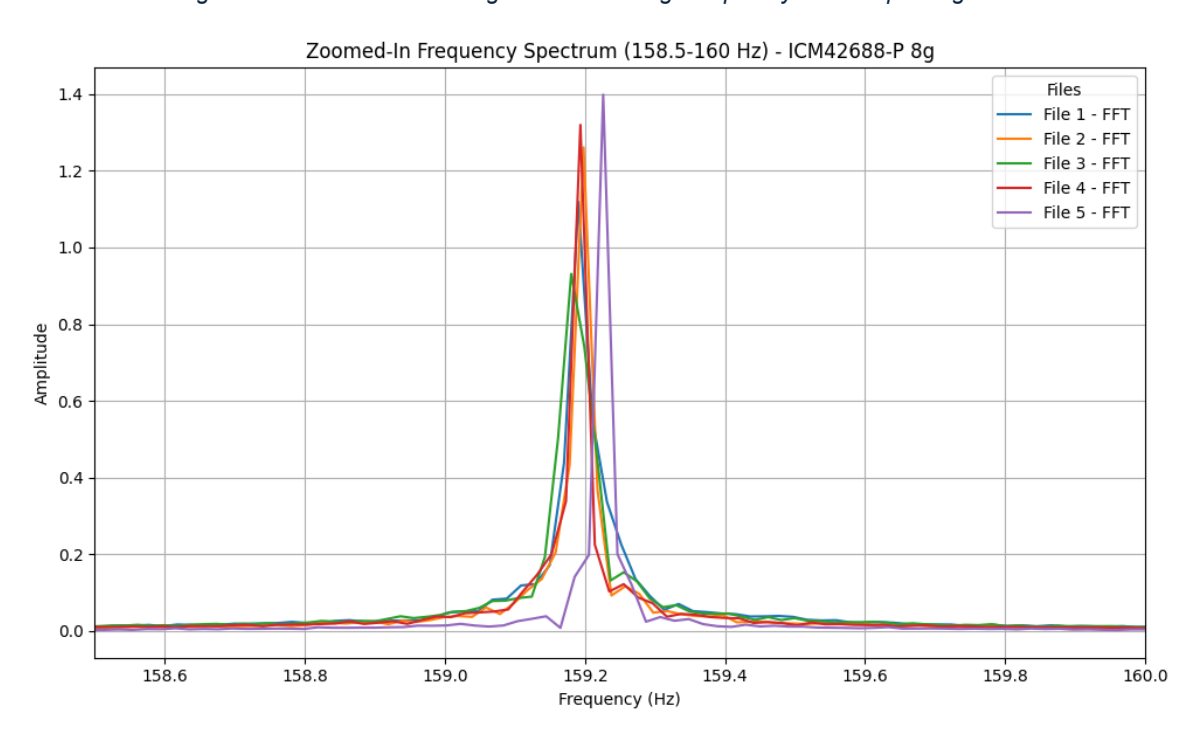


Figure 132: ICM-42688-P magnet mounted 8 g Frequency-domain plot peak 1 g RMS

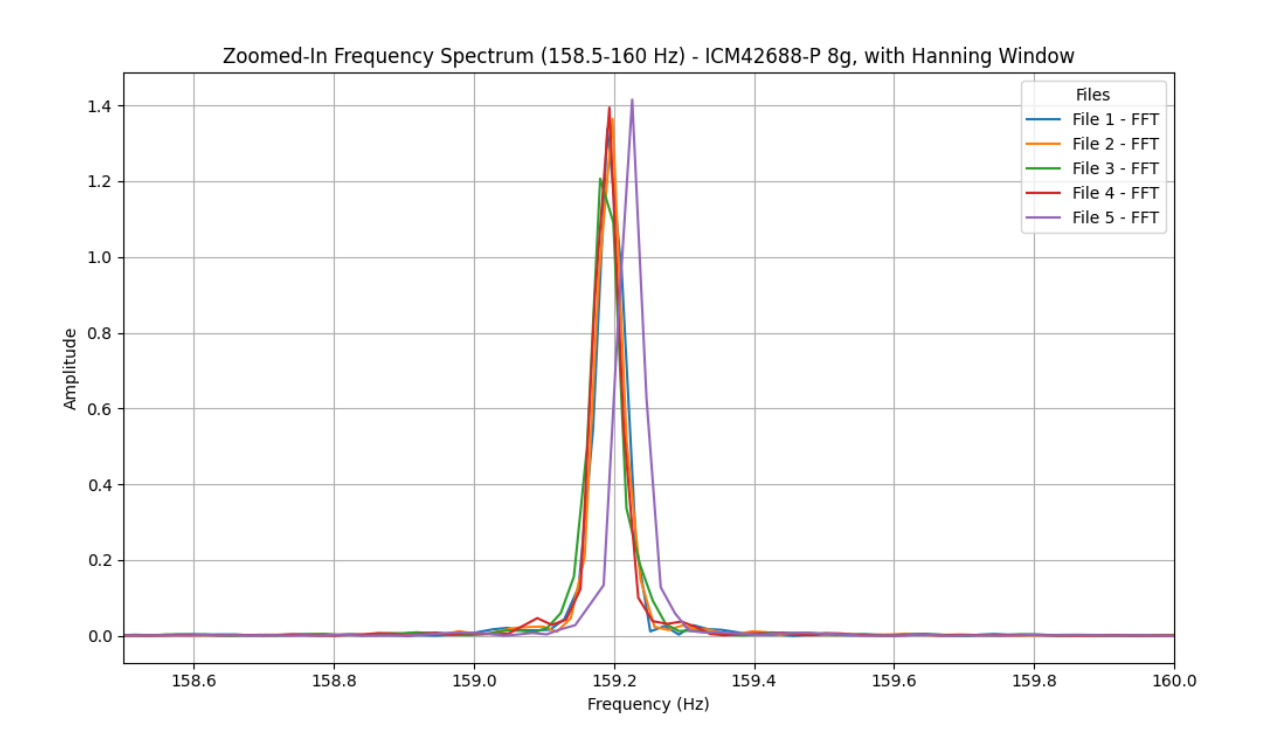


Figure 133: ICM-42688-P magnet mounted 8 g Frequency-domain plot peak windowed 1 g RMS

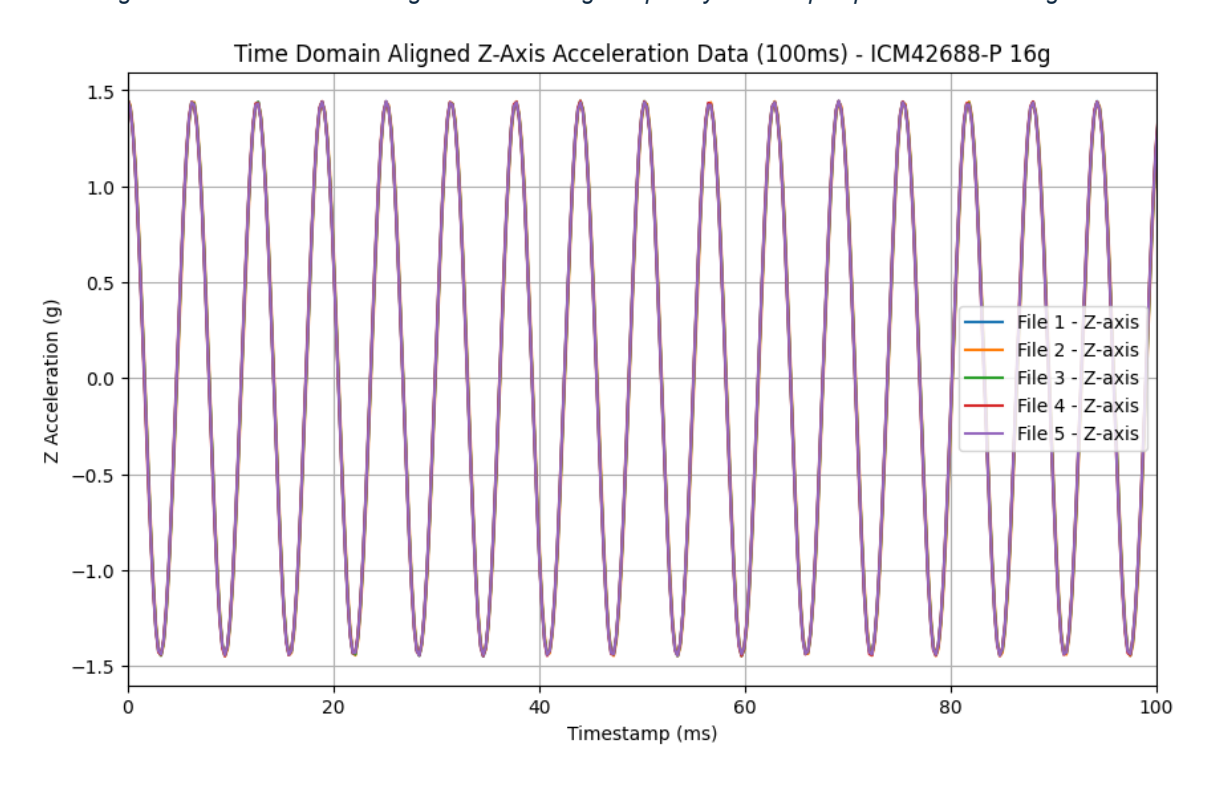


Figure 134: ICM-42688-P magnet mounted 16 g Time-domain plot 1 g RMS

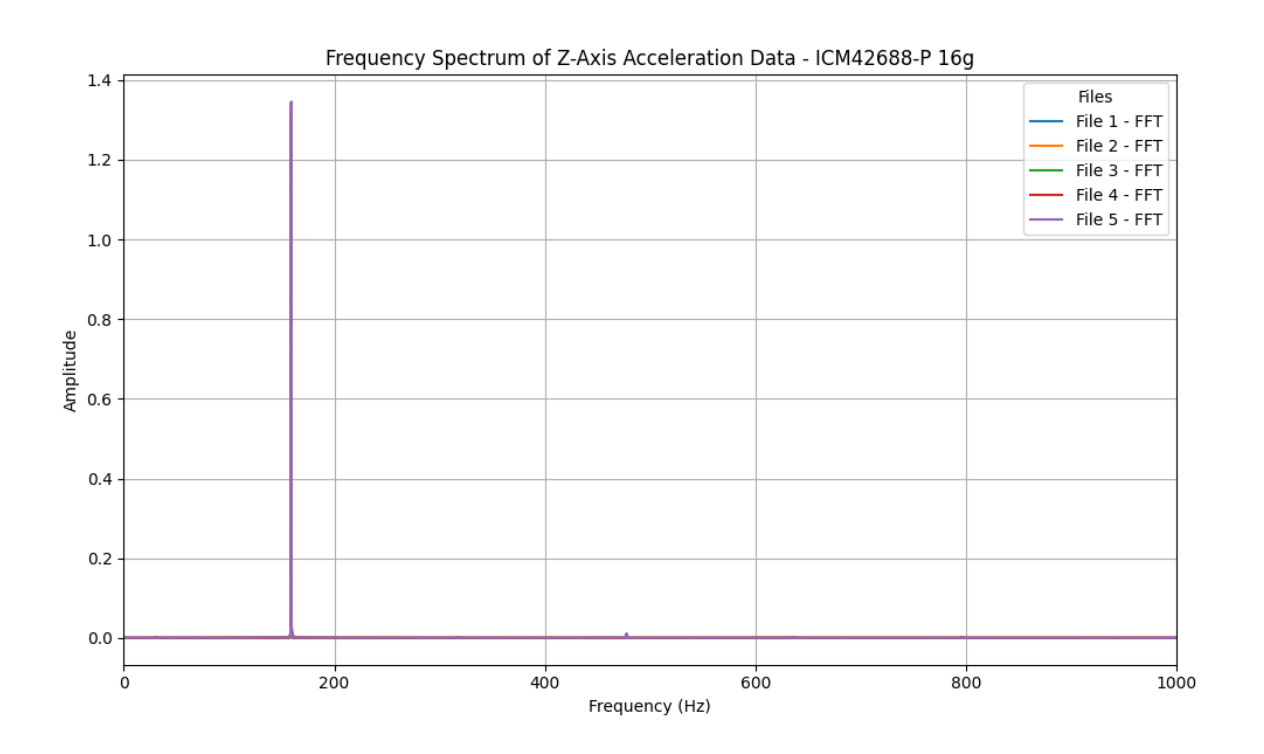


Figure 135: ICM-42688-P magnet mounted 16 g Frequency-domain plot 1 g RMS

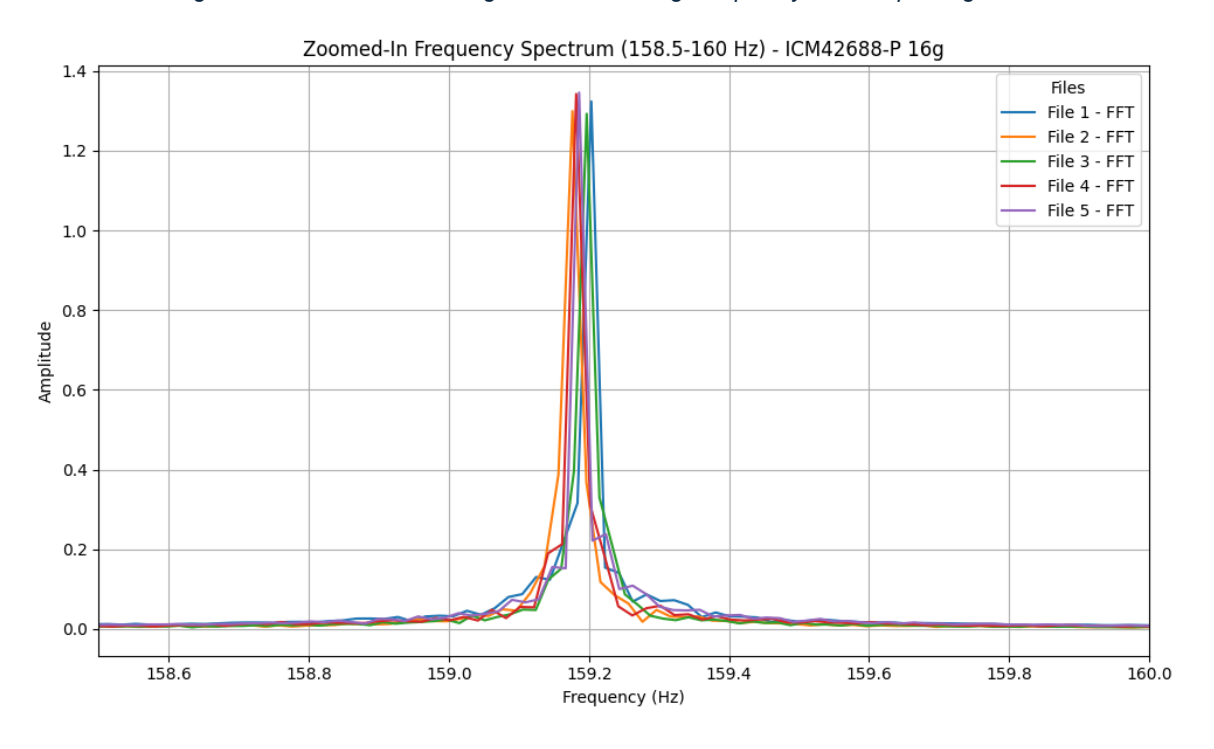


Figure 136: ICM-42688-P magnet mounted 16 g Frequency-domain plot peak 1 g RMS

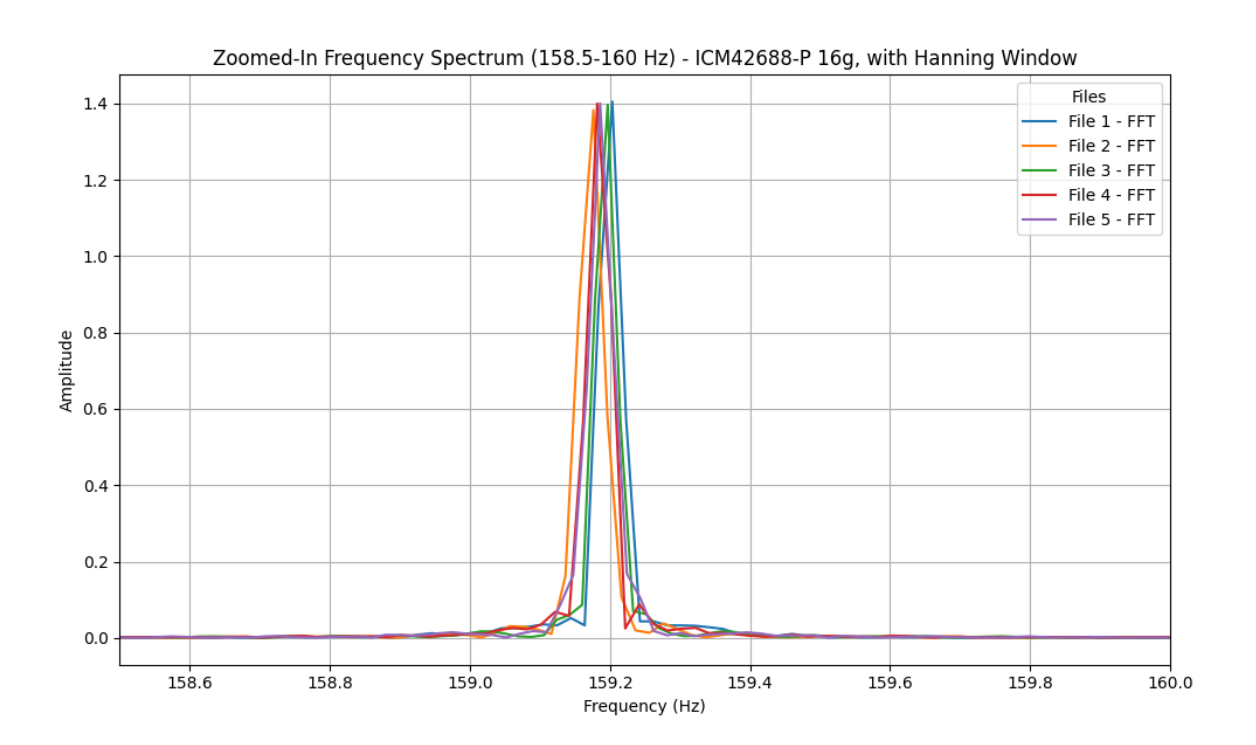


Figure 137: ICM-42688-P magnet mounted 16 g Frequency-domain plot peak windowed 1 g RMS

8.1.4.2 1 g Pk

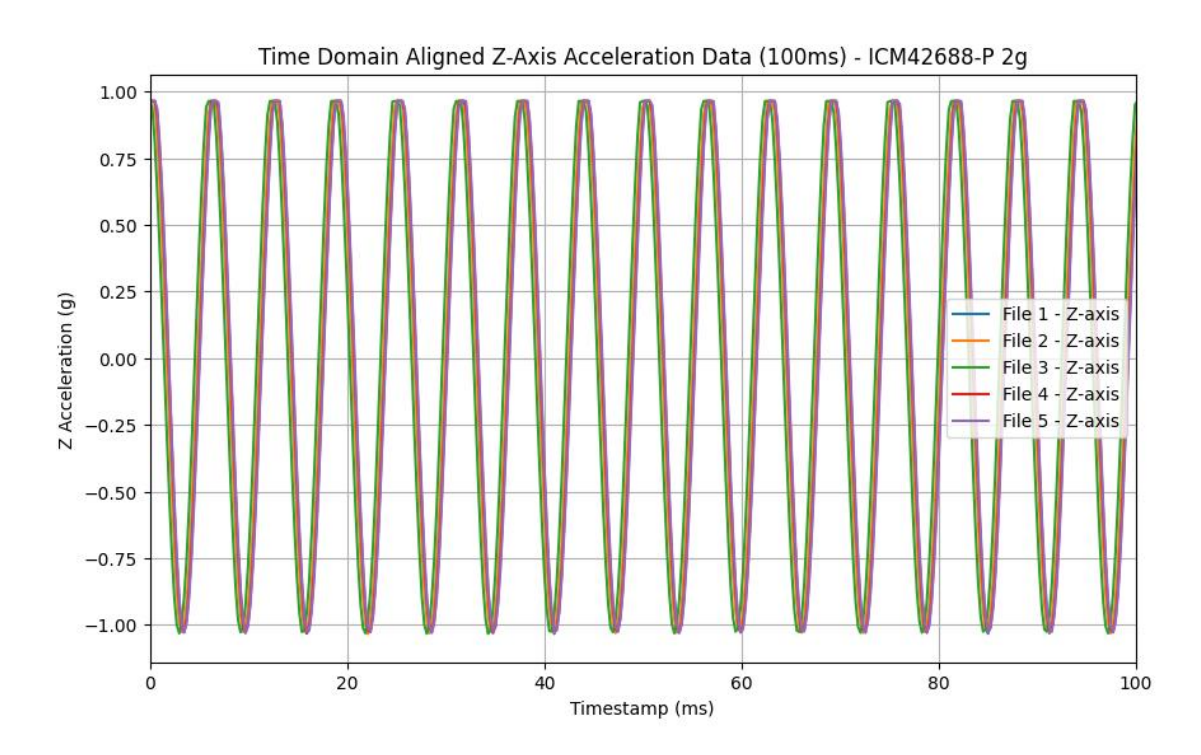


Figure 138: ICM-42688-P magnet mounted 2 g Time-domain plot 1 g Pk

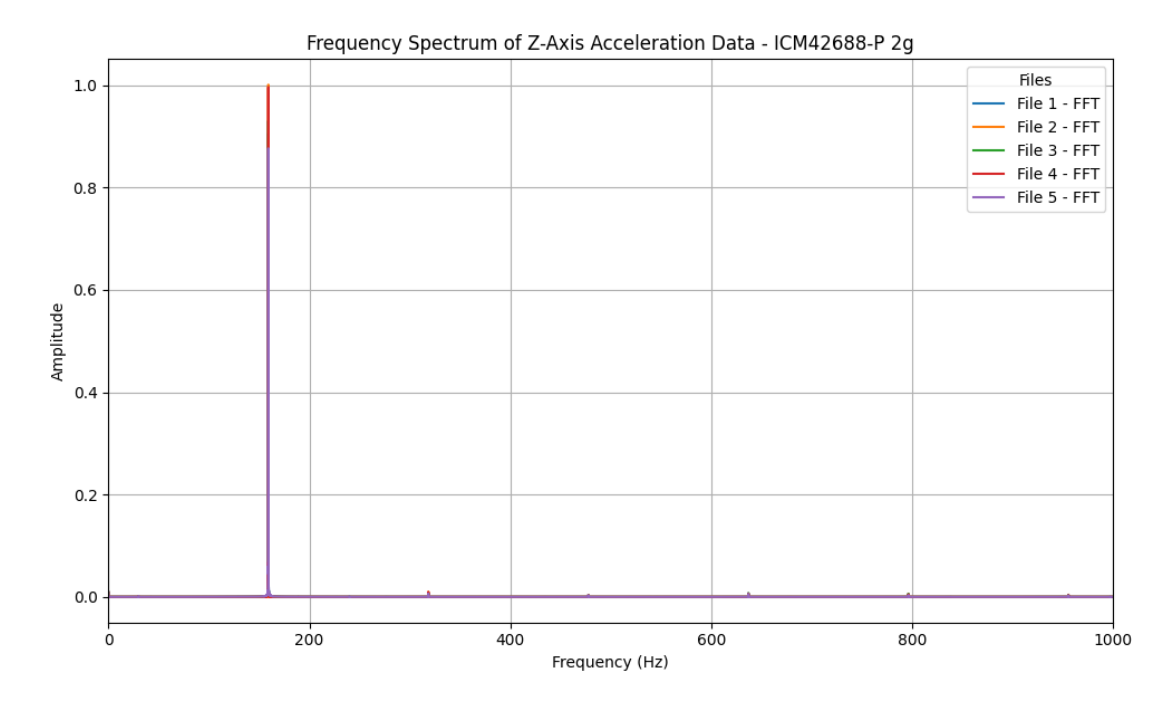


Figure 139: ICM-42688-P magnet mounted 2 g Frequency-domain plot 1 g Pk

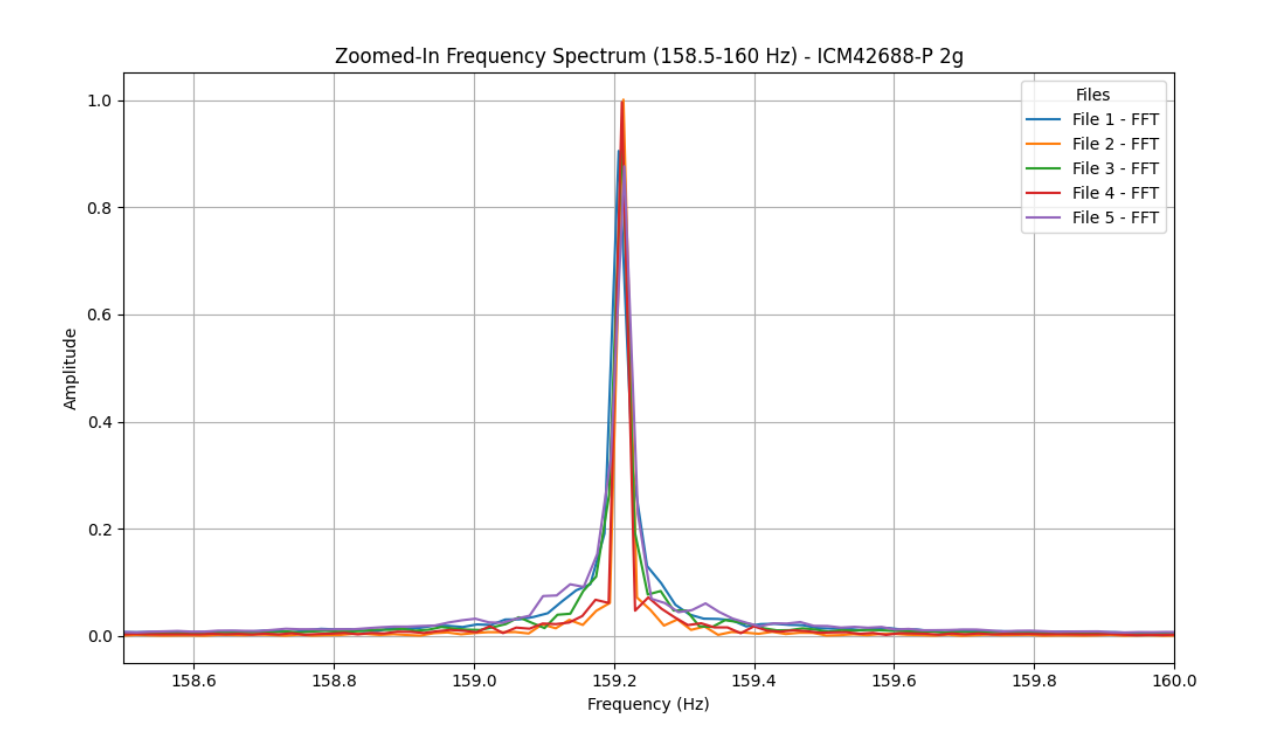


Figure 140: ICM-42688-P magnet mounted 2 g Frequency-domain plot peak 1 g Pk

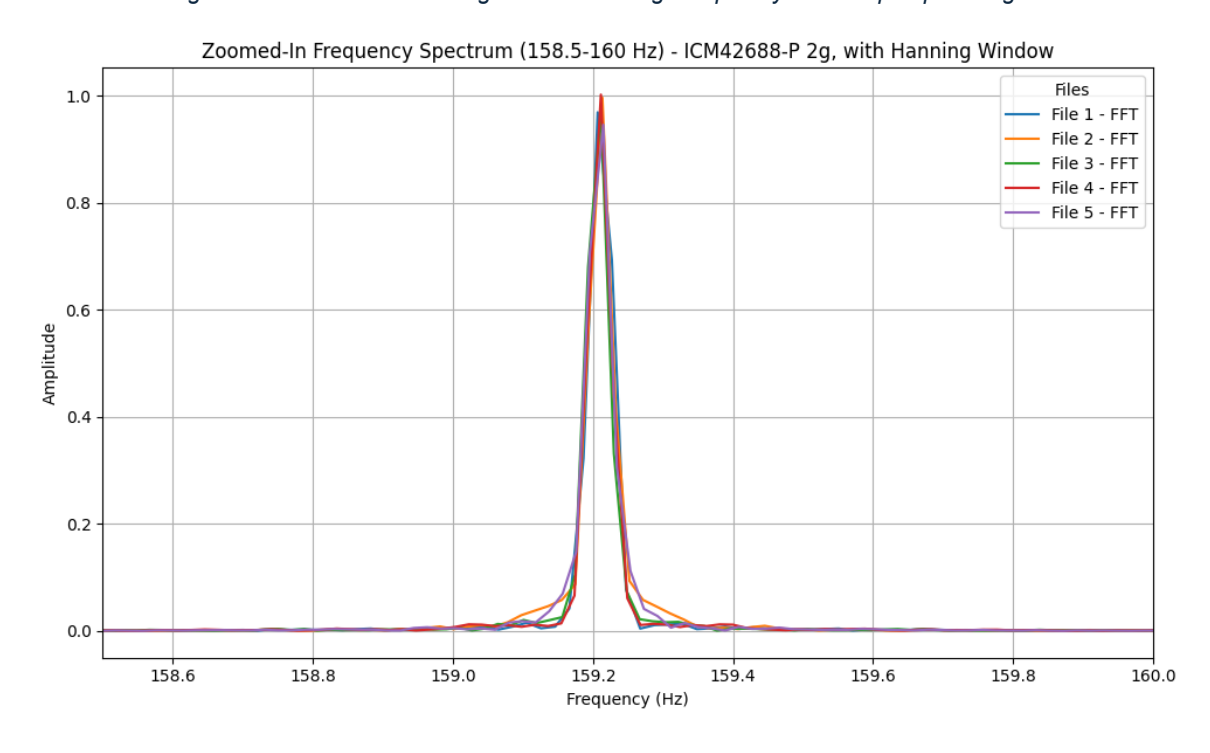


Figure 141: ICM-42688-P magnet mounted 2 g Frequency-domain plot peak windowed 1 g Pk

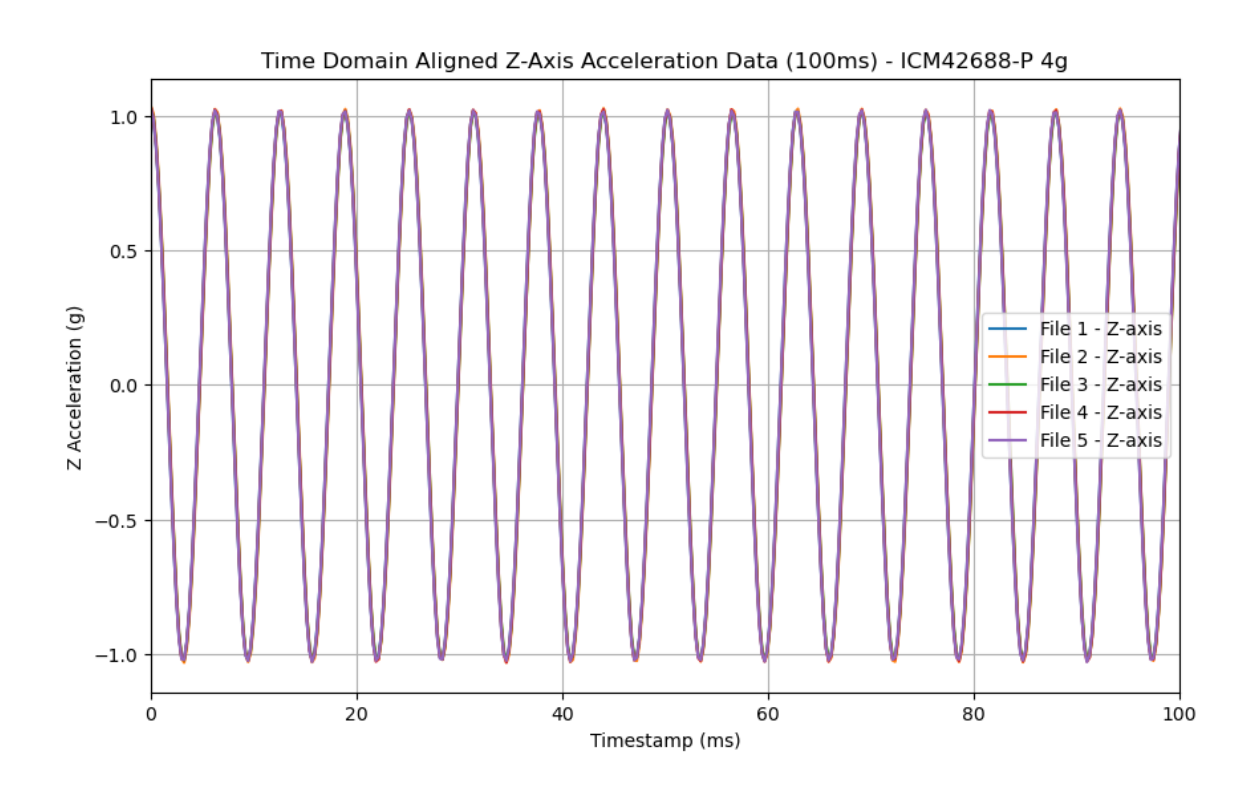


Figure 142: ICM-42688-P magnet mounted 4 g Time-domain plot 1 g Pk

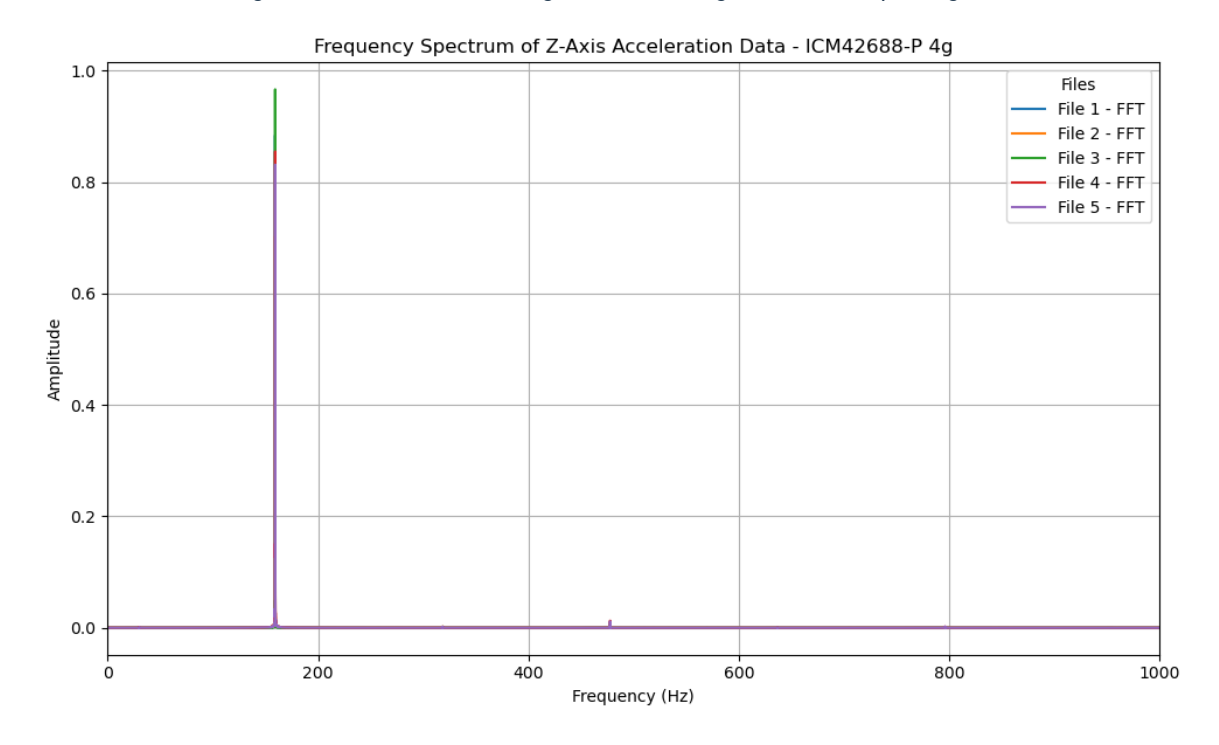


Figure 143: ICM-42688-P magnet mounted 4 g Frequency-domain plot 1 g Pk

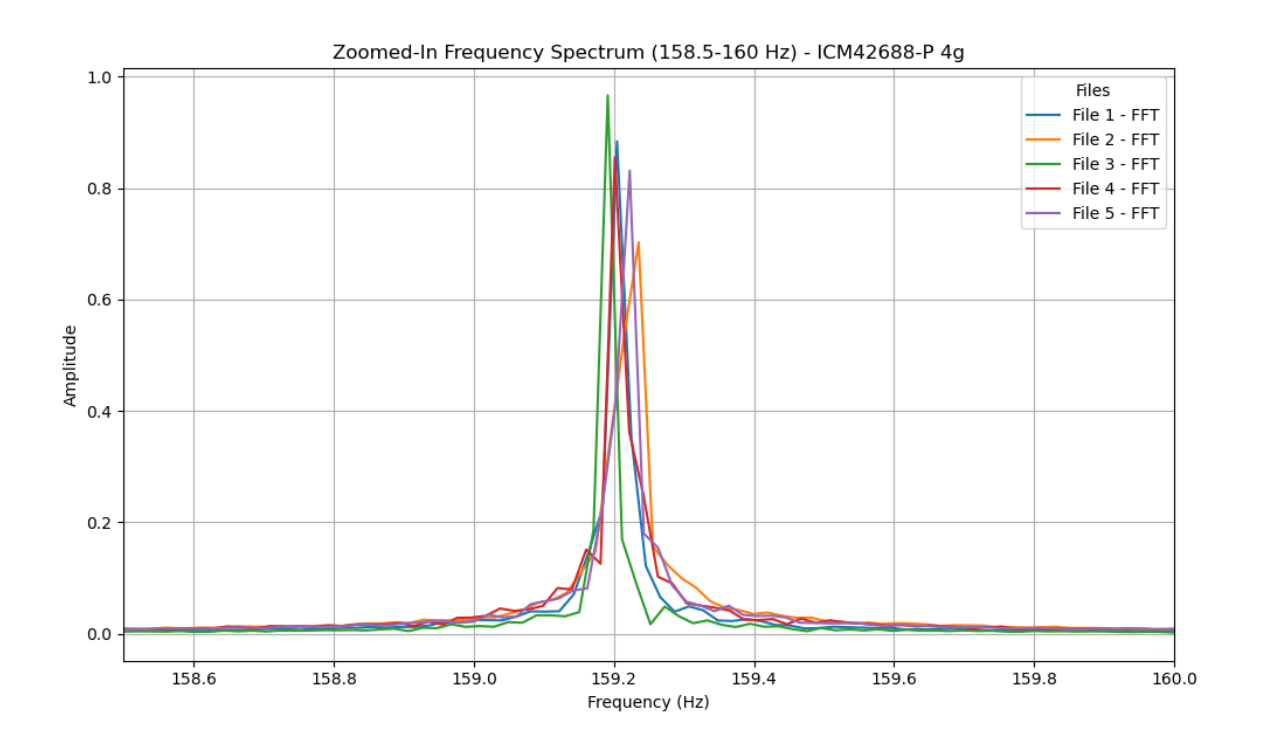


Figure 144: ICM-42688-P magnet mounted 4 g Frequency-domain plot peak 1 g Pk

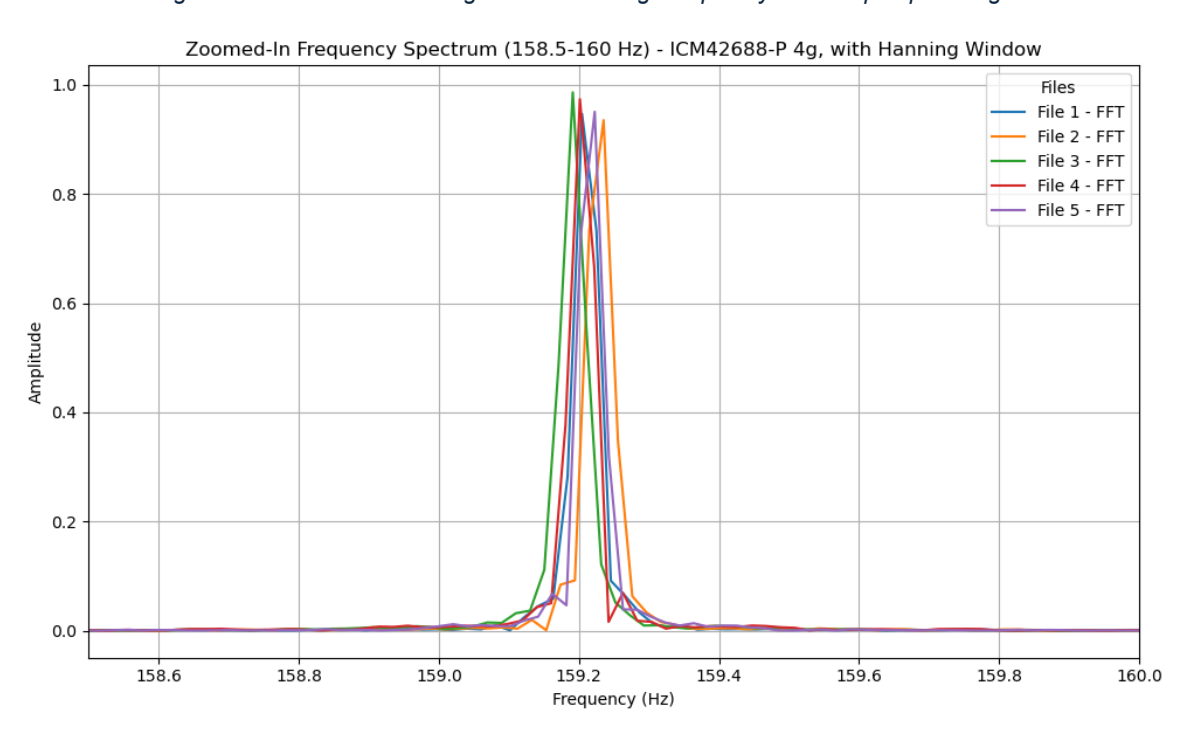


Figure 145: ICM-42688-P magnet mounted 4 g Frequency-domain plot peak windowed 1 g Pk

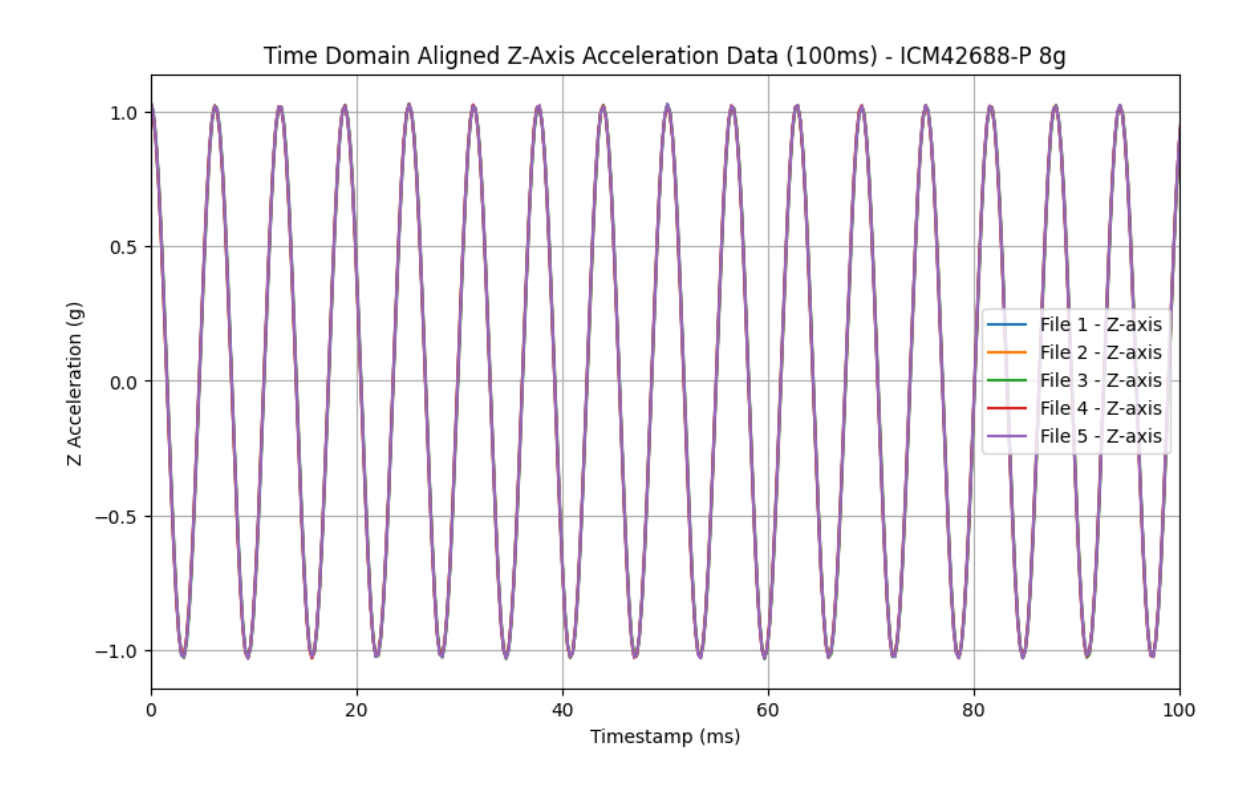


Figure 146: ICM-42688-P magnet mounted 8 g Time-domain plot 1 g Pk

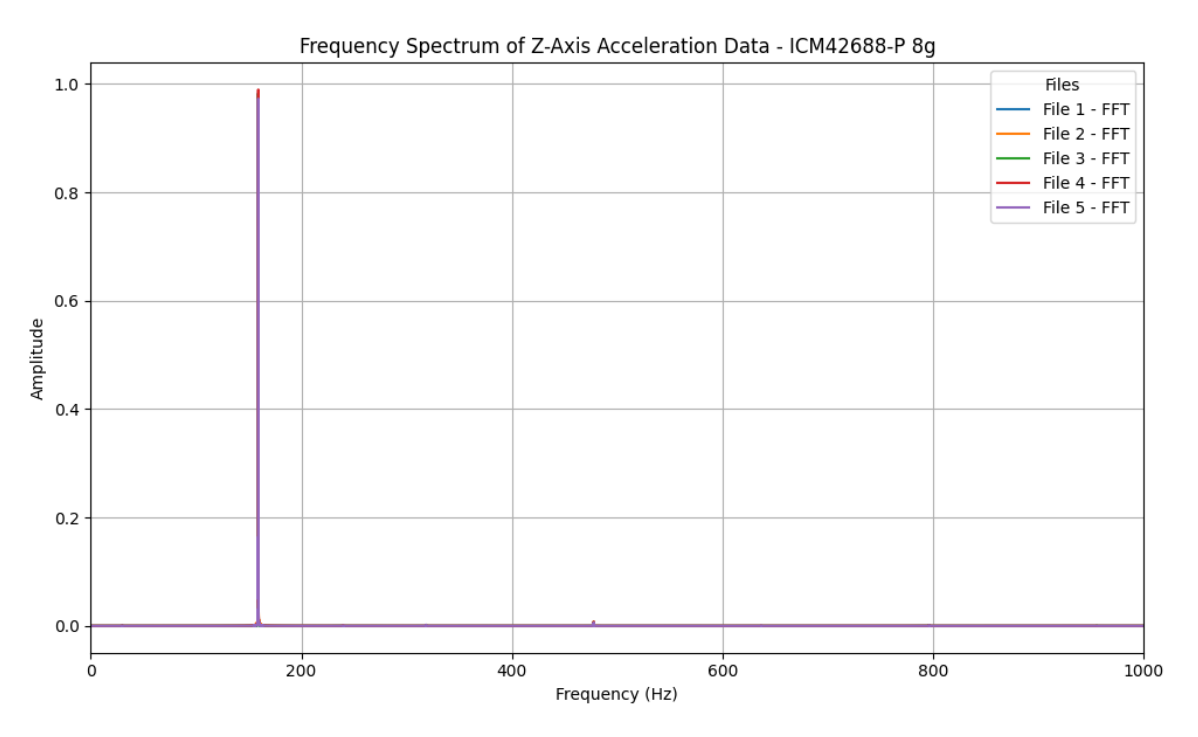


Figure 147: ICM-42688-P magnet mounted 8 g Frequency-domain plot 1 g Pk

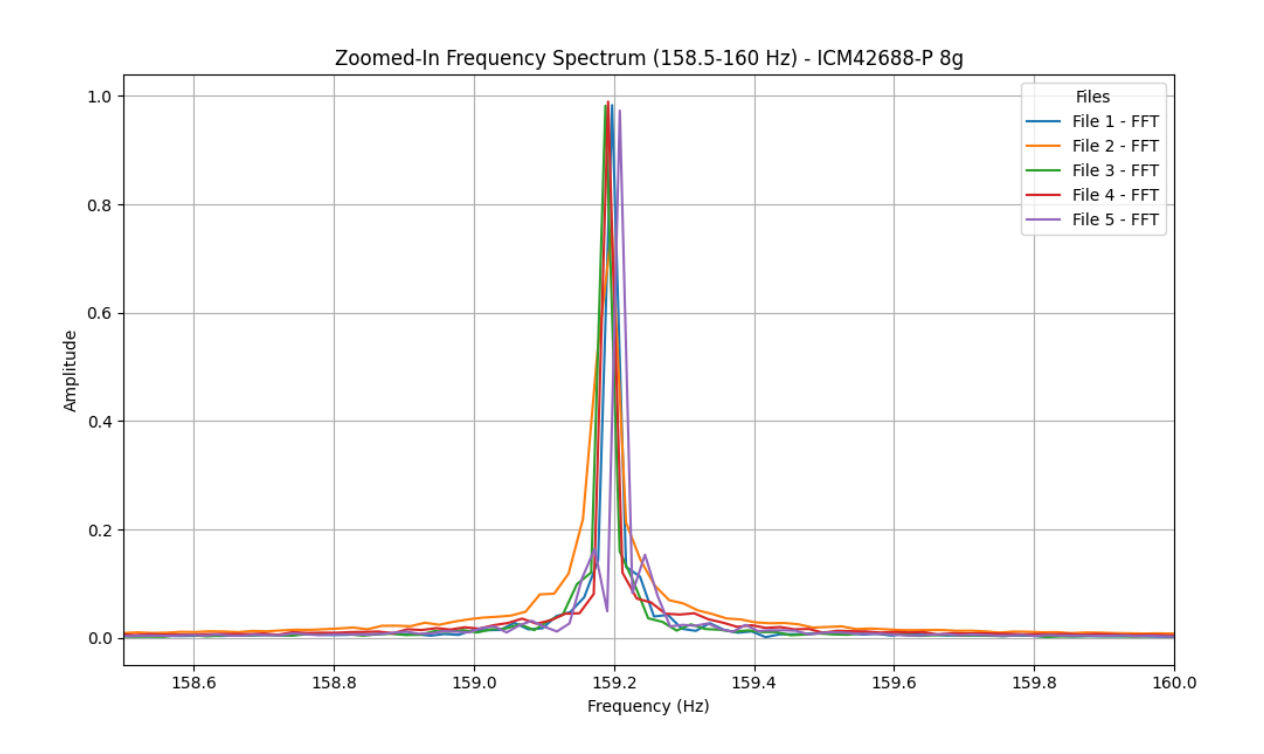


Figure 148: ICM-42688-P magnet mounted 8 g Frequency-domain plot peak 1 g Pk

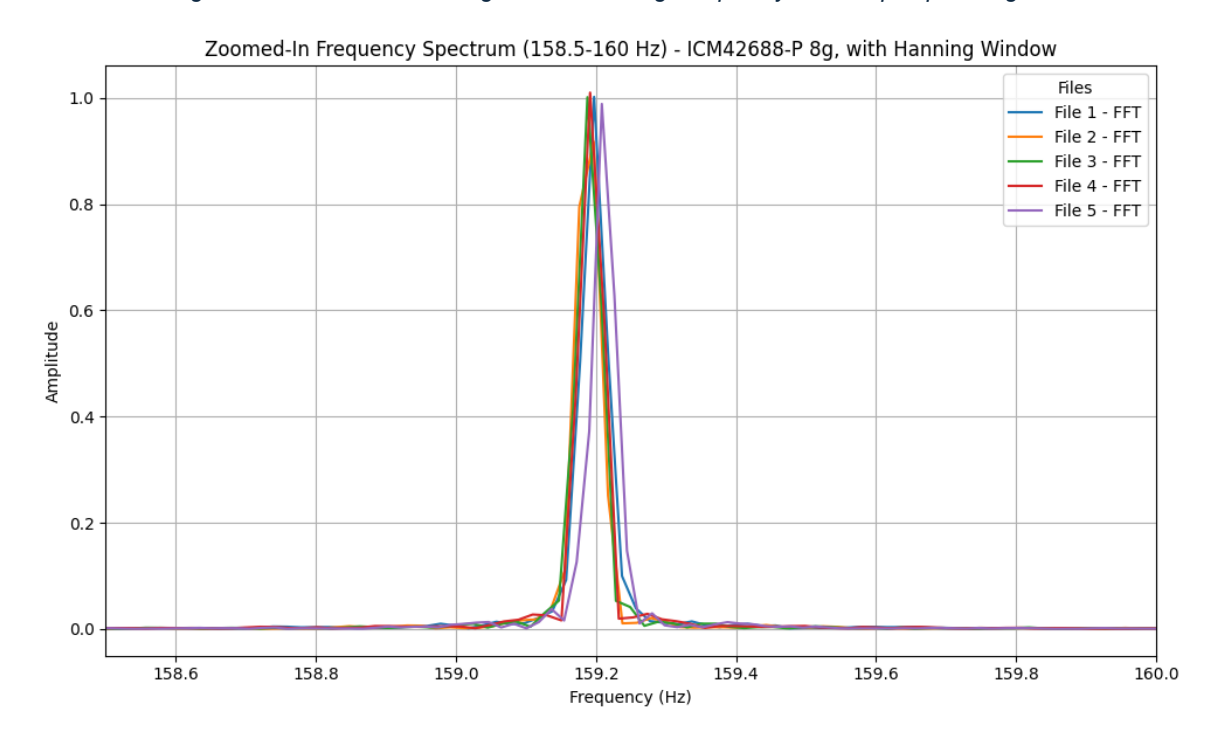


Figure 149: ICM-42688-P magnet mounted 8 g Frequency-domain plot peak windowed 1 g Pk

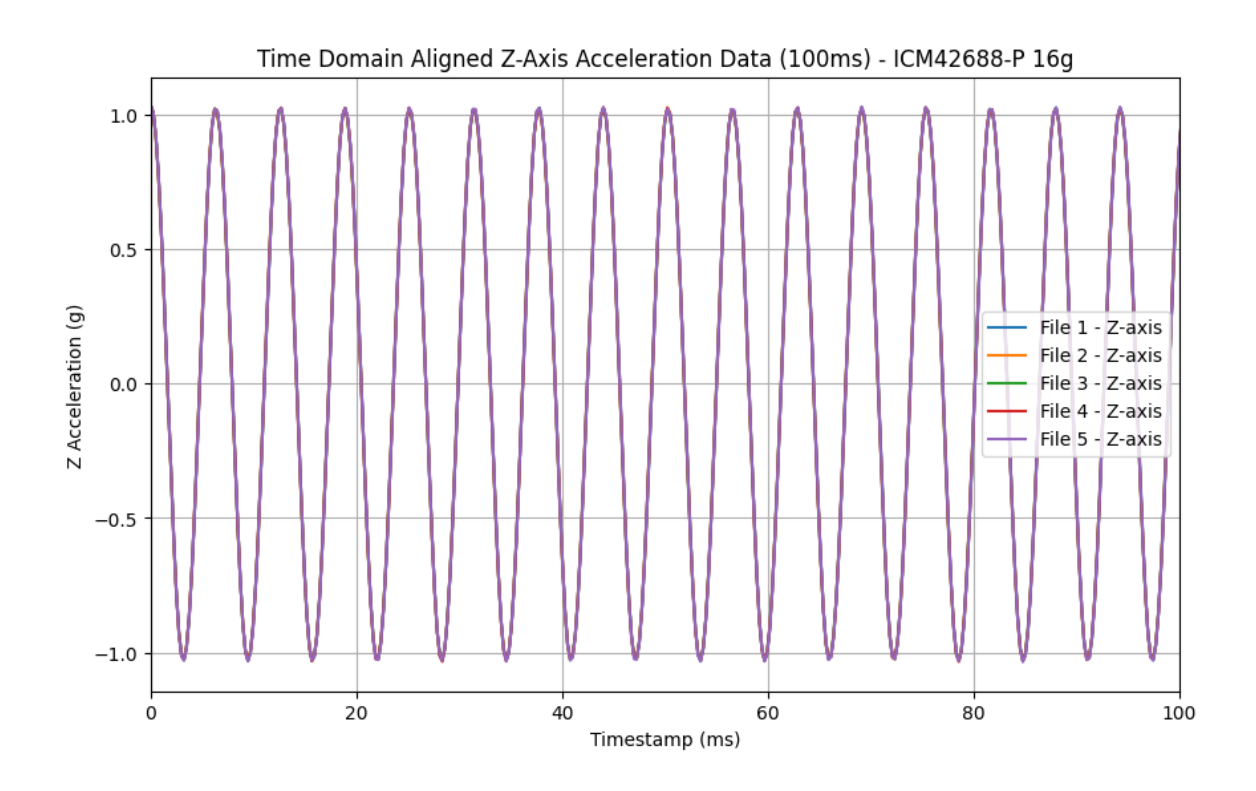


Figure 150: ICM-42688-P magnet mounted 16 g Time-domain plot 1 g Pk

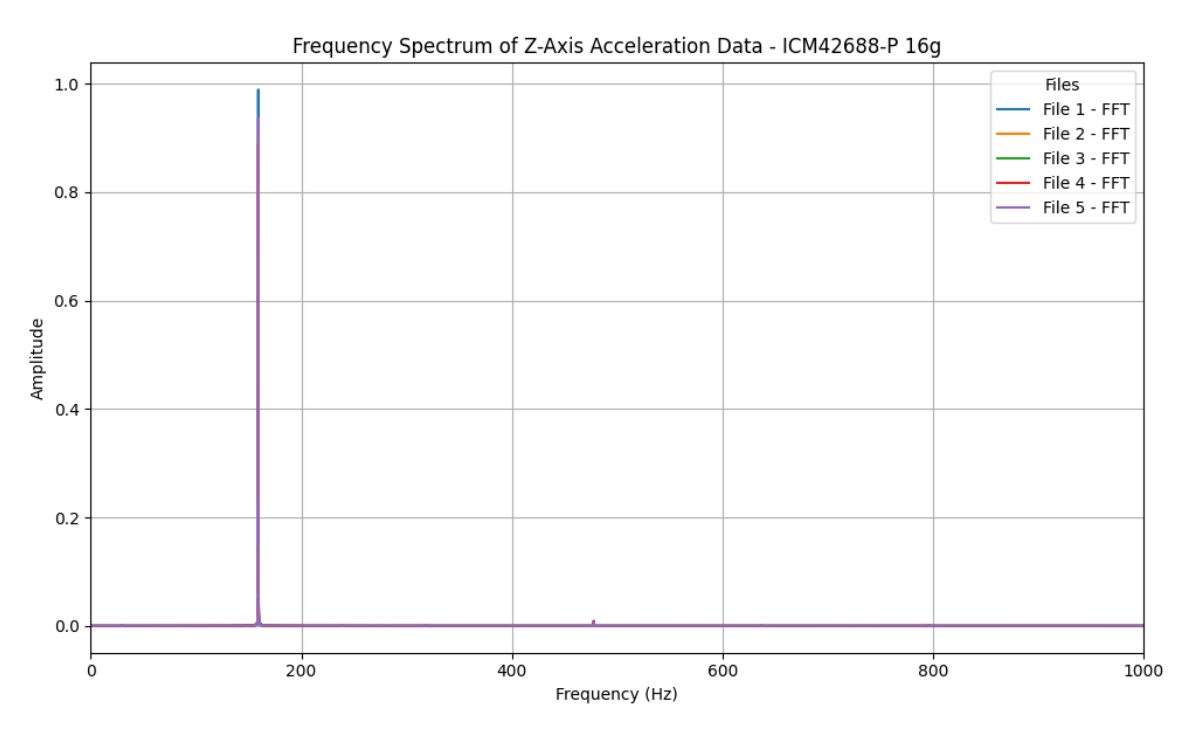


Figure 151: ICM-42688-P magnet mounted 16 g Frequency-domain plot 1 g Pk

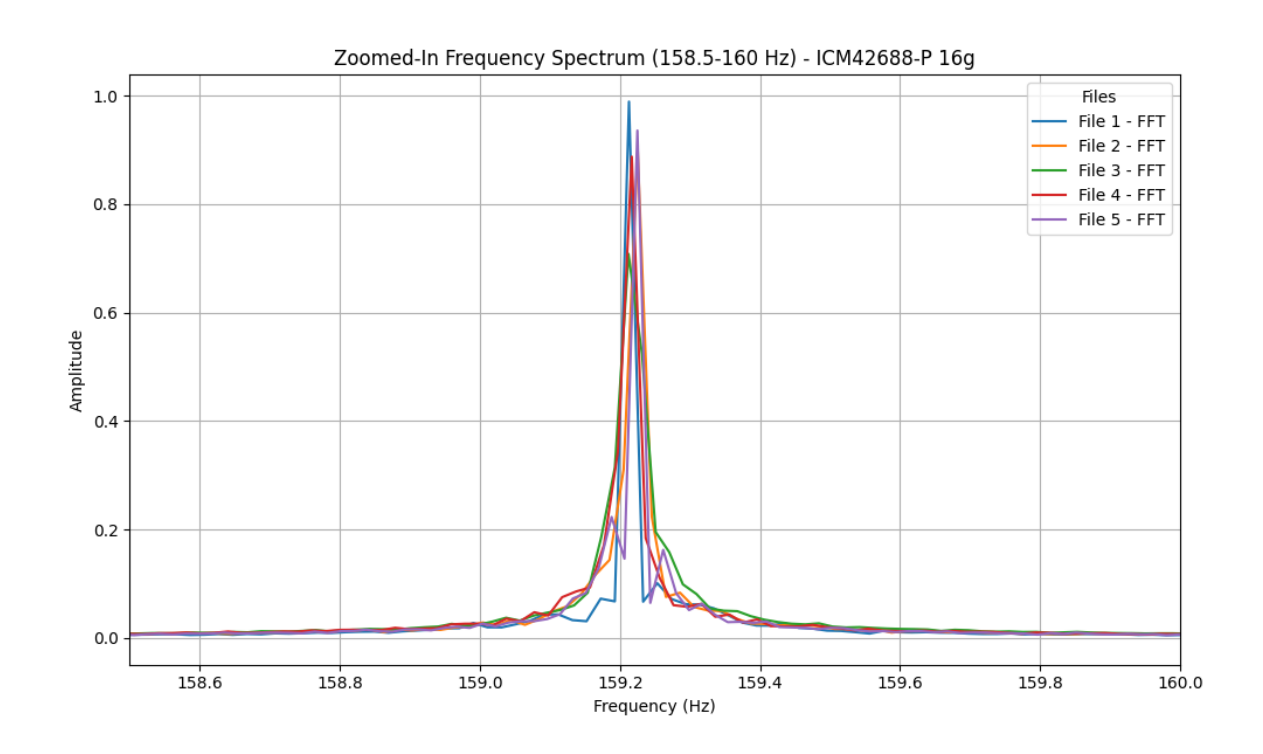


Figure 152: ICM-42688-P magnet mounted 16 g Frequency-domain plot peak 1 g Pk

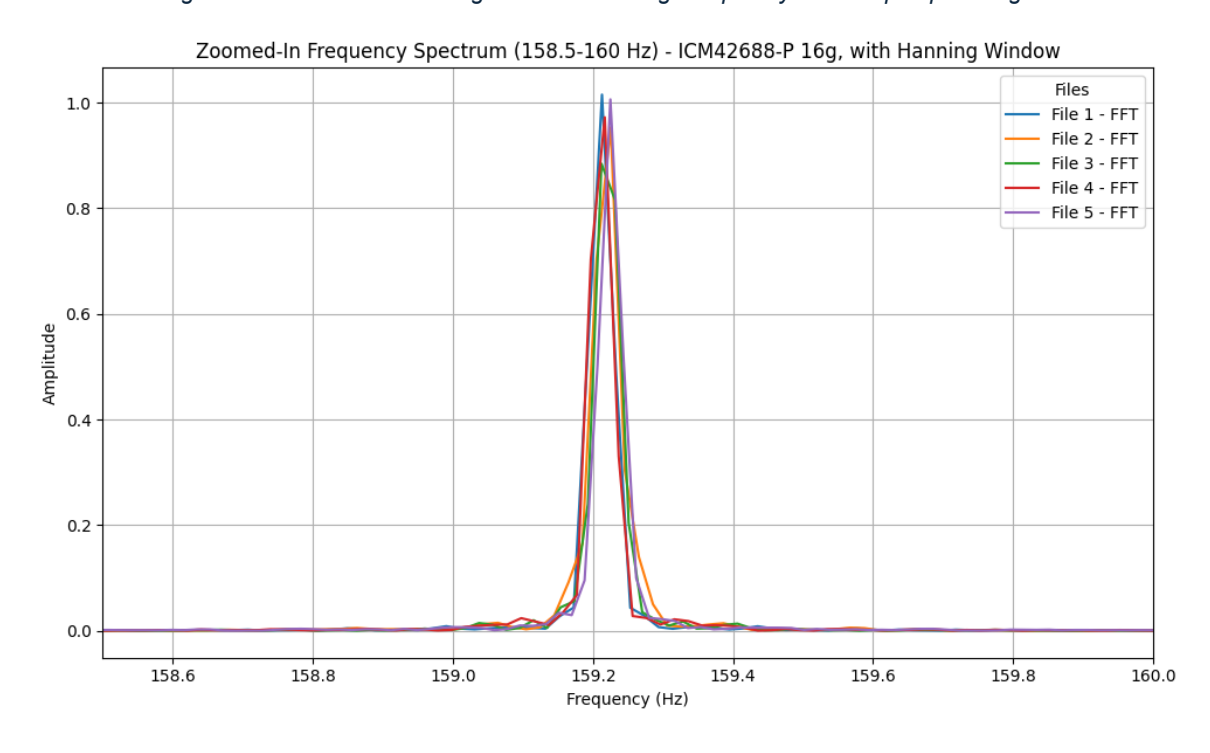


Figure 153: ICM-42688-P magnet mounted 16 g Frequency-domain plot peak windowed 1 g Pk

8.1.5 IEPE Reference - PB352C03

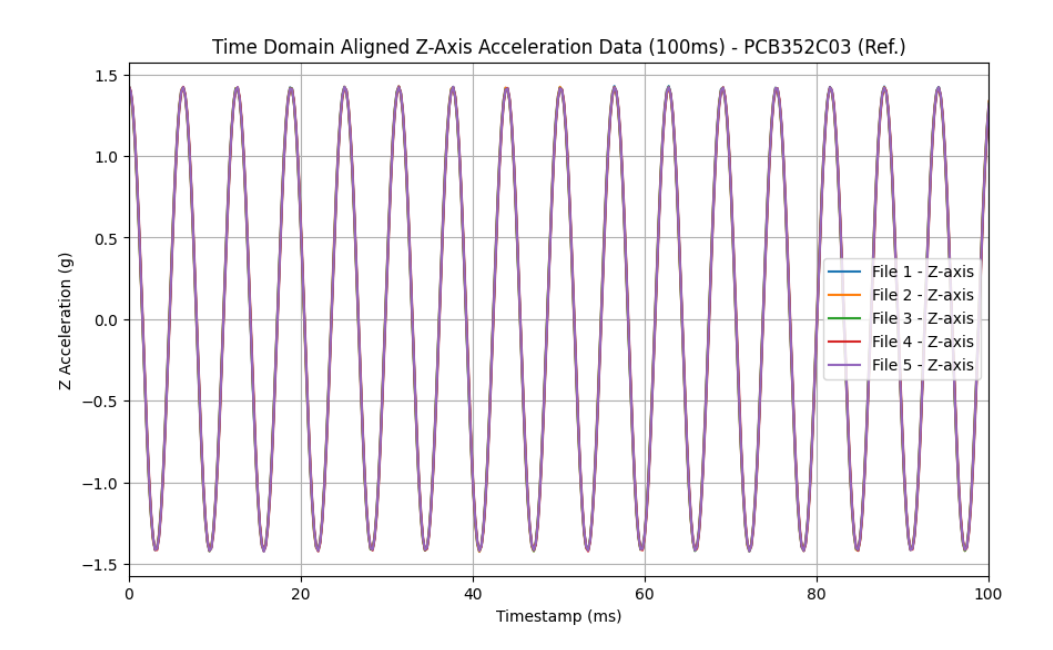


Figure 154: IEPE Reference PB352C03 Time-domain plot

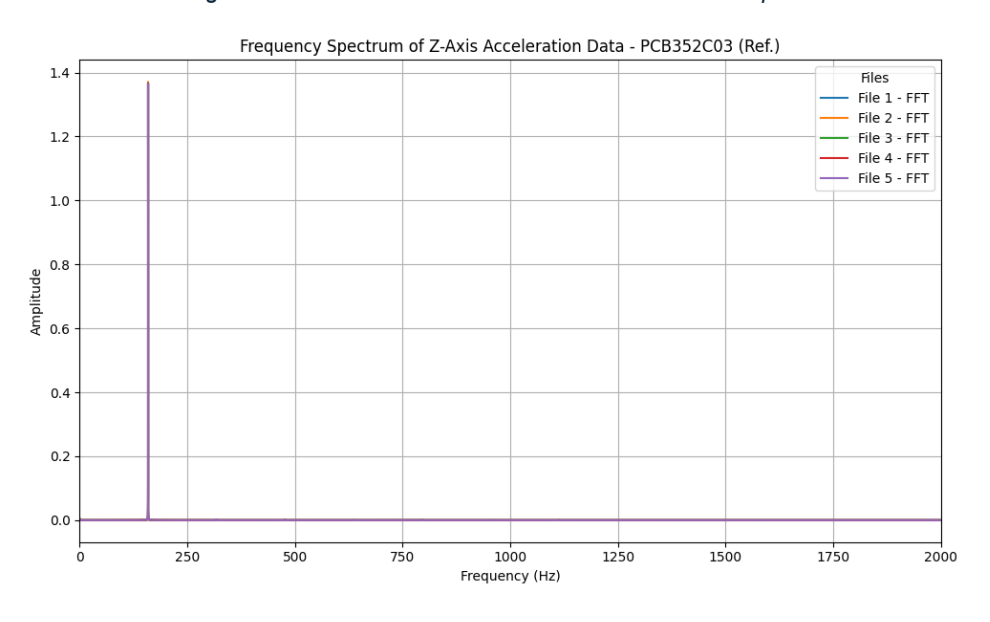


Figure 155: IEPE Reference PB352C03 Frequency-domain plot

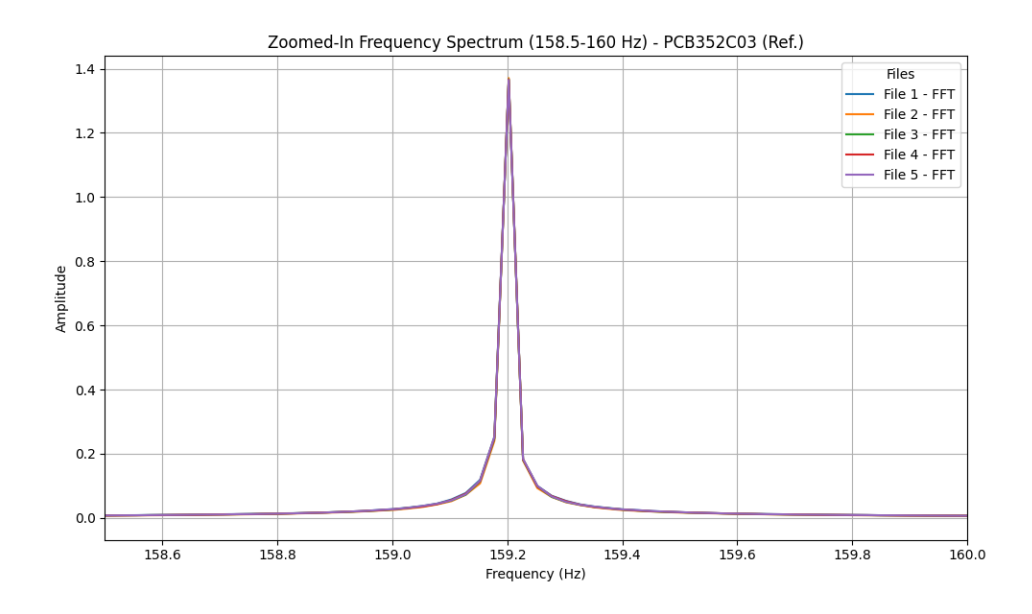


Figure 156: IEPE Reference PB352C03 Frequency-domain plot peak

8.2 Test 2 Graphs Static Data (Powered On vs Off)

Below, the IEPE static PSD plots from test 2 are presented. These plots are the same as those shown in test 1 static testing but are included to show the baseline noise levels measured at the testbed locations. In addition to the powered off static noise, the plots also include measurements taken while the testbed was powered on, as described in the test 2 section above, showing the B3 noise increases from the testbed moving to maintain position while the LRR sensor stayed consistent.

8.2.1 ADXL-357 & IEPE (4 kHz Sampling Rate)

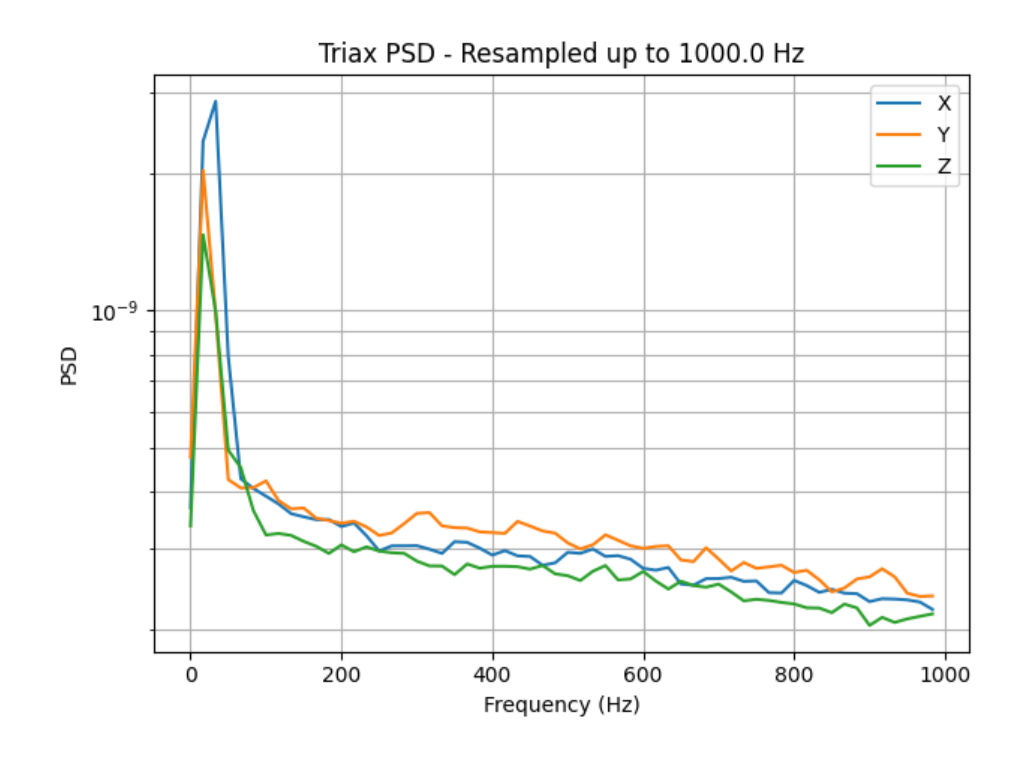


Figure 157: Test 2 static powered off – IEPE B3

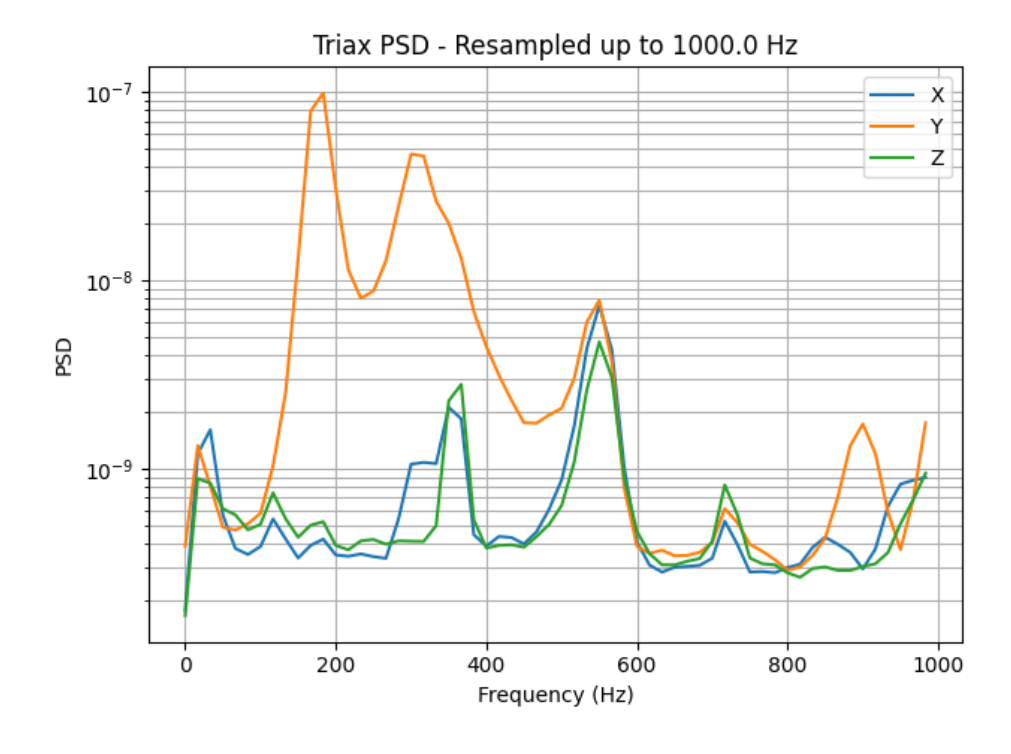


Figure 158: Test 2 static powered on – IEPE B3

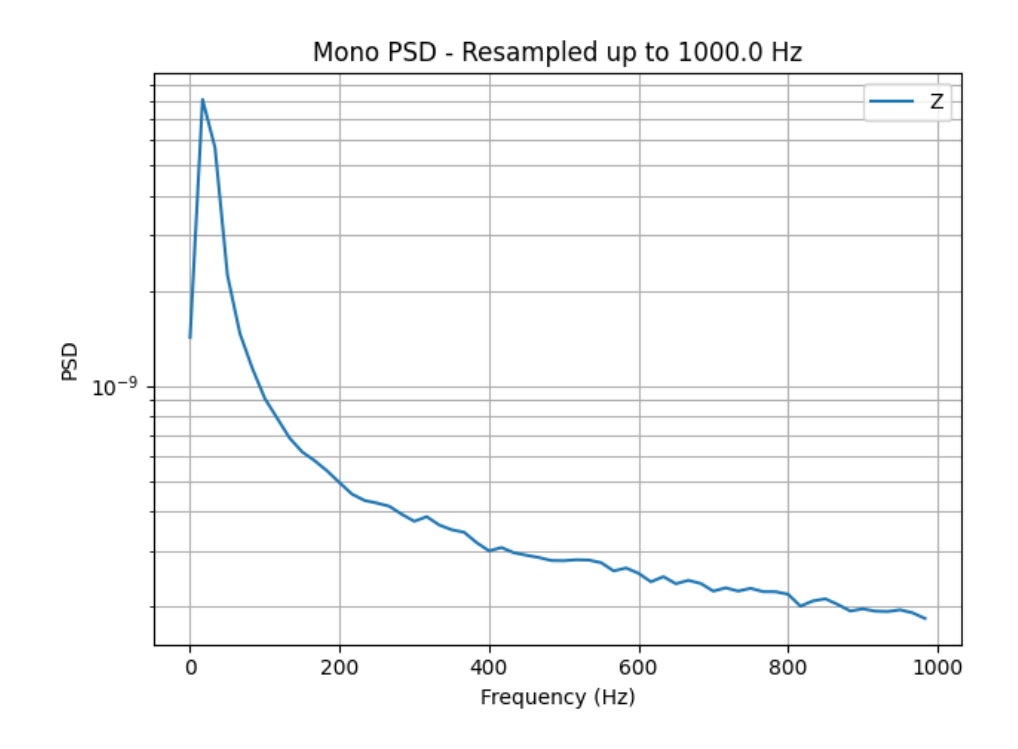


Figure 159: Test 2 static powered off – IEPR LRR

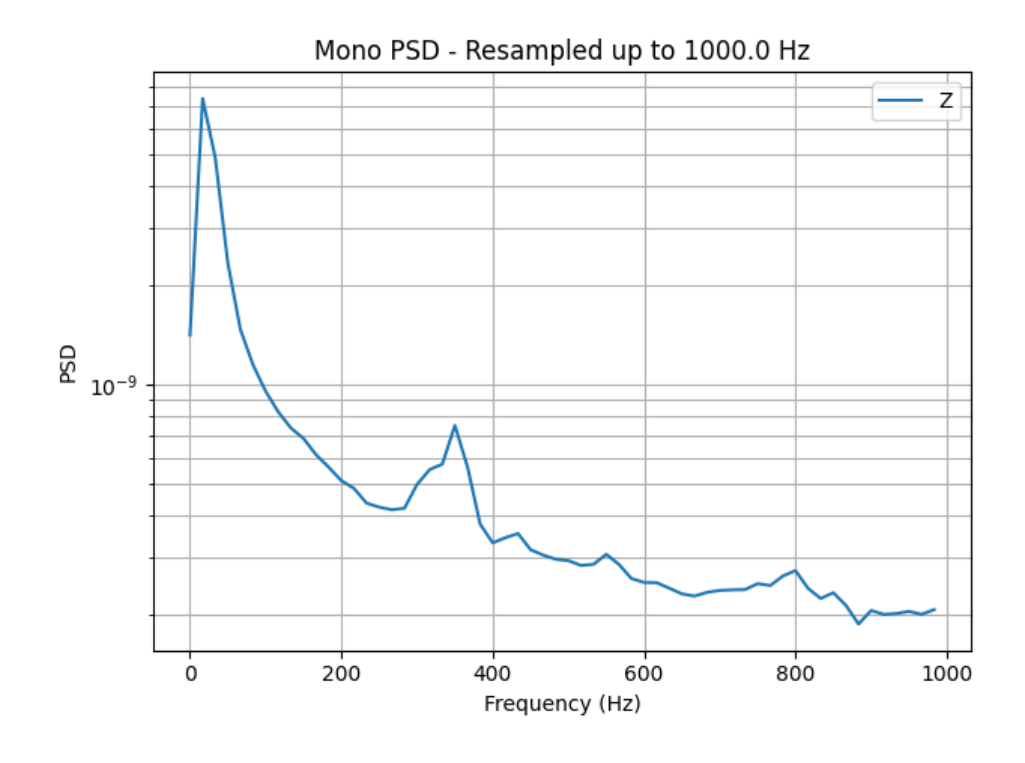


Figure 160: Test 2 static powered on – IEPE LRR

8.2.2 ICM-42688-P & IEPE (16 kHz Sampling Rate)

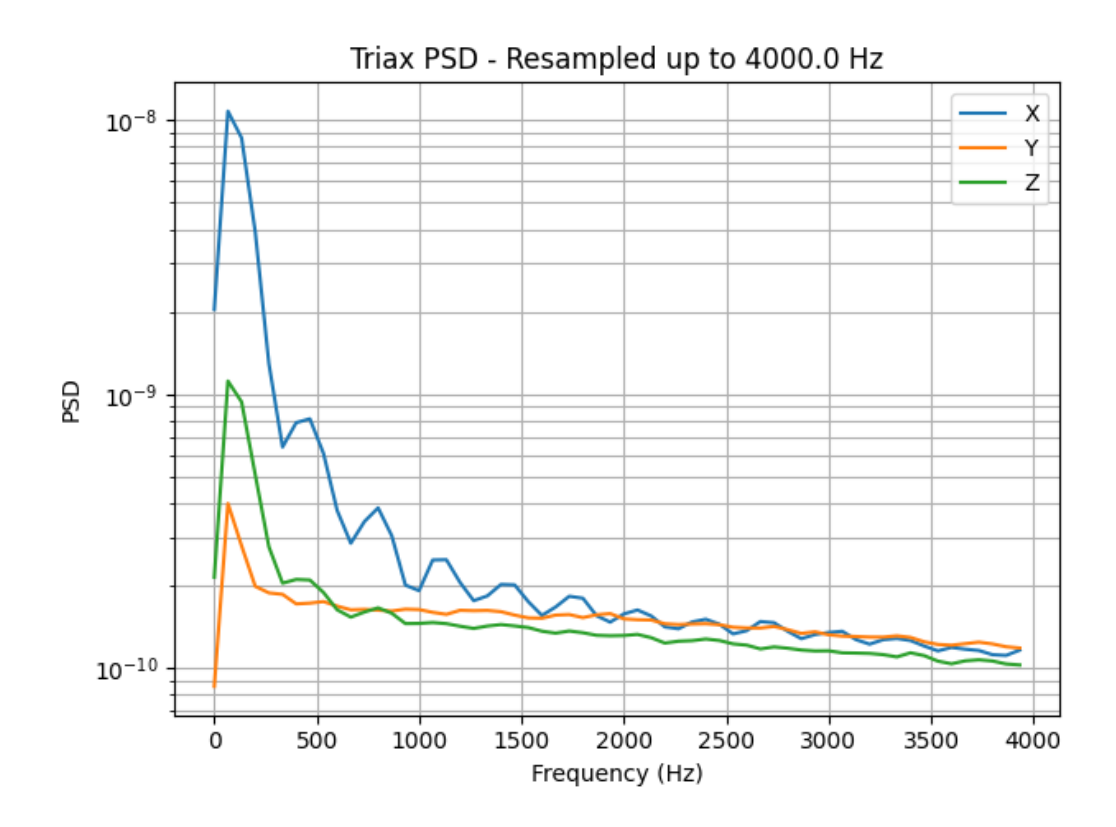


Figure 161: Test 2 static powered off, IEPE B3

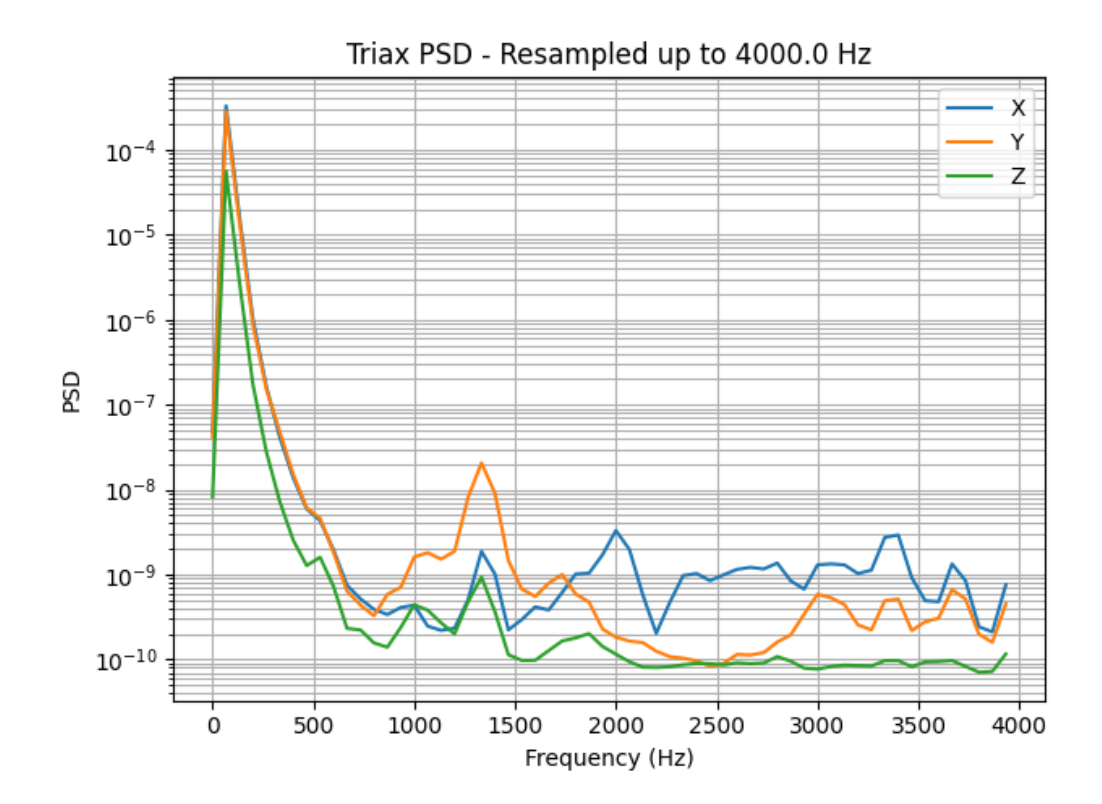


Figure 162: Test 2 static powered on, IEPE B3

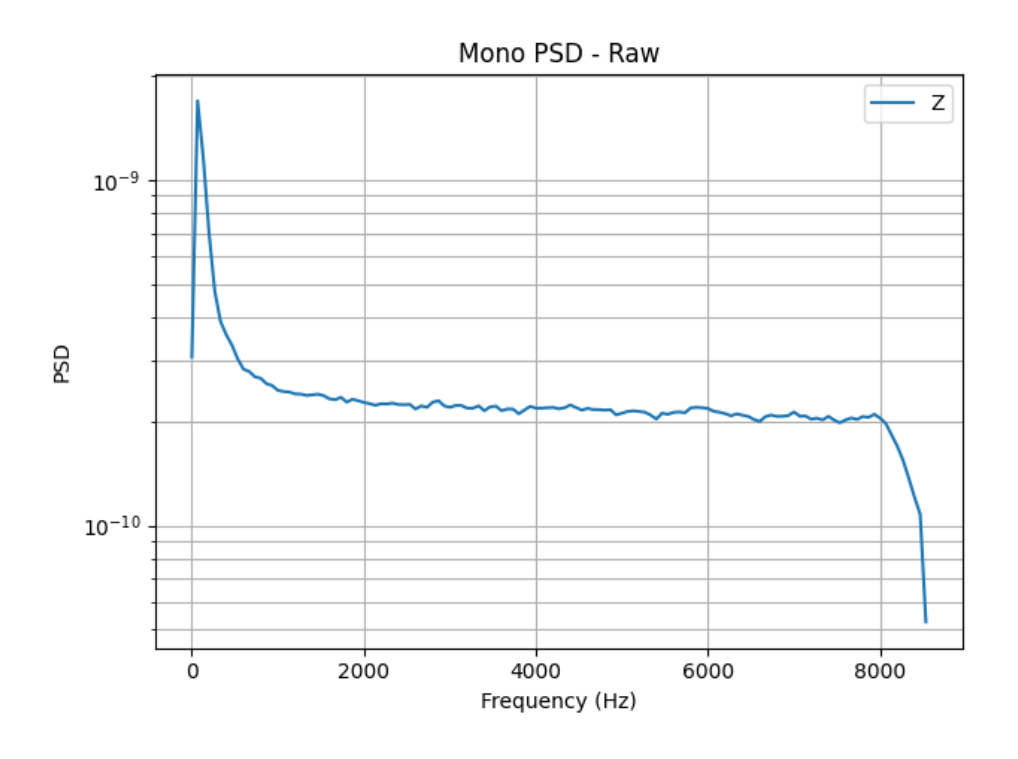


Figure 163: Test 2 static powered off, IEPE LRR (Full 8 kHz)

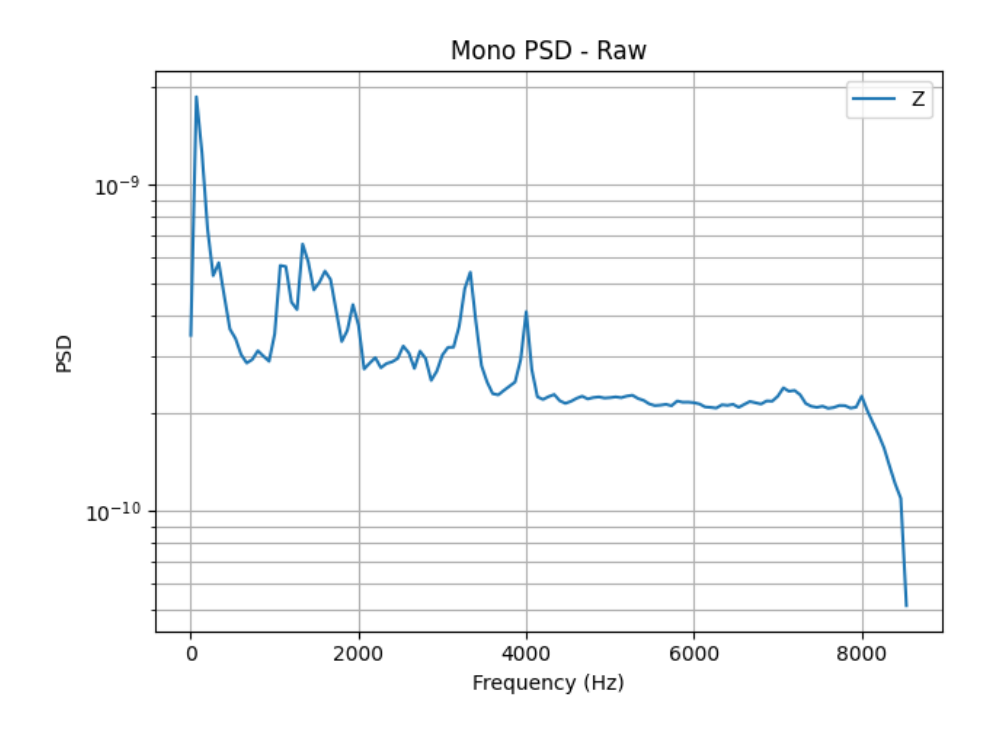


Figure 164: Test 2 static powered on, IEPE LRR (Full 8 kHz)

8.3 Test 2 High-Speed B3

The graphs from the high-speed tests have been included below for reference.

Due to the high peaks of the IEPE measurements, these were not used for comparison. The peaks can be seen most clearly in the Z axis. The sensors were moved, switched out with other sensors, and re-wired without getting rid of these errors.

Although this means the samples are not useful for comparing the IEPE to MEMS, this shows one of the challenges of using wired sensors, especially for moving components, as errors like this can be caused by any part of the signal measurement chain. There were no visible peaks in the other low and medium speed tests, but this error may also be affecting those measurements to a lower, less noticeable extent.

8.3.1 ADXL-357 High-Speed B3 Graphs

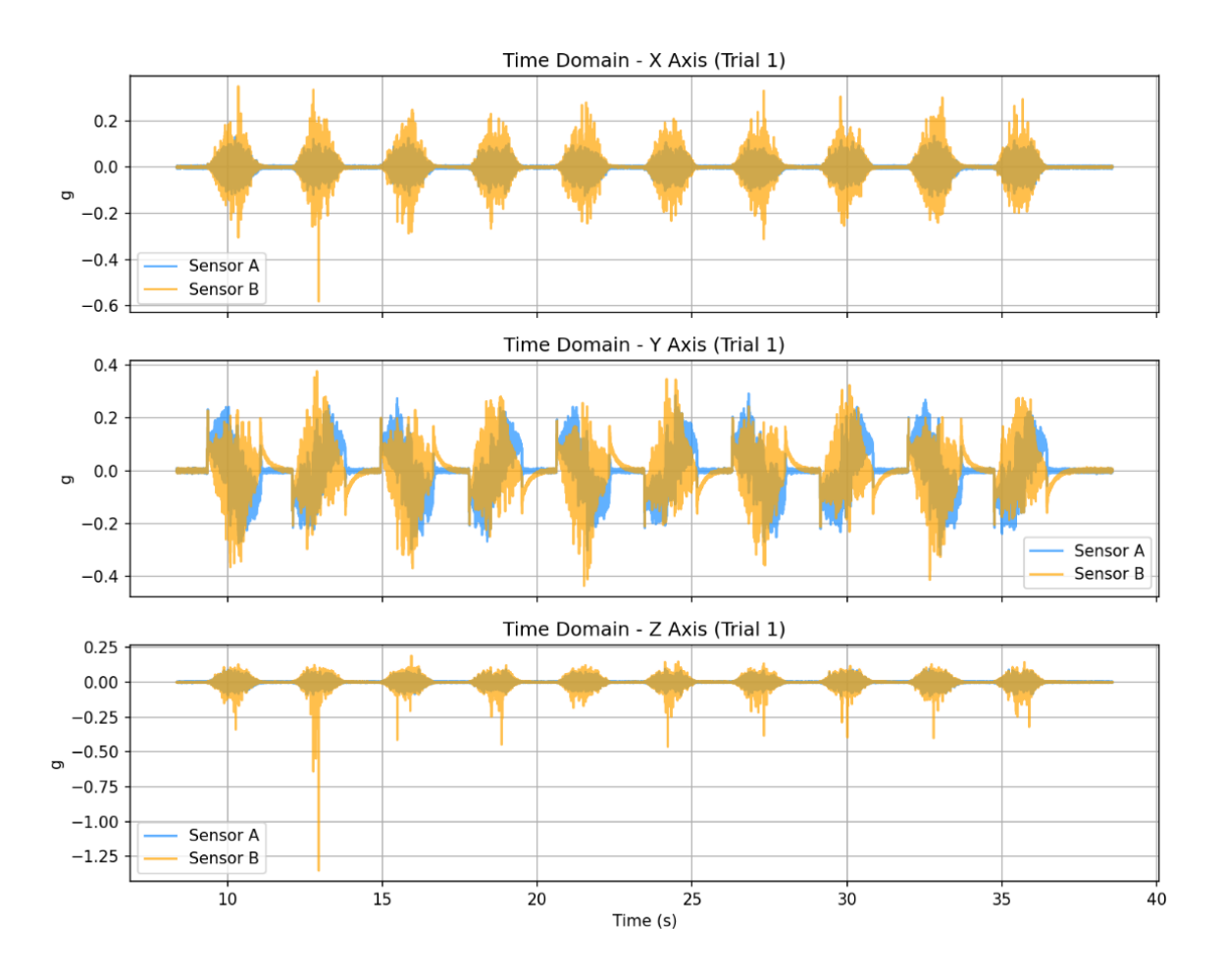


Figure 165:Time domain B3 ADXL-357 (Blue) vs IEPE (Yellow), high speed

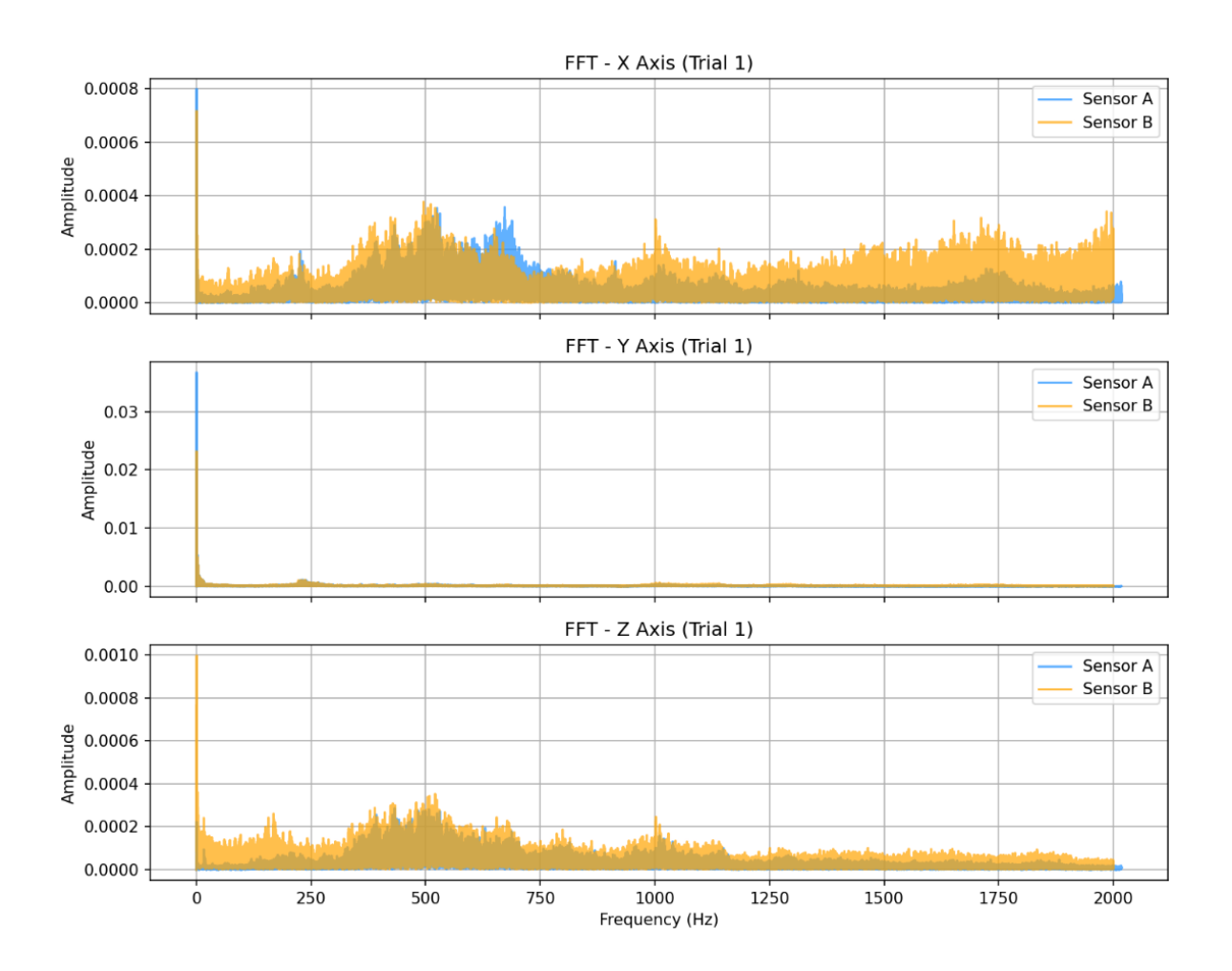


Figure 166: FFT B3 ADXL-357 (Blue) vs IEPE (Yellow), high speed

8.3.2 ICM-42688-P High-Speed B3 Graphs

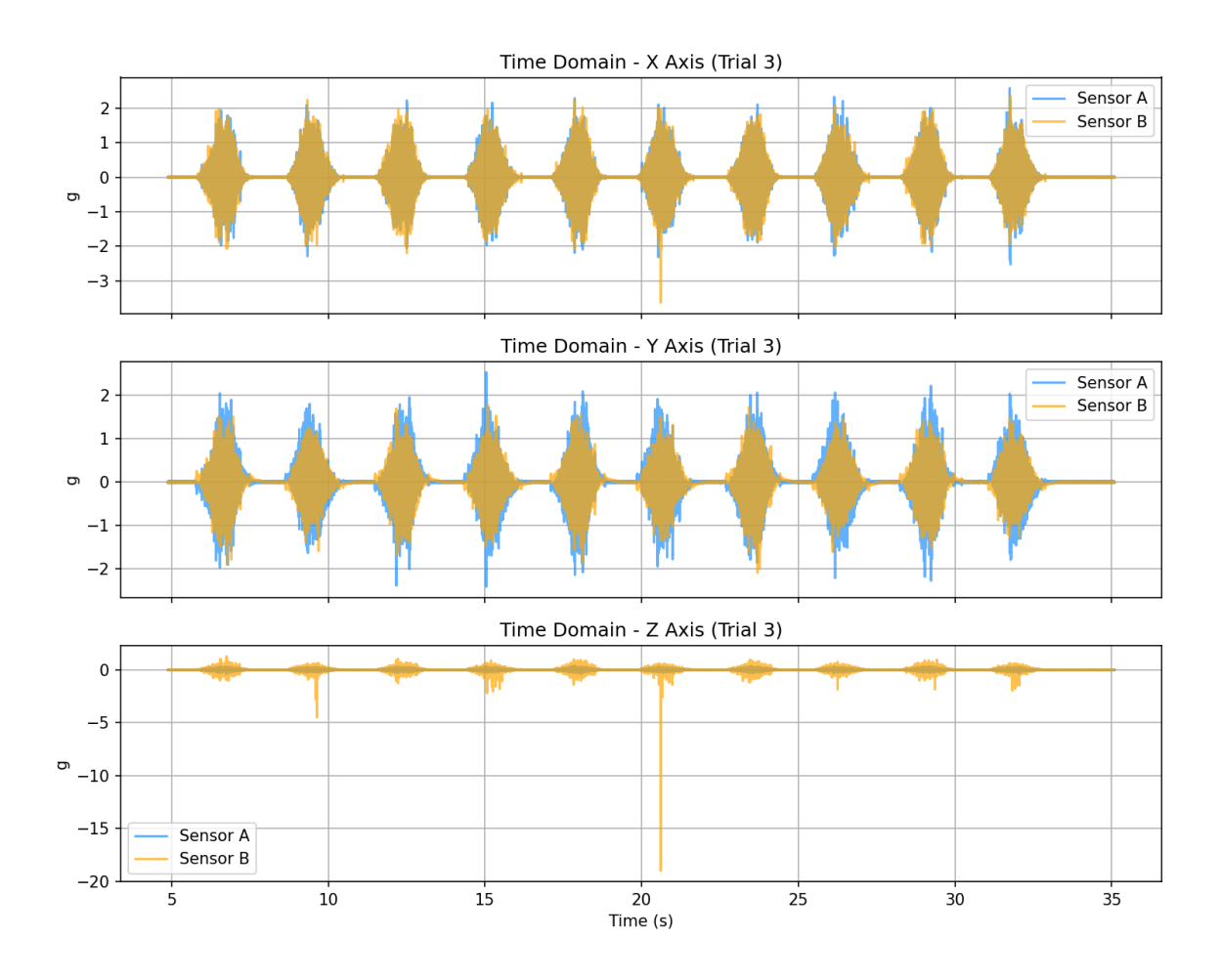


Figure 167: Time domain B3 ICM-42688-P (Blue) vs IEPE (Yellow), high speed

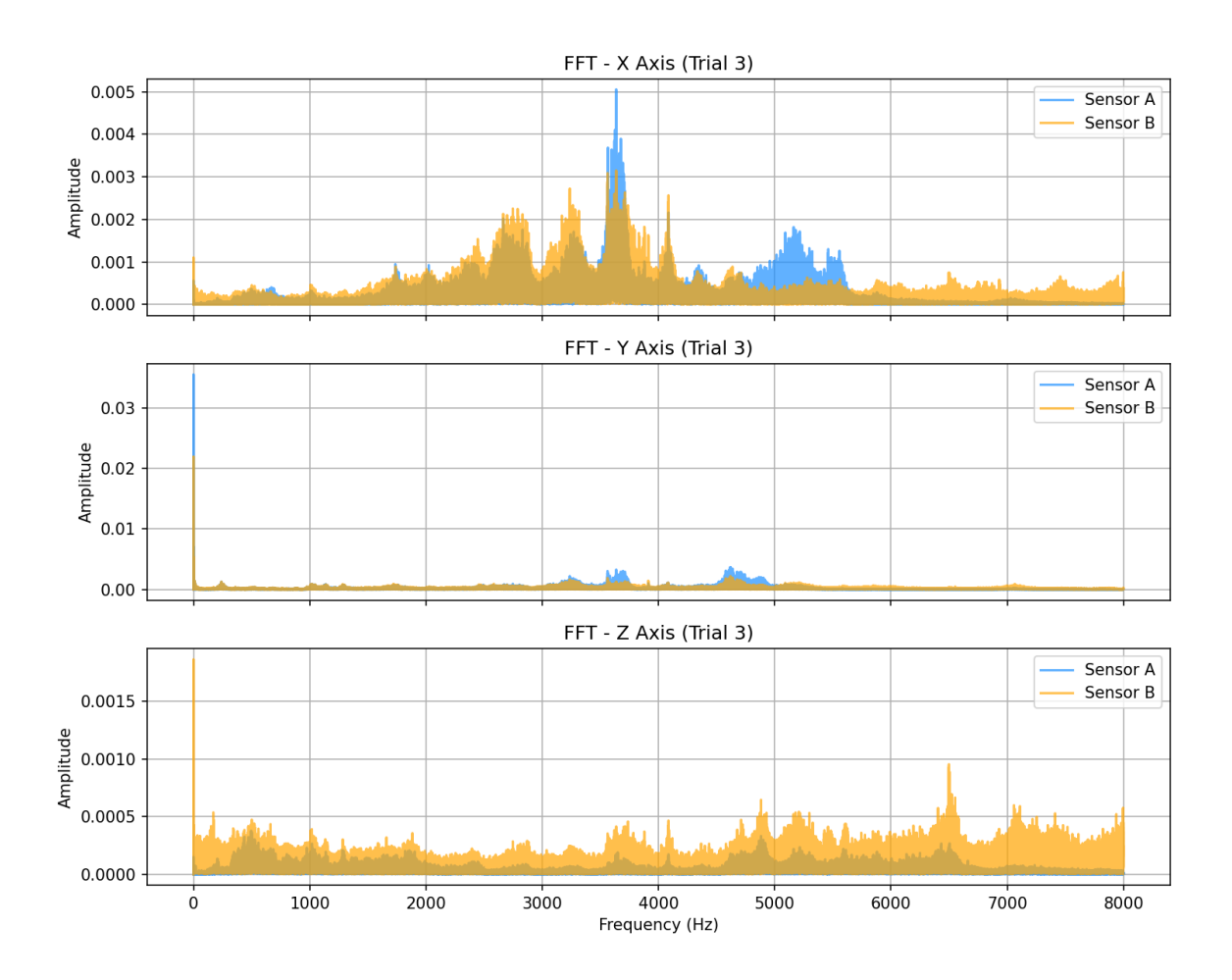


Figure 168: FFT B3 ICM-42688-P (Blue) vs IEPE (Yellow), high speed